

Infrared spectroelectrochemical study of *E. coli* NiFe hydrogenase 1



Ricardo Hidalgo González

Lincoln College

Trinity Term 2016

A thesis submitted to the Board of the Faculty of Physical Sciences, for the degree of

Doctor of Philosophy, University of Oxford

Infrared spectroelectrochemical study of *E. coli* NiFe hydrogenase 1

Ricardo Hidalgo González, Lincoln College, University of Oxford

A thesis submitted for the degree of Doctor of Philosophy, Trinity Term 2016

This thesis investigates the catalytic mechanism of NiFe hydrogenases. The specific enzyme studied in this work, *E. coli* Hyd-1, is an efficient catalyst for H₂ oxidation even in the presence of O₂. A method for studying the chemistry of the active site of this enzyme, under catalytic conditions, is developed. The combination of IR spectroscopy with protein film electrochemistry *in situ* is demonstrated. This was achieved by adsorbing the hydrogenase on a high surface area carbon nanoparticle electrode; and by the design of a spectroelectrochemical flow cell that provides efficient mass transport conditions.

A complete redox characterisation of the active site for a hydrogenase immobilised on a carbon electrode is described for the first time. The study of the effect of pH on the distribution of redox states demonstrates the existence of a pH equilibrium between the Ni-C and the Ni-L states. It is shown that the active site responds to the pH of the external solution, and that the increase in pH acts as a driving force that removes the proton further away from the active site.

Studies under electrocatalytic conditions provides direct evidence of intermediates of the catalytic cycle. The role of Ni-SI, Ni-R, and Ni-C is confirmed. Furthermore, Ni-L is detected under turnover conditions and therefore shown to be an important intermediate in the cycle. The detection of different protonation states of Ni-L and Ni-R is proposed to provide information on the transport of the protons as they start to move away from the active site.

In the investigation of O₂ inhibition, Ni-B (detected spectroscopically) is directly related to the loss in activity upon the attack of O₂ for the first time. Also, the formation of solely Ni-B from the reaction with O₂ (no other O₂-damaged species are detected) provides further evidence on the ability of O₂-tolerant hydrogenases of having an effective mechanism for dealing with O₂ tolerance.

A thorough study on the interaction of CO with Hyd-1 proves unequivocally that this O₂-tolerant hydrogenase does bind CO, and that CO does inhibit its catalytic activity (both H₂ and H⁺ reduction). This helps clarify how CO interacts with O₂-tolerant hydrogenases.

Overall, the work in this thesis contributed to the understanding of key mechanistic aspects in O₂-tolerant hydrogenases. The technique for combining protein film electrochemistry with IR spectroscopy *in situ* shall provide valuable opportunities for providing new insight into the mechanisms of hydrogenases and other metalloenzymes that bind small molecules.

Acknowledgements

I would first like to thank my supervisor Kylie Vincent. She has been supportive and helpful at all times over the past years. I am grateful to her for having given me for the opportunity to be here, and for the guidance and encouragement provided whenever needed throughout my life as a DPhil student.

Special thanks go to Philip Ash. He “patiently” guided me through the early days of my DPhil, and always provided very helpful discussion and input thereafter. My project would not have been the same without his most valuable assistance.

I sincerely thank Jonathan Quinson. I remember he taught me how to do electrochemistry of FMN on particles in my first day in the lab, he has become a good friend since. I thank him for helpful discussion and advice on carbon materials throughout my project. Ian McPherson always provided helpful comments and very clever discussion about our work, and about chemistry in general (he still makes me doubt whether I really understand spoken English at all). I also thank Min-Wen for all the discussion and input on the mysterious art of adsorbing hydrogenases on carbon particles, as well as on hydrogenase chemistry in general.

I thank all the members of the Vincent group. I thank Holly for always being very helpful on all matters. Gary, Tom, Tianze, Ceren, Pong, Adam, Dan, Simantini, made every day in the lab a pleasant one. Matteo, for his unique and cheerful character and for incredibly interesting philosophical discussions about the nature of chemistry and science, which diverted us from doing “real” science a couple of times.

I am grateful to Ministerio de Ciencia y Tecnología de Costa Rica, and Universidad de Costa Rica for supporting my studies. I also thank Lincoln College for financial support.

I thank my parents for their immense support and motivation, especially when it comes to education. Most important of all, I thank my wife Silvia. For her company, unconditional support, patience and love that have made all this possible.

Abbreviations

<i>A. aeolicus</i>	<i>Aquifex aeolicus</i>
A	ampere
ATR	attenuated total reflectance
E	electrode potential
E⁰	reduction potential
SEC	spectroelectrochemistry / spectroelectrochemical
CV	cyclic voltammetry
IR	infrared
<i>D. vulgaris MF</i>	<i>Desulfovibrio vulgaris Miyazaki F</i>
<i>R. eutropha</i>	<i>Ralstonia eutropha</i>
EPR	electron paramagnetic resonance
DFT	density functional theory
ν_{CO}	carbon monoxide stretch
ν_{CN}	cyanide stretch
RDE	rotating disc electrode
PFE	protein film electrochemistry
FMN	flavin mononucleotide
<i>E. coli</i>	<i>Escherichia coli</i>
SHE	standard hydrogen electrode
SCE	saturated calomel electrode
PFIRE	protein film infrared electrochemistry
RE	reference electrode
IRE	Internal reflection element

Table of contents

Chapter 1 Introduction	1
1.1 Hydrogenase enzymes	2
1.1.1 H ₂ chemistry and its role in nature	2
1.1.2 Hydrogenases as models for future energy technology	3
1.2 Classification of hydrogenases	4
1.2.1 Fe-only hydrogenases	4
1.2.2 FeFe hydrogenases	5
1.3 NiFe hydrogenases	7
1.3.1 Structure	9
1.3.2 Activity and dynamics of NiFe hydrogenases	17
1.3.3 More on the O ₂ -tolerance of NiFe hydrogenases	21
1.3.4 The catalytic mechanism	23
1.4 Aims and scopes of this thesis	25
References	27
Chapter 2 Theory	37
2.1 Electrochemistry	38
2.1.1 Electron transfer reactions	38
2.1.2 Electrode processes	43
2.1.3 Equilibrium Electrochemistry	47
2.1.4 Electrocatalysis and non-equilibrium electrochemistry	51

2.2 Infrared spectroscopy	57
2.2.1 Physical principles of IR absorption	57
2.2.2 Attenuated total reflection IR spectroscopy	61
2.2.3 IR spectra of metal carbonyls	63
References	65
Chapter 3 Method development	67
3.1 Introduction	68
3.1.1 Justification and background	68
3.2 Challenges in combining PFE and IR <i>in situ</i>	71
3.2.1 IR detection and protein loading	71
3.2.2 Mass transport	72
3.2.3 Addressing the challenge of surface coverage	73
3.3 The design of a new spectroelectrochemical flow cell	78
3.3.1 Cell design	79
3.3.2 Performance of the new SEC cell	84
3.4 Experimental	88
3.4.1 Chemicals, materials and preparations	88
3.4.2 Experimental procedures	90
References	93
Chapter 4 Redox characterisation of Hyd-1	97
4.1 Introduction	98

4.1.1 IR spectroelectrochemical studies of NiFe hydrogenases	98
4.2 Spectroelectrochemical characterisation of Hyd-1 on carbon	103
4.2.1 Initial IR SEC characterisation	103
4.2.2 Redox titrations and reduction potentials	110
4.2.3 More oxidised inactive states	112
4.3 The effect of pH. Part 1: distribution of redox states with potential	116
4.3.1 Redox titrations as a function of pH: reduction potentials and PCET	116
4.3.2 Potential controlled spectral analysis at low and high pH	123
4.4 The effect of pH. Part 2: acid-base equilibria between states	127
4.4.1 Ni-C and Ni-L as different protonation species of the same state	127
4.4.2 The equilibrium between the Ni-R species	135
4.5 The effect of pH. Part 3: shift in wavenumber positions of bands	137
4.6 Summary	139
References	143
Chapter 5 Infrared spectroelectrochemistry under turnover	149
5.1 Introduction	150
5.1.1 Mechanism and the active site of NiFe hydrogenases	150
5.1.2 Bringing PFIRE to the discussion of the catalytic mechanism	154
5.2 H₂ oxidation: PFIRE	154
5.2.1 Mechanistic investigations of the H ₂ by Hyd-1	154
5.2.2 The effect of H ₂ concentration on the distribution of states	167

5.2.3 The effect of pH on the distribution of states	174
5.3 PFIRE of H ⁺ reduction by Hyd-1	176
5.4 Summary	179
References	182
Chapter 6 Inactivation and O₂ inhibition	187
6.1 Introduction	188
6.1.1 The inactivation of NiFe hydrogenases	188
6.1.2 IR spectroscopy as a structural insight into the mechanism	190
6.2 Inactivation of Hyd-1	190
6.2.1 Anaerobic oxidation of Hyd-1	190
6.2.2 Aerobic oxidation of Hyd-1	194
6.3 O ₂ inhibition of catalytic H ₂ oxidation	197
6.4 Summary	201
References	202
Chapter 7 CO binding and inhibition of Hyd-1	205
7.1 Introduction	206
7.1.1 CO interaction with NiFe hydrogenases	206
7.1.2 Structural characterisation of CO-bound states	206
7.2 CO binding to Hyd-1	208
7.3 PFIRE studies of CO inhibition of Hyd-1	212
7.3.1 Inhibition of H ₂ oxidation	212

7.3.2 Inhibition of H ⁺ reduction	216
7.4 Summary	218
References	220
Chapter 8 Conclusions	223

Chapter 1

Introduction

1.1 Hydrogenase enzymes

1.1.1 H₂ chemistry and its role in nature

The reversible interconversion of H₂ to protons and electrons is an important reaction in biology. Many microorganisms are able to use H₂ as an energy source; and other prokaryotes are efficient at producing H₂.¹ Table 1.1 summarises some of the main metabolic activities in which H₂ is involved. In biological processes like fermentation and anaerobic CO oxidation, H₂ is produced. Additionally, the fixation of N₂ and the oxidation of phosphite also result in the formation of H₂ as a by-product. In the case of the consumption of H₂ by microorganisms; the aerobic oxidation of H₂, methanogenesis, acetogenesis, sulfur and sulfate reduction, are amongst these metabolic activities.²

Table 1.1 Summary of some of the main metabolic activities involving H₂ in prokaryotes

<i>process</i>	<i>net chemical reaction</i>	<i>class of hydrogenase involved</i>
fermentation	$\text{CH}_3\text{CH}_2\text{CH}_2\text{COOH} + 2\text{H}_2\text{O} \rightarrow 2\text{CH}_3\text{COOH} + 2\text{H}_2$	FeFe ^{3,4}
	$\text{CH}_3\text{CH}_2\text{COOH} + 2\text{H}_2\text{O} \rightarrow 2\text{CH}_3\text{COOH} + \text{CO}_2 + 3\text{H}_2$	
anaerobic CO oxidation	$\text{CO} + \text{H}_2\text{O} \rightarrow \text{CO}_2 + \text{H}_2$	NiFe ^{5,6}
N₂ fixation	$\text{N}_2 + 8\text{H}^+ + 8\text{e}^- + 16\text{MgATP} \rightarrow 2\text{NH}_3 + \text{H}_2 + 16\text{MgADP} + 16\text{P}_i$	Mo nitrogenase ⁷
PO₃³⁻ oxidation	$\text{H}_3\text{PO}_3 + \text{H}_2\text{O} \rightarrow \text{H}_3\text{PO}_4 + \text{H}_2$	alkaline phosphatase ⁸
aerobic H₂ oxidation	$2\text{H}_2 + \text{O}_2 \rightarrow 2\text{H}_2\text{O}$	NiFe ⁹
methanogenesis	$4\text{H}_2 + \text{CO}_2 \rightarrow \text{CH}_4 + 2\text{H}_2\text{O}$	NiFe ^{10,11}
	$\text{CH}_3\text{OH} + \text{H}_2 \rightarrow \text{CH}_4 + \text{H}_2\text{O}$	
acetogenesis	$2\text{CO}_2 + 4\text{H}_2 \rightarrow \text{CH}_3\text{COOH} + 2\text{H}_2\text{O}$	NiFe, FeFe ²
sulfur/sulfate reduction	$4\text{H}_2 + \text{H}_2\text{SO}_4 \rightarrow \text{H}_2\text{S} + 4\text{H}_2\text{O}$	NiFe, FeFe ²
	$\text{H}_2 + \text{S} \rightarrow \text{H}_2\text{S}$	

The reactions depicted in Table 1.1 represent the overall net chemical processes which result from several steps in a metabolic pathway. At the heart of these chemical processes are hydrogenases, metalloenzymes which catalyse the reversible conversion of H_2 to protons and electrons. However, the N_2 fixation and PO_3^{3-} oxidation reactions in Table 1.1 are exceptions in the sense that it is not a hydrogenase enzyme that performs the reduction of H^+ to H_2 , but the whole process is carried out by a single enzyme that exhibits hydrogenase activity (a nitrogenase and a phosphatase respectively).

Hydrogenases are able to provide energy to organisms by the oxidation of H_2 . The electrons that are obtained from this reaction may be used for the reduction of substrates such as NAD^+ to form $NADH$ (as in the case of the soluble hydrogenase from *Ralstonia eutropha*);¹² or more commonly, the reduction of O_2 , nitrate, fumarate in the respiratory chain.¹ They can also function to balance the redox potential of the cell and to remove reducing equivalents by the formation of H_2 . The role that a specific hydrogenase performs in an organism is often related to its location inside the cell, they may be either tuned for H_2 oxidation or H^+ reduction.¹³

1.1.2 Hydrogenases as models for future energy technology

H_2 has been considered as a clean energy carrier for the future. A H_2 -based technology would require efficient catalysts for both the oxidation of H_2 (release of energy), and the formation of H_2 (storage of energy) from renewable sources. The study of hydrogenases is of relevance in terms of gaining understanding of how these biological systems are tuned to perform this reaction efficiently, and with the use of earth abundant metals (Fe, Ni), as opposed to Pt which is used in current technology, in fuel cells. Hydrogenases can actually rival the efficiency of Pt as H_2 oxidation catalysts, in terms of activity of per active site: $> 10\,000\ s^{-1}$ (NiFe hydrogenase) vs $1.2\ s^{-1}$ (Pt).^{14,15} It must be noted however that these enzymes are not as robust as Pt.^{16,17} A thorough understanding of the principles of how hydrogenases work is therefore important for the design of efficient, non-expensive catalysts for future H_2 -based energy technology.

1.2 Classification of hydrogenases

According to phylogenetic analyses, which relate the sequence alignment of genes that code for hydrogenase subunits, three distinct classes of these proteins have evolved. These three classes vary on the metal content of their active site. They are NiFe hydrogenases, FeFe hydrogenases and Fe-only hydrogenases. The main focus of this thesis is on NiFe hydrogenases. The two other classes will be briefly described before a detailed account of NiFe hydrogenases.

1.2.1 Fe-only hydrogenases

Fe-only hydrogenases are the only class of hydrogenases that do not contain Fe-S clusters, which function as an electron relay in the two other classes. The function of these hydrogenases is to catalyse the reversible reduction, with H_2 , of methenyltetrahydromethanopterin (methenyl- H_4MPT^+) to methylene- H_4MPT .¹⁸ Figure 1.1 shows the structure of an Fe-only hydrogenase and the reaction that it catalyses.

The catalytic centre has an Fe ion in an octahedral coordination environment. It is bound to the guanilylpyridinol cofactor (Figure 1.1A inset) via a N atom (sp^2) and an acyl bond. A cysteine binds it to the protein backbone in the wild-type enzyme (The structure in Figure 1.1 is of a variant that does not have that cysteine and therefore this ligand is not shown).¹⁹ Additionally, it has two further CO organometallic ligands.²⁰ The sixth position, trans to the acyl (see Figure 1.1), is occupied by solvent and it is suggested to be the position where H_2 binds.¹³

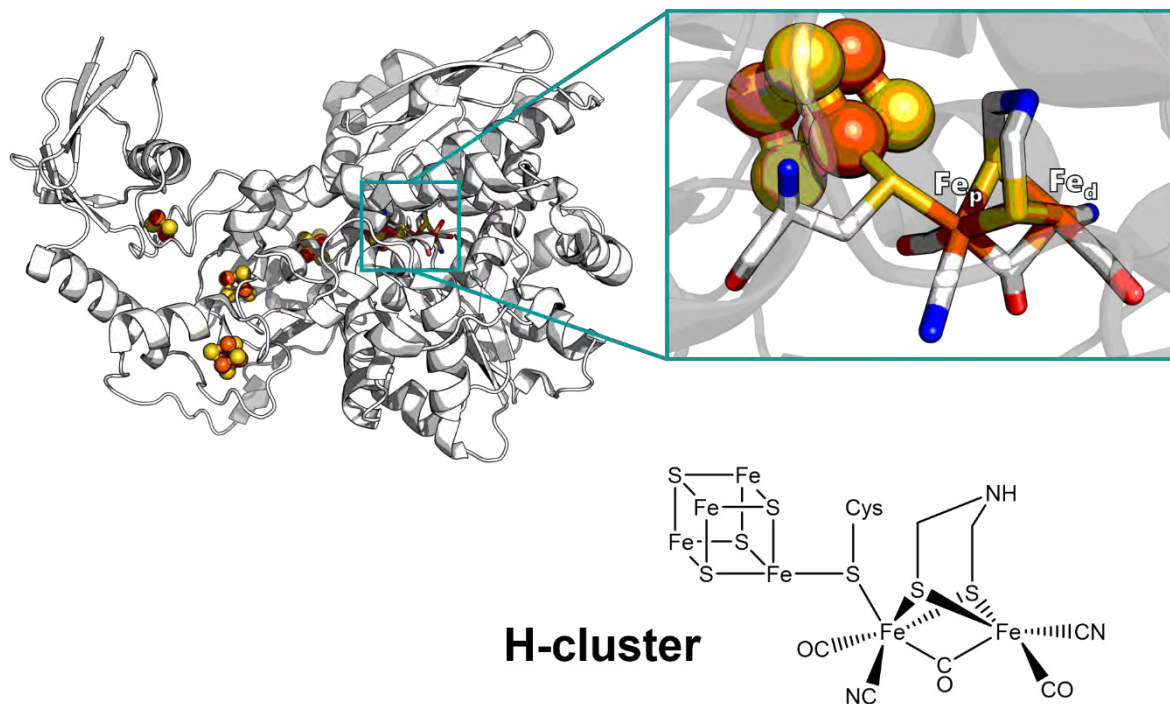


Figure 1.2 X-ray crystal structure of FeFe hydrogenase from *C. pasteurianum*. PDB 3C8Y. The inset shows a zoomed-in view of the H-cluster, the catalytic active site. Fe_p and Fe_d are the proximal and distal Fe centres of the active site. A drawn structure of the H-cluster is shown for clarity.

The active site of FeFe hydrogenases consists of a two-Fe centre. It is connected to a 4Fe-4S cluster through a cysteine sulfur. The Fe closest to the Fe-S cluster is called the proximal Fe, Fe_p; and the other one, furthest from the Fe-S cluster, the distal Fe, Fe_d. Each of these Fe atoms is bound to one CO and one CN⁻ ligand, and an additional CO is bound in a bridging position between these two metal ions. A dithiolate ligand is bound also in a bridging position between the metals.

The dithiolate ligand has been of great interest, as the chemical identity of the atom in the γ position (bridgehead) has been a subject of debate. C, N, S and O have been suggested as possible options.^{24–26} Nonetheless, such discussion was settled after synthetic active site mimics, which varied only on the composition of the atom in the γ position (C, N or O), were introduced into the active site pocket of the apoenzyme.^{27,28} Only when the mimic containing the amine dithiol ligand

was introduced to the enzyme, it resulted in a fully active hydrogenase. In Figure 1.2 the H-cluster is shown with the amine in the dithiolate ligand.

1.3 NiFe hydrogenases

NiFe hydrogenases are the main focus of this thesis so they shall be explained in greater detail. These enzymes are considered to be efficient H_2 oxidisers,^{17,21} although different NiFe hydrogenases present degrees of activity towards H^+ reduction.²⁹

Phylogenetic analyses distinguish 4 groups of NiFe hydrogenases. Each group has the following types of hydrogenases, according to function:¹

- 1) Membrane bound uptake hydrogenases. These enzymes perform respiratory H_2 oxidation linked to quinone reduction.

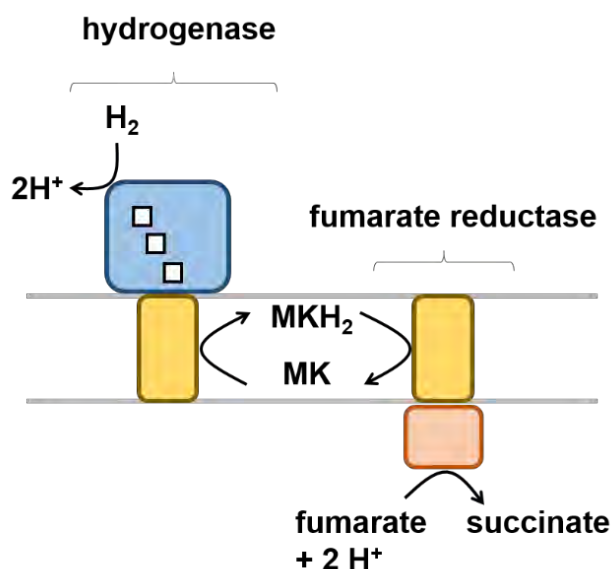


Figure 1.3 The proposed mechanism of fumarate respiration in *W. succinogenes*.³⁰ H_2 is oxidised at a membrane-bound hydrogenase. The electrons from this oxidation are transported through a menaquinone pool (MK/MKH₂) in the lipid membrane. A fumarate reductase uses these electrons to catalyse the reduction of fumarate to succinate.

The oxidation of H_2 is coupled to the reduction of electron acceptors, like fumarate NO_3^- , SO_4^{2-} , CO_2 , and even O_2 for the case of aerobic respiration. Figure 1.3 shows the mechanism of fumarate respiration, which uses a group 1 membrane-bound uptake hydrogenase.

- 2) Uptake and regulatory hydrogenases. Regulatory hydrogenases exhibit very low H_2 oxidation activity, they function as H_2 sensors.
- 3) Bidirectional heteromultimeric soluble hydrogenases: These enzymes couple the oxidation of H_2 to the reduction of F_{420} , NAD^+ or $NADP^+$, in a reversible way (Figure 1.4). The hydrogenase module is associated with other subunits that are able to bind these soluble cofactors.

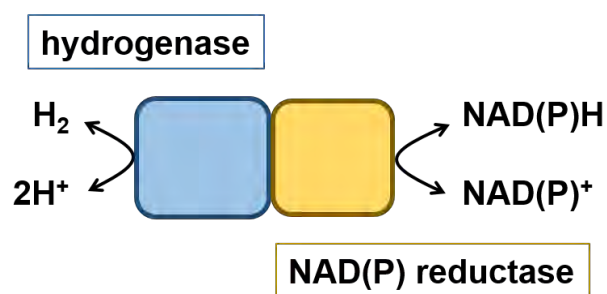


Figure 1.4 Group 3 hydrogenases are composed of hydrogenase modules bound to reductases in a heteromultimeric protein structure. The reversible oxidation of H_2 can be coupled to the reversible reduction of $NAD(P)^+$, by the transport of electrons between the protein subunits.

- 4) Multimeric enzymes which function as H_2 producers. They remove excess reducing equivalents by reducing protons from water.

In addition to these groups just mentioned, a fifth group of NiFe hydrogenases has been recently identified and characterised.^{31,32} These hydrogenases are efficient H_2 oxidisers and play an important role in the earth's H_2 cycle, responsible for up to 80 % of the annual H_2 consumption of the troposphere. Further discussion about these hydrogenases will take place later when discussing the O_2 tolerance in NiFe hydrogenases.

The enzyme that will be studied in this thesis, *E. coli* hydrogenase 1 (Hyd-1), is a group 1 NiFe hydrogenase. The results will be discussed in the context of group 1 NiFe hydrogenases, which have been extensively studied.^{1,13,33}

1.3.1 Structure

NiFe hydrogenases consist of two subunits. The X-ray crystal structure of *E. coli* Hyd-1 was obtained by Volbeda et al.³⁴ and it is shown in Figure 1.5.

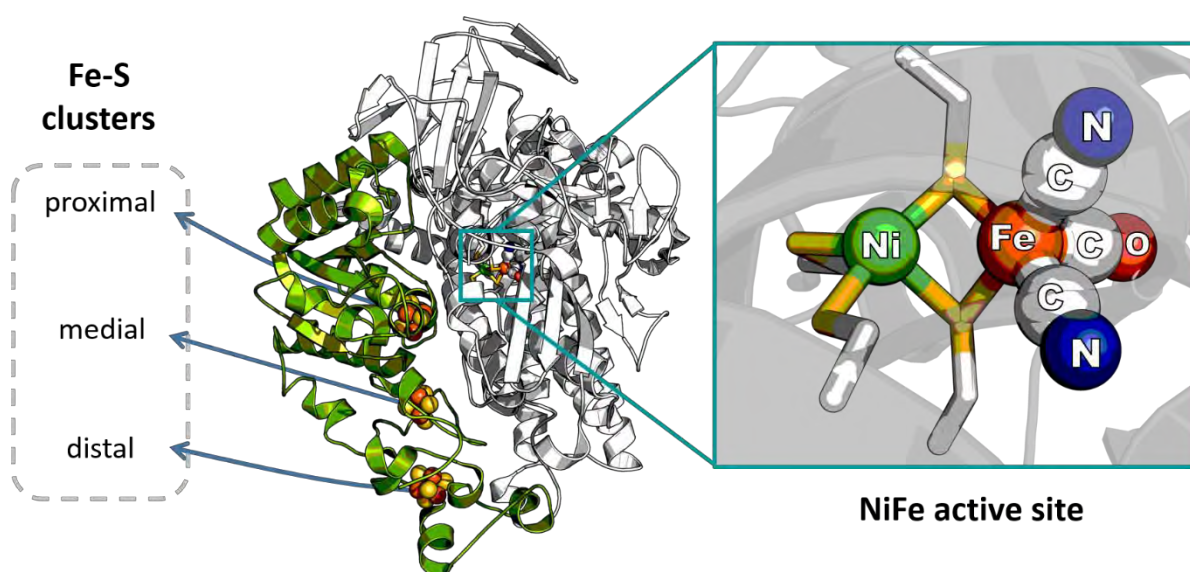


Figure 1.5 X-ray crystal structure of *E. coli* Hyd-1 (PDB 3USC). The small subunit is coloured green, and the large subunit white. The Fe-S clusters are named proximal, medial, and distal, based on their proximity to the active site. Inset: a zoomed-in view shows the structure of the $[(\text{Cys-S})_2\text{-Ni-(}\mu^2\text{-Cys-S)}_2\text{-Fe(CO)(CN)}_2]$ active site.

The large subunit (shown in white) contains the bimetallic active site; and the small subunit (shown in green) contains three Fe-S clusters, which are responsible for the electron transport to and from the active site.^{13,17,35–37} X-ray crystallographic structures of group 1 NiFe hydrogenases of about 10 different organisms have been elucidated to date.¹³ Additionally, a structure of the so-called group 5 NiFe hydrogenases has been elucidated recently.³² The overall structures of these are almost identical. The slight differences between them, which have implications in their chemistry, will be discussed later in this section.

The Fe-S clusters: O₂-tolerant vs standard hydrogenases

NiFe hydrogenases, unlike FeFe hydrogenases, are not irreversibly damaged by O₂. Although standard NiFe hydrogenases are inactivated by trace amounts of O₂, they can be reactivated by electrochemical reduction or by the exposure to H₂, after O₂ has been removed. More interestingly, O₂-tolerant NiFe hydrogenases are able to sustain their catalytic activity even in the presence of important amounts of O₂.^{29,38} *E. coli* Hyd-1 is an O₂-tolerant hydrogenase. An important structural difference between these two types of NiFe hydrogenases resides in their proximal Fe-S cluster. Standard NiFe hydrogenases have a 4Fe-4S cluster,¹³ whereas O₂-tolerant hydrogenases possess an unusual 4Fe-3S cluster.^{34,39-41} Figure 1.6 shows the structure of this special proximal Fe-S cluster and its redox transformations. Unlike the proximal cluster; the structures of the medial and distal clusters, 3Fe-4S and 4Fe-4S respectively, do not differ significantly between O₂-tolerant and standard hydrogenases.^{34,39,42}

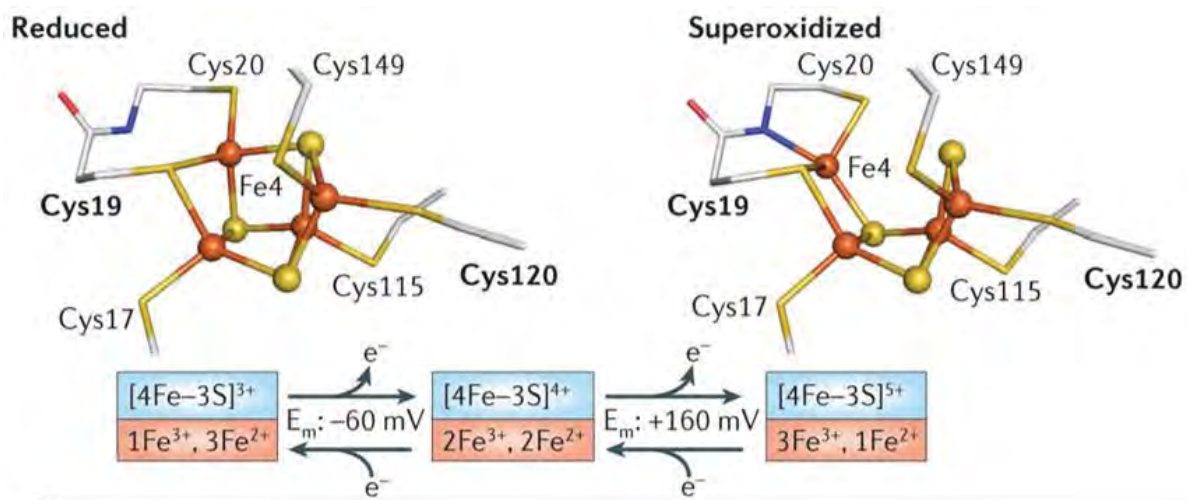


Figure 1.6 The proximal Fe-S cluster of *R. eutropha* membrane-bound hydrogenase. A scheme of its redox transitions is shown below the structures. The cluster undergoes important structural rearrangements along with its redox transformations. Adapted by permission from Macmillan Publishers Ltd: NATURE REVIEWS MICROBIOLOGY, vol 11, 106-114, copyright 2013.

This special proximal cluster plays an important role in the O₂-tolerance of these enzymes, as it can undertake two redox transitions at physiologically attainable potentials (see redox diagram in Figure 1.6). This allows for the quick transfer of enough electrons to the active site where O₂ can then be fully reduced to water.^{40,43}

EPR spectroscopy, as well as Moessbauer spectroscopy, has been applied to investigate the Fe-S clusters in NiFe hydrogenases and their redox behaviour, by sampling the enzyme under different redox potentials with the aid of mediators.^{36,44–47} Roessler et al.³⁶ determined the redox potentials of the Fe-S clusters of the *E. coli* Hyd-1. Table 1.2 compares these values to those of another O₂-tolerant hydrogenase, from *A. aeolicus*,⁴⁷ and the ones from the much studied standard hydrogenase from *D. vulgaris MF*.⁴⁸

Table 1.2 Reduction potential of the redox transitions of the Fe-S clusters of NiFe hydrogenases.

	<i>Fe-S clusters reduction potential / V vs SHE</i>			
	<i>proximal</i>	<i>proximal</i>	<i>medial</i>	<i>distal</i>
<i>E. coli</i> Hyd-1	+ 0.230 ^a	+ 0.030 ^b	+ 0.190	-
<i>A. aeolicus</i>	+ 0.232 ^a	+ 0.087 ^b	+ 0.068	-0.078
<i>D. vulgaris MF</i>	< -0.300		-0.070	< -0.300

^aThe superoxided ⇌ oxidised transition. ^b The oxidised ⇌ reduced transition

An immediate and most noticeable contrast in Table 1.2 corresponds to the significant difference between the reduction potential of the proximal cluster in the standard hydrogenase from *D. vulgaris MF*, and the reduction potentials of the proximal cluster for the other two O₂-tolerant hydrogenases (for both of its transitions). The fact that these potentials are higher for the O₂-tolerant hydrogenase, has been related to these enzymes' ability to fully reduce O₂ when it attacks the active site.^{43,49} This will be discussed in more detail later.

Proton and gas channels

NiFe hydrogenases exhibit remarkably high H_2 oxidation activities ($> 10\,000\text{ s}^{-1}$) which are comparable to those of Pt.^{15,50} This implies that the transport of the substrate (H_2) to the active site, and the removal of the products (H^+ and electrons) must be fast and efficient. These enzymes are equipped with gas channels that provide access to H_2 , and/or other inhibitors (such as CO and O_2); as well as with proton channels to remove these from the active site.^{17,51,52}

Gas channels

X-ray structures of the NiFe hydrogenase from *D. fructosovorans* have permitted the identification of hydrophobic gas channels, by the trapping of Xe atoms in the protein at high pressures.^{53,54}

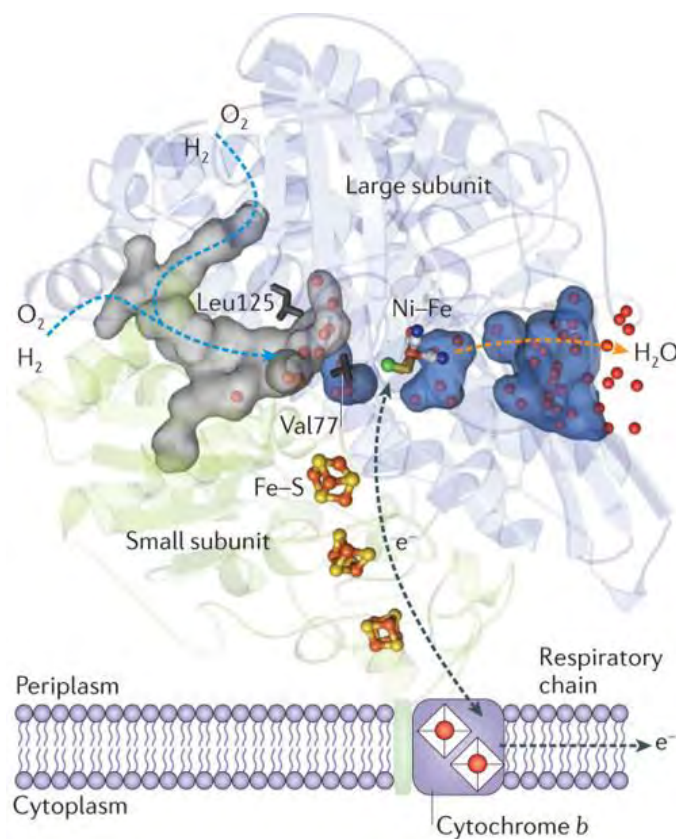


Figure 1.7 X-ray crystal structure of the NiFe membrane-bound hydrogenase from *R. eutropha*. Gas and water channels have been identified in this structure. The hydrophobic gas channels are shaded in grey and the water channel shaded in blue. Adapted by permission from Macmillan Publishers Ltd: NATURE REVIEWS MICROBIOLOGY, vol 11, 106-114, copyright 2013.

These channels connect the active site to the outside of the protein. Figure 1.7 shows the X-ray crystal structure of the O₂-tolerant membrane-bound NiFe hydrogenase from *R. eutropha*, it indicates the gas and water channels, as proposed by Fritsch et al.³⁹

Proton and water channels

Different proton and water channels have been identified in several NiFe hydrogenases.^{34,39,42,51,52,55} Although none of these has been demonstrated to be the channel whereby protons are transported from and to the active site, they are likely paths through which protons can be quickly transported between the active site and the surface of the enzyme. Figure 1.7 shows a water channel identified in *R. eutropha* membrane-bound hydrogenase, shaded in blue to the right of the active site in the figure.

The active site

The binuclear active site of NiFe hydrogenases is formulated as a [(Cys-S)₂-Ni-(μ²-Cys-S)₂-Fe(CN)₂CO] (Figure 1.5, inset). The Ni is coordinated to two terminal cysteines and two bridging cysteines that connect it to the Fe atom. The Fe is further coordinated by three organometallic ligands: two CN⁻, and one CO. The active site of NiFe hydrogenases exhibits a rich redox chemistry. Figure 1.8 gives detail of the most common redox states of the active site of NiFe hydrogenases. The techniques that have informed on the structure of different states of the active site include X-ray crystallography, IR spectroscopy, EPR spectroscopy, Raman spectroscopy, nuclear resonance vibrational spectroscopy (NRVS), and X-ray absorption spectroscopy (XAS). More detail about what information each technique has provided will be given as each redox state is described.

The inactive oxidised states: Ni-A, Ni-B, and their one-electron reduced counterparts

As-isolated preparations of NiFe hydrogenases show an oxygenic species in the bridging position between the two metals of the active site.^{34,54,56,57} From EPR (by detecting Ni paramagnetic states) two distinct states have been identified in these aerobically prepared samples, corresponding to a Ni(III) for both species.^{13,36,37,58,59} Based on their kinetics of activation these two states have been distinguished; Ni-A takes hours to activate, whereas Ni-B takes minutes.

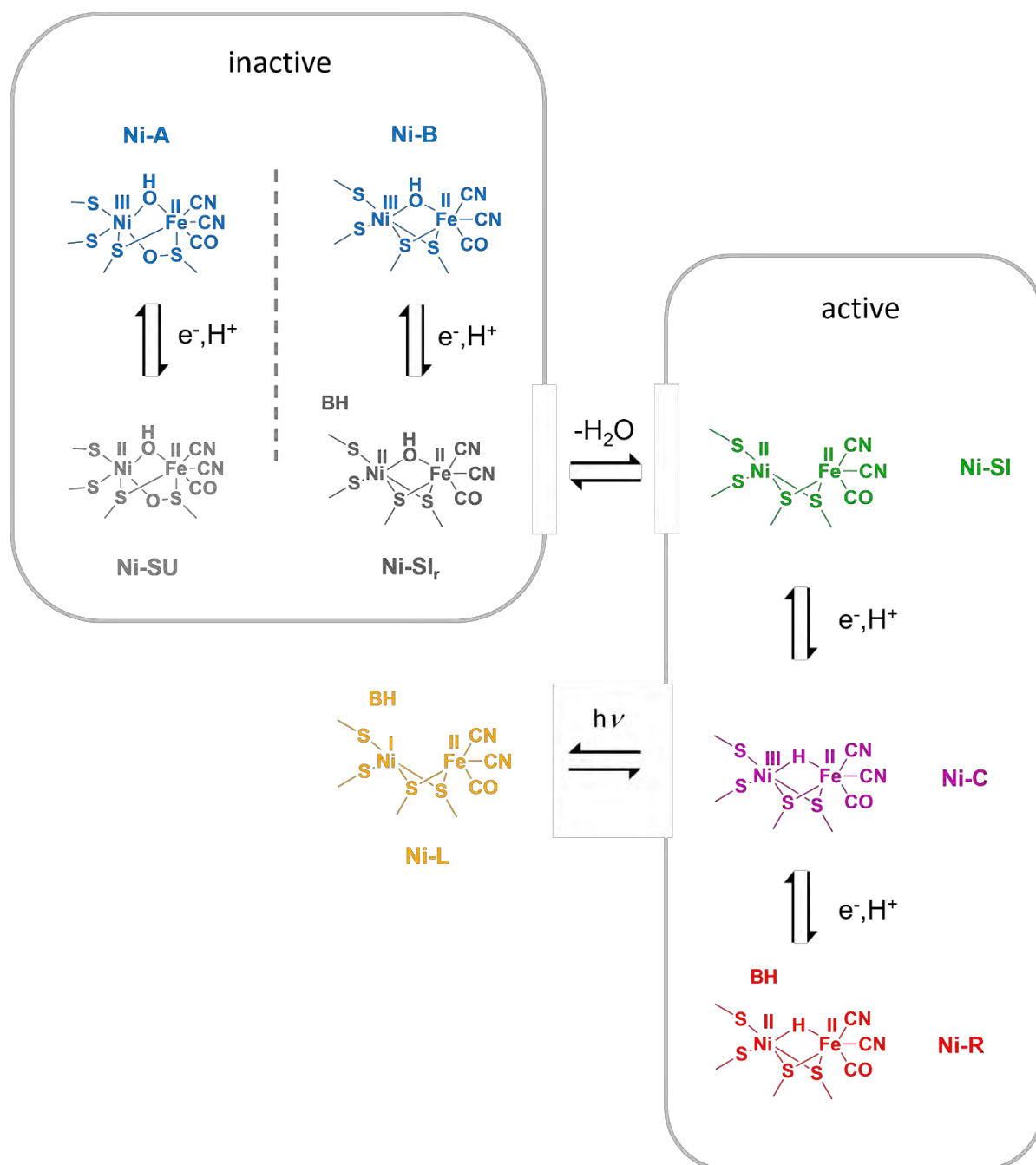


Figure 1.8 Scheme of the most common active site redox states of NiFe hydrogenases and their transformations. The structure of the Ni-SI_r state remains uncertain. B represents a generic proton acceptor within the active site (it does not preclude one of the cysteines' sulfur).

There has been a consensus over the structure of Ni-B. A crystal structure of *D. vulgaris* MF in the Ni-B (ready) state was solved by Ogata et al. in 2005.⁶⁰ The structure of Ni-B consists of a hydroxide ligand bound in the bridging position between the two metals (as shown in Figure 1.8).^{57,59,60} Nevertheless, the exact structure of Ni-A has been a subject of debate and several alternatives have

been proposed, most commonly a peroxide species bound in the bridging position.^{56,57,60–63} However, Volbeda et al.⁵⁶ reported X-ray crystal structures of *D. fructosovorans* NiFe hydrogenases for which they were able to report a convincing interpretation of the structure of Ni-A. It consists on a hydroxide bridging ligand, as in Ni-B; and a sulfenated cysteine, one of the bridging cysteines. Figure 1.9 shows the crystal structure of this active site state, as determined by Volbeda et al.⁵⁶

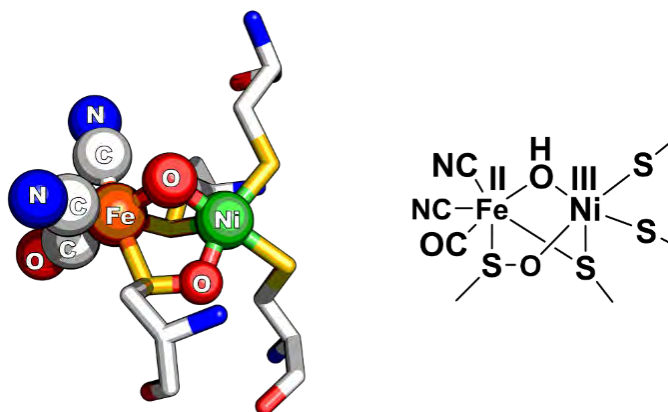


Figure 1.9 X-ray crystal structure of the active site of *D. fructosovorans* NiFe hydrogenase in the Ni-A state, solved by Volbeda et al.⁵⁶ (PDB 4URH). One of the bridging cysteines is oxidised to a sulfenated form. The oxygenic species is assigned as a hydroxide ion.

One electron reduction of these Ni(III) states, Ni-A and Ni-B, give the EPR silent states Ni-SU and Ni-SI_r respectively.⁶⁴ These states have been detected and characterised in IR spectroelectrochemical studies.^{13,65–67} The structure of Ni-SU is considered to be similar to that of Ni-A but with a Ni(II), according to X-ray crystal structures analysed by Volbeda et al.⁵⁶ The one electron reduction of Ni-B gives the Ni-SI_r state. This state has been found in different protonation states.⁶⁸ The Ni-SI_r state is inactive and it is thought to have the same structure of Ni-B, but with a Ni(II), and an extra proton in a nearby aminoacid (although no structural information is available).⁶⁹ For the other protonation state, it has been suggested that the proton, of the proton-coupled electron transfer from Ni-B to Ni-SI_r, binds the OH⁻ directly to form water as a loosely bound bridging ligand.^{70,71} Independent of protonation states of Ni-SI_r, it is agreed that an oxygenic ligand is bound to the active site which prevents it from being active.^{66,69,72,73} This oxygenic ligand has been found to be dissociated upon photoillumination at low temperatures.⁷⁴

The states assumed to be active in catalysis

The removal of the oxygenic species from Ni-SI_r gives the active Ni-SI state, which has a vacant bridging position (see Figure 1.8). It has been suggested that the active Ni-SI state is actually in pH equilibrium with Ni-SI_r.⁶⁵ In several hydrogenases, the one electron reduction of Ni-B gives the active Ni-SI species directly, with no intermediate inactive Ni-SI_r state detected.^{75,76}

A one electron reduction of the Ni-SI state gives the Ni-C state (Figure 1.8), which consists of a Ni(III) and a hydride bound in the bridging position between the metals. This redox state has been extensively characterised by EPR spectroscopy, as it is paramagnetic; this technique has contributed to the identification of the bound hydrogenic species in this state.^{77–80}

The most reduced state, Ni-R, is obtained by a one electron reduction of Ni-C. IR has been the main technique whereby this state has been characterised.^{65–67,76,81} Several bands, corresponding to up to three different species at this redox level, are observed for this state and it has been proposed that this is a result of there being multiple protonation states of this redox level.^{66,68,82,83}

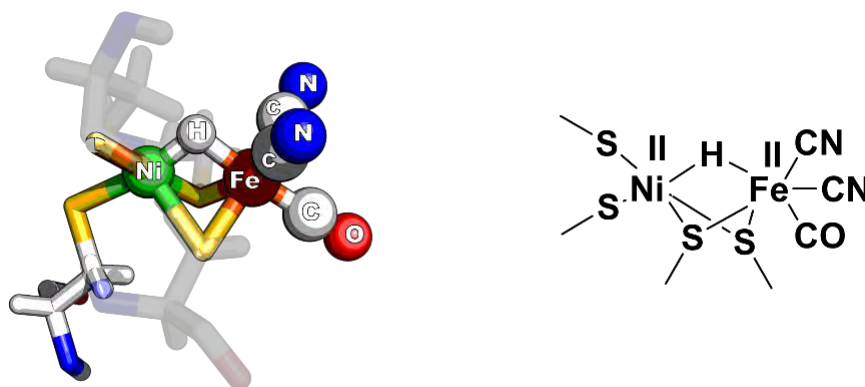


Figure 1.10 Ultra-high resolution X-ray crystal structure of NiFe hydrogenase from *D. vulgaris* MF shows the structure of the active site in the Ni-R state. Solved by Ogata et al,⁸⁴ (PDB 4U9H). The hydrogen in the bridging position was detected at a 0.89 Å resolution.

Recently, high resolution X-ray crystallographic studies of the reduced NiFe hydrogenase from *D. vulgaris* led to the detection of a hydrogen in the bridging position. Figure 1.10 shows this structure, determined by Ogata et al.⁸⁴

In addition to this recent crystal structure determination; nuclear resonance vibrational spectroscopy (NRVS), in conjunction with DFT modelling, has been applied to detect a vibrational mode that is attributed to the wagging mode of a bridging hydride, in a ^{57}Fe -labelled active site hydrogenase.⁸⁵

Ni-L state

The illumination of Ni-C at cryogenic temperatures results in the dissociation of the bound hydride, which is lost as a proton. This reaction has been studied by EPR and IR spectroscopy in several hydrogenases, in many cases multiple (up to three) Ni-L spectral signatures appear. This is thought to be different protonation species of this state.^{77,80,86–89} The Ni-L state consists of a Ni(I) and the bridging position between the metals is vacant (see Figure 1.8). The proton is considered to reside in a cysteine sulfur after the dissociation, and experiments on synthetic models have provided grounds for such a hypothesis.⁹⁰ DFT studies have proposed the existence of a metal-metal bond in the Ni-L state. This would provide a sound rationale for the low wavenumbers at which its ν_{CO} and ν_{CN} appear in the IR spectrum, since it would lead to delocalisation of charge from the Ni towards the Fe.⁹¹

The Ni-L state and its significance in the catalytic cycle of *E. coli* Hyd-1 will be investigated extensively on Chapters 4 and 5. A more detailed comparison to existing data on Ni-L for other hydrogenases will be developed in those chapters.

1.3.2 Activity and dynamics of NiFe hydrogenases

In addition to biochemical assays which report on enzyme activity in solution with artificial electron donors or acceptors; much of the research on the catalytic investigations of NiFe hydrogenases has been done by means of protein film electrochemistry (PFE).^{17,92,93,16,94} In this technique, a hydrogenase enzyme is directly adsorbed on an electrode surface and it can readily exchange electrons with the electrode. Since the process is not slowed down by diffusion, the electron transfer properties of the system can be studied in detail. If H_2 is present in the solution, and there

is efficient mass transport in the system, the adsorbed enzyme can engage in electrocatalytic activity. The current at the electrode is a direct measurement of the activity of the enzyme.⁹⁵

O₂-tolerant vs standard hydrogenases: PFE as a tool for understanding enzymatic activity

Overview of electrocatalytic properties

Lukey et al. showed the difference in catalytic properties, by means of PFE, between two hydrogenases present in *E. coli*: the O₂-tolerant hydrogenase 1 (Hyd-1), and the standard hydrogenase 2 (Hyd-2).²⁹ Figure 1.11 shows the cyclic voltammograms of these two enzymes. Hyd-1 does not exhibit any H⁺ reduction activity, whereas Hyd-2 does. This catalytic bias is common in O₂-tolerant NiFe hydrogenases, which normally do not show activity towards H⁺ reduction.^{96–98}

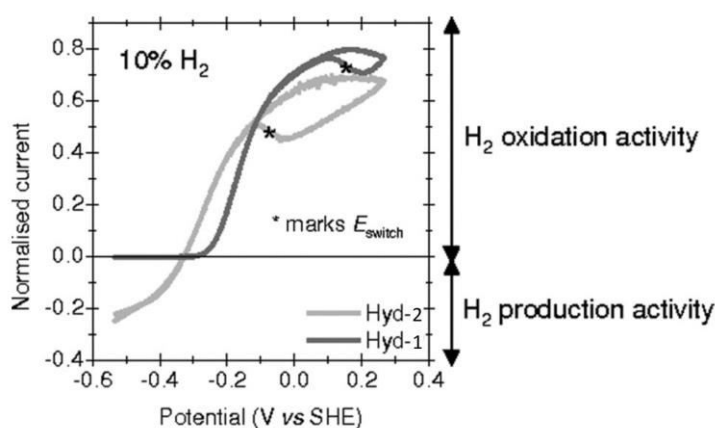


Figure 1.11 Cyclic voltammograms, under 10 % H₂, of Hyd-1 and Hyd-2 adsorbed on a carbon electrode. Hyd-1 results are indicated by dark grey, and Hyd-2 by light grey. Positive currents correspond to enzyme-catalysed H₂ oxidation; and negative currents to enzyme-catalysed H⁺ reduction. This research was originally published in *The Journal of Biological Chemistry*. Lukey, M. J.; Parkin, A.; Roessler, M. M.; Murphy, B. J.; Harmer, J.; Palmer, T.; Sargent, F.; Armstrong, F. A. How *Escherichia coli* is equipped to oxidize hydrogen under different redox conditions. *J. Biol. Chem.* 2010; 285: 3928–3938. © the American Society for Biochemistry and Molecular Biology.

The catalytic bias is related to the overpotential, that is, difference between the thermodynamic potential of the redox couple and the onset potential at which the enzyme starts to show catalytic activity. Hyd-1 shows an overpotential for H₂ oxidation (see Figure 1.11), it can be clearly seen

when compared to the onset potential of Hyd-2, which behaves as a reversible electrocatalyst. According to an electrocatalytic model proposed for hydrogenases adsorbed on electrodes, an important basis for the catalytic bias is the overpotential.⁹⁹ Moreover, recent work on Hyd-1 showed that at low pH values, this enzyme becomes an efficient H₂ producer and exhibits no overpotential.¹⁰⁰

Effect of O₂ on the catalytic activity

O₂-tolerant hydrogenases are able to maintain substantial activity in the presence of O₂. They can fully reduce O₂ to water, and they recover their full activity quickly after O₂ is removed from the system.^{35,37,43}

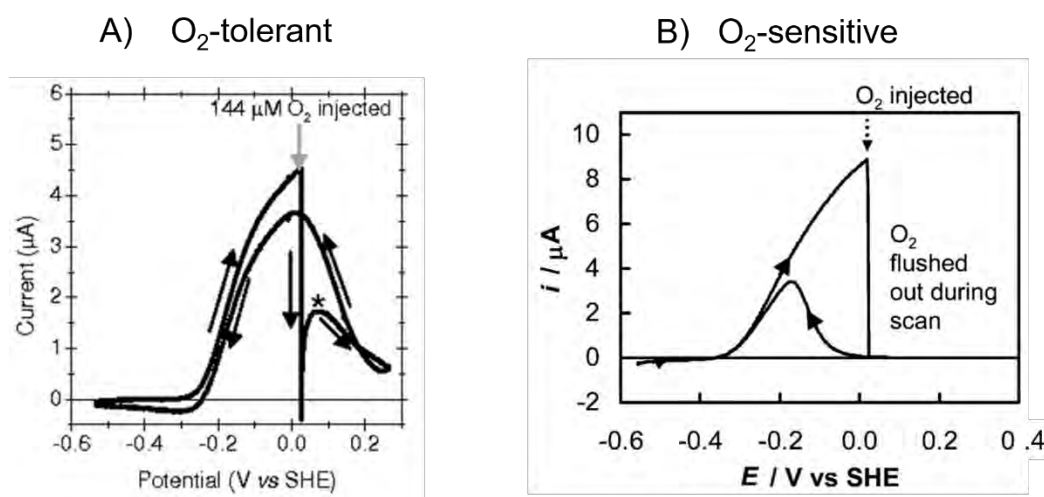


Figure 1.12 The effect of injecting O₂ on the H₂ oxidation activity of NiFe hydrogenases. A) The O₂-tolerant hydrogenase 1 from *E. coli* recovers quickly from O₂. Experimental conditions: pH 6.0, 100 % H₂. Adapted from Lukey, M. J.; Parkin, A.; Roessler, M. M.; Murphy, B. J.; Harmer, J.; Palmer, T.; Sargent, F.; Armstrong, F. A. *J. Biol. Chem.* 2010, 285 (6), 3928–3938. B) The standard NiFe hydrogenase from *A. vinosum* is completely inactivated by O₂. It reactivates at low potential. Experimental conditions: pH 6.0, 100 % H₂. Adapted with permission from Vincent, K. A.; Parkin, A.; Lenz, O.; Albracht, S. P. J.; Juan, C.; Cammack, R.; Friedrich, B.; Armstrong, F. A.; Fontecilla-camps, J. C. *J. Am. Chem. Soc.* 2005, 127 (7), 18179–18189. Copyright 2005 American Chemical Society.

Standard hydrogenases, on the other hand, are inactivated by O₂; and they require electrochemical reduction at low potentials to reactivate.^{29,101} Figure 1.12 shows this effect of the addition of O₂ to

the electrocatalytic activity of an O₂-tolerant hydrogenase, and a standard (O₂-sensitive) hydrogenase.

It can be seen that in the case of the O₂-tolerant hydrogenase 1 from *E. coli* (Figure 1.12A), it starts to reactivate quickly after the addition of O₂, even at high potentials (> 0 V vs SHE). Moreover, the addition of O₂ does not cause a complete inactivation. This is in contrast to the behaviour of the standard hydrogenase of *A. vinosum* (Figure 1.12B), for which the addition of O₂ causes a complete inactivation, and its activity only begins to recover at low potentials (< 0 V vs SHE).

Recovery from O₂: the unready (Ni-A) and ready (Ni-B) states

Ni-B and Ni-A can be distinguished electrochemically, based on their kinetics of reactivation. O₂ inactivation results in the formation of a mixture of Ni-A and Ni-B in the case of standard hydrogenases,^{102,103} and on the formation of Ni-B exclusively, in the case of O₂-tolerant hydrogenases.^{35,37,43}

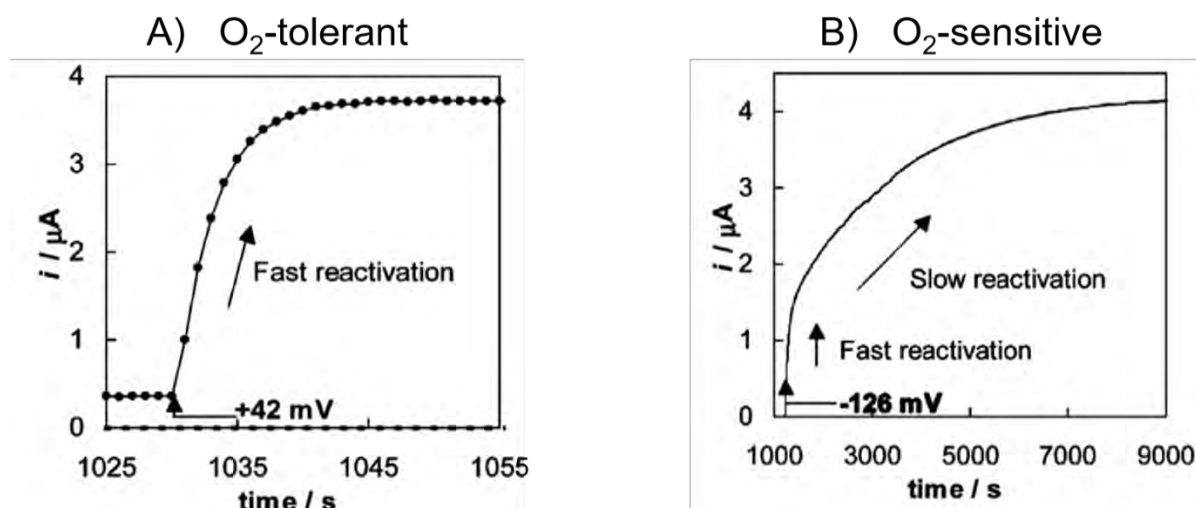


Figure 1.13 The reductive reactivation of NiFe hydrogenases after O₂ inactivation. Current-time trace showing the reactivation stage at: A) +42 mV for *R. eutropha* membrane-bound hydrogenase, and B) -126 mV for the NiFe hydrogenase of *A. vinosum*. Adapted with permission from Vincent, K. A.; Parkin, A.; Lenz, O.; Albracht, S. P. J.; Juan, C.; Cammack, R.; Friedrich, B.; Armstrong, F. A.; Fontecilla-camps, J. C. *J. Am. Chem. Soc.* 2005, 127 (7), 18179–18189.

Figure 1.13 shows a comparison of the kinetics of reactivation of an O_2 -tolerant, and a standard NiFe hydrogenase. It can be seen in Figure 1.13A, that the activity of the O_2 -tolerant membrane-bound hydrogenase from *R. eutropha* is gained fully in a matter of a few seconds. Such behaviour is consistent with the activation of the Ni-B state. On the contrary, the standard NiFe hydrogenase from *A. vinosum* (Figure 1.13B) takes hours to activate and exhibits two different behaviours: a fast initial activation, and a slower process that takes overall more than 2 hours to finish. These two different kinetic behaviours are consistent with there being a mixture of Ni-B (fast activation) and Ni-A (slow activation) states.

1.3.3 More on the O_2 -tolerance in NiFe hydrogenases

Group 1 membrane-bound hydrogenases

The O_2 -tolerant membrane-bound hydrogenases of group 1 have been extensively studied. The special 4Fe-3S cluster that has been found in these enzymes is considered to play a major role on this O_2 -tolerance property.^{39–43,47,49,104} This cluster is coordinated to six cysteines which have been found to be highly conserved residues in the sequence of these enzymes.^{35,37,39,41}

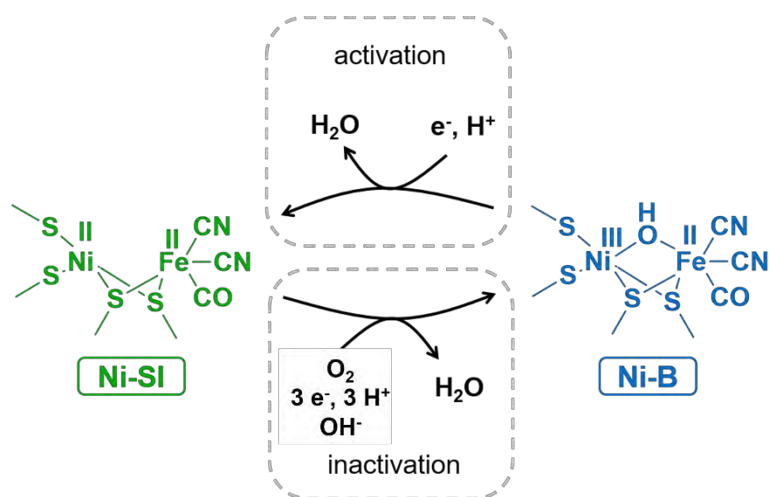


Figure 1.14 The attack of O_2 to the active site of O_2 -tolerant NiFe hydrogenases. One electron from the active site, and three from the Fe-S clusters are quickly provided to fully reduce O_2 to water. Ni-B can then be quickly reactivated to give Ni-SI and continue the catalytic cycle. The OH^- ligand is obtained from solvent and not from the incoming O_2 as has been proposed in the literature.^{105,106}

The proximal 4Fe-3S cluster allows the donation of two electrons to the active site upon the attack of O₂.^{40,43,49} It is able to undergo two redox transitions at physiologically attainable potentials (Figure 1.6). Together with one electron from the active site, and another from the medial cluster (which has a high reduction potential as well – see Table 1.2); the enzyme is able to catalyse the four electron reduction of O₂ to water.⁴³ Thus, avoiding damaging reactive oxygen species (ROS) and forming solely the Ni-B state (which can quickly be reactivated) as indicated by Figure 1.14.

Group 3 and group 5 NiFe hydrogenases: redefining O₂ tolerance

O₂-tolerance has been widely associated with the formation of a single inactive state, Ni-B, as described in Figure 1.14. However, recent electrochemical investigations on a group 3 NiFe hydrogenase challenge this view.¹⁰⁷ This enzyme was shown to be an O₂-tolerant hydrogenase; that is, it sustained catalytic activity in the presence of O₂. Nonetheless, its reactivation kinetics showed the formation of two inactive states, both of which were quickly reactivated (< 150 s). Furthermore, this NiFe hydrogenase does not possess a special proximal cluster, but a 4Fe-4S cluster (the same as standard hydrogenases).¹⁰⁷ Another group 3 NiFe hydrogenase has been shown to be O₂-tolerant, and to be able to fully reduce O₂ to water.^{12,108,109}

The newly-discovered group 5 NiFe hydrogenases (actinobacterial type) show remarkable O₂-tolerance. Activity measurements have shown that, even under atmospheric O₂ concentrations, a group 5 NiFe hydrogenase is able to maintain full activity.³¹ X-ray crystallographic studies have shown a 4Fe-4S proximal cluster coordinated to three cysteines and one aspartate. This is in contrast with standard NiFe hydrogenases, for which the proximal 4Fe-4S cluster is coordinated to four cysteines. This aspartate residue is proposed to be related to the O₂ insensitivity of these enzymes. Mutagenesis experiments showed loss of the O₂-resistance in different variants of this enzyme that had the aspartate substituted by another amino acid.³²

1.3.4 The catalytic mechanism

The mechanism of H₂ oxidation by NiFe hydrogenases has been addressed extensively in the literature, mainly by theoretical approaches.^{13,110–114} On the other hand, experimental direct evidence of catalytic intermediates is scarce. Many of the techniques normally applied to study hydrogenases use frozen samples. This is the case for EPR, NRVS, and EXAFS. X-ray crystallography is also impractical. IR spectroscopy is good for solution experiments; however, the generally thin pathlengths make the access of H₂ difficult. More sophisticated spectroscopic methods have attempted to make progress in this area.^{76,115} However, there remains little direct evidence of catalytic species and very few studies under true catalytic turnover.

The individual steps of the cycle (as has been most commonly proposed) will be discussed in detail, along with the evidence that has led to the current understanding of each step.

Hydrogen activation

It has been known for a long time that H₂ is heterolytically split in NiFe hydrogenases, proven by isotope exchange experiments.¹¹⁶ However, a clear identification of the base that participates in this reaction has not been demonstrated. It has been suggested that a cysteine sulfur takes on this role.¹³ Nonetheless, recent investigations by Evans et al. provide evidence in support of an arginine (which suspends a guanidine N atom in close proximity above the Ni and Fe atoms) being the Lewis base that participates in the heterolytic cleavage of H₂ (Figure 1.15).¹¹⁷

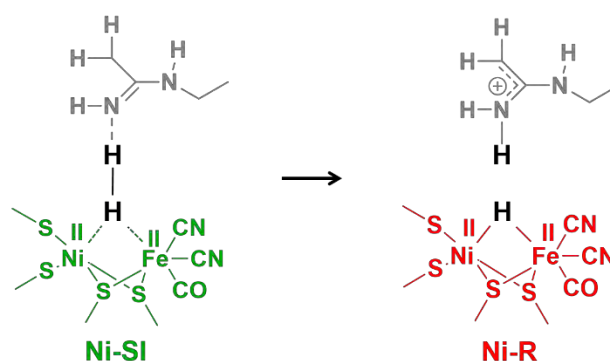


Figure 1.15 Frustrated Lewis pair H₂-activation mechanism. A conserved arginine (coloured grey) functions as the Lewis base involved in the heterolytic split of H₂, and the bimetallic centre as the Lewis acid.

Under equilibrium conditions, it is possible that the proton in the Ni-R state resides in one of the cysteine sulfurs near the active site, as has been shown by X-ray crystallography.⁸⁴ However, this does not preclude that the active base, which participates in the heterolytic splitting of H₂ is the arginine, as proposed by Evans et al.¹¹⁷

The first proton-coupled electron transfer

The Ni-R state carries the products of the heterolytic splitting of H₂; that is, the H⁻ in the bridging position between the metals, and the H⁺ in the sulfur of one of the terminal cysteines.^{84,85,118} A removal of a proton and an electron gives the Ni-C state, which has a bound H⁻ and a Ni(III).

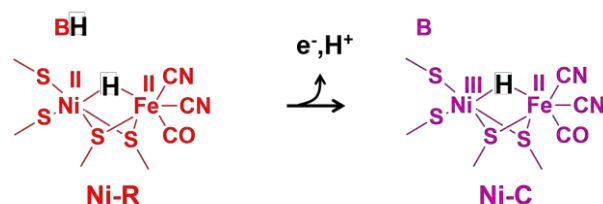


Figure 1.16 The second step in the catalytic mechanism of H₂ oxidation by a NiFe hydrogenase. A one-electron oxidation and removal of a proton from Ni-R state gives the paramagnetic Ni-C state.

A generic base B is represented in Figure 1.16, as was mentioned in section 1.3.1, several Ni-R spectral signatures have been identified and this could represent different protonation species of the same redox level. Different protonation states of a Ni-R-like state have been proposed, by DFT studies, to be involved in the catalytic mechanism.¹¹⁰

The proton created from the splitting of H₂ is no longer located near the active site in the Ni-C state.^{65,96,119} Electrons are withdrawn through the Fe-S cluster relay whereas the proton may exit to the enzyme surface via one of the proton channels (see section 1.3.1).

The second proton coupled electron transfer

The mechanism whereby the second proton and electron are removed from the active site has been a subject of debate. Classically, this transformation is represented as a concerted proton-coupled electron transfer step.¹³ However; computational, synthetic, and spectroscopic studies have pointed to a stepwise proton-coupled electron transfer mechanism, which involves a Ni(I)

intermediate.^{110,111,113,114} Figure 1.17 shows these alternative pathways of the last step of the mechanism.

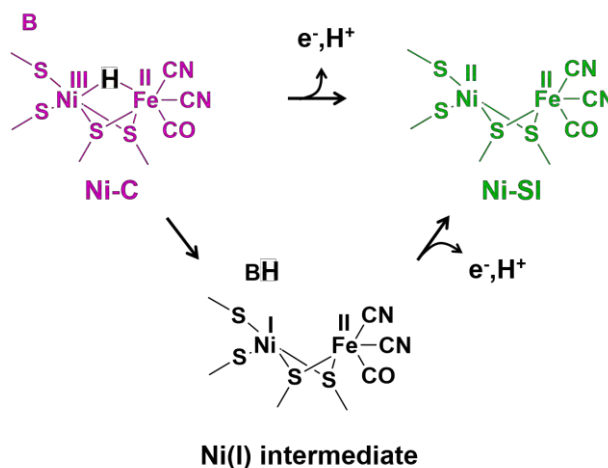


Figure 1.17 Possible routes of the last step of the mechanism of H₂ oxidation by NiFe hydrogenases. The concerted pathway gives Ni-SI directly in one step. The stepwise mechanism has a Ni(I) intermediate between Ni-C and Ni-SI.

This last step completes the cycle with the formation of Ni-SI. Chapters 4 and 5 of this thesis will focus in depth on discussing the alternatives presented in Figure 1.17, together with some recent experimental reports that address this topic.^{120–122}

1.4 Aims and scope of this thesis

This thesis will focus on investigating the active site chemistry of *E. coli* Hyd-1. This shall be done by means of IR spectroscopy and electrochemistry.

Chapter 3 will focus on the development of a new experimental approach which combines protein film electrochemistry with IR spectroscopy *in situ*. This allows for the measurement of catalytic activity of the enzyme, with simultaneous measurement of IR spectra. The experimental design will be described in detail: adsorption of hydrogenase on conductive carbon nanoparticles, design of a spectroelectrochemical flow cell and optimisation of mass transport conditions. The concept of this new approach will be demonstrated to be mass-transport efficient, by the fact that high quality

electrochemical data is obtained for Hyd-1; as well as IR spectra recording changes in redox states measured in the new system.

The redox equilibria of the active site of Hyd-1 will be thoroughly investigated in Chapter 4. The states and their redox transformations will be studied to provide a full picture of the redox chemistry and attainable states in Hyd-1. Specific attention will be given to the effect of pH on these equilibria. Moreover, pH equilibria of Ni-C/Ni-L states, and Ni-R species will be described over a wide potential and pH window. Such information will be valuable for understanding the available states of the active site and their possible implications in the catalytic cycle.

An investigation of the mechanism, using IR spectroelectrochemistry, will be undertaken in Chapter 5. IR data obtained under turnover conditions will reveal new insight into the mechanism and catalytic cycle of NiFe hydrogenases. This represents the first investigation of this kind; that is, obtaining structural information of a hydrogenase adsorbed on a carbon electrode as it is engaging in catalysis. The effect of potential and on pH will provide information of the role of different protonation species in the catalytic cycle, such as that of Ni-L, and the multiple Ni-R species. Proton-coupled electron transfer processes of the active site will be a main focus of Chapters 4 and 5.

Chapter 6 will focus on the chemistry of anaerobic and aerobic inactivation. The technique developed in this thesis will be used to understand the different mechanisms of inactivation, including the inactivation by O₂ under turnover conditions. The results of this chapter provide information on the 'clean' chemistry of the O₂ attack on O₂-tolerant NiFe hydrogenases, which produces exclusively Ni-B and recovers quickly, without the formation of any detectable O₂-damaged species.

Finally, Chapter 7 will discuss the inhibition of CO in the activity of Hyd-1. A potential controlled addition of CO will allow the determination of the states to which CO can bind. This information will

be then used to interrogate the catalytic mechanism under different conditions in which CO binding traps short-lived catalytic intermediates that are otherwise not present.

References

- 1 P. M. Vignais and B. Billoud, *Chem. Rev.*, 2007, **107**, 4206–72.
- 2 E. Schwartz, J. Fritsch and B. Friedrich, in *The Prokaryotes-Prokaryotic Physiology and Biochemistry*, eds. E. Rosenberg, E. F. DeLong, E. Stackebrandt, S. Lory and F. Thompson, Springer, Heidelberg, 4th edn., 2013, pp. 120–174.
- 3 M. W. W. Adams, E. Eccleston and J. B. Howard, *Proc. Natl. Acad. Sci. U. S. A.*, 1989, **86**, 4932–4936.
- 4 M. W. W. Adams, J. F. Holden, A. L. Menon, G. J. Schut, A. M. Grunden, C. Hou, M. Andrea, F. E. J. Jr, C. Kim, K. Ma, G. Pan, R. Roy, R. Sapra, S. V Story, M. F. J. M. Verhagen and A. L. A. L. Menon, *J. Bacteriol.*, 2001, **183**, 716–724.
- 5 J. D. Fox, R. L. Kerby, G. P. Roberts and P. W. Ludden, *J. Bacteriol.*, 1996, **178**, 1515–1524.
- 6 J. D. Fox, H. E. Yiping, D. Shelver, G. P. Roberts and P. W. Ludden, *J. Bacteriol.*, 1996, **178**, 6200–6208.
- 7 B. M. Hoffman, D. Lukoyanov, D. R. Dean and L. C. Seefeldt, *Acc. Chem. Res.*, 2013, **46**, 587–95.
- 8 K. Yang and W. W. Metcalf, *Proc. Natl. Acad. Sci. U. S. A.*, 2004, **101**, 7919–24.
- 9 H. Nishihara, Y. Miyashita, K. Aoyama, T. Kodama, Y. Igarashi and Y. Takamura, *Biochem. Biophys. Res. Commun.*, 1997, **232**, 766–770.
- 10 U. Deppenmeier, *J. Bioenerg. Biomembr.*, 2004, **36**, 55–64.
- 11 R. Hedderich, *J. Bioenerg. Biomembr.*, 2004, **36**, 65–75.
- 12 T. Burgdorf, O. Lenz, T. Buhrke, E. van der Linden, A. K. Jones, S. P. J. Albracht and B. Friedrich, *J. Mol. Microbiol. Biotechnol.*, 2005, **10**, 181–196.
- 13 W. Lubitz, H. Ogata, O. Ruediger and E. Reijerse, *Chem. Rev.*, 2014, **114**, 4081–4148.

- 14 T. Matsumoto, S. Eguchi, H. Nakai, T. Hibino, K.-S. Yoon and S. Ogo, *Angew. Chem. Int. Ed.*, 2014, **53**, 8895–8898.
- 15 A. K. Jones, E. Sillery, P. J. Albracht and F. A. Armstrong, *Chem. Commun.*, 2002, 866–867.
- 16 F. A. Armstrong, N. A. Belsey, J. A. Cracknell, G. Goldet, A. Parkin, E. Reisner, K. A. Vincent and A. F. Wait, *Chem. Soc. Rev.*, 2009, **38**, 36–51.
- 17 K. A. Vincent, A. Parkin and F. A. Armstrong, *Chem. Rev.*, 2007, **107**, 4366–413.
- 18 T. Hiromoto, E. Warkentin, J. Moll, U. Ermler and S. Shima, *Angew. Chem. Int. Ed.*, 2009, **48**, 6457–6460.
- 19 M. Korbas, S. Vogt, W. Meyer-Klaucke, E. Bill, E. J. Lyon, R. K. Thauer and S. Shima, *J. Biol. Chem.*, 2006, **281**, 30804–30813.
- 20 E. J. Lyon, S. Shima, R. Boecher, R. K. Thauer, F.-W. Grevels, E. Bill, W. Roseboom, S. P. J. Albracht, S. Strasse and D.- Mu, *J. Am. Chem. Soc.*, 2004, **126**, 14239–14248.
- 21 R. Cammack, *Nature*, 1999, **397**, 214–215.
- 22 E. C. Hatchikian, N. Forget, V. M. Fernandez, R. Williams and R. Cammack, *Eur. J. Biochem.*, 1992, **209**, 357–365.
- 23 B. K. J. Pohorelic, J. K. Voordouw, A. Dolla, J. Harder, G. Voordouw and E. Lojou, *J. Bacteriol.*, 2002, **184**, 679–686.
- 24 A. S. Pandey, T. V. Harris, L. J. Giles, J. W. Peters and R. K. Szilagyi, *J. Am. Chem. Soc.*, 2008, **130**, 4533–4540.
- 25 Y. Nicolet, C. Piras, P. Legrand, C. E. Hatchikian and J. C. Fontecilla-Camps, *Structure*, 1999, **7**, 13–23.
- 26 J. W. Peters, J. W. Peters, W. N. Lanzilotta, B. J. Lemon and L. C. Seefeldt, *Science*, 1998, **282**, 1853–1858.
- 27 J. Esselborn, C. Lambertz, A. Adamska-Venkatesh, T. Simmons, G. Berggren, J. Noth, J. Siebel, A. Hemschemeier, V. Artero, E. Reijerse, M. Fontecave, W. Lubitz and T. Happe, *Nat. Chem. Biol.*, 2013, **9**, 607–9.

- 28 G. Berggren, A. Adamska, C. Lambertz, T. R. Simmons, J. Esselborn, M. Atta, S. Gambarelli, J. M. Mouesca, E. Reijerse, W. Lubitz, T. Happe, V. Artero and M. Fontecave, *Nature*, 2013, **499**, 66–69.
- 29 M. J. Lukey, A. Parkin, M. M. Roessler, B. J. Murphy, J. Harmer, T. Palmer, F. Sargent and F. A. Armstrong, *J. Biol. Chem.*, 2010, **285**, 3928–38.
- 30 C. R. D. Lancaster, U. S. Sauer, R. Gross, A. H. Haas, J. Graf, H. Schwalbe, W. Mäntele, J. Simon and M. G. Madej, *Proc. Natl. Acad. Sci. U. S. A.*, 2005, **102**, 18860–5.
- 31 C. Schäfer, B. Friedrich and O. Lenz, *Appl. Environ. Microbiol.*, 2013, **79**, 5137–5145.
- 32 C. Schäfer, M. Bommer, S. E. Hennig, J.-H. Jeoung, H. Dobbek and O. Lenz, *Structure*, 2015, 1–8.
- 33 J. Fritsch, O. Lenz and B. Friedrich, *Nat. Rev. Microbiol.*, 2013, **11**, 106–14.
- 34 A. Volbeda, P. Amara, C. Darnault, J.-M. Mouesca, A. Parkin, M. M. Roessler, F. A. Armstrong and J. C. Fontecilla-Camps, *Proc. Natl. Acad. Sci.*, 2012, **109**, 5305–10.
- 35 R. M. Evans, A. Parkin, M. M. Roessler, B. J. Murphy, H. Adamson, M. J. Lukey, F. Sargent, A. Volbeda, J. C. Fontecilla-Camps and F. A. Armstrong, *J. Am. Chem. Soc.*, 2013, **135**, 2694–2707.
- 36 M. M. Roessler, R. M. Evans, R. A. Davies, J. Harmer and F. A. Armstrong, *J. Am. Chem. Soc.*, 2012, **134**, 15581–94.
- 37 M. J. Lukey, M. M. Roessler, A. Parkin, R. M. Evans, R. A. Davies, O. Lenz, B. Friedrich, F. Sargent and F. A. Armstrong, *J. Am. Chem. Soc.*, 2011, **133**, 16881–16892.
- 38 M. Ludwig, J. A. Cracknell, K. A. Vincent, F. A. Armstrong and O. Lenz, *J. Biol. Chem.*, 2009, **284**, 465–477.
- 39 J. Fritsch, P. Scheerer, S. Frielingsdorf, S. Kroschinsky, B. Friedrich, O. Lenz and C. M. T. Spahn, *Nature*, 2011, **479**, 249–252.
- 40 S. Frielingsdorf, J. Fritsch, A. Schmidt, M. Hammer, J. Löwenstein, E. Siebert, V. Pelmeshnikov, T. Jaenicke, J. Kalms, Y. Rippers, F. Lendzian, I. Zebger, C. Teutloff, M. Kaupp,

- R. Bittl, P. Hildebrandt, B. Friedrich, O. Lenz and P. Scheerer, *Nat. Chem. Biol.*, 2014, **10**, 378–85.
- 41 T. Goris, A. F. Wait, M. Saggiu, J. Fritsch, N. Heidary, M. Stein, I. Zebger, F. Lenzian, F. A. Armstrong, B. Friedrich and O. Lenz, *Nat. Chem. Biol.*, 2011, **7**, 310–8.
- 42 Y. Shomura, K.-S. Yoon, H. Nishihara and Y. Higuchi, *Nature*, 2011, **479**, 253–6.
- 43 P. Wulff, C. C. Day, F. Sargent and F. A. Armstrong, *Proc. Natl. Acad. Sci. U. S. A.*, 2014, **111**, 6606–11.
- 44 K. Knuttel, K. Schneider, A. Erkens, W. Plass, A. Mueller, E. Bill and A. X. Trautwein, *Bull. Pol. Acad. Sci. Chem.*, 1994, **42**, 495–511.
- 45 J. Aiguier, J. Ebel and A. Martyrs, *Proc. Natl. Acad. Sci. U. S. A.*, 1998, **95**, 11625–11630.
- 46 M. Teixeira, I. Moura, A. V. Xavier, J. J. Moura, J. LeGall, D. V. DerVartanian, H. D. Peck and B. H. Huynh, *J. Biol. Chem.*, 1989, **264**, 16435–16450.
- 47 M.-E. Pandelia, W. Nitschke, P. Infossi, M.-T. Giudici-Ortoni, E. Bill and W. Lubitz, *Proc. Natl. Acad. Sci. U. S. A.*, 2011, **108**, 6097–102.
- 48 M. Asso, B. Guigliarelli, T. Yagi and P. Bertrand, *Biochim. Biophys. Acta*, 1992, **1122**, 50–56.
- 49 I. Dance, *Chem. Sci.*, 2015, **6**, 1433–1443.
- 50 H. R. Pershad, J. L. C. Duff, H. A. Heering, E. C. Duin, S. P. J. Albracht and F. A. Armstrong, *Biochemistry*, 1999, **38**, 8992–8999.
- 51 V. H. Teixeira, C. M. Soares and A. M. Baptista, *Proteins*, 2008, **70**, 1010–1022.
- 52 I. Sumner and G. A. Voth, *J. Phys. Chem. B*, 2012, **116**, 2917–26.
- 53 Y. Montet, P. Amara, A. Volbeda, X. Vernede, E. C. Hatchikian, M. J. Field, M. Frey and J. C. Fontecilla-Camps, *Nat. Struct. Biol.*, 1997, **4**, 523–526.
- 54 A. Volbeda, Y. Montet, X. Vernède, E. C. Hatchikian and J. C. Fontecilla-Camps, *Int. J. Hydrogen Energy*, 2002, **27**, 1449–1461.
- 55 E. Szóri-Dorogházi, G. Maróti, M. Szóri, A. Nyilasi, G. Rákhely and K. L. Kovács, *PLoS One*, 2012, **7**, e34666.

- 56 A. Volbeda, L. Martin, E. Barbier, O. Gutiérrez-Sanz, A. L. De Lacey, P.-P. Liebgott, S. Dementin, M. Rousset and J. C. Fontecilla-Camps, *J. Biol. Inorg. Chem.*, 2015, **20**, 11–22.
- 57 A. Volbeda, L. Martin, C. Cavazza, M. Matho, B. W. Faber, W. Roseboom, S. P. J. Albracht, E. Garcin, M. Rousset and J. C. Fontecilla-Camps, *J. Biol. Inorg. Chem.*, 2005, **10**, 239–249.
- 58 M. van Gastel, C. Fichtner, F. Neese and W. Lubitz, *Biochem. Soc. Trans.*, 2005, **33**, 7–11.
- 59 M. van Gastel, M. Stein, M. Brecht, O. Schröder, F. Lenzian, R. Bittl, H. Ogata, Y. Higuchi and W. Lubitz, *J. Biol. Inorg. Chem.*, 2006, **11**, 41–51.
- 60 H. Ogata, S. Hirota, A. Nakahara, H. Komori, N. Shibata, T. Kato, K. Kano and Y. Higuchi, *Structure*, 2005, **13**, 1635–1642.
- 61 H. Ogata, P. Kellers and W. Lubitz, *J. Mol. Biol.*, 2010, **402**, 428–444.
- 62 J. L. Barilone, H. Ogata, W. Lubitz and M. van Gastel, *Phys. Chem. Chem. Phys.*, 2015, **17**, 16204–16212.
- 63 K. G. V Sigfridsson, N. Leidel, O. Sanganas, P. Chernev, O. Lenz, K.-S. Yoon, H. Nishihara, A. Parkin, F. a Armstrong, S. Dementin, M. Rousset, A. L. De Lacey and M. Haumann, *Biochim. Biophys. Acta*, 2015, **1847**, 162–70.
- 64 K. A. Bagley, J. C. J. Van Garderen, S. M. Chen, S. J. E. C. Duin, S. P. J. Albracht and W. H. Woodruff, *Biochemistry*, 1994, **33**, 9229–9236.
- 65 C. Fichtner, C. Laurich, E. Bothe and W. Lubitz, *Biochemistry*, 2006, **45**, 9706–9716.
- 66 B. Bleijlevens, F. A. van Broekhuizen, A. L. De Lacey, W. Roseboom, V. M. Fernandez and S. P. J. Albracht, *J. Biol. Inorg. Chem.*, 2004, **9**, 743–752.
- 67 A. L. de Lacey, E. C. Hatchikian, A. Volbeda, M. Frey, J. C. Fontecilla-Camps and V. M. Fernandez, *J. Am. Chem. Soc.*, 1997, **119**, 7181–7189.
- 68 A. L. De Lacey, A. Pardo, V. M. Fernández, S. Dementin, G. Adryanczyk-Perrier, E. C. Hatchikian and M. Rousset, *J. Biol. Inorg. Chem.*, 2004, **9**, 636–642.
- 69 S. J. George, S. Kurkin, R. N. F. Thorneley and S. P. J. Albracht, *Biochemistry*, 2004, **43**, 6808–6819.

- 70 A. L. De Lacey, V. M. Fernandez, M. Rousset and R. Cammack, *Chem. Rev.*, 2007, **107**, 4304–30.
- 71 M. Bruschi, G. Zampella, P. Fantucci and L. De Gioia, *Coord. Chem. Rev.*, 2005, **249**, 1620–1640.
- 72 J. C. Fontecilla-Camps, A. Volbeda, C. Cavazza and Y. Nicolet, *Chem. Rev.*, 2007, **107**, 4273–303.
- 73 A. K. Jones, S. E. Lamle, H. R. Pershad, K. A. Vincent, S. P. J. Albracht and F. A. Armstrong, *J. Am. Chem. Soc.*, 2003, **125**, 8505–14.
- 74 M.-E. Pandelia, H. Ogata, L. J. Currell, M. Flores and W. Lubitz, *J. Biol. Inorg. Chem.*, 2009, **14**, 1227–41.
- 75 A. J. Healy, University of Oxford, 2013.
- 76 D. Millo, M.-E. Pandelia, T. Utesch, N. Wisitruangsakul, M. A. Mroginski, W. Lubitz, P. Hildebrandt and I. Zebger, *J. Phys. Chem. B*, 2009, **113**, 15344–51.
- 77 M. Brecht, M. van Gastel, T. Buhrke, B. Friedrich and W. Lubitz, *J. Am. Chem. Soc.*, 2003, **125**, 13075–83.
- 78 J. P. Whitehead, R. J. Gurbiel, C. Bagynka, B. M. Hoffman and M. J. Maroney, *J. Am. Chem. Soc.*, 1993, **115**, 5629–5635.
- 79 C. Fan, M. Teixeira, J. Moura, I. Moura, B.-H. Huynh, J. Le Gall, H. D. Peck and B. M. Hoffman, *J. Am. Chem. Soc.*, 1991, **113**, 20–24.
- 80 S. Foerster, M. Stein, M. Brecht, H. Ogata, Y. Higuchi and W. Lubitz, *J. Am. Chem. Soc.*, 2003, **125**, 83–93.
- 81 M. Saggu, I. Zebger, M. Ludwig, O. Lenz, B. Friedrich, P. Hildebrandt and F. Lendzian, *J. Biol. Chem.*, 2009, **284**, 16264–16276.
- 82 B. Bleijlevens, University of Amsterdam, 2002.
- 83 A. L. DeLacey, C. Stadler, V. M. Fernandez, E. C. Hatchikian, H. J. Fan, S. Li and M. B. Hall, *J. Biol. Inorg. Chem.*, 2002, **7**, 318–326.

- 84 H. Ogata, K. Nishikawa and W. Lubitz, *Nature*, 2015, **520**, 571–574.
- 85 H. Ogata, T. Krämer, H. Wang, D. Schilter, V. Pelmeshnikov, M. van Gastel, F. Neese, T. B. Rauchfuss, L. B. Gee, A. D. Scott, Y. Yoda, Y. Tanaka, W. Lubitz and S. P. Cramer, *Nat. Commun.*, 2015, **6**, 7890.
- 86 M.-E. Pandelia, P. Infossi, M. Stein, M.-T. Giudici-Orticoni and W. Lubitz, *Chem. Commun.*, 2012, **48**, 823–825.
- 87 J. W. van der Zwaan, S. P. J. Albracht, R. D. Fontijn and E. C. Slater, *FEBS Lett.*, 1985, **179**, 271–277.
- 88 P. Kellers, M.-E. Pandelia, L. J. Currell, H. Görner and W. Lubitz, *Phys. Chem. Chem. Phys.*, 2009, **11**, 8680–8683.
- 89 H. Tai, K. Nishikawa, S. Inoue, Y. Higuchi and S. Hirota, *J. Phys. Chem. B*, 2015, **119**, 13668–13674.
- 90 K. Weber, T. Krämer, H. S. Shafaat, T. Weyhermüller, E. Bill, M. Van Gastel, F. Neese and W. Lubitz, *J. Am. Chem. Soc.*, 2012, **134**, 20745–20755.
- 91 M. Kampa, M.-E. Pandelia, W. Lubitz, M. van Gastel and F. Neese, *J. Am. Chem. Soc.*, 2013, **135**, 3915–25.
- 92 C. Léger, S. J. Elliott, K. R. Hoke, L. J. C. Jeuken, A. K. Jones and F. A. Armstrong, *Biochemistry*, 2003, **42**, 8653–8662.
- 93 F. A. Armstrong, H. A. Heering and J. Hirst, *Chem. Soc. Rev.*, 1997, **26**, 169–179.
- 94 C. Léger and P. Bertrand, *Chem. Rev.*, 2008, **1084**, 2379–2438.
- 95 J. N. Butt and F. A. Armstrong, in *Bioinorganic Electrochemistry*, eds. O. Hammerich and J. Ulstrup, Springer, Dordrecht, 2008, pp. 91–128.
- 96 M.-E. Pandelia, V. Fourmond, P. Tron-Infossi, E. Lojou, P. Bertrand, C. Léger, M.-T. Giudici-Orticoni and W. Lubitz, *J. Am. Chem. Soc.*, 2010, **132**, 6991–7004.
- 97 G. Goldet, A. F. Wait, J. A. Cracknell, K. A. Vincent, M. Ludwig, O. Lenz, B. Friedrich and F. A. Armstrong, *J. Am. Chem. Soc.*, 2008, **130**, 11106–11113.

- 98 J. A. Cracknell, K. A. Vincent, M. Ludwig, O. Lenz, B. Friedrich and F. A. Armstrong, *J. Am. Chem. Soc.*, 2008, **130**, 424–425.
- 99 S. V Hexter, F. Grey, T. Happe, V. Climent and F. A. Armstrong, *Proc. Natl. Acad. Sci.*, 2012, **109**, 11516–11521.
- 100 B. J. Murphy, F. Sargent and F. A. Armstrong, *Energy Environ. Sci.*, 2014, **7**, 1426.
- 101 K. A. Vincent, A. Parkin, O. Lenz, S. P. J. Albracht, C. Juan, R. Cammack, B. Friedrich, F. A. Armstrong and J. C. Fontecilla-camps, *J. Am. Chem. Soc.*, 2005, **127**, 18179–18189.
- 102 S. E. Lamle, S. P. J. Albracht and F. A. Armstrong, *J. Am. Chem. Soc.*, 2004, **126**, 14899–909.
- 103 J. A. Cracknell, A. F. Wait, O. Lenz, B. Friedrich and F. A. Armstrong, *Proc. Natl. Acad. Sci. U. S. A.*, 2009, **106**, 20681–20686.
- 104 J. M. Mouesca, J. C. Fontecilla-Camps and P. Amara, *Angew. Chem. Int. Ed.*, 2013, **52**, 2002–2006.
- 105 A. Abou Hamdan, B. Burlat, O. Gutiérrez-Sanz, P.-P. Liebgott, C. Baffert, A. L. De Lacey, M. Rousset, B. Guigliarelli, C. Léger and S. Dementin, *Nat. Chem. Biol.*, 2013, **9**, 15–18.
- 106 M. Carepo, D. L. Tierney, C. D. Brondino, T. C. Yang, A. Pamplona, J. Telser, I. Moura, J. J. G. Moura and B. M. Hoffman, *J. Am. Chem. Soc.*, 2002, **124**, 281–286.
- 107 P. Kwan, C. L. McIntosh, D. P. Jennings, R. C. Hopkins, S. K. Chandrayan, C.-H. Wu, M. W. W. Adams and A. K. Jones, *J. Am. Chem. Soc.*, 2015, 151005185304006.
- 108 M. Horch, L. Lauterbach, M. A. Mroginski, P. Hildebrandt, O. Lenz and I. Zebger, *J. Am. Chem. Soc.*, 2015, **137**, 2555–2564.
- 109 L. Lauterbach and O. Lenz, *J. Am. Chem. Soc.*, 2013, **135**, 17897–905.
- 110 S. Niu, L. M. Thomson and M. B. Hall, *J. Am. Chem. Soc.*, 1999, **121**, 4000–4007.
- 111 P. E. M. Siegbahn, J. W. Tye and M. B. Hall, *Chem. Rev.*, 2007, **107**, 4414–35.
- 112 O. A. Ulloa, M. T. Huynh, C. P. Richers, J. A. Bertke, M. J. Nilges, S. Hammes-Schiffer and T. B. Rauchfuss, *J. Am. Chem. Soc.*, 2016, **138**, 9234–9245.
- 113 S. O. N. Lill and P. E. M. Siegbahn, *Biochemistry*, 2009, **48**, 1056–66.

- 114 A. Pardo, A. L. De Lacey, V. M. Fernández, H.-J. Fan, Y. Fan and M. B. Hall, *J. Biol. Inorg. Chem.*, 2006, **11**, 286–306.
- 115 D. Millo, P. Hildebrandt, M.-E. Pandelia, W. Lubitz and I. Zebger, *Angew. Chem. Int. Ed.*, 2011, **50**, 2632–4.
- 116 T. Yagi, M. Tsuda and H. Inokuchi, *J. Biochem.*, 1973, **73**, 1069–1081.
- 117 R. M. Evans, E. J. Brooke, S. A. M. Wehlin, E. Nomerotskaia, F. Sargent, S. B. Carr, S. E. V Phillips and F. A. Armstrong, *Nat. Chem. Biol.*, 2015, **12**, 46–50.
- 118 T. Krämer, M. Kampa, W. Lubitz, M. van Gestel and F. Neese, *ChemBioChem*, 2013, **14**, 1898–1905.
- 119 M. Kampa, W. Lubitz, M. Van Gestel and F. Neese, *J. Biol. Inorg. Chem.*, 2012, **17**, 1269–1281.
- 120 B. L. Greene, C.-H. Wu, P. M. McTernan, M. W. W. Adams and R. B. Dyer, *J. Am. Chem. Soc.*, 2015, **137**, 4558–4566.
- 121 B. L. Greene, C.-H. Wu, G. E. Vansuch, M. W. W. Adams and R. B. Dyer, *Biochemistry*, 2016, **55**, 1813–1825.
- 122 H. Tai, K. Nishikawa, M. Suzuki, Y. Higuchi and S. Hirota, *Angew. Chem. Int. Ed.*, 2014, **53**, 13817–13820.

Chapter 2

Theory

Hydrogenases are redox enzymes that exchange electrons with molecules, such as H₂ and O₂, that bind their bimetallic active site. Additionally; electrons are transported through a relay of Fe-S clusters between the enzyme and a redox partner. The latter can be a biological one, such as another redox protein, or an electrode (which is the case of the experiments described in this work). Electrochemical methods, protein film electrochemistry specifically, will be used in this thesis to investigate hydrogenase chemistry. In this chapter, the fundamental theory of electrochemistry will be described; with a special emphasis in protein film electrochemistry, which is the main electrochemical technique used in this work.

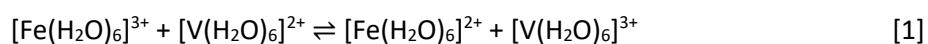
IR spectroscopy is the other main technique used in this work because it provides useful structural information on the active site of NiFe hydrogenases, due to their intrinsic CO and CN⁻ ligands. The fundamental theory of IR spectroscopy will be presented in this chapter, along with a basic explanation of attenuated total reflectance IR spectroscopy; which is the specific technique that will be implemented in this work.

2.1 Electrochemistry

2.1.1 Electron transfer reactions

The relation between chemical changes and flow of electrons is a fundamental focus of this work. Electron transfer to and from transition metal complexes can happen either via another molecule (a chemical redox agent) or by means of an electrode in an electrochemical cell. For example, the reduction of the aqueous Fe(III) ion can be written accordingly depending on how this reaction takes place:

Through a reducing agent in a homogenous phase



Or, through an electrode in a heterogeneous phase



The above equations give only an overall picture of the redox process, but electron transfer reactions occur through a series of intermediate steps:

i) Diffusion of reactants through the solution.

ii) Interactions between the two reactants, for a homogenous case like the one represented by equation 1. Or between the reactant and the electrode for a heterogeneous process like the one represented by equation 2.

iii) Formation of intermediates between the reactants in solution, or between the reactants and electrode. These intermediates can be short or long lived and can involve, or not, chemical changes such as the formation or breaking of bonds.

The transfer of an electron, reduction or oxidation of a species, can result in chemical changes *i.e.* breaking or formation of chemical bonds and dramatic structural changes. Such is the case of the tetrahedral carbonyl cluster $[\text{Rh}_4(\text{CO})_{12}]$, the addition of electrons to this compound causes a collapse of its molecular frame. Redox changes can also happen without considerable changes in structure. The one-electron oxidation of ferrocene gives the ferrocenium ion, and this electron transfer process results in no significant structural change to the molecule.¹

Inner and outer sphere mechanisms of electron transfer

In terms of mechanism, electron transfer reactions involving metal complexes in a homogeneous phase can be commonly classified as outer sphere and inner sphere reactions. We will later see that a similar classification can be made for redox reactions at an electrode in the following sections.

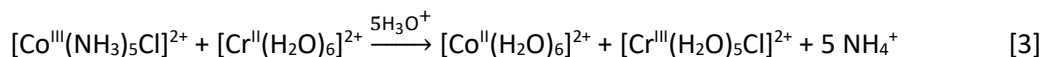
An inner sphere reaction involves the formation of a chemical bond between the reactants (electron donor and electron acceptor). The steps of such mechanism are therefore:

i) Formation of the covalent bond.

ii) Electron transfer.

iii) Breaking of the bond.

The classical example of an inner sphere reaction is the one-electron reduction of Co(III) by Cr(II):



The two reduced species, Co(II) and Cr(II), in this reaction are both labile in terms of their ligand substitution. On the contrary, the oxidised ions are both inert. The fact that all the Cr(III) produced is in the form of $[\text{Cr}^{\text{III}}(\text{H}_2\text{O})_5\text{Cl}]^{2+}$ suggests that the reaction must proceed through the formation of an intermediate state that allows the transfer of the chlorine from the cobalt to the chromium (Figure 2.1). Even the addition of $^{36}\text{Cl}^-$ to the solution does not result in the incorporation of this isotope into the Cr(III) product.¹⁻³

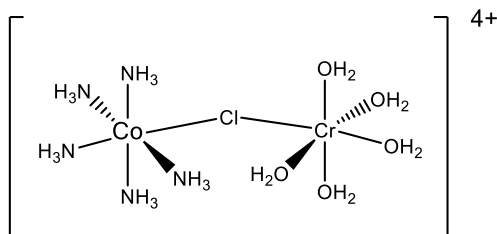


Figure 2.1 Intermediate of the inner sphere electron transfer reaction. The chloride functions as a bridging ligand between the metal centres.

An outer sphere electron transfer reaction, as opposed to the inner sphere mechanism, happens without the formation of a covalent bond between the reactants. The electron tunnels from the donor to the acceptor. There is, however, a small interaction (less than $\sim 1 \text{ kcal mol}^{-1}$) between donor and acceptor, this is referred to in the literature as “coupling”, “electronic overlap” or “electronic interaction”.²

Outer sphere electron transfer reactions obey the Franck-Condon principle. Such principle states that because the nuclei are much more massive than electrons, electron transfer happens much

faster than the nuclei can respond. This means that nuclear coordinates are effectively unchanged during the electron transfer process and therefore, that the geometry of the reactants must be equal to that of the products.^{1,3,4} The electron transfer must also comply with the first law of thermodynamics (conservation of energy). This means that the total potential energy of the reactants and their surrounding medium must be equal to that of the products.

How these two conditions (the Franck-Condon principle and conservation of energy) for the outer sphere electron transfer are met can be graphically exemplified by means of potential energy surfaces. Considering the one electron transfer from a donor D to an acceptor A:

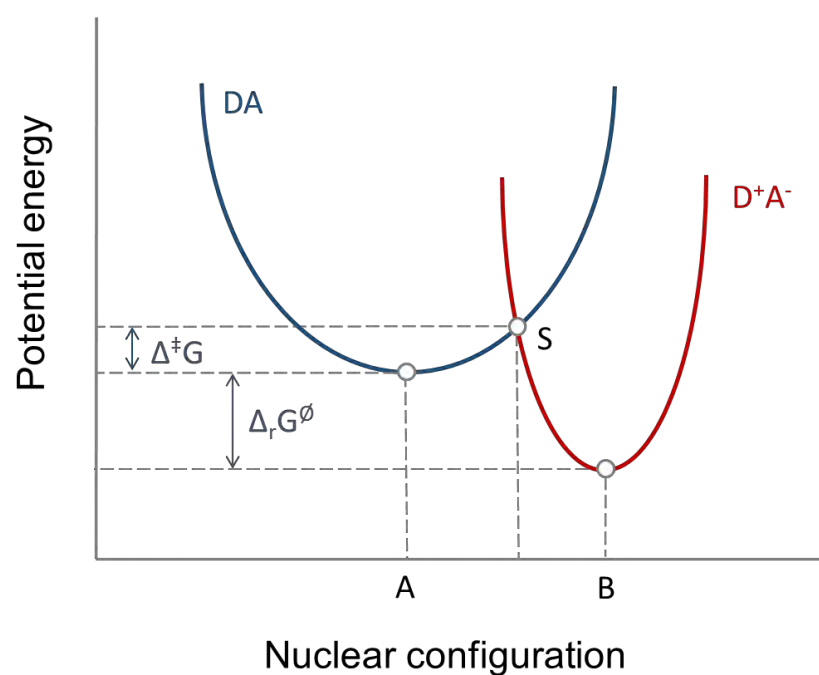


Figure 2.2 Potential energy surfaces for outer sphere electron transfer. The blue curve represents the potential energy surface of the precursor complex DA plus surrounding medium. The red curve represents the potential energy of the successor complex D^+A^- plus surrounding medium. A and B represent the nuclear coordinates for equilibrium configurations of the reactants and products respectively. $\Delta^\ddagger G$ is the activation energy and $\Delta_r G^\ominus$ the standard reaction Gibbs energy for the $DA \rightarrow D^+A^-$ electron transfer process.

The reactants, D and A, must collide and interact to form the short-lived precursor DA. Then, the electron transfer can occur at this point to produce the successor complex D^+A^- which can then dissociate to give the products D^+ and A^- .

In Figure 2.2, the intersection of the two surfaces S is the only point at which the two aforementioned conditions for the outer sphere electron transfer are met. At this point the nuclear configurations of the precursor and successor complexes are the same, and the potential energy of the reactants and surrounding medium and of the products and surrounding medium are equal too. This is the point at which an outer sphere electron transfer reaction takes place.¹⁻⁴

Proton-coupled electron transfer

A main concern of this thesis has to do with the electron transfer processes that are accompanied by proton transfers within the active site of NiFe hydrogenases. This means the combined addition, or removal, of one proton and one electron. In terms of the mechanism by which such reactions can occur, there exist two possibilities: *i*) That the electron and proton are transferred in a stepwise fashion, one preceded by the other; or *ii*) that both the electron and the proton are transferred simultaneously. Figure 2.3 illustrates these two routes:

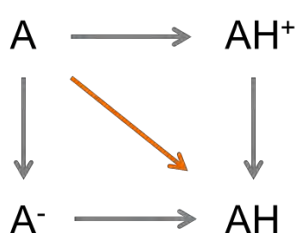


Figure 2.3 Concerted (orange) and stepwise (grey) PCET routes.

Because there exists some ambiguity about the terminology of PCET and similar processes, here we are going to state what is meant by proton-coupled electron transfer in this work. PCET will be understood as any transfer of an electron accompanied by the transfer of a proton in its broadest sense. This includes the cases where the electron and the proton come from the same bond as well as when the sources of these are not the same. It will also include the stepwise and the concerted

mechanistic pathways by which such process can occur. When talking about a specific mechanism it will be clearly stated whether the PCET is stepwise or concerted. The coupling of protons to electron transfer reactions has an effect both on the kinetics as well as the energetics of a process and these will be discussed in following sections.⁵⁻⁷

2.1.2 Electrode processes

Electron transfer at electrodes is always a heterogeneous process that involves the passage of an electron from an electrode, which can be a metal or a semiconductor, to a species in solution, or *vice versa*.

The electrode/solution system

The interface between an electrode and the solution consists, depending on the model, of roughly three sections: the electrode, the double layer, the diffusion layer, and the bulk of the solution.

Figure 2.4 shows these regions.

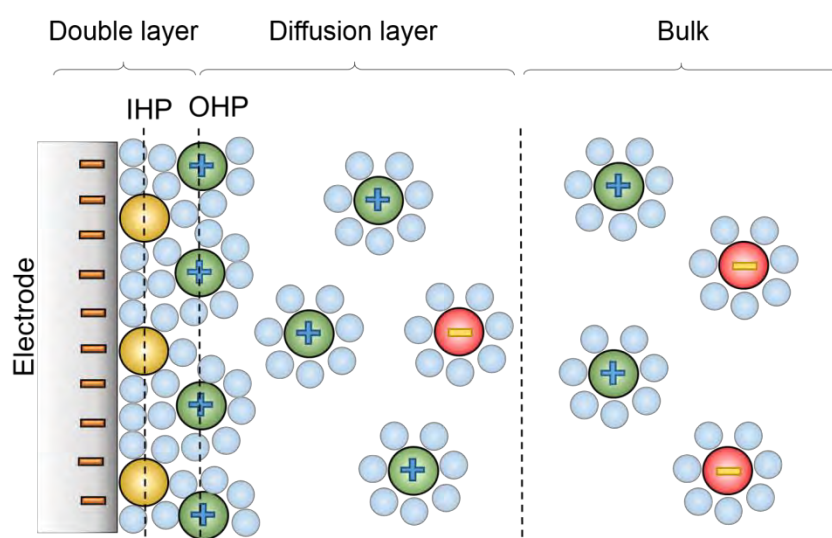


Figure 2.4 Structure of the electrode/solution interface. IHP: inner Helmholtz plane. OHP: outer Helmholtz plane. Yellow spheres: specifically-adsorbed ions. The green and red spheres represent cationic and anionic species respectively. The smaller blue spheres represent solvent molecules.

This “structure” of the electrode/solution interface is discontinuous with respect to the distribution of electrical charge. The excess charge of the electrode, negative in Figure 2.4, results in the formation of a layer with positive excess charge because of electrostatic interaction. This negatively charged surface (electrode) in direct contact with a surface of excess charge is called the double layer and has consequences on electrode processes that will be discussed later. The solution side of this double layer is thought to be made of several layers. First, closest to the electrode there is what is called the inner layer. This layer contains species that are considered to be *specifically adsorbed*, these could be ions or solvent molecules. The region where the charge is aligned in this first inner layer is called the inner Helmholtz plane (IHP) (Figure 2.4).

A second layer of solvated ions can approach the electrode next to the inner layer. The locus of charge of these solvated ions nearest to the inner layer is called the outer Helmholtz plane (OHP). Because these solvated ions are considered to be *nonspecifically adsorbed*, thermal agitation of the solution arranges them in a three-dimensional region called the diffusion layer. The diffusion layer is defined as a region which is dominated by an unequal distribution of charge (opposite to the excess charge on the electrode), this is in contrast to the bulk of the solution which is the region that is considered to be electroneutral.^{1,4,8}

Redox reactions at electrodes

As mentioned in the last section, an electron transfer reaction involves several steps. For the case where such reaction happens at an electrode, this reaction proceeds in at least three steps:

i) migration from the bulk solution to the surface of the electrode.

ii) electron transfer at the electrode

iii) migration from the electrode back to the bulk

As well as for reactions in the homogeneous phase, the concepts of inner sphere and outer sphere mechanisms of electron transfer exist for redox reactions at electrodes (Figure 2.5). They are

known as inner-layer and outer-layer electron transfers. The inner-layer mechanism occurs when the electron transfer takes place through a shared ligand between the electrode and the electroactive species; that is, the redox species is in direct contact with the electrode in the inner Helmholtz plane. An outer-layer mechanism happens when the electron is transferred through the layer of solvent between the electrode and the electroactive species which is in the outer Helmholtz plane.

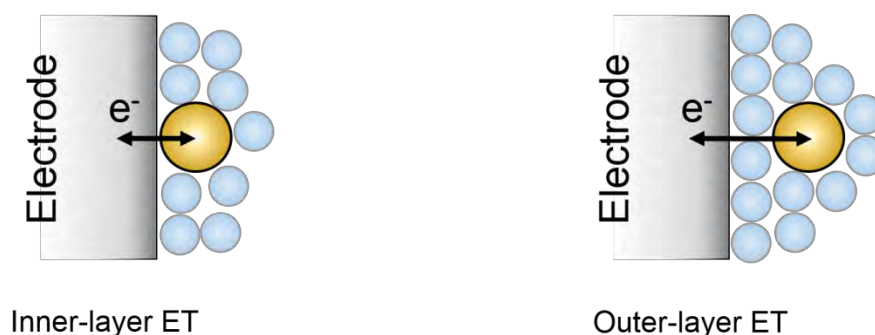


Figure 2.5 Mechanisms of heterogeneous electron transfer. The inner-layer mechanism takes place when the redox species is directly in contact at the electrode *i.e.* in the inner Helmholtz plane. In the outer-layer mechanism, there are molecules of solvent (at least one layer) between the redox species and the electrode, the redox molecule is located in the outer Helmholtz plane.

The overall rate of a heterogeneous redox process will be dependent on which of the steps involved in the reaction is the slowest elementary step. If the rate determining step has to do with the migration of species to the electrode or the migration of products back to the bulk of the solution, then it is the mass transport that will have a greater component in the overall rate of the reaction.

Alternatively, the slowest elementary step could be associated with the heterogeneous electron transfer rate; step ii) above. In this case, the mechanism by which the transfer occurs, that is, inner-layer or outer-layer, will have an effect on the rate. Also the chemical identity of the electrode (for the case of the inner layer mechanism) can have an important influence. The same is true for other factors that could be involved in the electron transfer; these can be adsorption of reactants or products, coupled chemical reactions, and/or formation of phases.^{1,9}

Adsorbed redox enzymes at electrodes

A main interest in this thesis has to do with redox enzymes adsorbed at electrode surfaces. Under these circumstances, the enzymes can exchange electrons quickly with the electrode; this process is not limited by diffusion. However, the substrate is in solution and it has to diffuse to the electrode (where the enzyme catalyst is immobilised) for the redox reaction to take place. Hence, the overall catalytic current may depend on diffusion of the substrate and products. These properties of mass transport will be discussed further later in this chapter, and also in Chapter 3.

The electrode potential

The energy of the electrons in an electrode is determined by the electrode potential. Electrons in the electrode populate the valence band up to the Fermi level, which represents the average energy of available electrons in this phase.

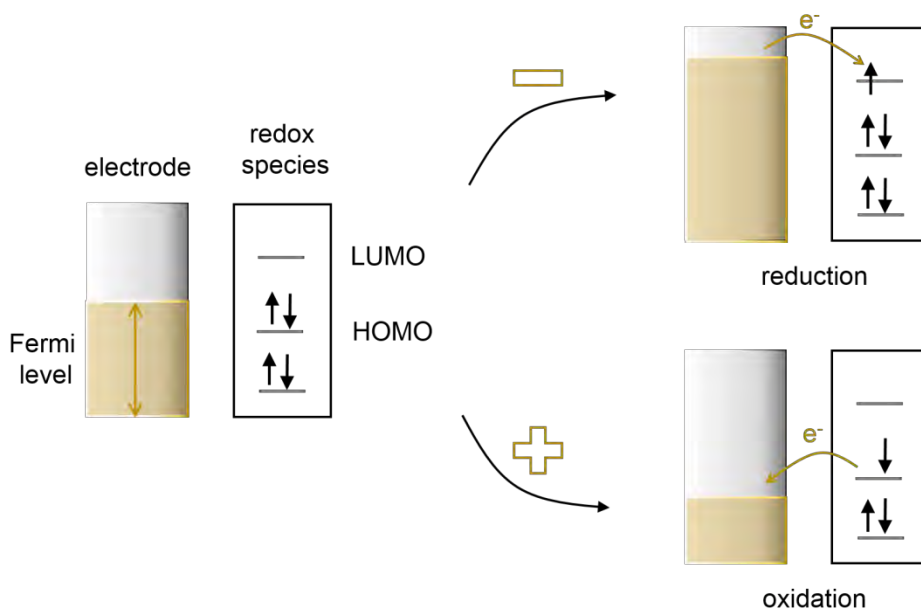


Figure 2.6 The effect of an applied potential on the fermi level of the electrode. A negative potential which raises this level above the LUMO of the redox species will result in a reduction whereas the application of a positive potential which lowers the Fermi level below the HOMO of the redox species will result in an oxidation.

Electrons will flow through an electrode in contact with a solution when the Fermi levels of the two phases are not equal. An applied potential results in the variation of the energy of the electrons in an electrode, and this can trigger redox reactions according to Figure 2.6.

The energy of the Fermi level can be increased by the application of a negative potential relative to the zero current potential. If the potential is increased such that the Fermi level is above the LUMO of the redox molecule, then electrons will flow from the electrode to the LUMO of the redox molecule and hence a reduction will occur. In the other hand, the electrode potential can be lowered to more positive values than the zero current potential. If it is lowered below the HOMO of the redox molecule, then electrons can flow from the HOMO to the electrode and hence an oxidation reaction will occur. The critical potential at which a redox reaction happens and the product species is stabilised is called the standard potential of that specific redox couple.^{1,8}

2.1.3 Equilibrium Electrochemistry

Nernst equation and redox equilibrium

This section will be concerned with redox systems at equilibrium. This is, where there is no net flux of electrons through the electrode of interest. Much of the work on NiFe hydrogenases, and the redox states of the active site, has been carried out under electrochemical-equilibrium conditions (redox titrations).

For a redox process involving reduction by n electrons,



The relation between the equilibrium potential and the concentration of the reduced and oxidised species is given by the Nernst equation:

$$E = E_{red}^0 + \frac{RT}{nF} \ln \frac{Ox}{Red} \quad [6]$$

E is the equilibrium potential. E^0 is the standard reduction potential of the Ox/Red couple.

The concentration of the species *Ox* and *Red* would be a function of the equilibrium potential as shown by Figure 2.7.

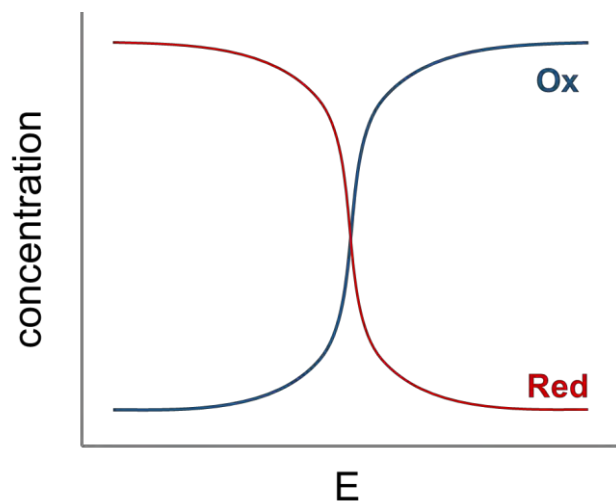


Figure 2.7 Concentration of the species *Ox* and *Red* as a function of the equilibrium potential.

It is important to distinguish the difference between the terms E , the equilibrium potential, and E^0 , the standard reduction potential. The equilibrium potential is a measured potential difference between the electrode of interest and a reference electrode (see below) whereas the standard reduction potential E^0 is a thermodynamic parameter related to the standard Gibbs free energy of the redox reaction according to the following equation:⁴

$$E^0 = -\frac{\Delta_r G^0}{nF} \quad [7]$$

Reference electrodes

The potential E as presented in equation 6 cannot be measured. Only a difference in potential between two electrodes can be measured. In order for this measured potential difference to reflect the potential of the electrode one is interested in, then the electrode against which the potential of the electrode of interest is measured should have a stable constant potential. Such an electrode is called a reference electrode. In this work all potentials will be reported relative to the standard hydrogen electrode (SHE). The SHE consists of a Pt wire immersed in an electrolyte solution of pH=1 and under 1 bar H_2 .^{1,10}

The electrode that will actually be used in the experiments, is the saturated calomel electrode (SCE). This consists of liquid Hg in contact with Hg_2Cl_2 (traditionally known as 'calomel'), in a saturated KCl solution. The potential of this electrode is +0.241 V vs SHE at 20 °C.⁸

Proton coupled electron transfer and redox thermodynamics

An important phenomenon investigated in this thesis, as mention previously, is PCET. The effect that it has on the thermodynamics of a redox process will be discussed here. This will be of relevance for the biomolecules and enzymes investigated in this work.

For a PCET reaction:



Standard reduction potentials are defined at pH 0, this is very impractical for physiologically relevant processes. For biological redox systems, the reduction potentials are stated for pH 7 and termed $E^{0'}$. They can also be reported for the pertinent pH.

Figure 2.8 shows a diagram of an electron transfer reaction that is coupled to a proton transfer. It takes into consideration the acidity constants and the standard reduction potentials of the species that could be potentially involved in this equilibrium.^{7,11}

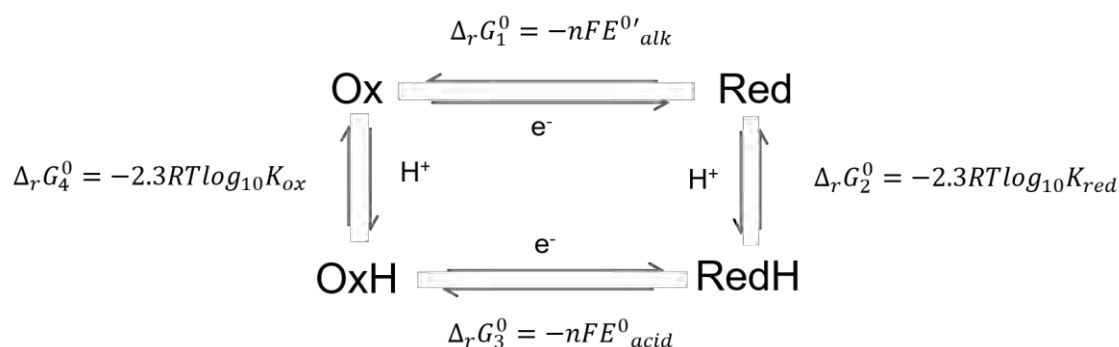


Figure 2.8 Square diagram for an electron transfer reaction coupled to a proton transfer.

Because these thermodynamic parameters ($\Delta_r G^0$) shown in the Figure 2.8 are state functions, it follows that the sum of all of them, which will result in a full cycle, should be equal to zero. The

acidity constants can be therefore related to the reduction potentials of the protonated and un-protonated species. The pH dependence of the reduction potential can be written as follows:

$$E^{0'}([H^+]) = E_{alk}^0 + \frac{2.3RT}{nF} \log_{10} \left(\frac{1 + \frac{[H^+]}{K_{red}}}{1 + \frac{[H^+]}{K_{ox}}} \right) \quad [9]$$

The dependence of the reduction potential on the pH can be more clearly grasped by means of a Pourbaix diagram. It shows the involved species (protonated or un-protonated versions of Ox and Red) and the reduction potential as a function of pH.

The redox transformations of the active site of NiFe hydrogenases, which are a fundamental focus of study in this work, are PCETs. Much of the results discussed in Chapter 4 will be concerned with the effect of pH on the redox transformations of the active site.

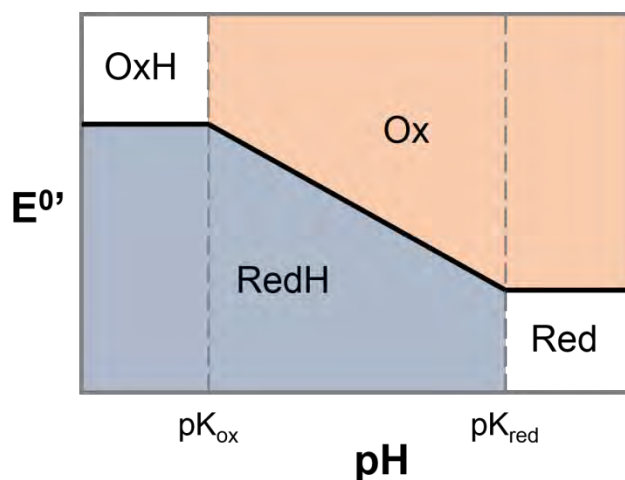


Figure 2.9 Pourbaix diagram. The black solid line represents the $E^{0'}$ values as a function of pH.

At pH values below the pK_{ox} the reduction potential is pH independent and equal to E_{acid}^0 . In this region the equilibrium of this redox process is dominated by the protonated versions of both reactants and products:



At pH values between pK_{ox} and pK_{red} the reduction potential is pH dependent and it decreases by $\frac{2.3RT}{nF}$ V pH^{-1} . The redox equilibrium happens between the un-protonated reactant and the protonated product:



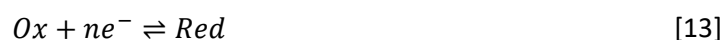
Finally, at pH values above pK_{red} the reduction potential is no longer dependent on pH and it is equal to E_{alk}^0 . The redox equilibrium at this pH involves both the un-protonated species:



2.1.4 Electrocatalysis and non-equilibrium electrochemistry

Current as a measurement of a rate of an electrode reaction

Considering a specific redox reaction that is catalysed at the surface of an electrode:



In order for there to be a continuous flow of electrons through the electrode the redox species must be transported efficiently. This means that there must be a continuous removal of the product *Red* of the reaction once it has taken place as well as a continuous provision of fresh reactant *Ox*. For each mol of reactant *Ox* that is reduced at the electrode, n moles of electrons will pass through the electrode. The amount of electrons that pass through the electrode per unit time (current measured at the electrode) will depend on both the mass transport as well as on the heterogeneous electron transfer.¹

Protein Film Electrochemistry (PFE): adsorbing redox enzymes on electrode surfaces

In this work we are interested in enzyme electrocatalysis, specifically of enzymes adsorbed on electrodes. When a redox enzyme is directly adsorbed on the surface of an electrode, it can directly exchange electrons with it and this rate of electron transfer will not depend on mass transport but on the heterogeneous electron transfer alone, and the factors that affect this rate. If the substrate

that this enzyme catalyses is present in the solution, then the enzymatic electrocatalytic process can occur (Figure 2.10). If the enzyme adsorbed on the electrode catalyses the reaction depicted in equation 13, and provided that there is efficient mass transport in the system, then the current measured at the electrode is directly related to the activity of the enzyme. This gives important information about the nature of the enzymatic catalysis as shall be seen in this work. This technique is called Protein Film Electrochemistry (PFE).¹²

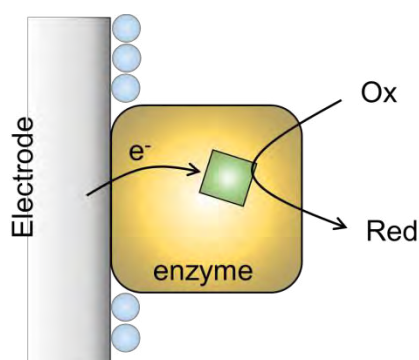


Figure 2.10 Redox enzyme on the surface of electrode. The enzyme interchanges electrons with the electrode directly without diffusion having to take place. The substrate Ox is reduced at the active site which has a continuous supply of electrons.

Three electrodes for voltammetry

When electrons are flowing through an electrode in an electrocatalytic process, for example the reduction given in equation 10, there must be a counter electrode where a half-reaction of the opposite sign (an oxidation in this case) is taking place. This is in order to maintain the electro-neutrality of the solution. The electrons will therefore flow from this counter electrode to the working electrode which is the electrode where the reaction of interest is taking place. Because there will always be a continuous flow of electrons in the counter electrode, it is impractical to measure the potential of an electrocatalytic reaction with only two electrodes, even if the counter electrode is a suitable reference electrode like the ones explained in previous sections. If there is a significant current flowing through the reference electrode, this will result in a change in the concentration of the redox species in the electrode compartment. This would cause a variation in

its potential; and therefore, make the measurement of the potential of the working electrode unreliable.

An accurate measurement of the potential of the working electrode is important in enzymatic, and in general, in electrocatalytic experiments. The rate of the electron transfer is dependent on the applied potential. It is also one of the main foci of these experiments to be able to measure the electrocatalytic current as a function of potential. In order to perform these experiments a three electrode system is required.^{1,8,13}

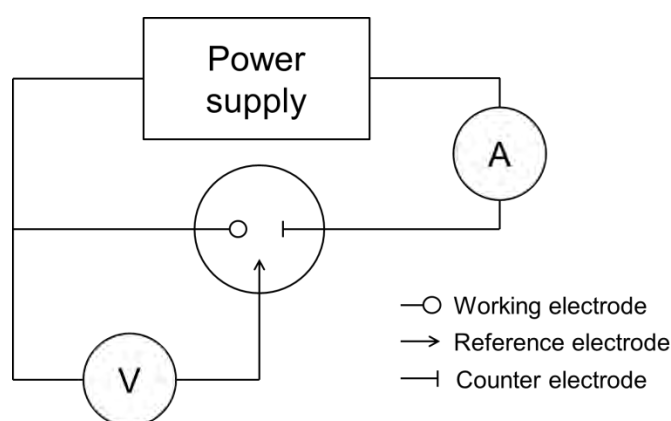


Figure 2.11 Three electrode system and electrode arrangement.

An auxiliary electrode, or counter electrode, is connected together with the working and reference electrode as shown in Figure 2.11. The potential difference between the working electrode and the reference electrode can be measured accurately. This is because the voltmeter V that monitors this potential is properly assembled to possess a high input resistance, it allows only a small amount of current to pass between these two electrodes. This way, the intrinsic potential of the reference electrode remains stable. Most of the current which results from applying a potential to the working electrode will flow then between the working and the counter electrodes. This current is measured by the ammeter A which is located between these electrodes.

Two different experiments using the three electrode configuration are of relevance in this thesis: cyclic voltammetry and chronoamperometry. In these experiments the potential is controlled in

the system and the resulting current is measured. This current, as mentioned above, is a direct measure of the activity of the enzyme for the case in study which is that when redox proteins are adsorbed on electrodes.

Cyclic voltammetry in Protein Film Electrochemistry

Figure 2.12 shows how the potential is controlled in a cyclic voltammetry (CV) experiment.

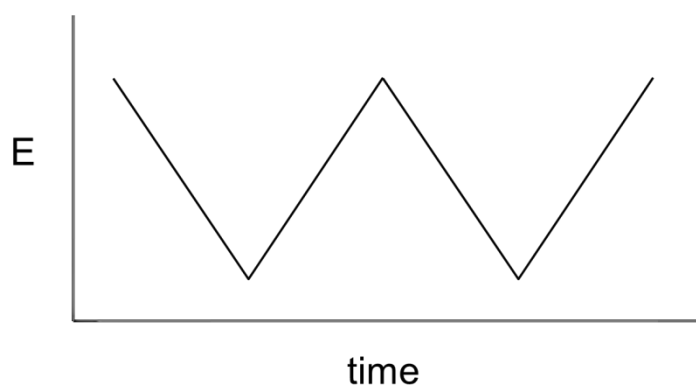


Figure 2.12 Potential sweep in a cyclic voltammetry experiment. The potential is swept back and forth between two potential values.

In a CV experiment, the potential is swept back and forth at a constant rate between two potential values. The current that flows through the working electrode as a response to this applied potential sweep will depend, for the case where there is a redox enzyme adsorbed on the electrode, on what else is present in solution (substrate, inhibitors). Figure 2.13 shows examples of how the cyclic voltammograms would look for an enzyme adsorbed on an electrode which catalyses the reaction depicted in equation 13, in the presence and absence of the substrate Ox:

For the case when there is no substrate present (Figure 2.13A); as the potential is scanned, electrons will be transferred from and to the electrode to reduce and oxidise the redox active centre inside the protein. This corresponds to the reduction in the first sweep from high to low potential and to oxidation when the potential is being swept back from low to high values. Raising the scan rate in a non-catalytic redox process of an adsorbed molecule will result in the separation

of the peaks. This separation as a function of scan rate gives information about the rate of interfacial electron exchange.

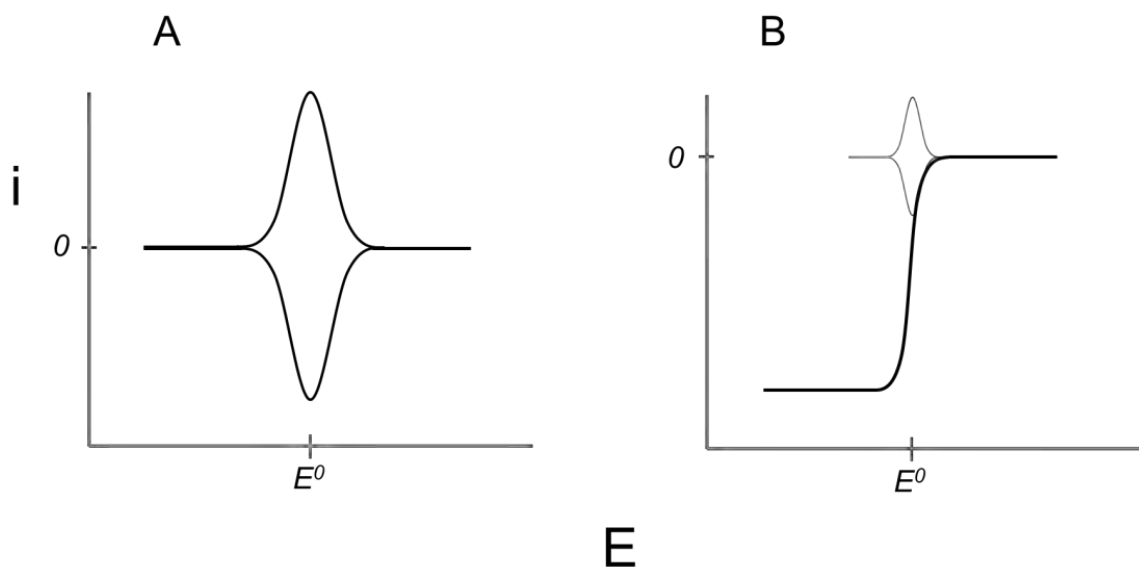


Figure 2.13 Cyclic voltammograms of an adsorbed redox protein: A) in the absence of substrate. B) in the presence of substrate. The grey voltammogram corresponds to that when there is no substrate present. It is shown for comparing the magnitude of the current when there is electrocatalytic activity.

For the case where there is substrate present (Figure 2.13B), and provided that there is efficient mass transport, there will be a potential after which the enzyme will start to catalyse the reduction of the substrate (this is called the onset potential). This will result in a reductive current, from the reduction of *Ox* to *Red* by the adsorbed enzyme, which is determined by the turnover frequency k_{cat} of the enzyme. The amplification of the current relative to the non-turnover case (shown in grey in Figure 2.13B) is caused by the continuous flow of electrons. More important parameters can be investigated by means of this technique such as the optimum potential, which most enzymes exhibit, *i.e.* the potential at which the enzyme exhibits its maximum activity. Other important parameters that can be measured by means of this technique shall be discussed later in this work.^{8,10,12}

Chronoamperometry in Protein Film Electrochemistry

In the case of chronoamperometry (CA) experiments, the potential is held at a specific value for a determined amount of time and then a sudden potential step follows. The behaviour of the current over time as a result of an applied potential is monitored. CA allows the deconvolution of the potential and time domains. The effect of substrate concentration, inhibitors, potential inactivation kinetics and other parameters can be investigated by means of CA.

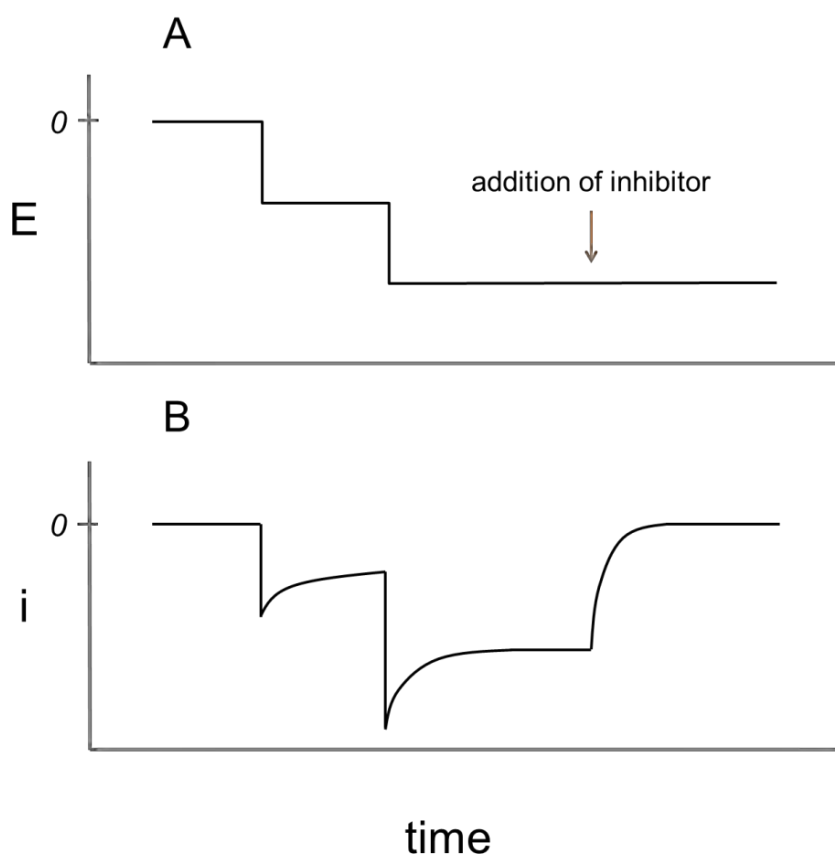


Figure 2.14 A) The potential control over time in a CA experiment. It also shows the time point at which the inhibitor was added to the experiment. B) Current-time trace. This shows the current that arises from the application of potential when there is substrate present in the system. The loss of current at the point at which the inhibitor is added shows the loss of electrocatalytic activity by the enzyme.

Figure 2.14 exemplifies how the potential is controlled in a CA experiment and how an enzyme that catalyses the reaction described by equation 10 would respond to the applied potentials. It also shows how this technique can be used to monitor the effect of an inhibitor in the catalytic activity of the enzyme.

When a sufficiently low potential, above the onset potential, is applied (Figure 2.14A), a reductive electrocatalytic current is measured (Figure 2.14B). This current remains stable if there is a continuous and fast enough supply of reactant. When an even lower potential is applied the current increases further, this is because an increase in the driving force has an effect on the heterogeneous electron transfer rate. A CA experiment is also appropriate for showing the effect of an inhibitor. Figure 2.14B shows how the current responds to the addition of the inhibitor. In this case the species added fully inhibits the enzyme resulting in a complete drop of the electrocatalytic current.¹²

2.2 Infrared Spectroscopy

2.2.1 Physical principles of IR absorption

Molecular vibrations

Vibrations in a molecule can result from the single stretch motion of two atoms in a diatomic molecule to the much more complex motion of every atom in a polyatomic molecule. A molecule that contains N atoms has $3N$ degrees of freedom; three of these represent translational motion in mutually perpendicular directions and the other three are due to rotation of the molecule as a whole. The number of vibrational modes, this is the number of ways in which a non-linear molecule can vibrate, is therefore $3N-6$. Typically, in a polyatomic molecule, each vibrational mode involves collective motions of many nuclei.

For each of these vibrational modes, the atoms in a molecule vibrate at a particular characteristic frequency. These vibrations can be represented in terms of quantized energy levels. Each molecule must exist in one of these discrete levels. Vibrational modes can be thought of as harmonic motions of the atoms in a molecule from their equilibrium positions, the system can be described as a system of masses joined by bonds with spring-like properties. For a diatomic molecule, a harmonic

oscillator model (described by Hooke's law) can be used to approximate the stretching modes between the atoms *i.e.* compression and elongation of the bond, at low energy values. Figure 2.15 shows the potential energy of a harmonic oscillator as a function of the distance between the atoms. It also shows an anharmonic Morse type oscillator, which describes more accurately the potential energy of the system for higher energy values.^{4,14,15}

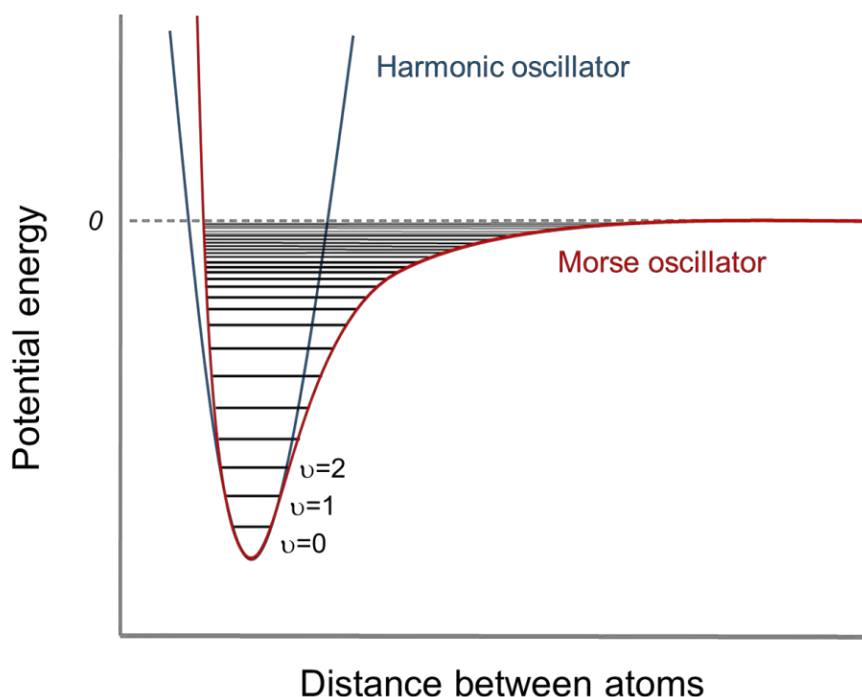


Figure 2.15 Potential energy of a diatomic molecule as a function of the distance between the two nuclei. The anharmonic Morse type oscillator represents accurately the behaviour of the potential energy as the atoms get too close where the repulsion of the positive nuclei increases this energy; it also accounts for the dissociation of the molecule where the atoms are not interacting any longer. At low v_i values the harmonic oscillator models well the potential energy of the system.

In Figure 2.15 it can be seen that at low v values the harmonic oscillator is a good approximation for calculating the potential energy of the molecular vibrations. This can be described by the following equation:

$$V_{in} = hn_i \left(v_i + \frac{1}{2} \right) \quad [14]$$

Where h is Planck's constant, n_i the fundamental frequency of the particular mode and ν_i the vibrational quantum number of the i th mode ($\nu_i = 0, 1, 2, \dots$). The energy difference for transitions that take place between the ground state ($\nu_i = 0$) and the first excited state ($\nu_i = 1$) of vibrational modes corresponds most often to the energy of the radiation of the mid-infrared region (400 – 4000 cm^{-1}).

Infrared spectrometry

It is the case that for many vibrational modes, only a few atoms are significantly displaced from their equilibrium positions. This means that the rest of the molecule is almost stationary for such transition. The frequency of such a vibrational mode is characteristic of the specific functional group in which the motion is centred but can be affected, within a range, by the surrounding chemical environment of this functional group. This allows infrared spectroscopy to be a powerful technique for identifying specific chemical functional groups within a molecule (qualitative analysis), by the observation of certain spectral features in a clearly defined region of the spectrum.

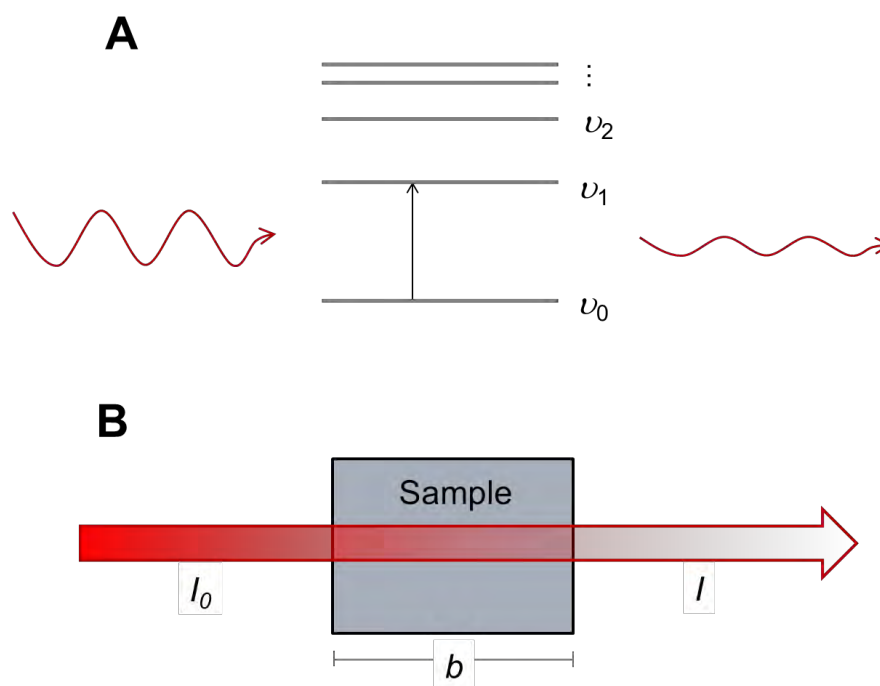


Figure 2.16 A) Absorption of an infrared photon results in the excitation to a higher energy vibrational state. B) Transmission of infrared light through a sample of path length b .

The variations in frequency of these functional-group specific bands also provide valuable information about the chemical environment of such groups. This will be discussed in more detail in following sections.

The selection rule for an infrared absorption is that the energy transition must involve a change in the dipole moment. A sample irradiated with mid-infrared light can absorb photons of energy equivalent to the energy difference between two states (Figure 2.16A): typically the ground state, and an excited vibrational state. If the dipole moment of a molecule changes with a vibration, infrared radiation with the frequency equal to the frequency of the molecular vibration will be absorbed.¹⁵

The transmittance of a sample at a wavenumber ν (this is how the energy of the radiation is represented normally in infrared experiments, in units of cm^{-1}) is given by:

$$T(\bar{\nu}) = \frac{I(\bar{\nu})}{I_0(\bar{\nu})} = e^{[-\alpha(\bar{\nu})b]} \quad [15]$$

Where b is the sample thickness (see Figure 2.16B), given in cm. $\alpha(\bar{\nu})$ is the linear absorption coefficient, in cm^{-1} . $I_0(\bar{\nu})$ and $I(\bar{\nu})$ are the incident and transmitted intensities. The absorbance of the sample at wavenumber ν , $A(\nu)$, is given by the base 10 logarithm of $1/T(\nu)$:

$$A(\bar{\nu}) = \log_{10} \frac{1}{T(\bar{\nu})} = a_i(\bar{\nu})bc_i \quad [16]$$

This formula given in equation 16 is the Bouguer-Beer-Lambert law (usually known only as Beer's law) and it is the fundamental law of quantitative spectroscopy. It relates the absorbance, at a particular wavelength, with the concentration c_i of the chemical species that contribute to that absorbance. The term a_i is the molar extinction coefficient (also known as molar absorptivity) and is typically reported in units of $\text{M}^{-1}\text{cm}^{-1}$.¹⁴ Infrared spectroscopy is therefore a useful quantitative tool and shall also be applied as such in this work.

2.2.2 Attenuated total reflection (ATR) IR spectrometry

The ATR experiment

The infrared technique that was used the most in this work is attenuated total reflection (ATR) IR spectroscopy. This technique consists in putting the sample in contact with an internal reflection element (Figure 2.17). The IR spectrum is recorded as a result of that contact. The radiation, in this technique, is not transmitted through the sample; as a consequence, there is no limitation regarding the thickness of the sample. The physical morphology of the sample represents no inconvenience, provided there is enough contact area between the sample and the surface of the sensing element. In general, sample preparation is minimal compared to other sampling techniques used in IR spectrometry (KBr discs, mineral oil mulls, cast films).

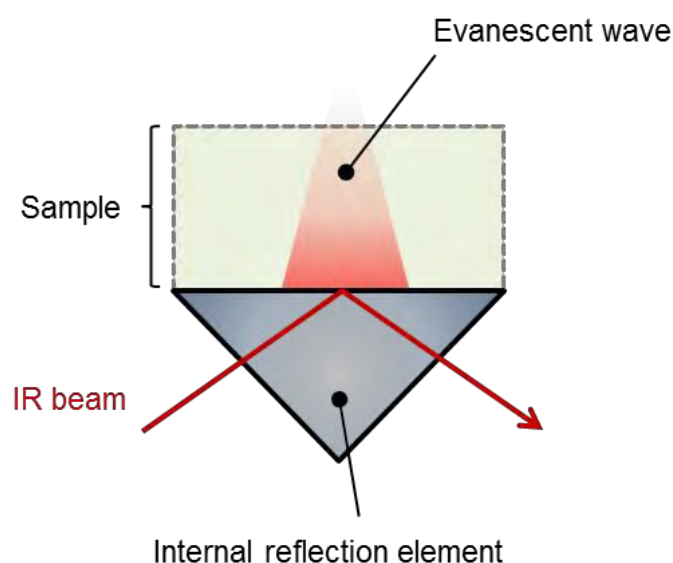


Figure 2.17 ATR IR configuration. The IR beam bounces at the interface between the IRE and the sample medium. The evanescent wave is the electric field that extends from the incident photons.

Internal reflection

When radiation passes from one transparent medium (with refractive index n_1) to another (with refractive index n_2) at an angle of incidence θ_1 , the angle of refraction θ_2 is given by Snell's law:

$$n_1 \sin \theta_1 = n_2 \sin \theta_2 \quad [17]$$

When $n_1 > n_2$ i.e. the medium where the light is coming from is more *optically dense*. There exists a critical angle θ_c at which the refracted light will travel along the interface. This means that the angle of refraction approaches 90° . For angles of incidence larger than the critical angle θ_c the incident beam reflects in the more optically dense medium as shown in Figure 2.18:

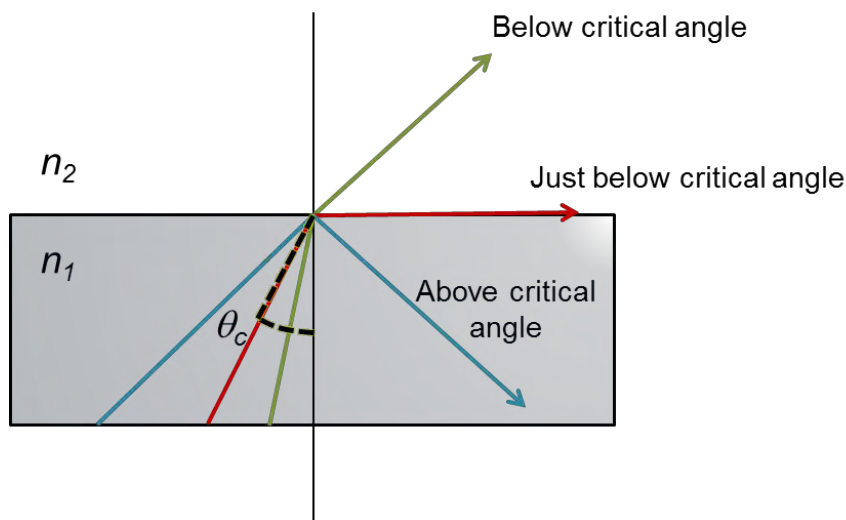


Figure 2.18 Beams that reach the interface at an angle lower to the critical angle θ_c will refract according to Snell's law (green and red arrows). Very close to the critical angle but lower than it, the beam will refract at an angle almost perpendicular to the surface (red arrow). Beams reaching the interface at incidence angles above θ_c will reflect internally (blue arrow).

The internal reflectance in the case described (where $n_1 > n_2$) is equal to 1, provided that the less optically dense material does not exhibit any light absorption.¹⁴

The evanescent wave and its interaction with the sample in ATR IR spectrometry

The evanescent wave shown in Figure 2.17 corresponds to the electric field that extends from the interface into the less optically dense medium. This electric field \mathbf{E} results from incident photons. The electric field of these extends perpendicularly from the surface of the more optically dense medium and decays exponentially with the distance z from the surface:

$$\mathbf{E} = \mathbf{E}_0 e^{-\gamma z} \quad [18]$$

E_0 is the electric field at the surface and γ is a constant. The distance from the surface over which this evanescent wave can effectively interact with the less optically dense medium is defined as the distance at which the strength of the electric field E has decayed to $1/e$ of its intensity at the surface E_0 . This distance is called the penetration depth d_p , and is equal to $1/\gamma$.

$$d_p = \frac{\lambda}{2\pi n_1 \sqrt{\sin^2 \theta_1 - \left(\frac{n_2}{n_1}\right)^2}} \quad [19]$$

As can be seen from equation 19, the penetration depth is a function of the wavelength λ of the incident radiation, of the refractive indices of the two media and of the angle of incidence. Since the penetration depth d_p depends on the wavelength, it follows that a spectrum recorded in an ATR experiment will differ from that obtained in a transmission experiment. The intensities at the high-wavenumber end will be lower than the intensities at the low-wavenumber end of the spectrum. Nonetheless, this can be easily corrected as the change in relative intensities is a linear function of the wavelength.¹⁴

2.2.3 IR spectra of metal carbonyls and cyanides

Backbonding in metal complexes

The infrared spectra of metal carbonyls exhibit strong and sharp stretching ν_{CO} bands. These bands are usually located at ~ 2100 - 1800 cm^{-1} . Because ν_{CO} is generally free from coupling with other vibrational modes, and it is not normally obscured by the presence of other vibrations; these bands provide valuable information about the structure and bonding of metal carbonyl compounds.

Carbonyl stretching frequencies are also very sensitive to their electronic environment. Table 2.1 shows the influence of charge in the ν_{CO} frequencies of hexacarbonyls of first row transition metals.^{3,16}

Table 2.1. Vibrational ν_{CO} frequencies of mononuclear hexacarbonyls shows the effect of the oxidation state of the metal on this bond.

<i>Compound</i>	$\nu(\text{CO}) / \text{cm}^{-1}$
$[\text{Fe}(\text{CO})_6]^{2+}$	2204
$[\text{Mn}(\text{CO})_6]^+$	2090
$\text{Cr}(\text{CO})_6$	2000
$[\text{V}(\text{CO})_6]^-$	1860
$[\text{Ti}(\text{CO})_6]^{2-}$	1750

The trend observed in Table 2.1 is explained, according to molecular orbital theory, by π backbonding. The chemical bond between the CO and the metal has two components: the σ -bond which results from the donation of electrons from the CO to the metal, and the π -bond which result from the backdonation of the $d\pi$ -electrons of the metal to the empty $2p\pi^*$ orbital of the CO, which is antibonding. The latter π -backbonding causes the strength of the C-O bond to decrease. The lower the oxidation state of the metal, the more electron density that will be backdonated and therefore, the lower the frequency of the ν_{CO} .



Figure 2.19 The σ and π bonding in metal carbonyls. The $2p\pi$ orbital of CO is antibonding, the backdonation of electron density to this orbital results in the weakening of the bond.

In the case of CN^- , its interaction with metals is more weighted towards σ -donation than to π -acceptance. Furthermore, its behaviour is less predictable than that of CO. Depending on the balance of σ - vs π -bonding, the ν_{CN} might be raised or lowered.¹⁷ Free CN^- in aqueous solution

presents the ν_{CN} band at 2080 cm^{-1} ; and $[\text{Fe}(\text{CN})_6]^{3-}$ exhibits one band at 2118 cm^{-1} . The antibonding σ -bond donation, from the ligand to the metal centre, strengthens the C-N bond; this results in a shift to higher wavenumber (relative to free CN^-). The one-electron reduction of this complex to form $[\text{Fe}(\text{CN})_6]^{4-}$ results in an increase in the π backbonding component of the M-CO bond; the ν_{CN} band of this reduced complex appears at 2044 cm^{-1} , which is less than that of the free CN^- . In general, the behaviour of the ν_{CN} band position is influenced by electronegativity, coordination number and oxidation state of the metal.¹⁸

The principle just described, of CO and CN^- ligands bound to transition metals, provides the basis for much of the work discussed in this thesis. The active site of NiFe hydrogenases has two CN^- ligands and one CO ligand coordinated to a Fe atom (see Figure 1.5). These function as probes of the electronic density of the active site. The wavenumber positions of the ν_{CO} and ν_{CN} bands are characteristic of the redox state of the active site. This will give valuable information about the redox chemistry of the active site, as well as mechanistic insight of the enzymatic activity, as shall be discussed in following chapters.

References

- 1 P. Zanello and N. G. Connelly, *Inorganic Electrochemistry: Theory, Practice and Application*, The Royal Society of Chemistry, Cambridge, 2003.
- 2 O. Snir and I. A. Weinstock, in *Physical Inorganic Chemistry: Reactions, processes and applications*, ed. A. Bakac, John Wiley & Sons, New Jersey, 2010, pp. 1–37.
- 3 P. Atkins, T. Overton, J. Rourke, M. Weller and F. Armstrong, *Shriver & Atkins Inorganic Chemistry*, Oxford University Press, Oxford, 4th edn., 2006.
- 4 P. Atkins and J. De Paula, *Atkins' Physical Chemistry*, Oxford University Press, Oxford, 9th edn., 2010.
- 5 M. H. V Huynh and T. J. Meyer, *Chem. Rev.*, 2007, **107**, 5004–5064.

- 6 D. Wang and J. T. Groves, *Proc. Natl. Acad. Sci. U. S. A.*, 2013, **110**, 15579–84.
- 7 S. Fukuzumi, in *Physical Inorganic Chemistry: Reactions, processes and applications*, ed. A. Bakac, John Wiley & Sons, New Jersey, 2010, pp. 39–74.
- 8 A. J. Bard and L. R. Faulkner, *Electrochemical Methods: Fundamentals and Applications*, John Wiley & Sons, New York, 2nd edn., 2001.
- 9 S. Tanimoto and A. Ichimura, *J. Chem. Educ.*, 2013, **90**, 778–781.
- 10 R. Compton and C. E. Banks, *Understanding Voltammetry*, Imperial College Press, London, 2nd edn., 2011.
- 11 C. Léger, in *Practical Approaches to Biological Inorganic Chemistry*, eds. R. R. Crichton and R. O. Louro, Amsterdam, 2013, pp. 179–216.
- 12 J. N. Butt and F. A. Armstrong, in *Bioinorganic Electrochemistry*, eds. O. Hammerich and J. Ulstrup, Springer, Dordrecht, 2008, pp. 91–128.
- 13 J. A. Cracknell, A. F. Wait, O. Lenz, B. Friedrich and F. A. Armstrong, *Proc. Natl. Acad. Sci. U. S. A.*, 2009, **106**, 20681–20686.
- 14 P. R. Griffiths and J. A. de Haseth, *Fourier Transform Infrared Spectroscopy*, John Wiley & Sons, New Jersey, 2nd edn., 2007.
- 15 B. H. Stuart, *Infrared Spectroscopy: Fundamentals and Applications*, John Wiley & Sons, West Sussex, 2004.
- 16 K. Nakamoto, *Infrared and Raman Spectra of Inorganic and Coordination Compounds*, John Wiley & Sons, New Jersey, 6th edn., 2009.
- 17 R. H. Crabtree, *The Organometallic Chemistry of Transition Metals*, Wiley, Somerset, 6th edn., 2014.
- 18 M. F. A. El-sayed and R. K. Sheline, *J. Inorg. Nucl. Chem.*, 1958, **6**, 187–193.

Chapter 3

Method development: a novel infrared spectroelectrochemical approach for studying enzymes on carbon electrodes

This chapter describes the development of an approach that combines protein film electrochemistry with IR spectroscopy *in situ*. This development has two components: *i)* The optimisation of the adsorption of Hyd-1 on high-surface area carbon nanoparticles. This is done to improve the signal in the IR spectroscopy. *ii)* The design of a spectroelectrochemical flow cell that permits efficient mass transport and good electrical conductivity. This is in order to simulate the conditions of a protein film electrochemistry experiments. This section finalises with a demonstration of this system at work. It shows electrochemical data that can be compared to that obtained from protein film electrochemistry in a rotating disc electrode configuration; and high quality IR spectra.

The second section in this chapter details the experimental procedures and methods. This includes the reagents and materials used, and the specific procedures carried out in the experiments performed for this thesis.

3.1 Introduction

3.1.1 Justification and background

PFE and the useful information it provides

Protein film electrochemistry (PFE) is a technique in which a redox protein is adsorbed on the surface of an electrode, usually as a sub-monolayer. The immobilisation of the protein on the electrode allows the direct electron transfer between these two components to be independent of the sluggish process of diffusion. When it is a redox enzyme that is adsorbed on the surface of the electrode and there is substrate present in solution, the current monitored through the electrode in a PFE experiment is a direct measure of the enzyme's activity.¹⁻⁴ A rotating disc electrode (RDE) configuration is commonly used to provide the mass transport conditions of substrate to the surface of the electrode, where the enzyme is immobilised, required for a PFE experiment This is described by Figure 3.1.

PFE is a versatile technique. The activity of the enzyme of interest can be studied under different experimental conditions in a very practical way. The concentration of the substrate, or of inhibitors, can be easily changed during an experiment by adding aliquots of concentrated solutions of these chemicals or by flowing gas in the headspace of the cell. Moreover, since the enzyme film is adsorbed on the electrode, the medium can be completely changed by transferring the electrode from one solution to another. This is useful, for example, for investigating the enzyme's activity at different pH values.

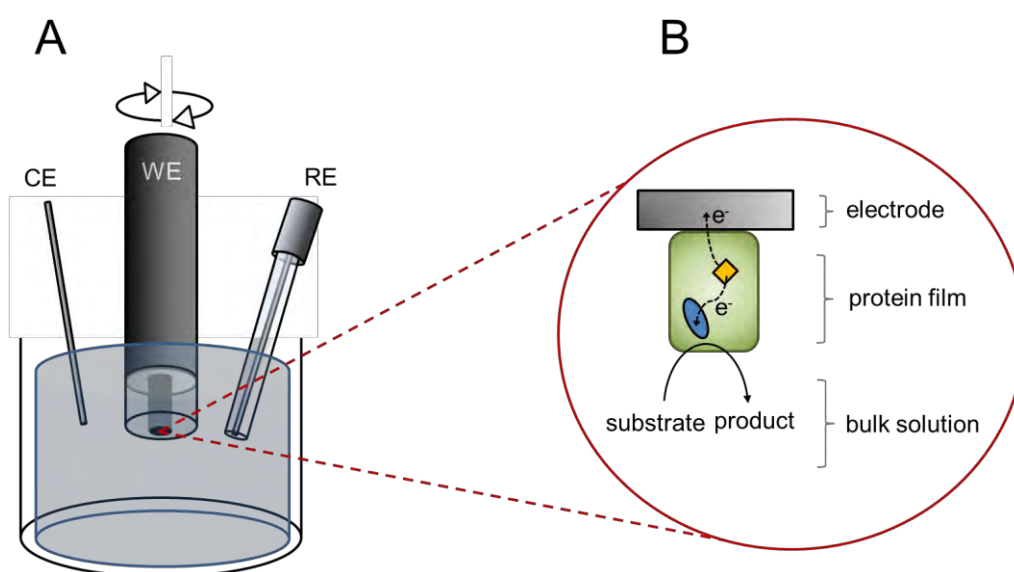


Figure 3.1 A) Electrochemical cell configuration for a PFE experiment. The rotation of the working electrode (WE) gives good mass transport conditions. B) Diagram of a redox protein on the surface of an electrode exchanging electrons with it while engaging in catalytic turnover.

In addition to this, the sample requirement is very small: a monolayer coverage of a 50 kDa protein would require no more than 10 picomoles cm^{-2} and the electrodes used are usually of about 0.02-0.04 cm^2 surface area.^{3,5} This technique has been extensively applied in the study of hydrogenases and has provided valuable insight into their chemistry.⁵⁻⁹

Infrared spectroscopy and its convenience for studying NiFe Hydrogenases

The organometallic ligands CO and CN^- that are bound to the Fe atom in the active site of NiFe hydrogenases give rise to intense vibrational bands in the mid-IR region (Figure 3.2). The positions of

these bands are highly sensitive to the electron density on the active site and therefore, IR spectroscopy has been widely applied to characterise the different redox states of the active site of many hydrogenases under a broad range of conditions like pH, presence of inhibitors, and presence of substrate.^{10–18}

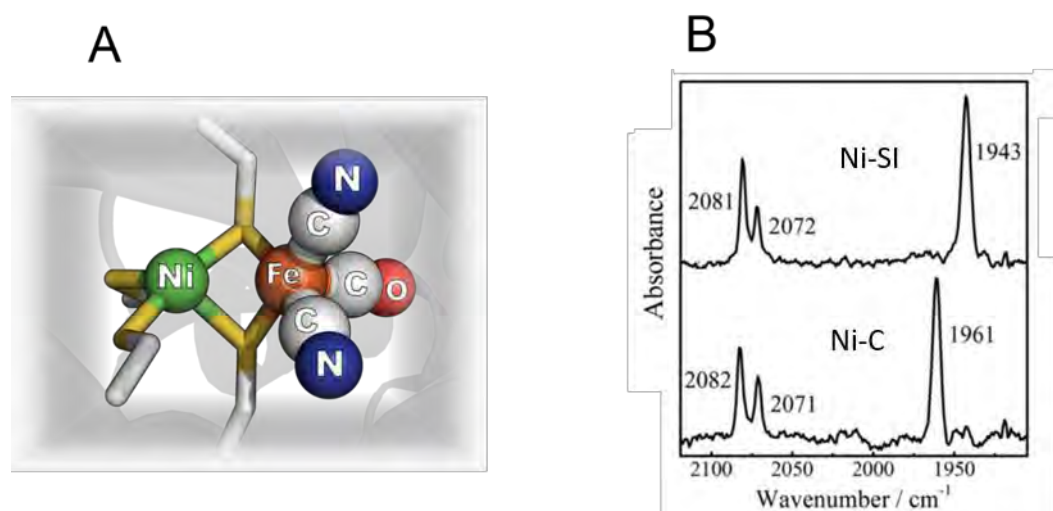


Figure 3.2. A) The active site of the O₂-tolerant [Ni-Fe] hydrogenase 1 from *E. coli* (PDB: 3USC), the organometallic ligands CO and CN⁻ are bound to the Fe atom. B) Infrared spectra, showing the active site region, before and after the one electron reduction (from the Ni-SI state to the Ni-C state), of the regulatory hydrogenase RH from *R. eutropha*. The change in electron density (reduction of the active site) results in the shift of the wavenumber positions of the $\nu(\text{CO})$ and $\nu(\text{CN})$ bands. Adapted from Ref 19 with permission of The Royal Society of Chemistry.

The different redox states of NiFe hydrogenases in solution phase, with the aid of mediators, have been studied by IR spectroelectrochemistry at gold electrodes.^{11,16,20} In an attempt to avoid mediators, the Vincent group has developed an IR spectroelectrochemical method for studying hydrogenases in solution at carbon electrodes. These have convenient advantages over metal electrodes for studying hydrogenases;¹⁹ proteins tend to denature on metal electrodes whereas they retain their native activity on carbon, the interactions with carbon resemble more those that occur between proteins and membranes in biological systems. Gold surfaces, on the other hand, can be modified in such a way that protein adsorption is facilitated (i.e. self-assembled monolayers) and IR spectroelectrochemistry of adsorbed NiFe hydrogenases has been performed already.^{21–23}

Towards the best of two worlds: Protein Film Infrared Electrochemistry

This project aims to develop an infrared spectroelectrochemical method for studying hydrogenases adsorbed on carbon electrodes, *i.e.* coupling PFE with IR spectroscopy to address the electrode-adsorbed species. Much of the hydrogenase electrochemical research has been done on carbon electrodes (e.g. pyrolytic graphite edge) because this material is very compatible with hydrogenases, the adsorption is easily attainable, often without any chemical modification of the electrode, and the film obtained is relatively stable (activity remains over long periods of time). Carbon electrodes also enable the study of inhibition by small molecules such as CO and CN⁻, which would react with metal electrode surfaces, adding undesirable features to the IR spectrum.^{2,24}

The development of such a method would couple the conditions and advantages of PFE to the structural information provided by IR spectroscopy. This new approach of Protein Film Infrared Electrochemistry (PFIRE) should provide new and direct structural information about the redox states of enzymes whilst they exchange electrons directly with the electrode under turnover or non-turnover conditions, as well as its interactions with inhibitors.

3.2 Challenges in combining PFE with IR spectroscopy *in situ*

3.2.1 IR detection and protein loading

In order to combine IR spectroscopy with PFE one of the main challenges to overcome is the low surface coverages obtained from proteins adsorbed on electrodes. The sensitivity of PFE is rather high, the lower limit of detection of electron transfers to individual redox centres is usually of about 1-3 pmol cm⁻², and when it is a catalytic process that is being studied, the enhancement of the signal because of the high turnover of redox enzymes allows the detection of these currents from even lower coverage films.²⁵ In addition to this, a low coverage can be advantageous because it prevents

problems with substrate provision to the enzyme film and minimises sample requirement.^{3,26,27} However, in the case of IR spectroscopy, a high concentration of the sample is desired in order to achieve an optimal signal to noise ratio so that the different peaks from different redox states can be distinguished.²⁵ In this work the active site is the main focus of investigation, which will be studied by the CO and CN⁻ ligand stretching vibrations as explained in previous sections. There is only one active site per hydrogenase unit (an enzyme with a molecular weight of ca 100 000 g mol⁻¹); so getting a high enough concentration of it on a surface, in order for these CO and CN⁻ vibrational modes at the active site to be detectable, is the first thing that needed to be tackled.

3.2.2 Mass transport

Another challenge when coupling PFE with IR spectroscopy has to do with mass transport. In order for the current to be a measure solely of the activity of the redox enzyme in a PFE experiment, the provision of fresh substrate and removal of product from the film should be efficient.¹ This means that the current measured at the working electrode should not depend on the rotation rate of the electrode, for the case of a RDE set up like the one explained in Figure 3.1, or on the flow rate of the solution to the surface of the electrode, for the case of other experimental configurations.

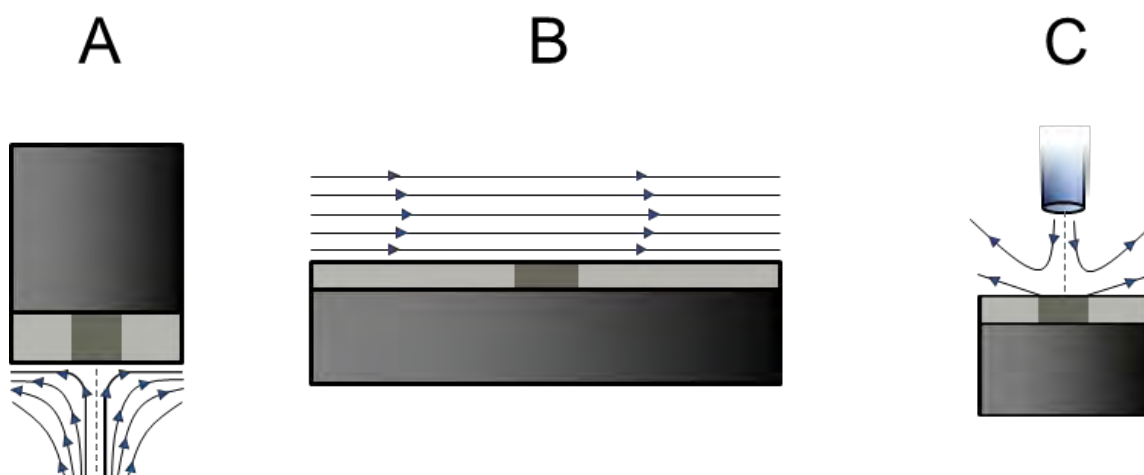


Figure 3.3. Hydrodynamic electrodes showing different types of convection: A) the rotating disc electrode, B) the channel electrode, and C) an impinging jet electrode.

Figure 3.3 shows different experimental configurations for providing good mass transport conditions in electrocatalytic experiments.²⁸ If it was the case that the current depended on flow or rotation rate, it would mean that this measured current would not only be related to the catalytic process but also to how fast the substrate can be supplied to the enzyme film, or the product removed away from it. When this happens the experiment is referred to as mass transport limited. The Reynolds number should also be taken into account when assessing these experimental conditions: whether the flow is steady or turbulent has an important effect in the mass transport conditions.^{28,29} An ideal PFE experiment should not be mass transport limited in order for the current to be a measure of the catalytic activity of the enzyme only.²⁹

It was mentioned above that it is desirable for the surface coverage of the protein to be maximised in order to get an optimal and clear signal for the IR spectroscopy. However, this brings up a compromise between having enough sample to be detected spectroscopically, and being able to provide efficient mass transport conditions to all the enzyme molecules adsorbed on the electrode surface. It follows that the more concentrated the protein is on the surface, the more challenging meeting the mass transport conditions is (fast enough provision of substrate and removal of product is required). In the following sections, it will be explained how these challenges were overcome by the development of an improved IR spectroelectrochemical technique.

3.2.3 Addressing the challenge of surface coverage

Carbon nanoparticles as electrodes

In order to address the challenge of the protein surface concentration, different commercial carbon nanoparticles were tested as electrode materials. The reason for choosing carbon is because much of the hydrogenase electrochemical research has been done on carbon, and some of the advantages of using carbon as an electrode were mentioned above. Table 3.1 shows the properties of the different carbon materials tested.

Table 3.1. Morphological attributes of the carbon nanomaterials studied.

Material	Particle diameter / nm	Specific surface area (BET) / m ² g ⁻¹
Nanopowder	50 ^a	>100 ^a
VXC72R	30 ^b	235 ^c
BP200	12 ^b	1487 ^c

^a Provided by Sigma-Aldrich. ^b Provided by Cabot Corp. ^c From reference 30.

FMN as a test system

Flavin mononucleotide (FMN) was used as a test system for comparing the performance of the carbon nanoparticles; as enzyme samples are time consuming, and costly, to produce.

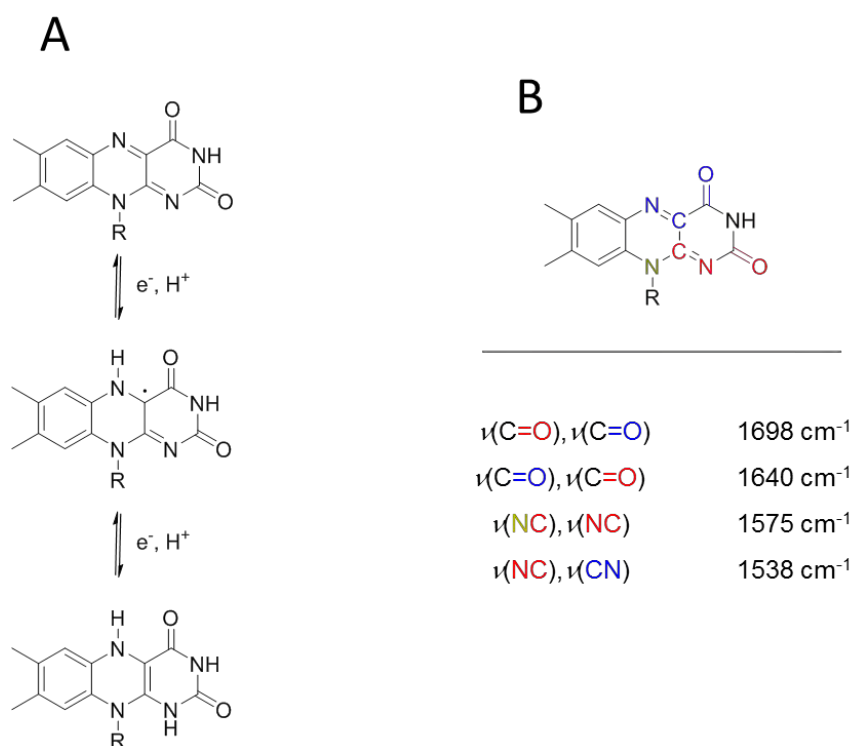


Figure 3.4. A) The structure and redox transitions of flavins. The semiquinone radical is reasonably stable inside protein cavities or in non-protic organic solvents. For FMN, R=CH₂(CHOH)₃CH₂OPO₃²⁻. B) Vibrational modes in flavins. The wavenumber position of the absorption bands corresponding to the main vibrational modes are given in the table. The assignment of these bands was made according to the literature.^{31,32}

FMN is a redox biomolecule which functions as a coenzyme for many oxidoreductases, including some hydrogenases like the soluble hydrogenase from *R. eutropha*.³³ It easily adsorbs on carbon surfaces and exhibits intense IR bands. The structure of FMN, its redox transitions and its most intense vibrational modes are shown in Figure 3.4.

Initially, to test the electrochemical behaviour of the FMN adsorbed on the carbon nanoparticles, cyclic voltammetry was used to assess the redox properties and extent of adsorption on these materials. These initial experiments were carried out using an RDE experimental set up like the one described in Figure 3.1. The potential was swept between 0.2 and -0.6 V vs SHE, which is about 0.4 V above and below the reduction potential of FMN at the pH of the experiment.

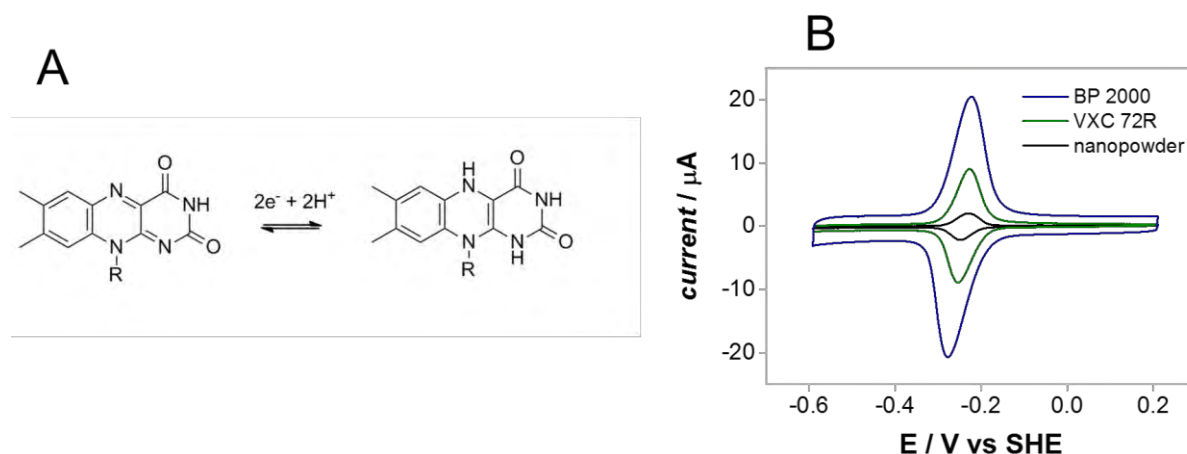


Figure 3.5. The 2-electron 2-proton redox reaction of FMN in aqueous solution (the semiquinone radical is not stabilised in aqueous solution). B) Cyclic voltammograms of FMN adsorbed on carbon nanoparticles, pH 6.6, scan rate = 10 mV s⁻¹.

As can be seen in Figure 3.5B, FMN shows reversible electrochemical behaviour for its two-proton two-electron redox reaction. In aqueous solution FMN undergoes the 2-electron reduction without going through the semiquinone radical, the reaction that corresponds to the redox current observed in the voltammograms is that described by Figure 3.5B. The current also shows that the amount of FMN present on the surface of the carbon nanomaterials correlates directly with the specific surface area, with BP 2000 exhibiting the highest loading (per unit weight of carbon nanoparticles) and the nanopowder the least.

Infrared spectroelectrochemistry of FMN

Infrared spectroelectrochemical measurements of FMN adsorbed on carbon nanoparticles were performed in an experimental set up developed by Adam Healy in the Vincent group³⁴, it is shown in Figure 3.6.

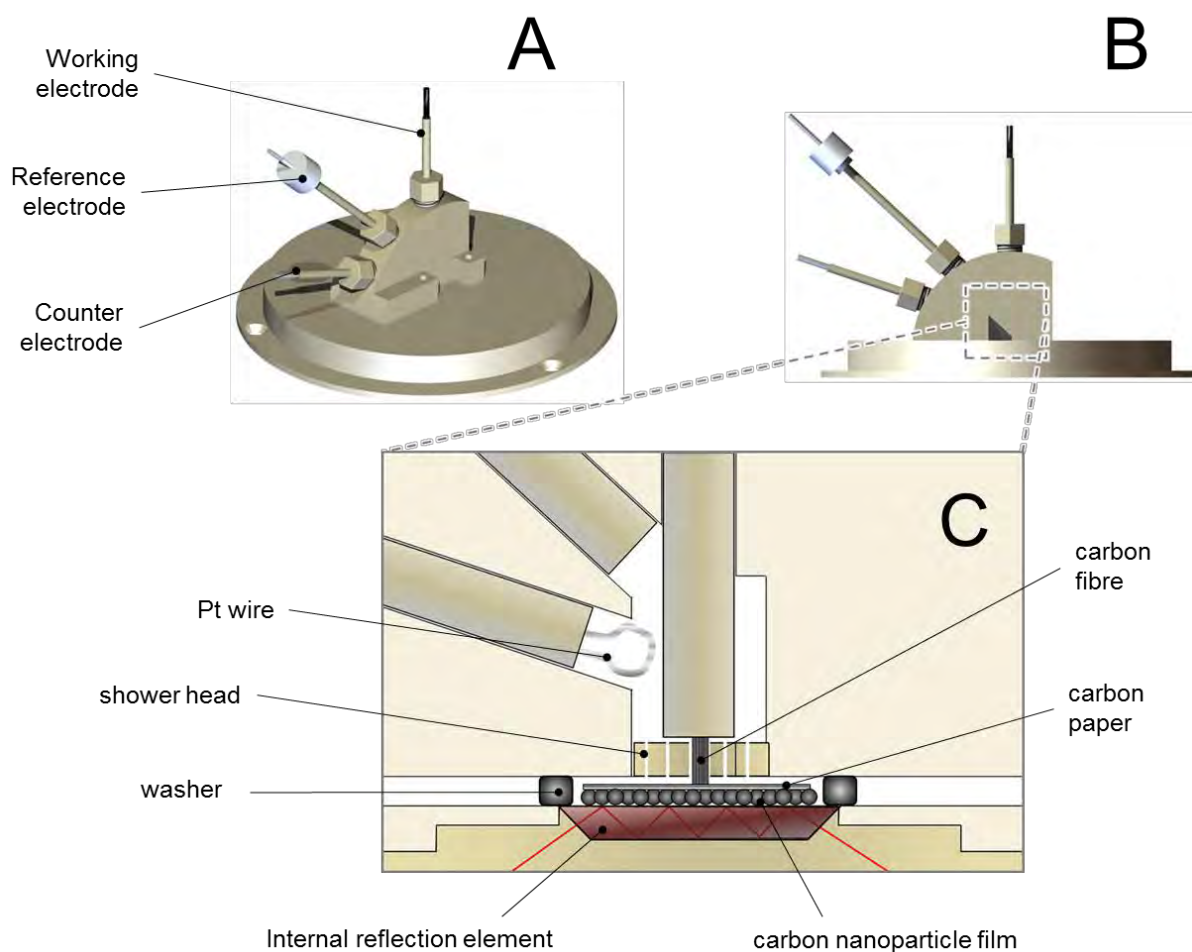


Figure 3.6. A) Infrared spectroelectrochemical cell used for measurements of FMN adsorbed on carbon nanoparticles. The working electrode connection is made of carbon fibre. B) Side view of the cell. C) Inside compartment of the cell showing electrode configuration. The working electrode connection is composed of the carbon fibre pressed down on the carbon paper, which is on top of the carbon nanoparticle film.

This spectroelectrochemical cell has three threaded holes through which the electrodes are inserted to the inside of the cell, where the nanoparticle film and electrolyte solution are contained. This cell body is screwed down to the baseplate which contains the internal reflection element (IRE). The particle film is deposited on the surface of the IRE, and the working electrode connection is made by

pressing down a piece of carbon paper on top of the nanoparticle film and then connecting that to the carbon fibre working electrode. The FMN adsorbed on the particle film can be reduced by the application of a potential to the working electrode, and the changes in the IR bands between the oxidised and reduced forms of the biomolecule can be monitored *in situ*.

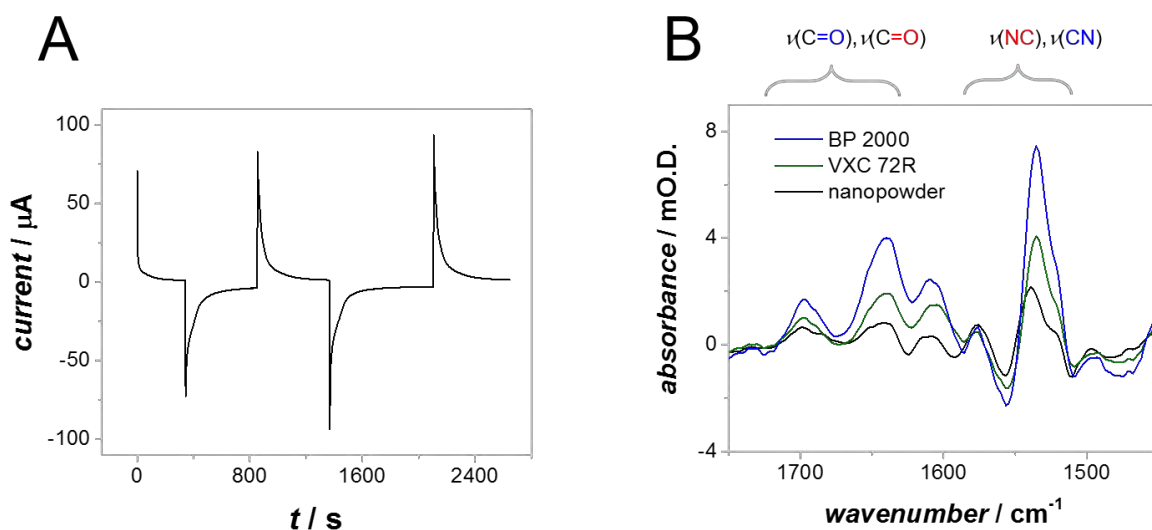


Figure 3.7. A) Current time trace for the reduction (at -0.6 V vs SHE) and the reoxidation (at $+0.2$ V vs SHE) for FMN adsorbed on carbon nanoparticles in a spectroelectrochemical cell shown in Figure 3.6. B) Difference spectra of FMN (oxidised minus reduced) adsorbed on the different carbon nanomaterials. The intensities of the bands correlate with the surface area of the specific nanoparticles.

The infrared difference spectra shown in Figure 3.7B show the main bands of the oxidised version of FMN as positive peaks. The intensities of these peaks relate directly with the specific surface area of this material, with the sample where the FMN was adsorbed on BP 2000 showing the most intense bands. The current that is shown in Figure 3.7A corresponds to the reduction and oxidation of the adsorbed FMN molecules and to the capacitive non-faradaic response of these high surface area nanoparticle electrodes. The higher the surface area of an electrode, the higher the capacitive current that results from a given potential step.

Given the results shown for the electrochemical and IR spectroelectrochemical experiments on FMN adsorbed on the three different carbon nanoparticles, BP 2000 was the material chosen for extending

this method to proteins were the surface coverage presents a challenge. FMN showed reversible electrochemical behaviour for all three materials (Figure 3.5B); and the IR spectra, exhibited no qualitative differences between the different carbon materials on which FMN was adsorbed (Figure 3.7B). Only the intensities of the signals, both electrochemical and spectroscopic, distinguished the results between different materials. The selection criteria came down to a matter of specific surface area available for adsorption, for this reason BP 2000 was selected for extending the method to redox enzymes.

3.3 The design of a new spectroelectrochemical flow cell

IR spectroscopy of Hydrogenase adsorbed on Carbon nanoparticles

Figure 3.8 shows a spectrum of hydrogenase 1 from *E. coli* adsorbed on BP 2000. It can be seen in the spectrum that the enzyme's amide bands, and the ν_{CO} and ν_{CN} bands are clearly detected.

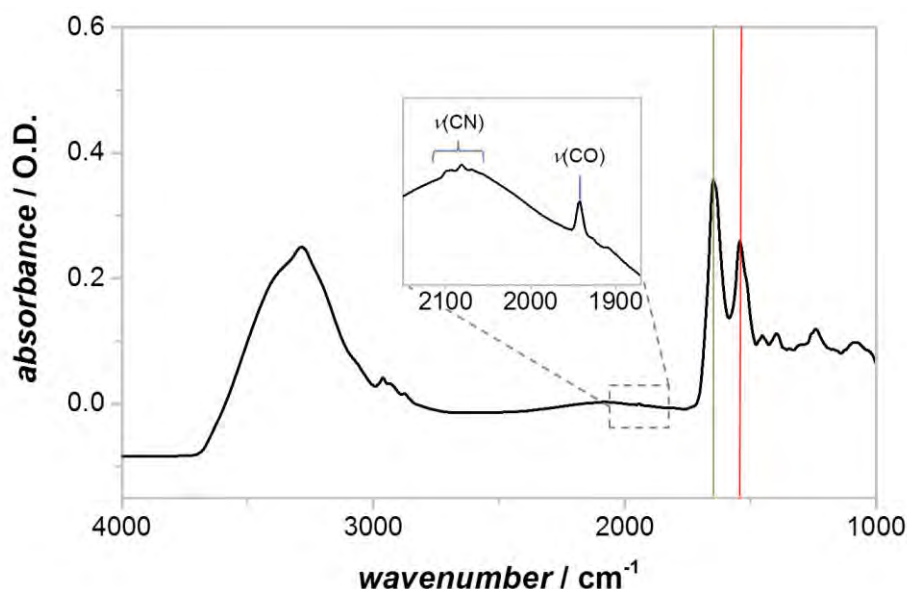


Figure 3.8. IR spectrum of Hyd-1 adsorbed on BP2000. The green and red lines indicate the amide I band (plus water) and the amide II band respectively. In the inset, the active site ν_{CO} and ν_{CN} bands are shown.

The band indicated by the green line at 1645 cm^{-1} results from overlay of the water bending mode and the amide I band. The amide I band (absorption from protein chain amino acids) is assigned to 80 % C=O stretching, 10 % N-H stretching, and 10 % N-H bending.³⁵ The band indicated by the red line, at 1541 cm^{-1} , is the amide II band. This absorption is attributed to 60 % N-H bending, and 40 % C-N stretching, in the protein structure.³⁵ The active site bands, the CO and CN stretching modes, are clearly detected (see inset in Figure 3.8).

In order to do infrared spectroelectrochemistry of redox enzymes it was necessary to improve some features of the cell, especially because one of the main objectives is to do electrochemistry under catalytic turnover. The two types of modifications that were made are: i) the electrode configuration and electric contact, and ii) the design of an efficient flow system and an air-tight cell capable of resisting high pressures.

3.3.1 Cell design

This section will elaborate on the modifications and improvements that were made on the spectroelectrochemical cell designed by Healy et al shown in Figure 3.6. The design of the new flow cell is shown in Figure 3.9. The new cell body has now five threaded holes. Three are for the working, reference, and counter electrodes. The remaining two (shown with blue taps in Figure 3.9) are for the inlet and outlet of the electrolyte solution. The cell is screwed in to the baseplate that holds the internal reflection element (IRE). In this new design, the reference electrode and working electrode are very close to each other, less than 2 mm apart. This provides optimum conditions in terms of minimisation of cell resistance and uncompensated resistance. The proximity of the reference electrode is of particular importance in an electrocatalytic system because higher currents, than non-catalytic experiments, are measured. This has an effect on the ohmic drop (iR) which can be minimised by placing the reference electrode very close to the working electrode, and by having a high concentration of electrolyte in the solution in order to improve the ionic conductivity.²⁹

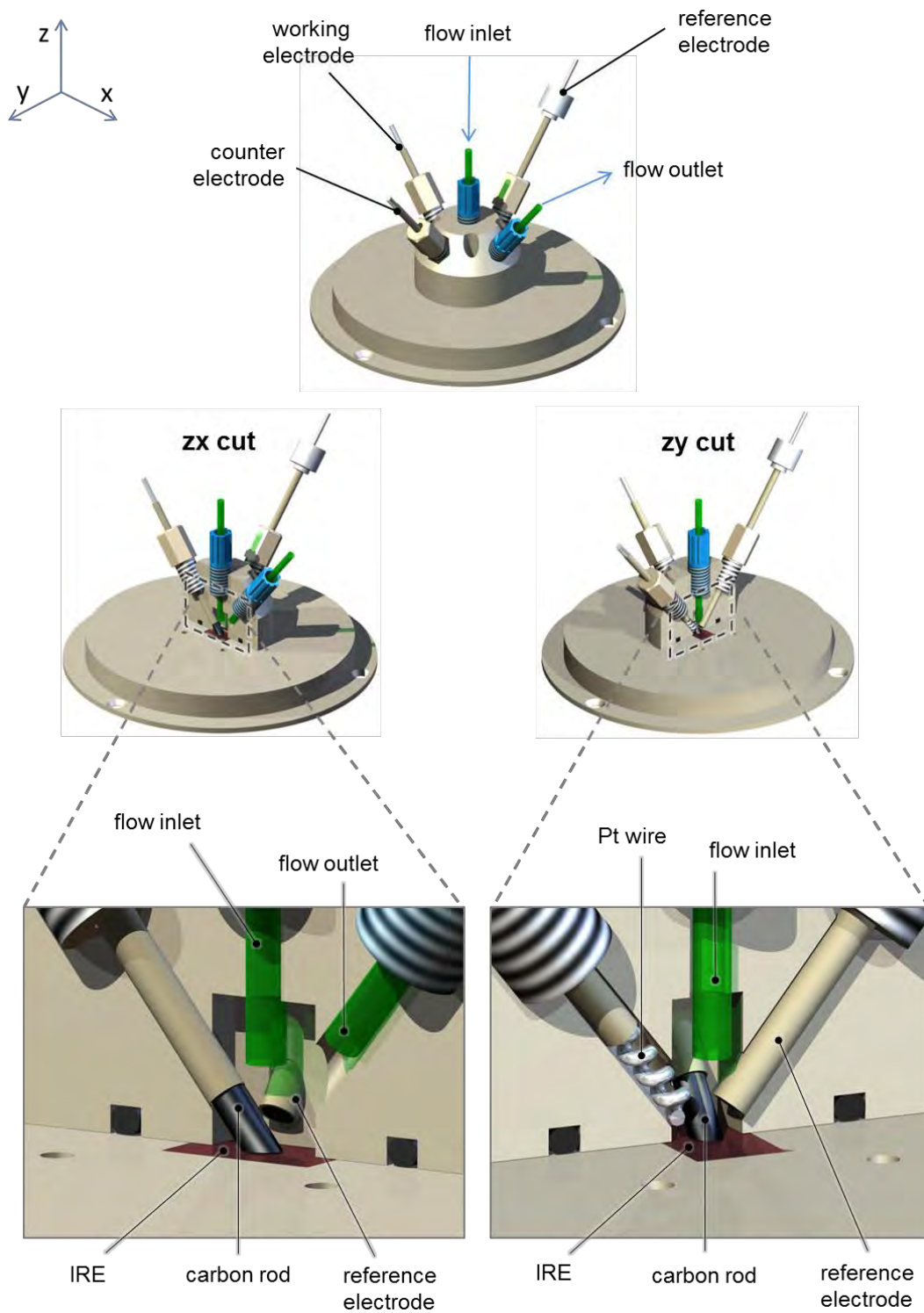


Figure 3.9. Computer-aided design model of the new spectroelectrochemical flow cell design. The cell body houses the three electrodes and the inlet and outlet of the solution. The reference electrode and counter electrode are close together in the inner-cell compartment. The working electrode provides good and solid contact to the carbon-particle film, on the surface of the IRE.

The counter electrode, on the other hand, is further away from the working electrode and has a large surface area. However, it cannot be defined as being *remote*.³⁶ Nevertheless, it will be seen in the following sections that for the currents measured in these experiments (in the 100 – 200 μA range) the potential of the film was accurately measured, and there was no sign of uncompensated resistance causing an error in this measurement.

The working electrode: nanoparticle film and connection

The electrical conductivity within the cell must be efficient mainly to have an accurate measure of the potential at the working electrode. The working electrode consists of a solid carbon rod (Figures 3.9 and 3.10), as opposed to carbon fibre in the previous design (Figure 3.6).

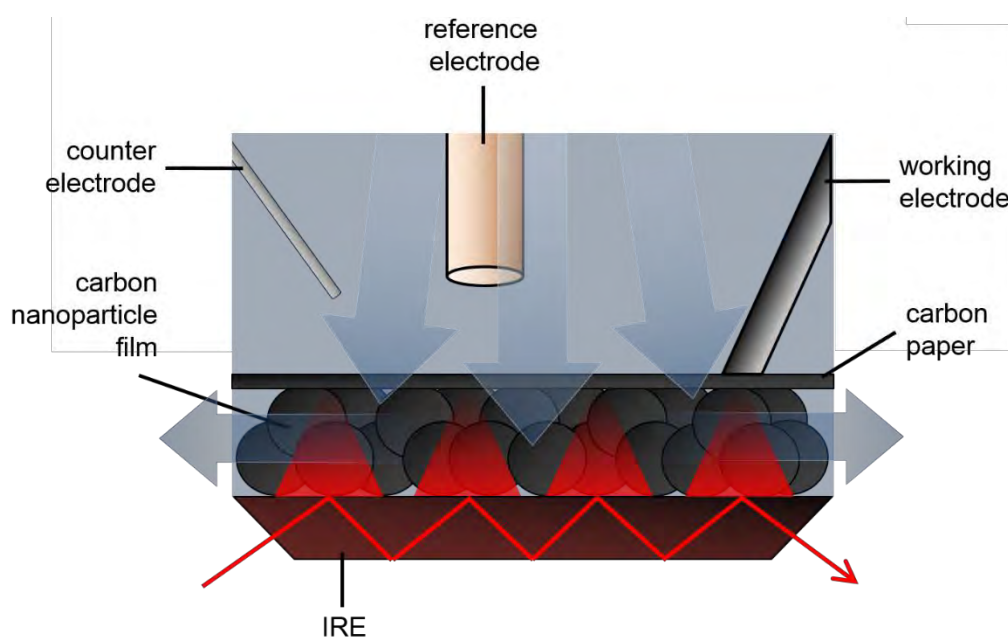


Figure 3.10. Diagram showing the electrode configuration at the internal reflection element (IRE). The carbon nanoparticle film is deposited on the IRE. A piece of carbon paper is put directly on this film and the working electrode (carbon rod) is pushed against it. The reference electrode is in close proximity to the working electrode. The blue arrows indicate the flow of the solution being forced through the film at high pressures.

This solid carbon rod allows for the presence of high flow rates through the inner cell compartment whilst maintaining good conductivity. A carbon fibre electrode like the one in the previous design (Figure 3.6) cannot maintain good electrical contact if the cell is under high flow rates because the

fibres would move. In this new set up, a piece of carbon paper is put on top of the carbon nanoparticle film, and this carbon paper is then pressed down against the film when the cell body is screwed in the baseplate to provide good contact between the particle film and the carbon paper. Furthermore, the carbon rod itself can be pushed down to improve the pressure that can be applied to the carbon paper and hence optimising the conductivity within the particle network. The carbon nanoparticle film is deposited directly on the IRE and it is connected as shown in Figure 3.10.

Tightness and flow considerations

This spectroelectrochemical flow cell is designed for measuring catalytic currents. As explained in Section 3.2.2, having a high surface area comes with the compromise of supplying a significant quantity of adsorbed enzyme with substrate and removing the product fast enough to keep up with the turnover frequency of the enzymatic reaction. This means that the flow rate of the system has to be high enough to meet that condition, and that the cell should be able to bear the pressure caused by this increased flow rate. The spectroelectrochemical experiments in this work were carried out in an anaerobic dry glovebox (see Figure 3.11) and it was therefore important for the spectroelectrochemical cell to be leak-free, in order to avoid moisture or gases being released into the glovebox. The new cell design consisted of sealed fittings: o-rings and inverted cones for the five threaded connections to the cell body, an o-ring at the bottom of the cell body to seal the cellbody/baseplate interface and silicone glue in the edges of the prism to seal the IRE/baseplate interface. These adaptations were sufficient to allow leak-free experiments in a reproducible way.

Pump and flow systems

The buffered electrolyte used for the experiments was flowed by means of a peristaltic pump as shown by figure 3.11.

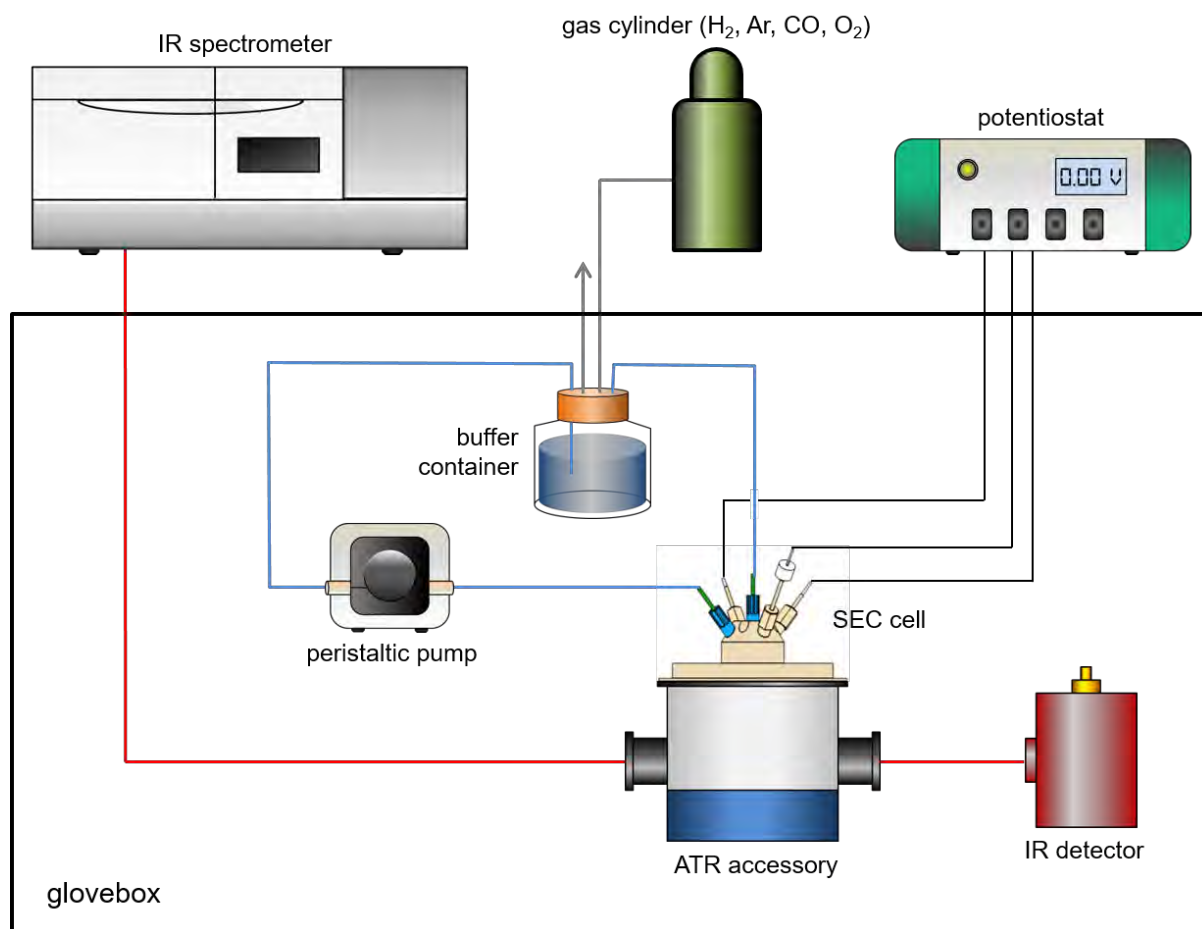


Figure 3.11. Diagram of the setup for a catalytic IR-spectroelectrochemistry experiment inside an anaerobic glovebox.

The peristaltic pump is connected to the buffer solution and to the inlet of the spectroelectrochemical cell. This pump is able to provide flow rates of up to 62 mL min^{-1} . Figure 3.11 shows how an infrared spectroelectrochemical experiment under anaerobic conditions is set up. The cell is screwed on the ATR accessory. It is also connected to the potentiostat (for electrochemical control and measurement) and to the pump flow system. The buffer container is connected to the gas cylinders outside the glovebox which allows different gases to be injected into the system. This provides the means to run a catalytic experiment of an enzyme film (adsorbed on the carbon nanoparticles) while recording IR spectra of the sample *in situ*. The optics: mirror alignment and detector inside the glovebox, was set by Dr. Philip Ash. In the next section, the performance of this system for protein film infrared electrochemistry will be assessed.

3.3.2 Performance of the new SEC cell

Cyclic voltammetry in SEC flow cell

Figure 3.12 shows a cyclic voltammogram of Hyd-1 in the presence of H₂ recorded in the new SEC flow cell and a CV of Hyd-1 H₂ oxidation recorded in a RDE set up like the one explained in Figure 3.1.

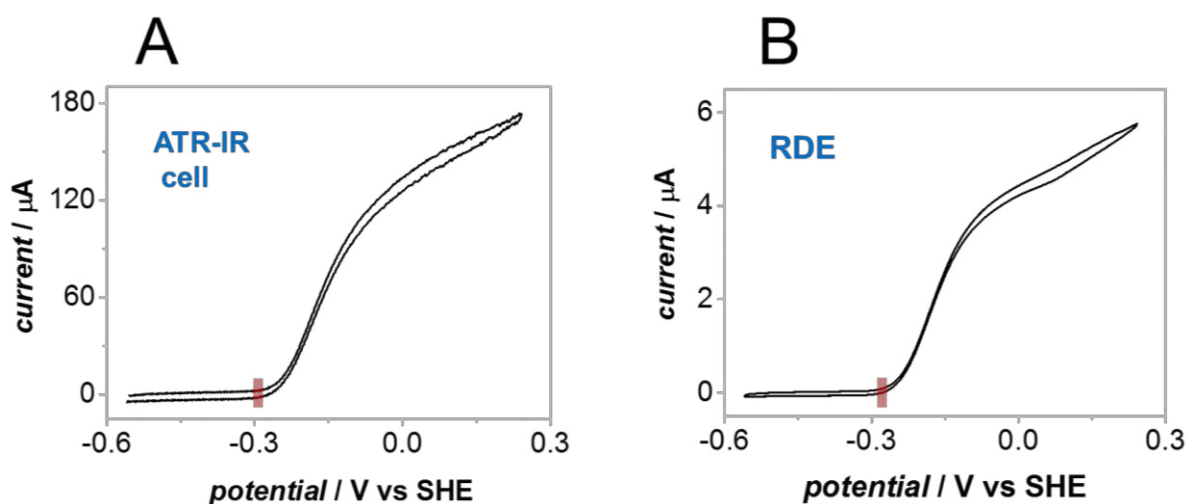


Figure 3.12. Cyclic voltammograms showing Hyd-1 under 1 bar H₂ at pH 6.0 show H₂ oxidation currents. A) In the new SEC flow cell, scan rate: 10 mV s⁻¹, flow rate: 60 mL min⁻¹. B) In an RDE set up, rotation rate: 2000 rpm, scan rate: 10 mV s⁻¹. The red lines indicate the onset potential for H₂ oxidation.

The similarity of the waveshapes suggests that there is efficient mass transport in the SEC flow cell. It is also important to note that the onset potential for H₂ oxidation is the same for both voltammograms. This is an indication that the potential measured at the working electrode in the new SEC flow cell is reliable, for these current ranges. The difference in currents, >150 μA for the SCE flow cell and about 6 μA in the RDE experiment, reflects the much larger sample of enzyme under electrochemical control

Mass transport: The effect of flow rate in the catalytic current and shape of the voltammogram

In order to assess the mass transport in the new cell, the effect of the flow rate in the catalytic current was investigated. As explained in previous sections, the flow rate should be such that a further increase in it would not cause an increase in the current; thus, indicating that the current is independent of mass transport.

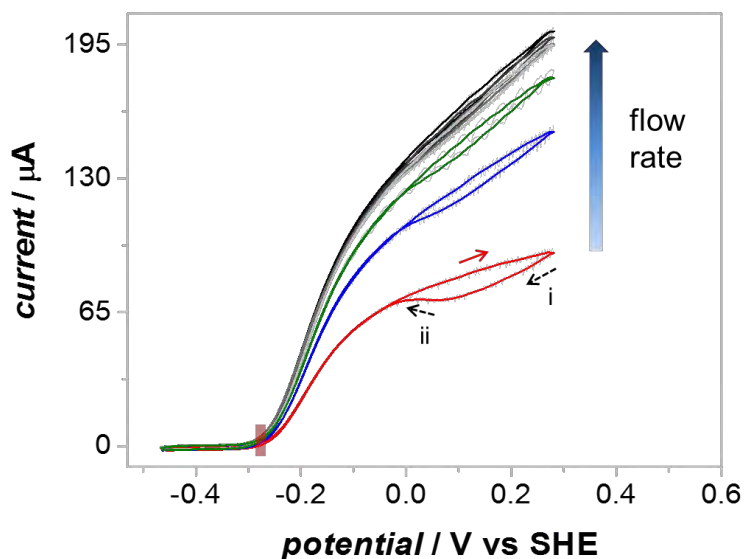


Figure 3.13. The effect of flow rate on the catalytic H₂-oxidation current for Hyd-1 adsorbed on carbon nanoparticles at pH 6.0, recorded in the new SEC cell. The flow rates go from 20 mL min⁻¹ (red) to 52 mL min⁻¹ (dark grey). After the latter value, the current nor the waveshape change any longer.

Figure 3.13 shows the effect of the flow rate on the catalytic current and voltammogram shape. It can be seen that at the lower flow rates the slope of the voltammograms presents lower values than at high flow rates. This is an indication of mass transport limitation: the substrate is not being provided fast enough to keep up with the enzyme's turnover frequency. As the flow rate is increased, the slope of the voltammogram increases. This is because the provision of substrate is increasingly keeping up with the turnover of the enzymatic catalysis. There comes a flow rate value after which the shape of the voltammogram, and the current it reports, no longer changes. This is the value after which it can be said that the experiment is no longer diffusion limited. In order for an experiment to be valid, *i.e.* that the current is a measure solely of the enzyme's activity, the flow rate should be high enough to meet the aforementioned criterion.

Another feature worth noting is the voltammogram shape. For the lower flow rate voltammograms, *e.g.* the red trace, there is a more noticeable inactivation at high potential than for the higher flow rate voltammograms. This is shown in Figure 3.13 by the dashed arrow labelled "i": when the scan is being swept back to low potential, the current is lower than on the forward scan. This is because

Hyd-1 is inactivated at high potential. The enzyme is then reactivated at lower potentials, a process which is indicated by the dashed arrow labelled “ii”. The extent of this inactivation clearly diminishes as the flow rate increases. This is because H_2 has the ability of protecting the enzyme from high potential inactivation,³⁷ and the higher the flow rates the better the provision of H_2 to the enzyme present in the sample. This is another indication that the flow rate is improving the mass transport conditions in the spectroelectrochemical flow cell.

Direct electrochemical control of the enzyme film

Figure 3.14 shows a change in the applied potential to the working electrode and the changes in the IR spectra that result from this electrochemical step.

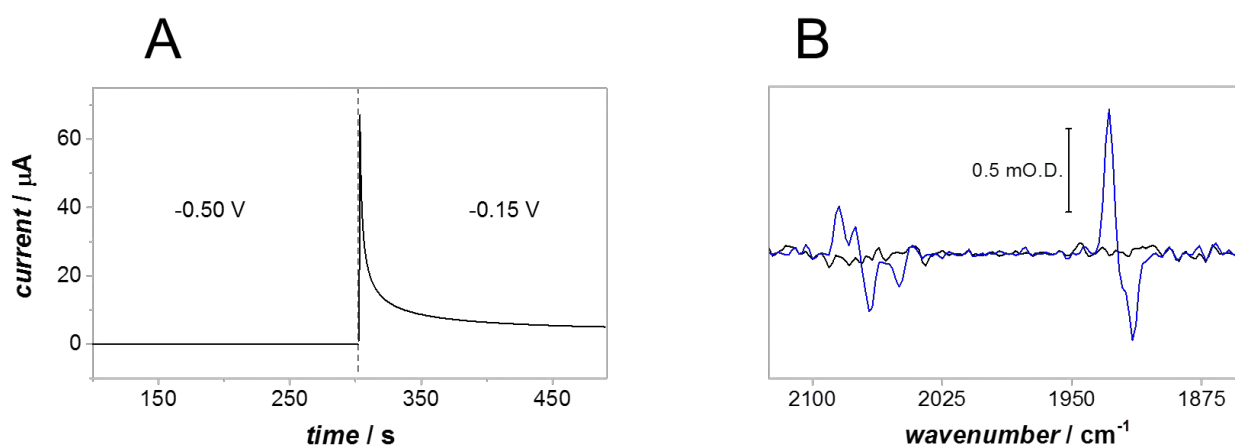


Figure 3.14. An electrochemical potential step applied to a nanoparticle film with adsorbed Hyd-1 under a N_2 atmosphere. A) The current-time trace for the potential step: from -0.50 V to -0.15 V vs SHE. B) Difference spectra, showing the $\nu(CO)$ and $\nu(CN)$ region, recorded against the -0.50 V spectrum. The black line is a spectrum recorded before the potential step, it shows no features because no change in potential has occurred yet. The blue line is a spectrum recorded immediately after the potential step: it shows the changes in wavenumber positions of the bands as a result of the oxidation of the active site.

The potential step results in a fast change (< 5 s) in the wavenumber positions of the ν_{CO} and ν_{CN} bands. This corresponds, in this case, to the two proton-two electron oxidation of the active site. This experiment shows that there is good and fast electrochemical control of the enzyme film in the new spectroelectrochemical flow cell.

Film stability

The enzyme film adsorbed on the carbon nanoparticles, as well as the carbon nanoparticles themselves deposited on the prism, proved to be very stable. Figure 3.15 shows the ν_{CO} band of a sample after 48 h. During this 48h period the cell was under very high flow rates (ca 60 mL min⁻¹) for about 10 hours and the rest of the time under a low flow rate (ca 12 mL min⁻¹). Over the course of the experiments potentials between -0.70 and +0.15 V vs SHE were applied, and substrate was flowed through the system too.

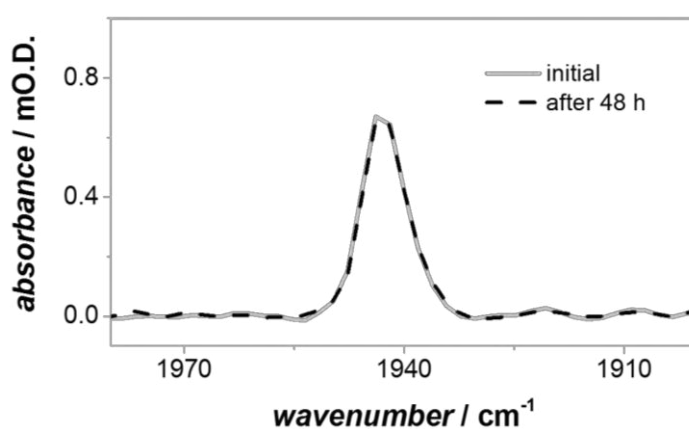


Figure 3.15. IR spectra showing the ν_{CO} region of a Hyd-1 film before and after two days of experiments. The intensity remains the same. Both the enzyme adsorbed on the particles, and the particles deposited in the film, are therefore very stable to different experimental conditions over an important period of time.

The signal is essentially the same after this period of time. This provides evidence of the stability of the sample in the new spectroelectrochemical flow cell. This represents an advantage in the sense that it is therefore possible to probe one same sample under different experimental conditions (since the film is stable over a long period of time).

Conclusion

It has been shown in this section that a new *in situ* IR spectroelectrochemical approach has been developed for the characterisation of adsorbed enzymes (*E. coli* Hyd-1 in this case) on a high surface area carbon nanoparticle electrode. This new method provides the efficient supply of substrate and the direct electrochemical control of protein film electrochemistry (PFE). This allows the monitoring

of structural changes in the active of the enzyme, by means of IR spectroscopy, whilst it is engaging in catalytic turnover. The development of this technique is paramount to this thesis and represents the foundation for most of the results and investigations that shall be discussed in subsequent chapters.

3.4 Experimental

3.4.1 Chemicals, materials and preparations

Buffers

Potassium phosphate dibasic anhydrous (K_2HPO_4), potassium phosphate monobasic (KH_2PO_4) anhydrous, 4-Morpholineethanesulfonic acid (MES), 4-(2-Hydroxyethyl)piperazine-1-ethanesulfonic acid (HEPES), N-[Tris(hydroxymethyl)methyl]-3-aminopropanesulfonic acid (TAPS), 2-(Cyclohexylamino)ethanesulfonic acid (CHES) and sodium acetate (CH_3COONa) were purchased from Sigma-Aldrich and used as received. NaCl, HCl 37 % and NaOH were purchased from Fisher Scientific. All buffers in this work, unless specified otherwise, were prepared in ultra-high purity water (MilliQ Millipore, 18 M Ω cm). All buffers were degassed, in order to remove O_2 , by blowing N_2 through the solution for at least 1.5 h before use in experiments.

Gases

N_2 , Ar, H_2 , CO and O_2 were purchased from BOC. All these gases, with the exception of O_2 , were passed through an O_2 -removal filter (Restek Super-Clean, gas outlet quality > 99.9999 %) before using them in experiments.

Electrodes and electrode materials

The working electrode in the initial experimental design for spectroelectrochemistry

Carbon fibre yarn (Advanced Research Materials) was incorporated in to the cell through a sealed fitting. This was used as the working electrode connection for the initial spectroelectrochemical set up (Figure 3.6).

Carbon nanoparticles

Carbon nanopowder was purchased from Sigma Aldrich. Dispersions of these particles (20 mg mL^{-1}) were sonicated in water or buffer before each experiment. The carbon nanoparticles Vulcan XC72R and Black Pearls (BP) 2000 were kindly provided by Cabot Corp, these were also prepared in dispersions (20 mg mL^{-1}) of water or buffered solutions before use in an experiment.

The mini working-electrode for the new SEC flow system

The working electrode of the new set up, as seen in Figure 3.9, consists of a Pentel 0.9 mm Ain Stein HB lead (WH Smith) connected to a Pt wire (Surepure Chemetals, 99.99 %, 26 gauge). This electrode was sealed, to avoid leaks, in a polyether ether ketone (PEEK) 2 mm-inner diameter tubing using insulating epoxy resin (Aradur hardener and Araldite resin, Robnor Resins).

The mini saturated-calomel reference electrode for the new SEC flow system

5 μL of Hg (Fisher Scientific) and *ca* 30 mg of HgCl (Bioanalytical Systems, Inc) were added to a glass fritted plastic tube, the tube was then filled with saturated KCl solution. An electrical connection to the Hg was made using a Pt wire. This tube was sealed with a septum and attached to a PEEK leak-free reference electrode body (Harvard Apparatus UK). This PEEK body was also filled with saturated KCl solution. This home-built saturated calomel reference electrode provided very stable potentials (less than 5 mV variations for over one month).

IRE preparation

The trapezoidal Si internal reflection element (Crystal GmbH, $8.39 \times 5 \times 1 \text{ mm}^3$) with a face angle of 39° was cleaned before use in each experiment according to the following procedure. It was sonicated in 0.5 mL of concentrated H_2SO_4 for *ca* 20 s. It was then washed with water. This step was

repeated three times. Then, the IRE was left in piranha solution (1:3, H₂O₂ : H₂SO₄) for 1h in order to remove all remaining organic matter, and to leave a clean hydrophilic surface. The IRE was then rinsed thoroughly with water to make sure all the acid and peroxide are removed.

Hydrogenase 1 from E. coli

This enzyme was prepared according to the published procedure.³⁷ Each preparation yielded, on average, 1.8 mL of *ca* 7 mg mL⁻¹ Hyd-1. This was then divided into 50 µL aliquots, then “snap-frozen” in liquid N₂, and stored in a -80° freezer.

3.4.2 Experimental procedures

All electrochemical and spectroelectrochemical experiments described in this section were carried out inside an anaerobic glovebox (< 1 ppm, Glove Box Technology Ltd).

Adsorption of FMN on carbon nanoparticles

Phosphate buffer (50 mM, pH 6.6) was prepared in D₂O (Sigma-Aldrich) and a 10 mM FMN solution was prepared in this buffer. For the adsorption, 50 µL of the FMN solution was mixed with 50 µL of 20 mg mL⁻¹ BP 2000 dispersion (also prepared in the deuterated buffer). The mixture was left at 4 °C for 1 h. The FMN-modified particles were then washed by centrifugation with buffer and finally concentrated down to give a *ca* 20 mg mL⁻¹ loading of carbon particles. These modified particles were then used for electrochemical or spectroelectrochemical experiments.

Electrochemistry of FMN on nanoparticles (RDE configuration)

A 2 µL aliquot of FMN-modified carbon nanoparticles was pipetted on the surface of a freshly-polished pyrolytic graphite electrode. It was left to dry for 1 – 2 min before immersing the electrode in the solution. The experimental set up for these experiments is represented by Figure 3.1. The electrolyte solution was 100 mM phosphate buffer pH 6.6. The reference electrode used was a commercial Ag/AgCl 3 M NaCl (BAS Inc) and a Pt wire was used as a counter electrode. The potential

was controlled with an Autolab PGSTAT 128N and electrochemical experiments were controlled using the software NOVA 1.10.

IR spectroelectrochemistry of FMN

2 μL of FMN-modified particles were cast on the surface of the IRE to make an evenly spread film of about 1 μm thickness. A piece of carbon paper (AvCarb P50, Ballard Power System) was placed on top of the nanoparticle film. The spectroelectrochemical cell was then assembled as shown by Figure 3.6, a hand-cut rubber washer was used to seal the system in the prism/baseplate interface and in the cell-body/baseplate interface. The cell was then filled with D_2O -phosphate buffer (ca 200 μL) and the electrodes put in place. All the preparations for the cell assembly up to the addition of the buffer and assembling of the electrodes were done inside the glovebox to maintain O_2 -free conditions. The gas tight cell was then taken out of the glovebox for the spectroelectrochemistry experiments. The cell assembly was fitted in a Varian FTS-6000 IR spectrometer with an ATR accessory (PIKE technologies, custom-modified GladiATR) in the sample compartment. The detector used was a narrow-band MCT detector. The potential was controlled using Metrohm $\mu\text{Autolab III/FRA2}$ potentiostat.

Adsorption of Hyd-1 on BP 2000 carbon nanoparticles

A 50 μL Hyd-1 aliquot of Hyd-1 was defrosted at 0°C in an icebox (ca 1 h). The buffer of the enzyme was then exchanged for phosphate buffer (15 mM, pH 5.8), or alternatively MES buffer (8 mM, pH 5.0). This was done by means of a centrifugal filter unit (Amicon Ultra – 0.5 mL, Ultracel – 50K membrane). The enzyme sample was then mixed with a 5 μL aliquot of BP 2000 dispersion (20 mg mL^{-1} as explained above) and left at 0°C for adsorption. These enzyme-modified particles were then washed by centrifugation with buffer to remove the non-adsorbed enzyme. Finally, the particles were concentrated down to give a 20 mg mL^{-1} dispersion of carbon nanoparticles.

Protein Film electrochemistry of Hyd-1 (RDE configuration)

2 μL of Hyd-1 solution, or Hyd-1 modified nanoparticles, was drop-cast on a freshly-polished pyrolytic graphite working electrode. The sample was left to dry for 1 min and then the electrode was immersed in a buffered solution. The experiments were carried out in a system like the one shown in Figure 3.1. Hydrogen (1 bar) was flowed over the headspace of the solution to saturate it and the working electrode was rotated at 2000 rpm to optimise mass transport within the cell. A commercial saturated calomel electrode (BAS Inc) was used as reference, and a Pt wire as a counter electrode.

Protein Film Infrared Spectroscopy (PFIRE) of Hyd-1

The IRE element was sealed into the baseplate with fast curing silicone sealant (SE4486CV, Dow Corning). 1 μL of enzyme-modified particles was evenly deposited on the surface of the prism. The nanoparticle film was covered with a piece of carbon paper (Toray, TGP-H-030) and the cell was then assembled as shown in Figure 3.9. The cell was then transferred to a second glovebox through a purged antechamber. This second glovebox is O_2 free and dry (<85 °C dew point). A diagram of the experimental set-up in this glovebox is shown in Figure 3.11.

The buffer used for most experiments of Hyd-1 was mixed buffer (MES, HEPES, TAPS, CHES, NaOAc at 15 mM each, and NaCl 100 mM). The buffer container was connected to the gas lines through which specific gases of interest could be added to the solution. The gases and gas mixtures were added to the buffer by means of a mass flow controller (Brooks) to accurately determine the concentrations and flow rates. The buffer solution was flowed through the cell using a peristaltic pump (QL-1000, Williamson Pumps Ltd).

The spectrometer was placed on a table connected to the dry glovebox and the IR beam was diverted into the glovebox through a short purged tube and 5 mm thick KBr window. An off-axis parabolic focusing mirror then diverted the beam into the ATR accessory. The IR beam was detected by a MCT detector cooled down to 77 K. The IR spectrometer was controlled by the software Resolutions Pro. The glovebox IR optics system was designed and installed by Dr. Philip Ash.

Potential control was achieved using a potentiostat (Autolab PGSTAT 128N) placed on a table secured to the rear of the dry glovebox.

References

- 1 J. N. Butt and F. A. Armstrong, in *Bioinorganic Electrochemistry*, eds. O. Hammerich and J. Ulstrup, Springer, Dordrecht, 2008, pp. 91–128.
- 2 K. A. Vincent, A. Parkin and F. A. Armstrong, *Chem. Rev.*, 2007, **107**, 4366–413.
- 3 F. A. Armstrong, H. A. Heering and J. Hirst, *Chem. Soc. Rev.*, 1997, **26**, 169–179.
- 4 C. Léger and P. Bertrand, *Chem. Rev.*, 2008, **1084**, 2379–2438.
- 5 C. Léger, S. J. Elliott, K. R. Hoke, L. J. C. Jeuken, A. K. Jones and F. A. Armstrong, *Biochemistry*, 2003, **42**, 8653–8662.
- 6 C. Léger, S. Dementin, P. Bertrand, M. Rousset and B. Guigliarelli, *J. Am. Chem. Soc.*, 2004, **126**, 12162–72.
- 7 P. Ceccaldi, M. C. Marques, V. Fourmond, I. C. Pereira and C. Léger, *Chem. Commun.*, 2015, 2–5.
- 8 V. Fourmond, C. Baffert, K. Sybirna, S. Dementin, A. Abou-Hamdan, I. Meynial-Salles, P. Soucaille, H. Bottin and C. Léger, *Chem. Commun.*, 2013, **49**, 6840–2.
- 9 R. M. Evans, A. Parkin, M. M. Roessler, B. J. Murphy, H. Adamson, M. J. Lukey, F. Sargent, A. Volbeda, J. C. Fontecilla-Camps and F. A. Armstrong, *J. Am. Chem. Soc.*, 2013, **135**, 2694–2707.
- 10 W. Lubitz, H. Ogata, O. Ruediger and E. Reijerse, *Chem. Rev.*, 2014, **114**, 4081–4148.
- 11 H. S. Shafaat, O. Rüdiger, H. Ogata and W. Lubitz, *Biochim. Biophys. Acta*, 2013, **1827**, 986–1002.
- 12 M.-E. Pandelia, H. Ogata and W. Lubitz, *Chemphyschem*, 2010, **11**, 1127–40.
- 13 P. Kellers, M.-E. Pandelia, L. J. Currell, H. Görner and W. Lubitz, *Phys. Chem. Chem. Phys.*, 2009, **11**, 8680–8683.

- 14 A. L. de Lacey, E. C. Hatchikian, A. Volbeda, M. Frey, J. C. Fontecilla-Camps and V. M. Fernandez, *J. Am. Chem. Soc.*, 1997, **119**, 7181–7189.
- 15 A. L. DeLacey, C. Stadler, V. M. Fernandez, E. C. Hatchikian, H. J. Fan, S. Li and M. B. Hall, *J. Biol. Inorg. Chem.*, 2002, **7**, 318–326.
- 16 C. Fichtner, C. Laurich, E. Bothe and W. Lubitz, *Biochemistry*, 2006, **45**, 9706–9716.
- 17 B. Bleijlevens, F. A. van Broekhuizen, A. L. De Lacey, W. Roseboom, V. M. Fernandez and S. P. J. Albracht, *J. Biol. Inorg. Chem.*, 2004, **9**, 743–752.
- 18 M.-E. Pandelia, H. Ogata, L. J. Currell, M. Flores and W. Lubitz, *Biochim. Biophys. Acta*, 2010, **1797**, 304–13.
- 19 A. J. Healy, P. A. Ash, O. Lenz and K. A. Vincent, *Phys. Chem. Chem. Phys.*, 2013, **15**, 7055–7059.
- 20 A. L. De Lacey, C. Gutiérrez-Sánchez, V. M. Fernández, I. Pacheco and I. A. C. Pereira, *J. Biol. Inorg. Chem.*, 2008, **13**, 1315–1320.
- 21 M. Sezer, S. Frielingsdorf, D. Millo, N. Heidary, T. Utesch, M.-A. Mroginski, B. Friedrich, P. Hildebrandt, I. Zebger and I. M. Weidinger, *J. Phys. Chem. B*, 2011, **115**, 10368–74.
- 22 M. Sezer, D. Millo, I. M. Weidinger, I. Zebger and P. Hildebrandt, *IUBMB Life*, 2012, **64**, 455–464.
- 23 D. Millo, P. Hildebrandt, M.-E. Pandelia, W. Lubitz and I. Zebger, *Angew. Chem. Int. Ed.*, 2011, **50**, 2632–4.
- 24 C. F. Blanford and F. A. Armstrong, *J. Solid State Electrochem.*, 2006, **10**, 826–832.
- 25 P. A. Ash and K. A. Vincent, *Chem. Commun.*, 2012, **48**, 1400–9.
- 26 J. N. Butt and F. A. Armstrong, in *Bioinorganic Electrochemistry*, eds. O. Hammerich and J. Ulstrup, Springer, Dordrecht, 2008, pp. 91–128.
- 27 F. A. Armstrong, N. A. Belsey, J. A. Cracknell, G. Goldet, A. Parkin, E. Reisner, K. A. Vincent and A. F. Wait, *Chem. Soc. Rev.*, 2009, **38**, 36–51.
- 28 R. Compton and C. E. Banks, *Understanding Voltammetry*, Imperial College Press, London,

- 2nd edn., 2011.
- 29 A. J. Bard and L. R. Faulkner, *Electrochemical Methods: Fundamentals and Applications*, John Wiley & Sons, New York, 2nd edn., 2001.
- 30 G. Wang, G. Sun, Z. Zhou, J. Liu, Q. Wang, S. Wang and J. Guo, *Electrochem. Solid State Lett.*, 2005, **8**, A16.
- 31 M. Abe and Y. Kyogoku, *Spectrochim. Acta Part A Mol. Spectrosc.*, 1987, **43**, 1027–1037.
- 32 M. Spexard, D. Immeln, C. Thöing and T. Kottke, *Vib. Spectrosc.*, 2011, **57**, 282–287.
- 33 V. Massey, *Biochem. Soc. Trans.*, 2000, **28**, 283–96.
- 34 A. J. Healy, University of Oxford, 2013.
- 35 B. H. Stuart, *Biological Applications of Infrared Spectroscopy*, Wiley, Chichester, 1997.
- 36 J. C. Myland and K. B. Oldham, *Anal. Chem.*, 2000, **72**, 3972–80.
- 37 M. J. Lukey, A. Parkin, M. M. Roessler, B. J. Murphy, J. Harmer, T. Palmer, F. Sargent and F. A. Armstrong, *J. Biol. Chem.*, 2010, **285**, 3928–38.

Chapter 4

*Redox characterisation of Hyd-1
under non-turnover conditions:*

the effect of pH

4.1 Introduction

4.1.1 IR spectroelectrochemical studies of NiFe hydrogenases

Infrared spectroelectrochemistry has allowed for the characterisation of both standard and O₂-tolerant NiFe hydrogenases from different organisms.^{1–16} IR spectroscopy provides the advantage, when the focus of investigation is the active site, of rendering all the redox states detectable. This is in contrast to EPR where only the paramagnetic states, those where the Ni ion is in the form of Ni(III) or Ni(I), can be detected.^{2,13,17–20} The study of different NiFe hydrogenases by IR spectroelectrochemistry has provided a general picture of the active site redox states.^{15,16,21} This is important to the discussion of mechanisms of the chemical reactions that occur at such a site. Figure 4.1 shows the most common redox states of the active site of NiFe hydrogenases and the redox relationships between them. There are, however, differences in the observed states of different hydrogenases.¹⁵

The inactive states

The inactive state Ni-A has been distinguished from the Ni-B state based on the different activation kinetics they show. Ni-A takes hours to activate, whereas Ni-B is activated in a matter of minutes.^{22,23} Structurally, it has been consistently agreed that the Ni-B state has a hydroxide ligand in the bridging position between the two metals.^{24–26} The Ni-A state structure, on the other hand, has been a subject of debate.^{24,25,27–30} It has been suggested to have different oxygenated species in the bridging position, such as a hydroxide, hydroperoxide or sulfenate. However, Dementin and collaborators have argued that this state can also be formed in the absence of O₂, by means of other oxidants.³¹ Recently, X-ray crystallographic studies on *Desulfovibrio fructosovorans* NiFe hydrogenase variants provided good evidence for the structure of Ni-A. The bridging ligand is proposed to be hydroxide, the same as in Ni-B, but one of the terminal cysteines coordinating the Ni atom is oxidised to give the motif $\text{S—O—Ni}^{3+}\text{—OH}$.²⁸ One electron reduction of these inactive

states, Ni-A and Ni-B, gives the Ni-SI_U and Ni-SI_R states respectively (see Figure 4.1). These reduced forms, which are also inactive, have been suggested to be structurally equivalent to their oxidised states with the difference that the Ni atom is in the +2 oxidation state.²⁸

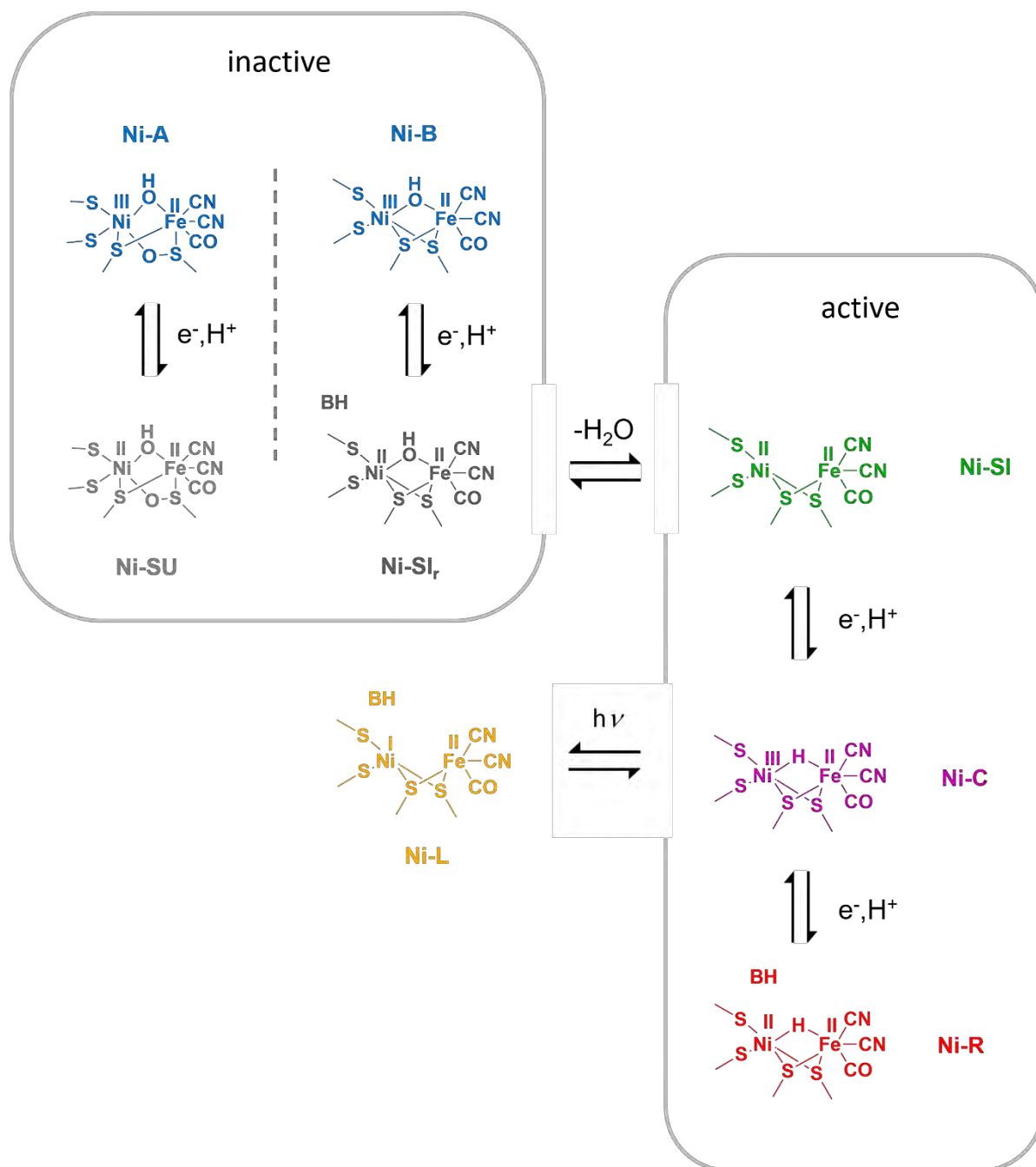


Figure 4.1 The most common redox states of the active site of NiFe hydrogenases and their transformations. This scheme is proposed based on spectroelectrochemical and x-ray characterisations of NiFe hydrogenases in the literature.^{1,3,15,28} Most as isolated hydrogenases exhibit a mixture of the inactive states Ni-A and Ni-B. The state Ni-SI is considered to be the resting state which binds H₂ initially in the catalytic cycle, with Ni-R and Ni-C being the other two intermediates (in that order). Ni-L has been widely detected by photoillumination of Ni-C at low temperatures.

The active states

The active redox states are considered to be Ni-SI, Ni-C and Ni-R. Ni-SI has a vacant position at the bridging position between the metal centres and hence is available for the attack of substrate or inhibitors. The Ni atom is in the form of Ni(II) for the Ni-SI state. The name of such state, Ni-SI, was given because it shows no signal ('silent') in the EPR: it is diamagnetic.

The addition of one electron and one proton to the Ni-SI state gives the Ni-C state, where a Ni(III) ion is coordinated to a bridging hydride. EPR studies have confirmed the presence of this hydride for different hydrogenases.^{17,32}

The most reduced state is the Ni-R state that has a hydride in the bridging position and a Ni(II) species: a one-proton / one-electron reduction of Ni-C gives this more reduced form, Ni-R.^{1,6} The structure of the Ni-R state has been confirmed by a recent high resolution X-ray crystallography study in which the bridging hydrogen atom was detected.³³ IR spectroelectrochemical studies of different hydrogenases have shown that there appear to be multiple Ni-R states.^{1,2,6,9} These are proposed to be different protonation states at the same redox level.² There are several amino acids in the immediate vicinity of the active site whose protonation state may have an effect in the electron density at the metal centre and hence, in the position of the ν_{CO} and ν_{CN} bands.

The Ni-L state

In addition to the states mentioned so far, for most hydrogenases a different state which results from the photoillumination of Ni-C at cryogenic temperatures has been identified (see Figure 4.2).^{21,32,34-36} The irradiation causes the hydride, which is bound as a bridging ligand between the two metals, to leave as a proton. The Ni(III) ion is reduced to Ni(I) as this metal receives the two electrons of the hydride that dissociated as a proton. The IR wavenumber position of the ν_{CO} of this light-induced state Ni-L is also consistent with it being a Ni(I) species as the band is shifted to a much lower wavenumber upon dissociation. Moreover, DFT calculations by Neese and co-workers have suggested a metal-metal bond in the Ni-L state; this would further contribute to a more

electron-rich Fe centre and therefore provide a rationale for the low wavenumber position at which the ν_{CO} appears.³⁷

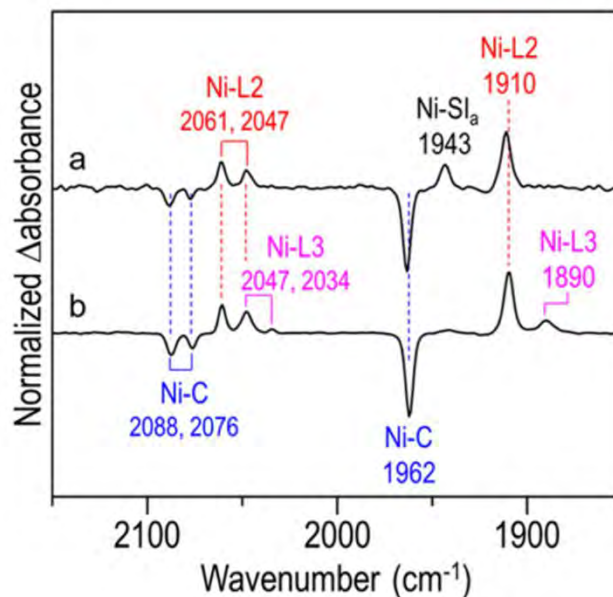


Figure 4.2 The photodissociation of Ni-C to Ni-L at cryogenic temperatures (178 K): Difference spectra between the illuminated and the not-illuminated sample (light minus dark), at pH (a) 8.0 and (b) 9.6. Adapted with permission from Tai, H.; Nishikawa, K.; Inoue, S.; Higuchi, Y.; Hirota, S. *J. Phys. Chem. B* 2015, 119 (43), 13668–13674. Copyright 2015 American Chemical Society.

Table 4.1 shows the wavenumber positions of the redox states of different hydrogenases. This is not an extensive data set. For a more complete table with data for more hydrogenases, see Lubitz et al.¹⁵ The following table shows the most comparable hydrogenases, in terms of wavenumber positions, to *E. coli* Hyd-1 which shall be investigated in this chapter.

The data from Table 4.1 was recorded, with the exception of the Ni-L states, using a spectroelectrochemical cell like the one described by Moss et al.³⁸ Such a system involves having the enzyme in solution, and electron transfer to a gold grid electrode is achieved via a redox mediator cocktail. The data for Ni-L was obtained by photoillumination of Ni-C at cryogenic temperatures.

Table 4.1 Wavenumber positions of ν_{CO} and ν_{CN} bands for different redox states of the active site of different NFe hydrogenases.

	<i>wavenumber / cm⁻¹</i>					
	<i>Desulfovibrio vulgaris</i> <i>MF</i> ^{1,15,34,35}		<i>Allochromatium vinosum</i> ^{2,39}		<i>Aquifex aeolicus</i> ^{6,21}	
	ν_{CO}	ν_{CN}	ν_{CO}	ν_{CN}	ν_{CO}	ν_{CN}
Ni-A	1956	2094, 2084	1945	2093, 2082	-	-
Ni-B	1955	2090, 2081	1943	2090, 2079	1939	2092, 2081
Ni-SU	1946	2086, 2075	1948	2100, 2088	-	-
Ni-SI_r	1922	2070, 2056	1910	2067, 2052	-	-
Ni-SI	1943	2086, 2075	1931	2084, 2073	1927	2087, 2077
Ni-C	1961	2085, 2074	1951	2085, 2073	1949	2088, 2078
Ni-L_I	-	-	-	-	1862	2045, 2024
Ni-L_{II}	1910	2061, 2047	1898	2060, 2044	1900	2068, 2049
Ni-L_{III}	1890	2047, 2034	-	-	1872	2056, 2033
Ni-R_I	1948	2074, 2061	1936	2072, 2059	-	-
Ni-R_{II}	1932	2066, 2052	1921	2064, 2048	-	-
Ni-R_{III}	1919	2065, 2050	1913	2058, 2043	1910	2066, 2047

What this chapter is about

In this chapter, the O₂-tolerant Hydrogenase-1 from *E. coli* is characterised by infrared spectroelectrochemistry. This represents the first characterisation of a hydrogenase directly adsorbed on a carbon electrode. There have been infrared spectroelectrochemical studies, by Millo et al, for a “standard” hydrogenase adsorbed on SAM-modified gold electrodes.^{40,41} The authors investigated the activation of the enzyme in the presence of H₂ (Ni-B to Ni-SI conversion by IR spectroelectrochemistry. The reduction potential of this transition was determined, both under H₂

and under Ar atmospheres, and compared to the E_{switch} calculated at the same electrode in a PFE experiment.⁴⁰

However, most of the hydrogenase electrochemistry research has been done on carbon electrodes, therefore this study makes a direct link to that important body of research. Moreover, several applications (such as bio-fuel cells and chemical synthesis) make use of hydrogenase enzymes adsorbed on carbon surfaces for electron transfer and catalysis.^{42,43}

The effect of pH on the distribution of states will also be a major focus of study in this chapter. Since most of the redox transformations of the active site are proton-coupled electron transfers, an investigation at different pH values provides useful information. It has been discovered that the catalytic properties of *E. coli* Hyd-1 can be significantly changed with pH, as it can be transformed into an effective H^+ reducer at low pH values.⁴⁴ In addition to that, for an enzyme whose function is to split H_2 into protons and electrons, and vice versa, the behaviour of its active site as a function of pH is of high interest. Proton transfers to and from the active site should play an important role in its catalytic processes.

4.2 Spectroelectrochemical characterisation of Hyd-1 adsorbed on a carbon electrode

4.2.1 Initial IR spectroelectrochemical characterisation

The experimental set-up used in these measurements is described in Chapter 3 (Figures 3.9, 3.10, and 3.11). For this study, the observed IR bands have been assigned to specific redox states of the active site on the basis of IR spectroelectrochemical studies of other NiFe hydrogenases in solution;^{1,2,6,21,34,35,39} and on the dependence of these bands with the applied potential.

The as-isolated enzyme

Figure 4.3 shows the ν_{CO} and ν_{CN} region of the IR spectrum of a sample of Hyd-1 adsorbed on carbon nanoparticles with no further treatment. The solution inside the spectroelectrochemical cell is mixed buffer, pH 6.0.

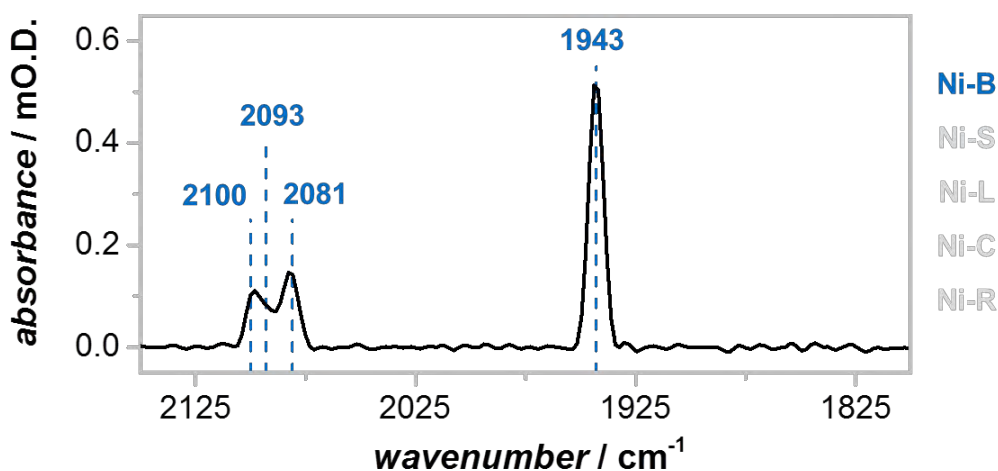


Figure 4.3 Infrared spectrum of the as isolated Hyd-1 adsorbed on carbon nanoparticles at open circuit potential, measured as +0.211 V vs SHE. Other experimental conditions: 100 % N₂, 20 °C.

The spectrum shows an intense band at 1943 cm⁻¹ and three smaller bands at 2081, 2093 and 2100 cm⁻¹. The open circuit potential of the spectroelectrochemical cell for an as-isolated sample varied between +0.191 and +0.276 V vs SHE for different as isolated samples showing this same spectrum. This hydrogenase sample was purified under air and hence it is expected to present a mixture of the oxidised inactive states. The wavenumber positions of the bands observed for this sample are consistent with it being Ni-B, Ni-A, or a combination of both. This assignment is based on the comparison with other spectroscopically characterised hydrogenases in the literature.² The fact that three bands are observed in the ν_{CN} region suggests that there are at least two different states present in this sample, that have similar ν_{CO} bands. Several studies of other hydrogenases show an assigned 1 cm⁻¹ difference between the Ni-A and the Ni-B ν_{CO} band.^{1,4,5} It is, therefore, a possibility that this combination of states observed correspond to a combination of the two inactive states,

Ni-A and Ni-B. This will be discussed later when analysing the redox behaviour of the species giving rise to these bands.

Electrochemical reduction of the sample

The application of a strongly-reductive potential, -0.594 V vs SHE, results in the spectrum shown in Figure 4.4.

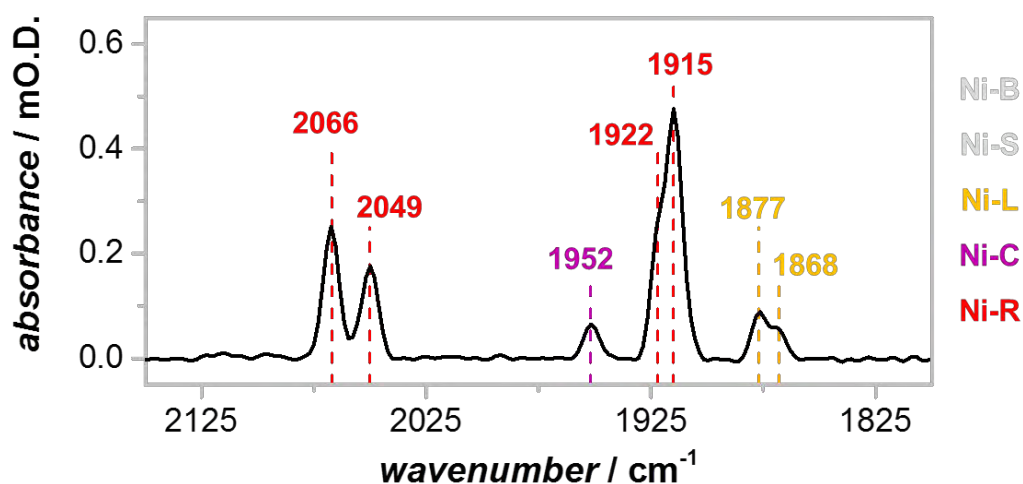


Figure 4.4 IR spectrum of Hyd-1 adsorbed on a carbon nanoparticle electrode. The applied potential is -0.594 V vs SHE.

The spectrum was taken in mixed buffer pH 6.0 at 20 °C, 100% N_2 atmosphere.

This reduced sample shows, in the ν_{CO} region, several bands. There are two intense bands at 1922 and 1915 cm^{-1} , which correspond to the most reduced state of the active site, Ni-R. Several bands for the Ni-R state have also been observed for other NiFe hydrogenases with similar wavenumber positions,^{1,2,6} and this is thought to be different protonation states at the same redox level. The bands at 1922 and 1915 cm^{-1} , in Figure 4.4, are assigned to the Ni-R_{II} and Ni-R_{III} states respectively. Another, much less intense band, is observed at 1952 cm^{-1} , and corresponds to the Ni-C state. This redox state of the active site consists of a Ni(III) with a hydride bound in the bridging position between the two metals. There are two other small bands in this reduced spectrum at 1877 and 1868 cm^{-1} . The position of these, is consistent with the Ni-L state that results from the photoillumination of Ni-C at cryogenic temperatures.²¹ As mentioned above, the low wavenumber position of such bands is consistent with a low oxidation state Ni(I) ion. It has also been suggested,

by means of DFT calculations, that the unusually low wavenumber position of the ν_{CO} stretch for these states is a result of a metal-metal double bond between the Ni and Fe in the Ni-L state.³⁷ The first observation of the Ni-L state at room temperature in the dark has been reported by Adam J. Healy for *E. coli* Hyd-1 in solution.⁴⁵ In this work the same observation is true for the enzyme adsorbed on a carbon electrode. The implication of this result will be discussed in more detail later in this chapter and also in Chapter 5, in which studies under turnover conditions will be examined in detail.

In the ν_{CN} region of the spectrum shown in Figure 4.4, only two bands are observed. These 2066 and 2049 cm^{-1} features correspond to the Ni-R state. It is possible that there is some overlap of bands at these positions. The bands are more intense than other ν_{CN} bands observed for other states, and it is known (from the ν_{CO} region of the spectrum) that there are multiple states at this potential. It was not possible, however, to determine the intensity nor the position of any overlapping bands. For other NiFe hydrogenases (see Table 4.1) the ν_{CN} bands shift less than the ν_{CO} bands for the Ni-R states, and have similar wavenumber positions. It is, therefore, not unlikely that the intense 2066 and 2049 cm^{-1} bands, in Figure 4.4, have contributions from both Ni-R_I and Ni-R_{III} states. The contribution from ν_{CN} bands from redox states other than Ni-R (Ni-L and Ni-C in this specific case) are not expected to be major, as these other states are present in much lower concentrations than Ni-R. Besides, the wavenumber positions of the centres of these two intense bands (as calculated from the corresponding peak fitting) is consistent with Ni-R ν_{CN} bands observed for other NiFe hydrogenases in solution.⁶

Oxidative potential steps

When the working electrode is poised at -0.199 V vs SHE, the distribution of the bands is shown by the following spectrum, Figure 4.5. Considering the ν_{CO} region at this more oxidising potential, there is an increase in the Ni-C and Ni-L (ν_{CO} at 1952, and 1877 and 1868 cm^{-1} respectively) concentrations.

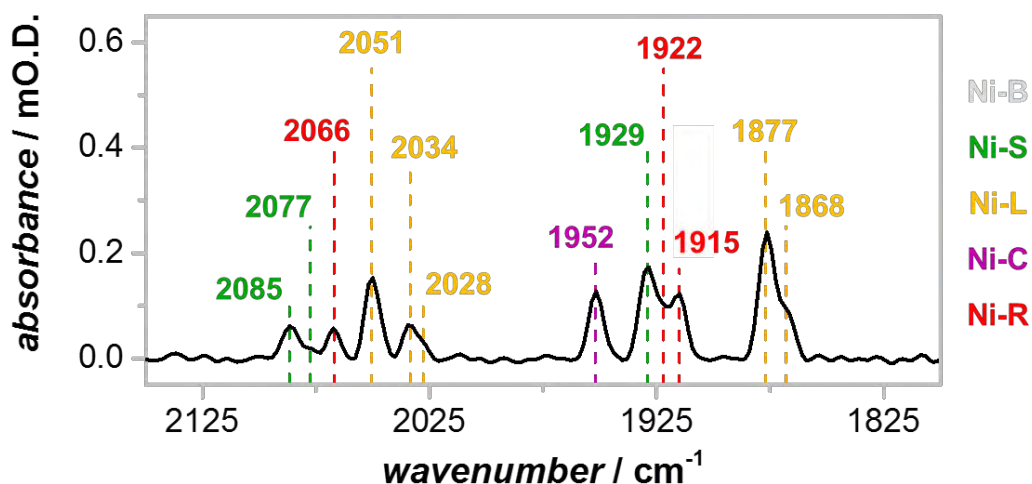


Figure 4.5 IR spectrum of Hyd-1 adsorbed on a carbon nanoparticle electrode. The applied potential is -0.199 V vs SHE. The spectrum was taken in mixed buffer pH 6.0 at 20 °C, under a 100 % N_2 atmosphere.

It is important to note that the Ni-L bands are responding to the applied potential, this was also noted by Adam J. Healy in his investigations of Hyd-1 in solution.⁴⁵ Previously, Ni-L has just been observed as a product of the photodissociation of Ni-C, and regarded as an artifact. In these experiments, Ni-L is shown to be a redox state which is responsive to the applied potential, in a manner consistent with it being at the same redox level as Ni-C.

The Ni-R bands at 1922 and 1915 cm^{-1} , decreased in intensity with this potential step. Additionally, a new band is present at 1929 cm^{-1} . This new spectral feature corresponds to the Ni-SI state, which consists of a Ni(II) redox state where the bridging-coordination position between the metals is vacant.

In the ν_{CN} region, the bands behave in accordance with to the observations just mentioned above. In fact, the concentration of Ni-L is now high enough that ν_{CN} bands of this state are detected at this potential. These bands are at 2051 , 2034 and 2028 cm^{-1} . Only three bands are detected, although four bands are expected as there are two distinct Ni-L states. It is likely that the intensity of the fourth band is not high enough to be detected, or is overlapping with another band of this now crowded ν_{CN} region. Considering that one of the Ni-L states, the one with a ν_{CO} band at 1868 cm^{-1} , is significantly less intense than the one at 1877 cm^{-1} , it is not surprising that not all the ν_{CN}

bands are detected. The ν_{CN} bands are, after all, less intense than the ν_{CO} ones. There are also another two new ν_{CN} bands, at 2085 and 2077 cm^{-1} . These correspond to the Ni-SI state.

Stepping the potential up again, to -0.074 V, gives the following spectrum shown in Figure 4.6.

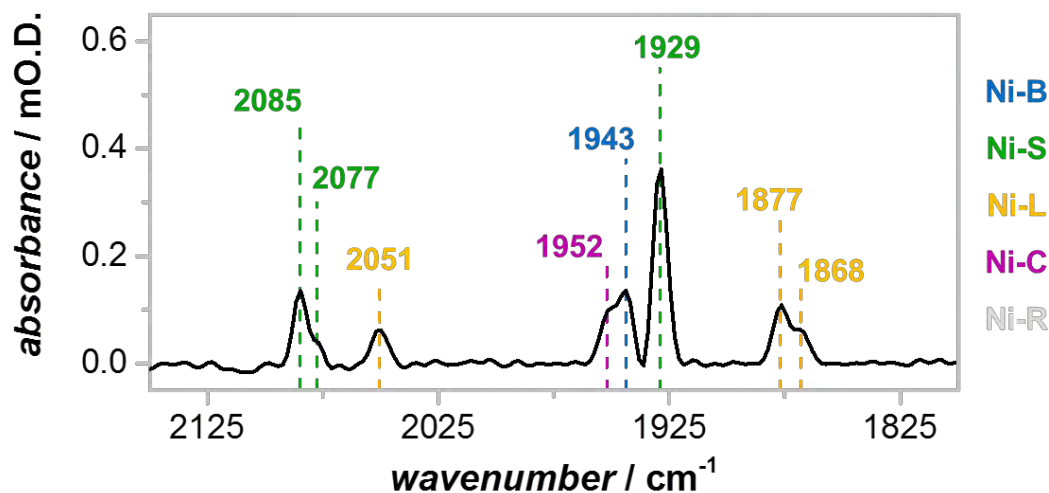


Figure 4.6 IR spectrum of Hyd-1 adsorbed on a carbon nanoparticle electrode. The applied potential is -0.074 V vs SHE. The spectrum was taken in mixed buffer pH 6.0 at 20 °C, under a 100 % N₂ atmosphere.

At this potential there is no Ni-R present any longer. Ni-SI has increased significantly, and Ni-C and Ni-L have decreased in concentration. A new band is observed at 1943 cm^{-1} . This is the same wavenumber position as the ν_{CO} band observed for the as-isolated enzyme and corresponds to the Ni-B state or a combination of Ni-B and Ni-A, provided that the wavenumber position of these bands is not sufficiently different. This matter will be clarified in subsequent chapters when analysing the aerobic and anaerobic inactivation of the enzyme.

A complete oxidation of the sample is achieved by stepping the potential up to +0.356 V vs SHE. After 90 min of holding the sample at this potential, the spectrum in Figure 4.7 was recorded. It shows the same distribution of states as that of the as-isolated enzyme from Figure 4.3.

At this potential, only the highest oxidation state of the active site is present. Compared to the spectrum at the previous potential, -0.074 V shown in Figure 4.6, Ni-SI (the most intense feature at that potential) and Ni-C and Ni-L are now absent as a result of the oxidation step.

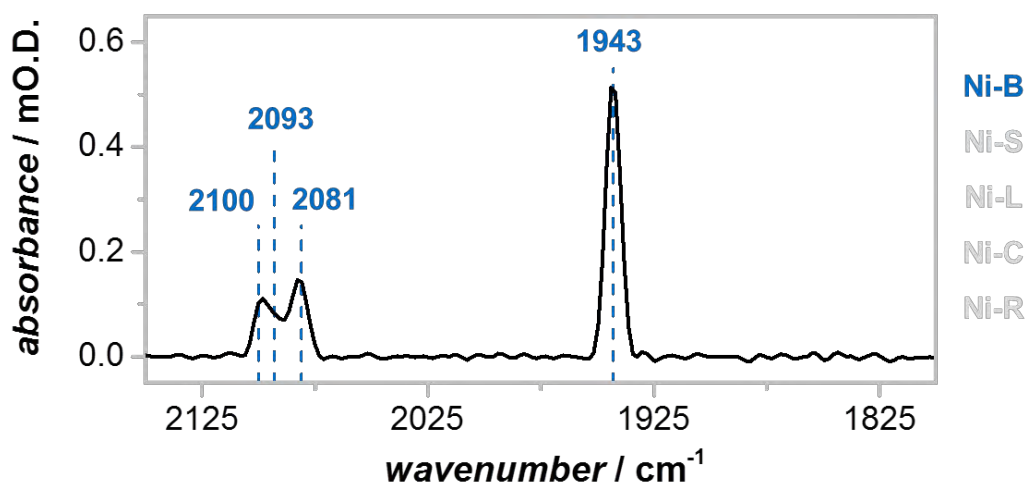


Figure 4.7 IR spectrum of Hyd-1 adsorbed on a carbon nanoparticle electrode. The applied potential is +0.356 V vs SHE. The spectrum was taken in mixed buffer pH 6.0 at 20 °C, under a N₂ atmosphere.

The fact that the set of bands observed in the spectrum in Figure 4.7 is exactly the same as those detected in the as-isolated sample (Figure 4.3), implies that these are all attributable to the ready species Ni-B. It has been shown that once activated, Hyd-1 only forms solely Ni-B upon re-oxidation.⁴⁶ These bands observed in Figure 4.7, and 4.3, correspond to the Ni-B state. The fact that there are three ν_{CN} bands (2100, 2093, and 2081 cm^{-1}) in this spectrum, suggests that another form of ready species is present. This could be a different protonation species of the Ni-B state.

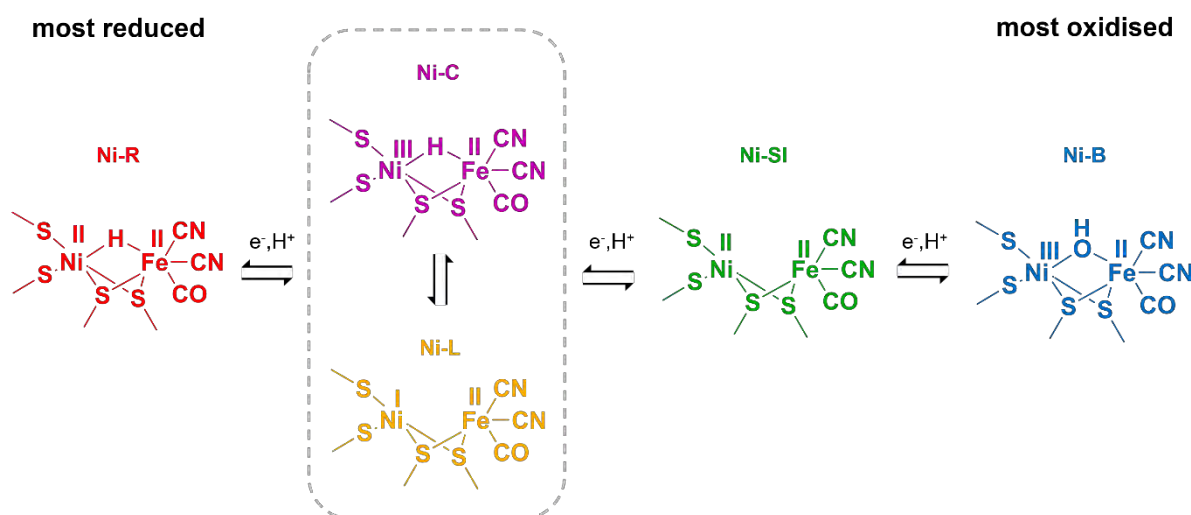


Figure 4.8 The redox transformations of the active site of *E. coli* Hyd-1. Ni-L and Ni-C states appear to be at the same redox level.

These potential-controlled experiments reveal a set of active site state redox transformation consistent with the scheme shown in Figure 4.8.

4.2.2 Redox titrations, and reduction potentials

In order to study this redox chemistry in more detail, a more complete redox titration of Hyd-1 adsorbed on the carbon nanoparticles was carried out. Figure 4.9 shows the redox titration as measured from low to high potential. At each potential, the spectrum was taken after a 13 minutes of equilibration, the total time the enzyme was held at each potential was of 20 min for this titration.

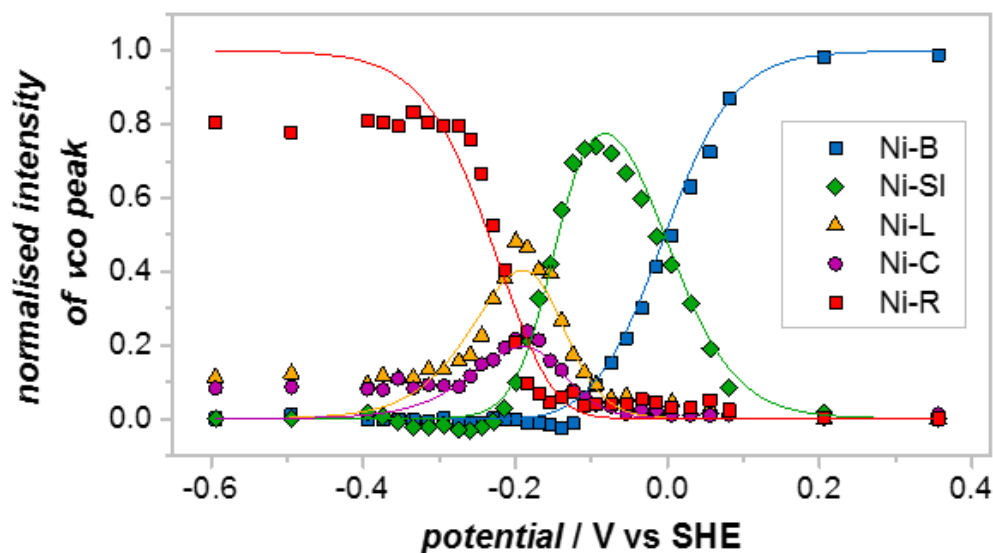


Figure 4.9 Normalised intensities of the ν_{CO} peaks as a function of the applied potential. The measurement was done from low to high potential. The electrolyte solution is mixed buffer pH 6.0. The lines show the Nernstian fits. The Ni-C and Ni-L ratio was fitted considering a generic chemical equilibrium between them.

One of the most important things to note from this redox titration is that the behaviour of Ni-L is indeed correlated to that of Ni-C. This suggests that these states are at the same redox level, that is, that the net number of electrons in the active site is the same for both species, just as the diagram in Figure 4.8 suggests. Ni-C and Ni-L are therefore, in chemical (not electrochemical) equilibrium. That aside, the redox behaviour of Hyd-1 adsorbed on carbon nanoparticles is consistent with what has been observed for other NiFe hydrogenases studied in solution.

The data were fitted using the Nernst equation. The determined reduction potentials from this fit are shown in Table 4.2.

Table 4.2 Reduction potentials, and n values, of the active site transformations of *E. coli* Hyd-1 adsorbed on a carbon electrode.

<i>redox step</i>	$E^{\circ} / \text{V vs SHE}$	n
Ni-B \leftrightarrow Ni-SI	-0.004	0.55
Ni-SI \leftrightarrow Ni-L / Ni-C	-0.148	1
Ni-L / Ni-C \leftrightarrow Ni-R	-0.231	1

In order to determine the reversibility of these processes, a reductive redox titration (from high to low potential) was carried out. Figure 4.10 shows this redox titration.

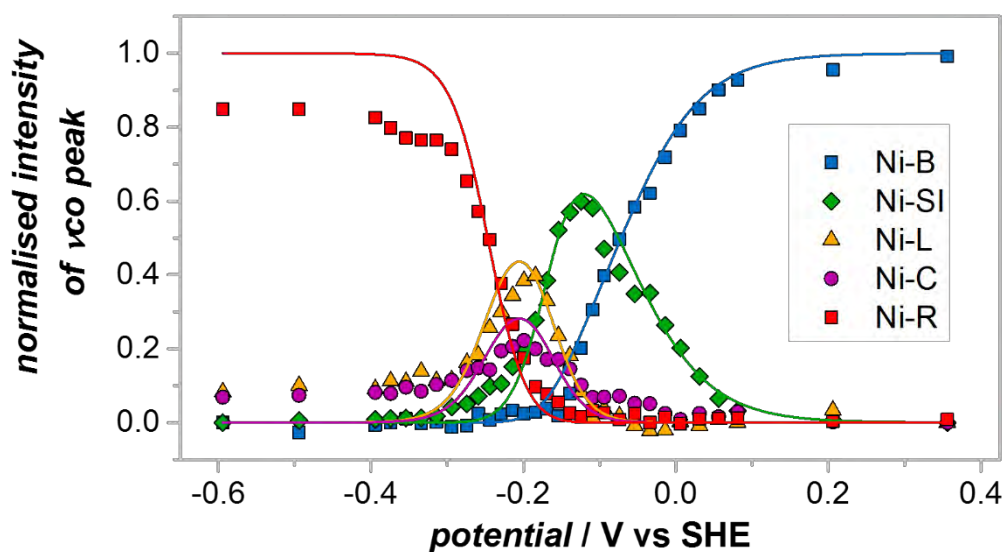


Figure 4.10 Normalised intensities of the ν_{CO} peaks as a function of the applied potential. The measurement was done from low to high potential. The electrolyte solution is mixed buffer pH 6.0. The lines show the Nernstian fits.

The data shown in Figure 4.10 shows that the redox transformations observed so far are fully reversible, including those involving Ni-L. This means that Ni-L is acting as a fully reversible redox state of the active site of the enzyme under physiologically relevant conditions (room

temperature). It is an accessible state of the active site that may have a part in the catalytic mechanism of the enzyme.

It can also be seen from Figure 4.10 that the redox behaviour of the Ni-B \leftrightarrow Ni-S process is not quite the same as that in the oxidative titration (Figure 4.9). An explanation for this could be that this redox process, unlike the other two, involves a chemical step. Ni-B has a hydroxide in the bridging position between the metals and therefore, this redox transformation is limited by how fast this chemical species can be incorporated into (or removed from) the active site.⁴⁷

Both Figure 4.9 and Figure 4.10 also show that a complete reduction, where the enzyme is fully converted to the Ni-R state, is never attained. No significant changes occur below about -0.30 V, Ni-R is a majority species under these conditions but Ni-C and Ni-L are always detected in smaller amounts. This distribution of states remains constant (like that of the spectrum shown in Figure 4.4) all the way down to -0.594 V.

4.2.3 More oxidised inactive states

A note on the as-isolated enzyme

It was common, for some preparations of the enzyme, that the initial spectrum showed different features in addition to those observed in Figure 4.3. Figure 4.11 shows the spectrum of an as-isolated enzyme sample that exhibits these other spectral bands.

In the ν_{CO} region, there appear two new bands at 1923 and 1910 cm^{-1} , the former being much less intense than the latter. Additionally, the main band at 1943 cm^{-1} (assigned to Ni-B) exhibits a clear shoulder at 1956 cm^{-1} . In the ν_{CN} region, two new bands are present at 2069 and 2060 cm^{-1} . Apart from this new features, the Ni-B bands (ν_{CO} : 1943 cm^{-1} , ν_{CN} : 2100, 2093, 2081 cm^{-1}) are present in this sample.

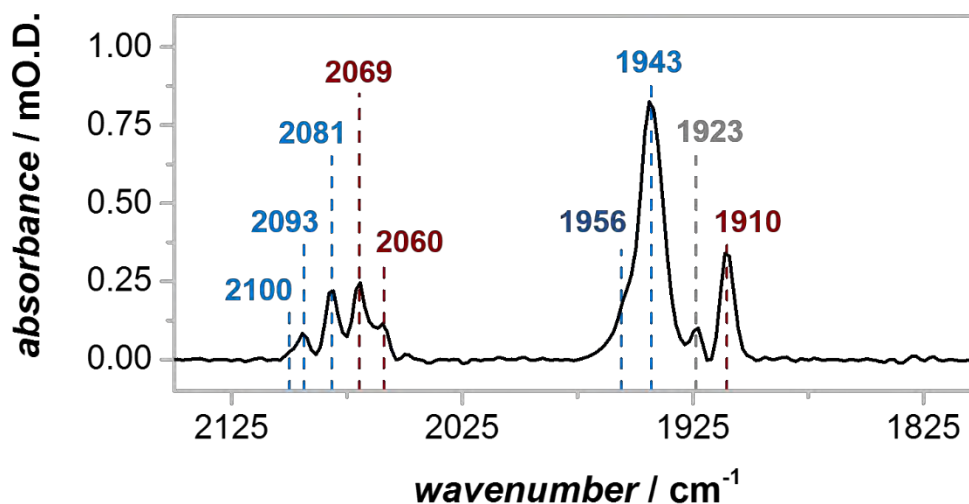


Figure 4.11 IR spectrum of the as-isolated Hyd-1 sample, adsorbed on carbon nanoparticles. This spectrum shows new bands in the ν_{CO} region and in the ν_{CN} region, relative to the as-isolated enzyme spectrum shown in Figure 4.3.

IR studies on other NiFe hydrogenases have shown that the as isolated sample occasionally contains additional features similar to those observed in the experiments presented here.^{2,28} Table 4.3 compares the wavenumber positions of these new bands observed here with the ones reported in the literature.

Table 4.3 Bands observed in the as-isolated sample for several NiFe hydrogenases.

<i>hydrogenase</i>	<i>wavenumber / cm⁻¹</i>	
	ν_{CO}	ν_{CN}
<i>E. coli</i> Hyd-1	1910	2069, 2060
<i>A. vinosum</i> MBH ²	1909	2066, 2057
<i>D. fructosovorans</i> ²⁸	1911	2068, 2059

When the enzyme is reduced (activated) with H₂ and by applying a reducing potential at the working electrode, -0.594 V vs SHE for example, the spectrum of the resulting sample is the same as that shown in Figure 4.4. These new bands observed in the sample were responsive to chemical and electrochemical reduction in such a way that the reduced enzyme is indistinguishable from a reduced sample that did not have these bands in the first place. More interestingly, when the

potential is stepped up to +0.356 V, the new features do not return and the spectrum is just like that shown in Figure 4.7 for a fully anaerobically oxidised sample. Figure 4.12 shows the reduction and re-oxidation of the sample with the corresponding spectra.

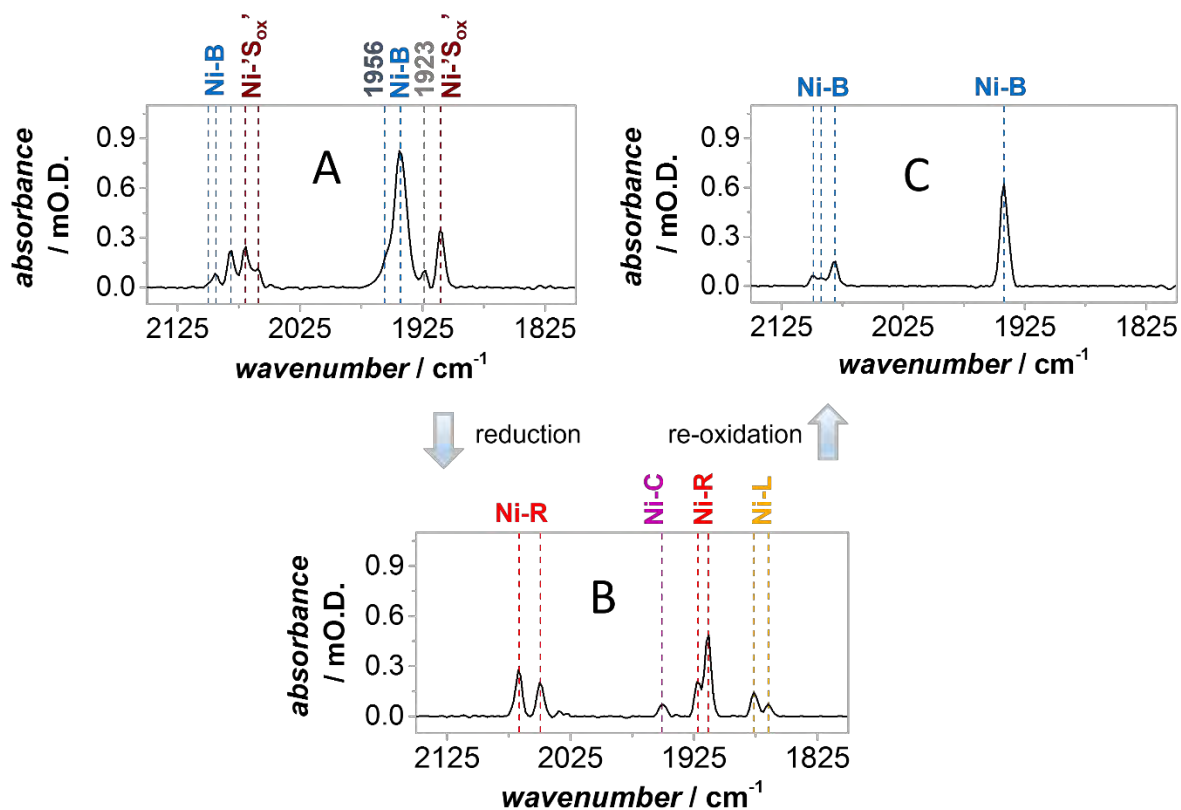


Figure 4.12 A) The as isolated sample of Hyd-1 adsorbed on carbon nanoparticles. The open circuit potential was of +0.025 V vs SHE. B) The reduced enzyme, reduction conditions: -0.594 V, 100 % H₂. C) A anaerobically re-oxidised sample; the applied potential was +0.356 V vs SHE.

The observation that the sample no longer shows the additional bands after being reduced and then re-oxidised, was also the case for the other studies mentioned above.^{2,28} Bleijlevens showed, however, that the addition of Na₂S to the reduced sample and the subsequent re-oxidation resulted in the re-appearance of the bands at 1909, 2066 and 2057 cm⁻¹.² This suggests that this state possesses an extra sulfur atom in the active site. It is also a diamagnetic state, showing no EPR signals which suggests a Ni(II). The position of the ν_{CO} band is consistent with a Ni(II) as well (see Table 4.1).

Based on X-ray crystallographic studies of variants of *Desulfovibrio fructosovorans* NiFe hydrogenase, Volbeda et al suggested that this state consists of a Ni(II) species with a persulfide group in one of the terminal cysteines and a vacant bridging position (see Figure 4.13).²⁸ This state has been called Ni-‘S_{ox}’. Volbeda et al suggest that it could be formed via the aerobic oxidation of inorganic sulfide in the active site; which is to say, the oxidation of the state that has been previously referred to as Ni-‘S’⁴⁸ (hence the name Ni-‘S_{ox}’). The reaction is shown in Figure 4.13.

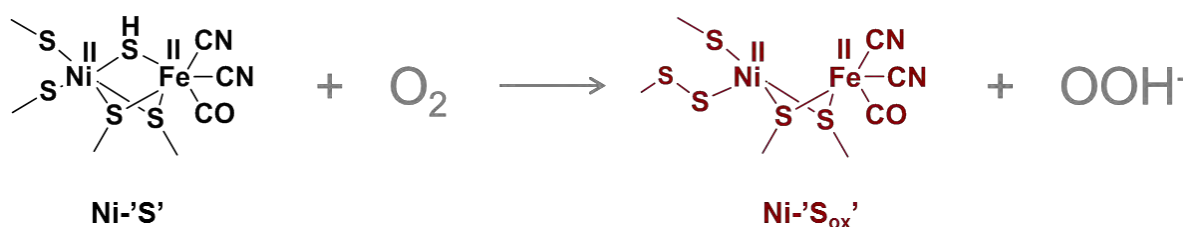


Figure 4.13 The aerobic oxidation of Ni-‘S’ to give Ni-‘S_{ox}’ as proposed by Volbeda et al. The structure for which they show crystallographic evidence is that for Ni-‘S_{ox}’.²⁸

The bands at 1910, 2069 and 2060 cm⁻¹ observed in the as-isolated spectrum of Hyd-1 in the experiments of the present study (Figure 4.11), are therefore assigned to Ni-‘S_{ox}’ based on the comparison discussed above. Regarding the other new bands at 1956 and 1923 cm⁻¹, it is not clear what these might represent. The higher wavenumber band is likely to be a Ni(III) species and the 1923 cm⁻¹ a Ni(II) species, based on the wavenumber position as compared to known NiFe hydrogenase states and their respective positions. Since these two species never come back once the sample has been activated, they could as well be related with some sulfur containing states such as the Ni(III)—SH⁻ or the Ni(II)—SH⁻ (This is Ni-‘S’ in Figure 4.13). There is, however, no direct evidence to support this hypothesis given the experimental data shown.

In the next section, the effect of pH on the distribution of the now identified redox states of the active site of *E. coli* Hyd-1 will be investigated.

4.3 The effect of pH. Part 1: distribution of states with potential

4.3.1 Redox titrations as a function of pH: determination of reduction potentials and PCET

Oxidative titrations

Redox titrations like the one shown in last section, which was measured at pH 6.0, were carried out at two other pH values, 4.0 and 8.0. Figure 4.14 shows the oxidative titrations at these two new pH values, along with the one recorded at pH 6.0 from last section, for comparison.

This data was fitted to the Nernst equation in order to determine the mid-point potentials for the redox transformations of the active site. Ni-L and Ni-C were plotted together as they represent the same redox level. All the redox steps were fitted to $n=1$, with the exception of the Ni-SI \rightarrow Ni-B transition, for which this parameter was allowed to vary during the calculation in order to find the best fit. Table 4.4 shows the n values, as determined from the Nernstian fits shown in Figure 4.14.

Table 4.4 Calculated n values for the Ni-SI \leftrightarrow Ni-B transition

<i>pH</i>	<i>n</i>
8.0	0.20
6.0	0.55
4.0	0.30

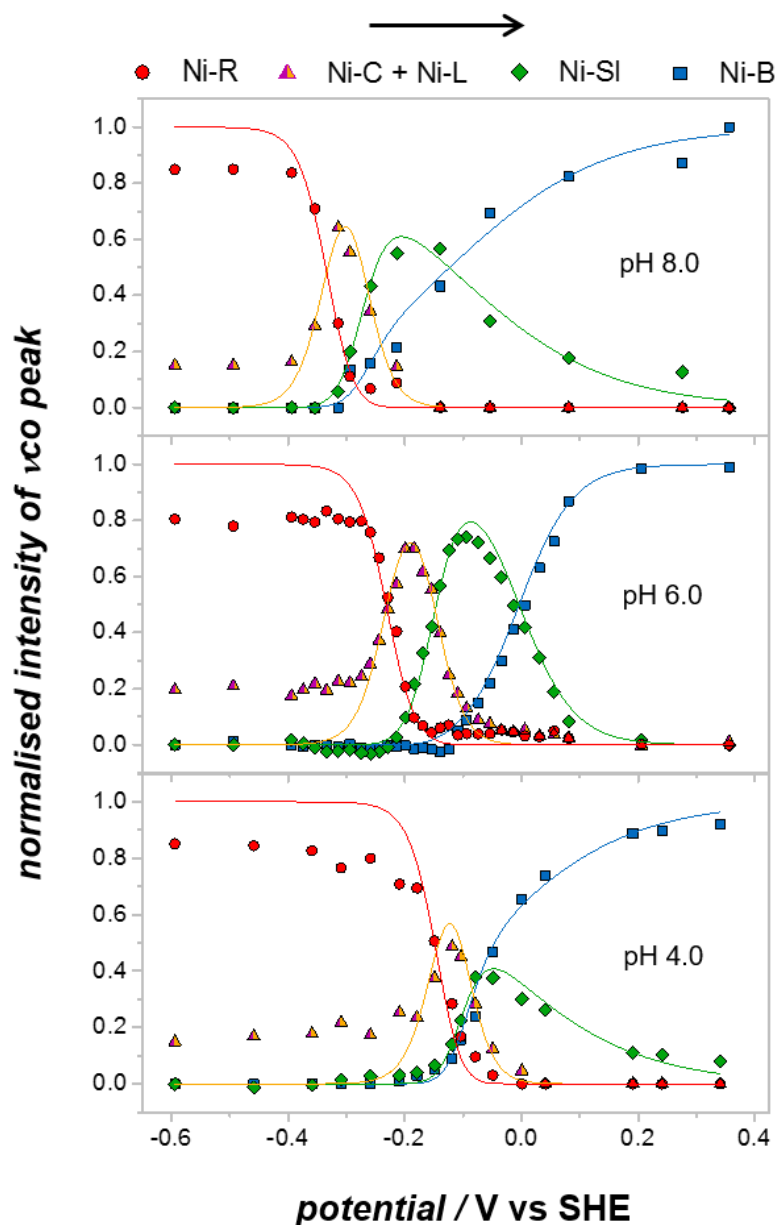


Figure 4.14 Oxidative titrations at different pH values for Hyd-1 adsorbed on a carbon nanoparticle electrode. The lines are the Nernstian fits.

It is likely that the reason why these values did not fit well to $n=1$ is due to a kinetic effect. The Ni-SI \leftrightarrow Ni-B transition is much slower than the others redox steps. Figure 4.15 shows that the time it takes to equilibrate an electrochemical step, where the Ni-SI \leftrightarrow is involved, is larger than that for the other transitions that do not include a chemical step.

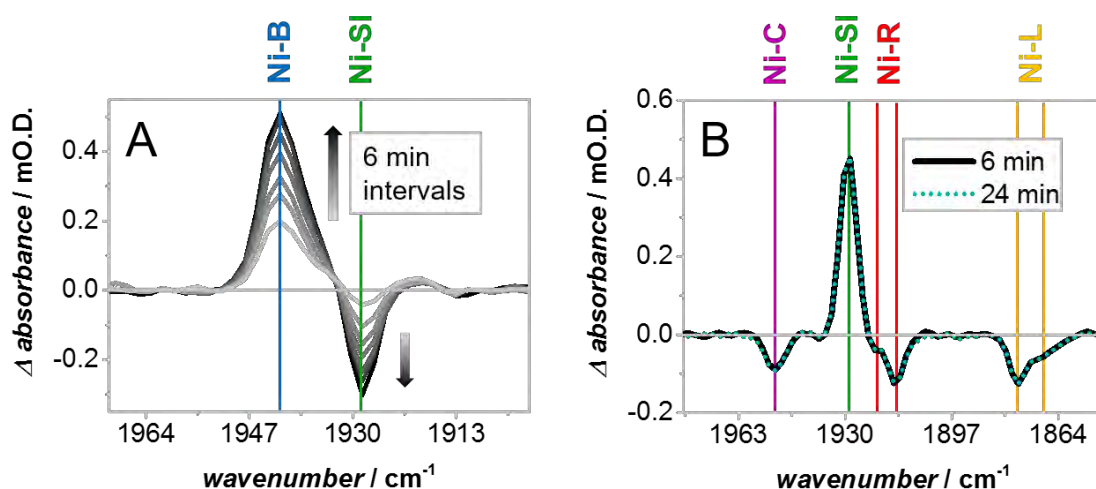


Figure 4.15 Time-dependent spectral changes, of the ν_{CO} region, after a potential step. A) A step from -0.030 to $+0.115$ shows the formation of Ni-B and the removal of Ni-SI. A spectrum was recorded every 6 minutes. B) A potential step from -0.200 to -0.100 V shows the formation of Ni-SI and the removal of Ni-L, Ni-C and Ni-R. A spectrum recorded after 24 min shows the same changes, in magnitude, as one recorded after 6 min.

The reduction potentials of the active site redox transformations

As a general observation, it can be noticed in Figure 4.14 that the higher the pH, the lower the reduction potentials. This is in accordance with these being proton coupled electron transfer processes (see Figure 4.8). When the concentration of protons is high, it follows that the reduction of a species (when it is coupled to protonation) is more thermodynamically favourable than for lower proton concentrations. This follows from the Nernst equation of a proton coupled electron transfer (See Section 2.1.3). Table 4.5 shows the reduction potentials calculated from the Nernstian fits showed in Figure 4.14.

Table 4.5 Reduction potentials for the redox transitions of the active site of Hyd-1, calculated from the fitting of the Nernst equation.

pH	$E^{0'}([H^+]) / V$ vs SHE		
	Ni-R \leftrightarrow Ni-C/Ni-L	Ni-C/Ni-L \leftrightarrow Ni-SI	Ni-SI \leftrightarrow Ni-B
8.0	-0.334	-0.263	-0.124
6.0	-0.231	-0.148	-0.004
4.0	-0.146	-0.073	-0.059

In chapter 2, the following equation which relates the reduction potential to the pH was discussed:

$$E^{0'}([H^+]) = E_{alk}^0 + \frac{2.3RT}{nF} \log_{10} \left(\frac{1 + \frac{[H^+]}{K_{red}}}{1 + \frac{[H^+]}{K_{ox}}} \right) \quad [4.1]$$

This equation describes the behaviour of the reduction potential as a function of pH, for a proton coupled electron transfer. A Pourbaix diagram (Figure 4.16) illustrates that there are three zones in the pH region that describe such behaviour:

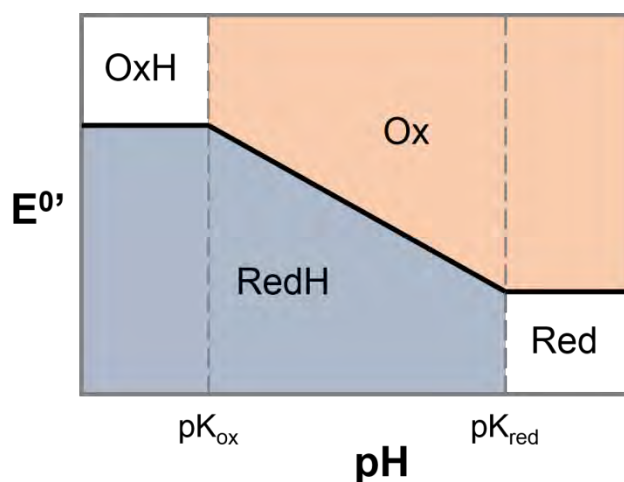


Figure 4.16 Pourbaix diagram. The black solid line represents the $E^{0'}$ values as a function of pH.

- i) When the pH is below pK_{ox} , this is the pK_a of the oxidised species, the reduction potential is independent of pH. Both the oxidised and reduced species are protonated:
 $OxH + e^- \rightarrow RedH.$
- ii) For pH values between pK_{ox} and pK_{red} (the pK_a of the reduced species), the reduction potential varies with pH with a slope of *ca* 58 mV per pH unit. The redox reaction involves the unprotonated oxidised species and the protonated reduced species: $Ox + e^- + H^+ \rightarrow RedH.$
- iii) At pH values higher than pK_{red} , the potential is again independent of pH. The redox equilibrium happens between the unprotonated species, both oxidised and reduced:
 $Ox + e^- \rightarrow Red.$

The change in the reduction potentials between pH 8.0 and pH 6.0, for all three redox levels in Table 4.5, falls (within error) in the region described by case 'ii' of the above list. This implies that all three redox equilibria ($Ni-SI \rightleftharpoons Ni-B$, $Ni-C/Ni-L \rightleftharpoons Ni-SI$ and $Ni-R \rightleftharpoons Ni-C/Ni-L$) consist of proton coupled electron transfer processes. This also provides some information about the proton acceptor, namely it does not have a pK_a in the 6.0 – 8.0 pH range.

Between pH 6.0 and pH 4.0 the reduction potentials of the $Ni-R \rightleftharpoons Ni-C/Ni-L$ and $Ni-C/Ni-L \rightleftharpoons Ni-SI$ processes change by *ca* 80 mV. This would suggest, assuming an ideal behaviour, that the pK_a of the proton acceptor lies at about 4.6 – 5.0. It also suggests that the proton acceptor in these two redox processes is either the same, or of similar pK_a .

The reduction potential of the $Ni-B \rightleftharpoons Ni-SI$, however, changes in an unexpected way at pH 4.0. It becomes more negative; this is not consistent with traditional proton coupled electron transfer behaviour. It is not clear what the explanation for this might be.

Reductive titrations

Figure 4.17 shows the reductive titrations of Hyd-1 adsorbed on carbon nanoparticles, at different pH values.

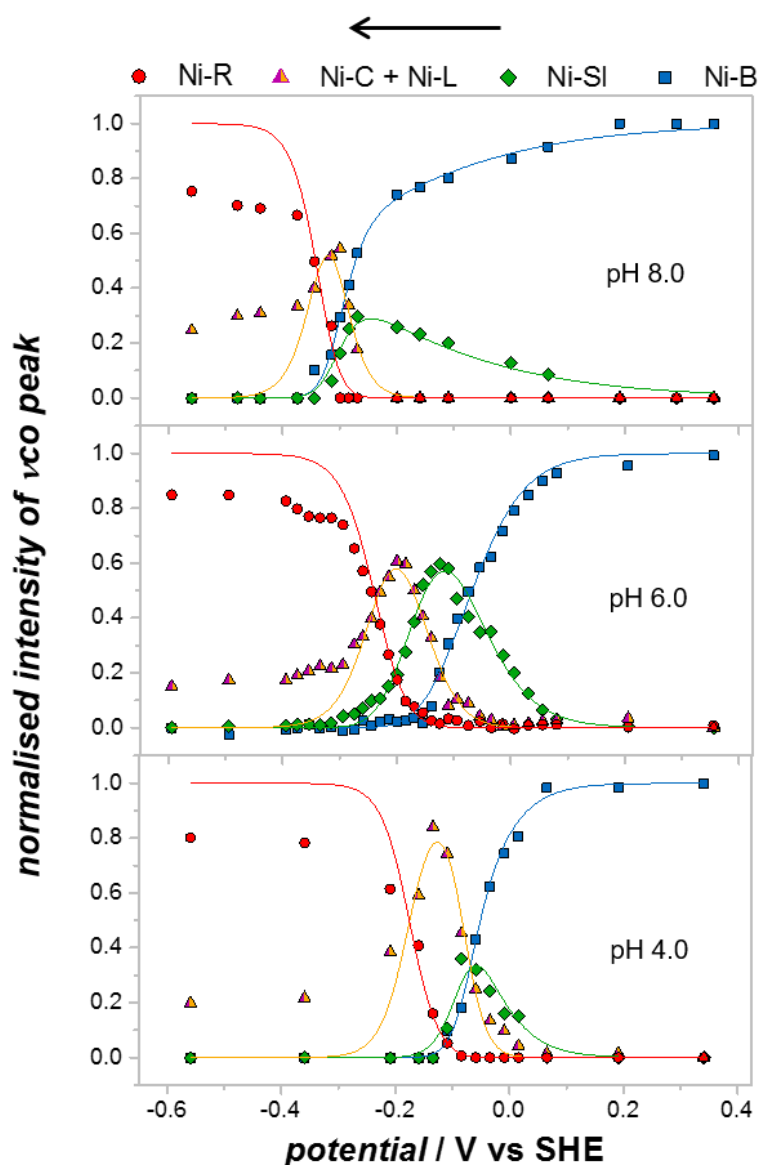


Figure 4.17 Reductive titrations at different pH values for Hyd-1 adsorbed on a carbon nanoparticle electrode. The lines are the Nernstian fits.

Figure 4.17 that the redox processes described so far are fully reversible at different pH values.

One of the main differences between the oxidative and the reductive titrations can be observed in the titration at pH 8.0. Noticeably, the Ni-B curve never intercepts that of Ni-SI for the reductive titration, whereas it clearly does in the oxidative case (Figure 4.14 top). There does not even seem

to be an actual reduction potential for this redox step in the reductive titration at pH 8.0. The Nernst fit gave an apparent redox potential of -0.388 V vs SHE, a potential where there is no Ni-SI present to start with.

This Ni-B \leftrightarrow Ni-SI transition appears to be much slower than the other redox steps, as demonstrated in Figure 4.15. Table 4.6 shows the reduction potentials calculated from Nernstian fits of the reductive titrations shown in Figure 4.17.

Table 4.6 Reduction potentials for the redox transitions of the active site of Hyd-1 in the reductive titration, calculated from the fitting of the Nernst equation.

<i>pH</i>	$E^{\circ'}([H^+]) / V \text{ vs SHE}$		
	Ni-R \leftrightarrow Ni-C/Ni-L	Ni-C/Ni-L \leftrightarrow Ni-SI	Ni-SI \leftrightarrow Ni-B
8.0	-0.338	-0.276	-0.388
6.0	-0.236	-0.159	-0.072
4.0	-0.169	-0.068	-0.070

It can be seen that the reduction potentials of the Ni-R \leftrightarrow Ni-C/Ni-L and the Ni-C/Ni-L couples do not vary as much, relative to those values for the oxidative titrations (see Table 4.5), as the reduction potential of the Ni-SI \leftrightarrow Ni-B redox transition. Moreover, the variation in the reduction potential of the latter couple is evidently proportional to the pH of the experiment. This variation is more than 200 mV at pH 8.0, less than 100 mV at pH 6.0, and about 10 mV at pH 4.0.

Although the purpose of these experiments was to determine thermodynamic parameters, there is clearly a kinetic effect observed in this data. Such an effect is the dependence on pH on the rate of conversion between Ni-B and Ni-SI. The higher the pH, the slower this reaction becomes. This is consistent not only with this reaction being a proton coupled electron transfer, but with the fact that the concentration of one of its participants (the hydroxide ion which occupies the bridging position in the Ni-B state) depends on pH. This kinetic effect might also provide an explanation for

the n values (number of electrons involved in a redox reaction as described by the Nernst equation) being lower than one, for this redox step, in the best fits (Table 4.4).

The timescale of the experiment did allow for a more accurate determination of the reduction potentials of the Ni-R \leftrightarrow Ni-C/Ni-L and the Ni-C/Ni-L couples at all pH values, and of the Ni-SI \leftrightarrow Ni-B reduction potential at pH 4.0. These potentials did not vary significantly (less than 10 mV) between the oxidative and the reductive titrations. However, the redox potentials for the Ni-SI \leftrightarrow Ni-B couple at pH 6.0 and 8.0 should be regarded as apparent for the reasons just discussed.

A detailed analysis of the spectra at these new pH values, 4.0 and 8.0, will follow next.

4.3.2 Potential-controlled spectral analysis at low and high pH

IR spectra at pH 4.0

Figure 4.18 shows spectra collected at four different potentials, at pH 4.0. These potentials were chosen to coincide with the maxima, in intensity, of each redox active site state, or level (see Figure 4.14).

Before proceeding with the analysis of these spectra, it is important to note that Hyd-1 becomes efficient at proton reduction at pH values below 4.⁴⁴ This enzyme is biased towards H₂ oxidation, and at pH values above 4.0 it does not show any significantly measurable activity for proton reduction. For these experiments, at the potentials where the enzyme exhibits proton reduction, no solution was flowed through the cell. This allowed for H₂, which inhibits this catalytic process, to build up in the system. The inhibition of this catalytic reaction permits for a more accurate measurement of the system at electrochemical equilibrium without catalytic turnover, which is the purpose of this experiment. Figure 4.19 shows the chronoamperometry trace for the oxidative titration at pH 4.0, the currents at low potentials are indeed small (compared to the catalytic currents when mass transport conditions are optimal), with a maximum reductive current of less than 1 μ A at -0.594 V. Analysis under catalytic turnover is the subject of Chapter 5.

The spectra in Figure 4.18 show the same bands that were observed at pH 6.0 (Figure 4.4 to Figure 4.7), although their distribution as a function of potential is different, as was discussed above. At -0.594 V, which is the lowest applied potential, there is a predominance of the Ni-R state with a small quantity of Ni-C and some hints of Ni-L being present.

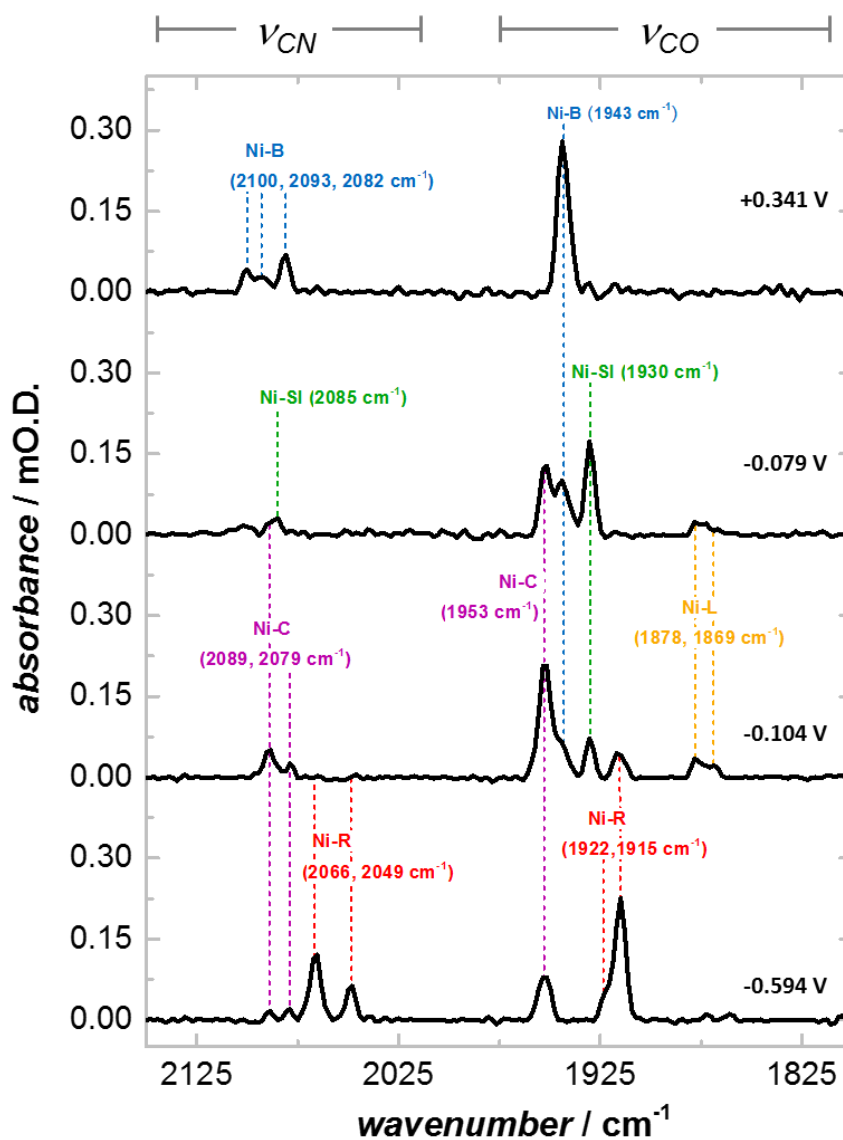


Figure 4.18 IR spectra at -0.594, -0.104, -0.079, and +0.341 V vs SHE. These were measured at pH 4.0 and the potential values correspond to the maxima of each state (or level). The wavenumber positions were determined based on a peak fitting analysis of the data.

For the second lowest potential, -0.104 V, there is a decrease in Ni-R and the Ni-C state is now the predominant one. Ni-L is also clearly present, although at lower concentrations (relative to the

corresponding maximum measured at pH 6.0 in Figure 4.5). Moreover, the intensity of Ni-C in this spectrum is now such, that the ν_{CN} bands corresponding to this state are detected at 2089 and 2079 cm^{-1} . Ni-SI is also present at this potential. Finally, there appears to be also a small amount of Ni-B, which can be observed as a shoulder of the Ni-C ν_{CO} band.

The Ni-SI state is the predominant species at -0.079 V. Ni-B is also clearly present in an important amount. Ni-C and Ni-L decreased, and the Ni-C state is still significantly more intense than Ni-L. This observation is true for all the other potentials at this pH. At the most oxidising potential, as was the case for pH 6.0, only Ni-B is present. This most oxidised state shows the same three ν_{CN} bands (at 2100, 2093 and 2082 cm^{-1}) that were observed at pH 6.0 at the highest potential.

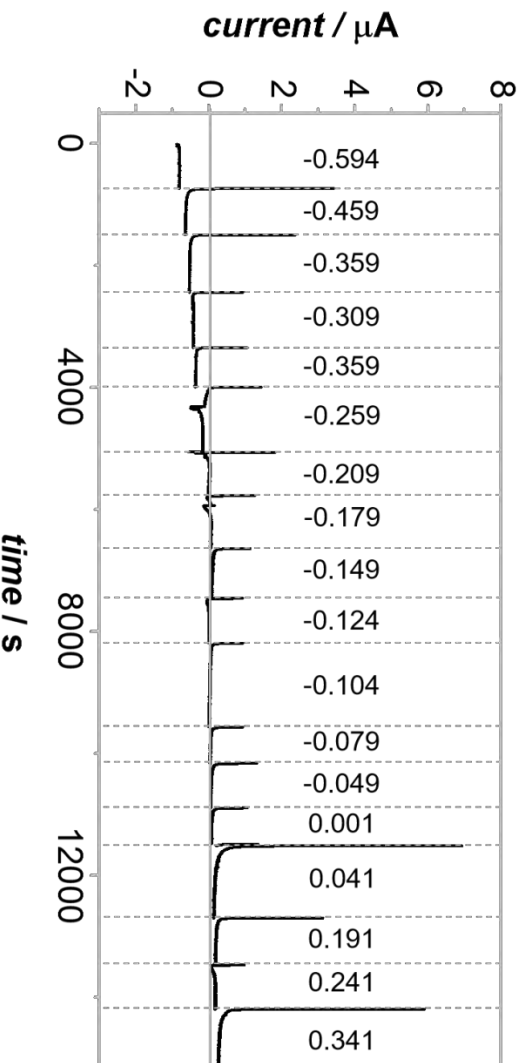


Figure 4.19 Time-current trace of a titration at pH 4.0. No solution was flowed through the spectroelectrochemical cell in this experiment. Other conditions: mixed buffer, 20 °C, 100 % N_2 atmosphere.

IR spectra at pH 8.0

Figure 4.20 shows spectra collected at four different potentials, at pH 8.0. These potentials were also chosen to coincide with the maxima, in intensity, of each redox active site state or level (see Figure 4.14).

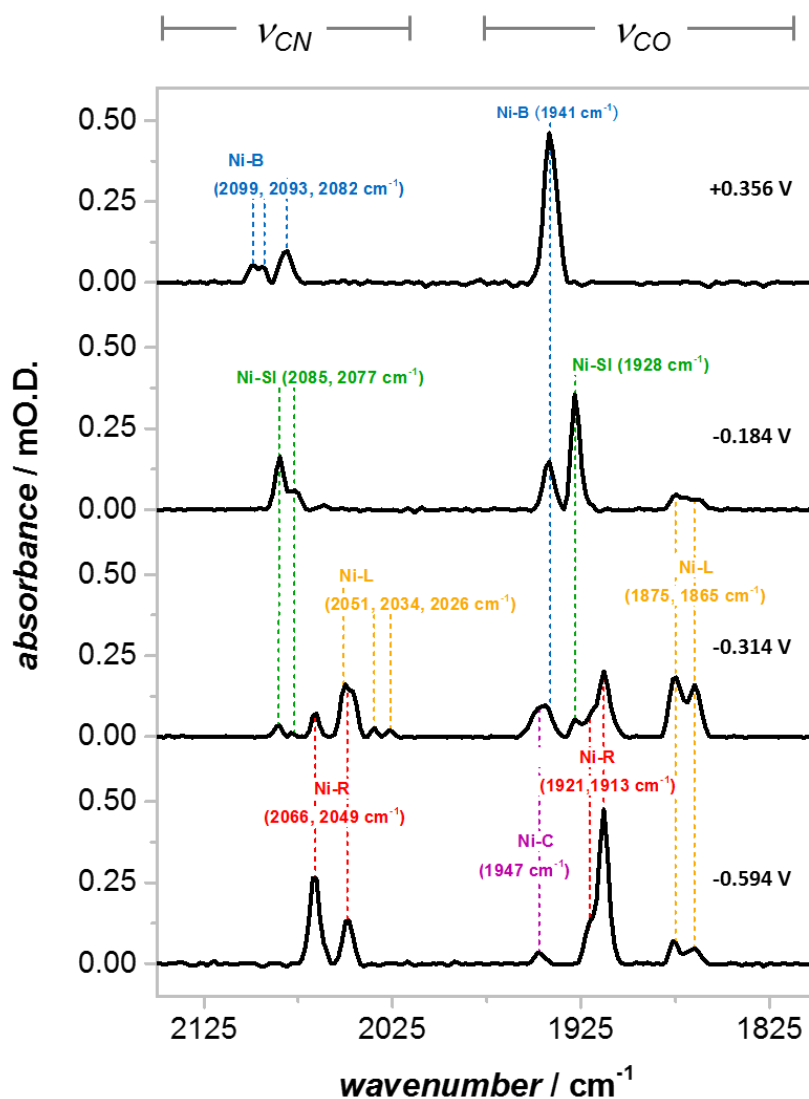


Figure 4.20 IR spectra at -0.594, -0.314, -0.184, and +0.356. These were measured at pH 8.0 and the potential values correspond to the maxima of each state (or level). The wavenumber positions were determined based on a peak fitting analysis of the data.

At -0.594 V Ni-R is, as expected, the predominant state. There is also Ni-C and Ni-L present at this potential, at low concentrations. However, in contrast to the pH 4.0 data just described above, Ni-L appears to be more intense than Ni-C in this region.

At a higher potential, at -0.314 V, shows the maximum of the Ni-C/Ni-L redox level. Ni-R has decreased and there is a small amount of Ni-SI present, as well as Ni-B. Again in this spectrum, the intensity of Ni-L greatly surpasses that of Ni-C, with Ni-C being the overall most intense state at this potential.

The Ni-SI state maximum occurs at -0.184 V. No Ni-C is detected at this potential, although a tiny amount of Ni-L is observed. The concentration of Ni-B has increased, relative to the previous potential. At the highest potential, $+0.356$ V, there is only Ni-B present. The three ν_{CN} bands of the Ni-B state are also present at this pH.

The analysis of these spectra at different pH values shows also that there exists a change in the relative intensities of some bands with pH. These, and other pH-dependent changes, will be discussed in detail in the next section.

4.4 The effect of pH. Part 2: acid-base equilibria of redox states

4.4.1 Ni-C and Ni-L as different protonation species of the same redox level

The equilibrium between Ni-C and Ni-L

In the spectra analysed in last section, at different pH values, there was a noticeable dependence of the ratio of Ni-C to Ni-L on pH. Figure 4.21 illustrates this more clearly. These data show two important points. First, that Ni-C and Ni-L behave the same way with potential, they appear in the exact same potential window. Ni-C and Ni-L are at the same redox level, independent of pH. Secondly, the ratio between these two species varies as a function of pH. This implies that the equilibrium between Ni-C and Ni-L is an acid-base equilibrium, as described by Figure 4.22. The data presented in this figure corresponds to three different samples, one for each pH value. The total absorbance of the species detected cannot be therefore related between samples, only their ratios can.

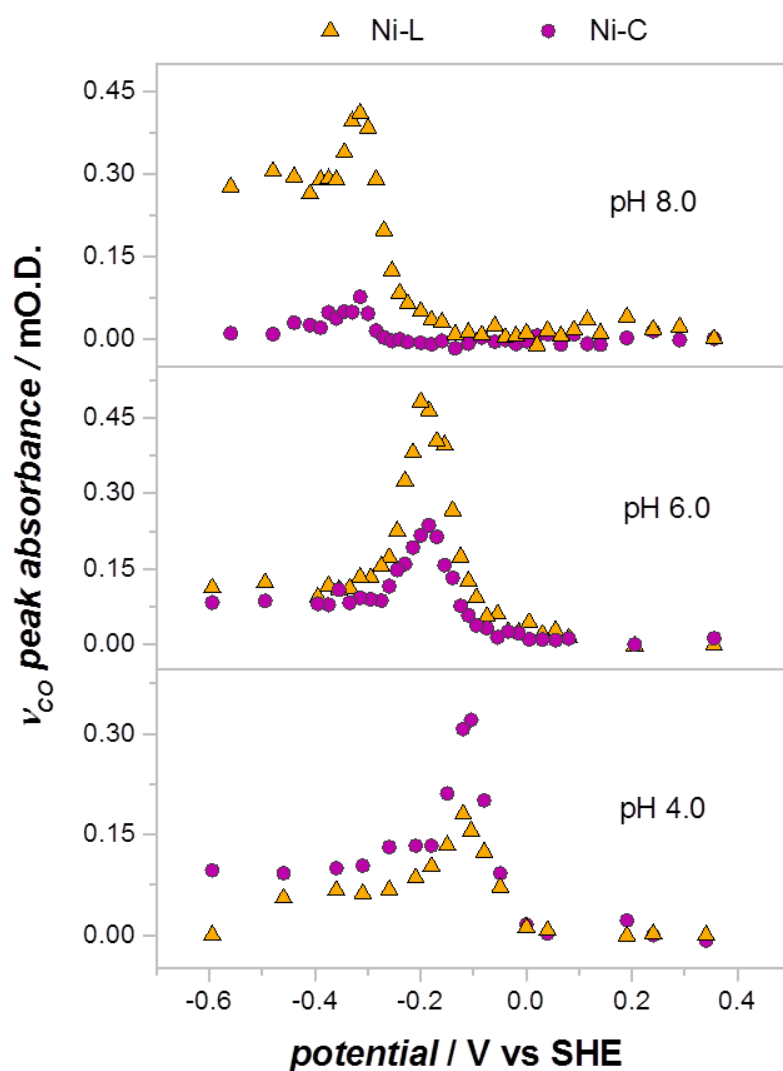


Figure 4.21 The dependence on pH of Ni-C and Ni-L as a function of applied potential. The Ni-L quantities represent the sum of the two Ni-L species observed in the spectra.

The hydride bound in the bridging position in Ni-C leaves as a proton, as shown in Figure 4.22, in the acid-base equilibrium. The two electrons of the hydride reside now in the Ni ion as the proton is abstracted by a nearby base. This results in a Ni centre in the formal oxidation state of +1. This is consistent with the low wavenumber position of the ν_{CO} of the Ni-L states (1877 and 1868 cm^{-1}). It has also been argued, by means of DFT calculations, that the low wavenumber position of the Ni-L states is explained by the formation of a metal-metal bond between the Ni and the Fe.³⁷ The scheme presented in Figure 4.22 has been

presented in the literature as a photodissociation reaction.^{7,32,34,35} Here it is proposed to be an acid base equilibrium, based on the data presented.

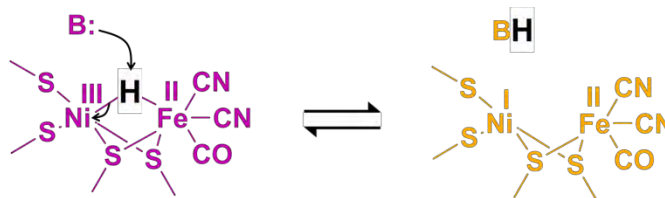


Figure 4.22 The acid-base equilibrium between Ni-C and Ni-L. The hydride, bound in the bridging position in Ni-C, leaves as a proton abstracted by a nearby base B. The two electrons of the hydride are gained by the Ni ion which exhibits a formal oxidation state of +1 in the Ni-L form.

According to the data presented in Figure 4.21, the pH of the system determines the relative concentrations of these two species. The higher the pH, the more favoured the un-protonated species (Ni-L) will be. Consequently, lower pH values will result in a more favourable protonated species (Ni-C). This implies that the active site, although buried inside the protein structure, responds quickly to the external pH of the solution. This is consistent with the fact that there are proton channels which have been identified in hydrogenases;⁴⁹⁻⁵⁴ and it is likely that through these, the active site responds to the pH of the external solution. A more detailed analysis of this chemical equilibrium was attained by collecting more spectra at pH values between 3.0 and 9.0. Figure 4.23 shows the ratio of Ni-L to Ni-C in this pH range.

There is a clear pH dependence of the relative intensities of Ni-L and Ni-C shown in Figure 4.23A. Each spectrum was taken at the potential where the Ni-C and Ni-L were at their maximum concentrations, for each pH. This potential value is dependent on the pH of the system, consistent with the expected Nernstian behaviour. All the redox transformations described so far are proton coupled electron transfers; therefore, the distribution of the redox levels as a function of potential depends on the pH.

Figure 4.23B shows the IR spectra at the two extreme pH values. At pH 3.0, Ni-C is much more favoured than Ni-L. The latter is just present in marginal quantities. Moreover, in the spectrum

recorded at pH 9.0 Ni-C is not even present any longer. At this pH only the un-protonated Ni-L is detected in the potential window of this redox level.

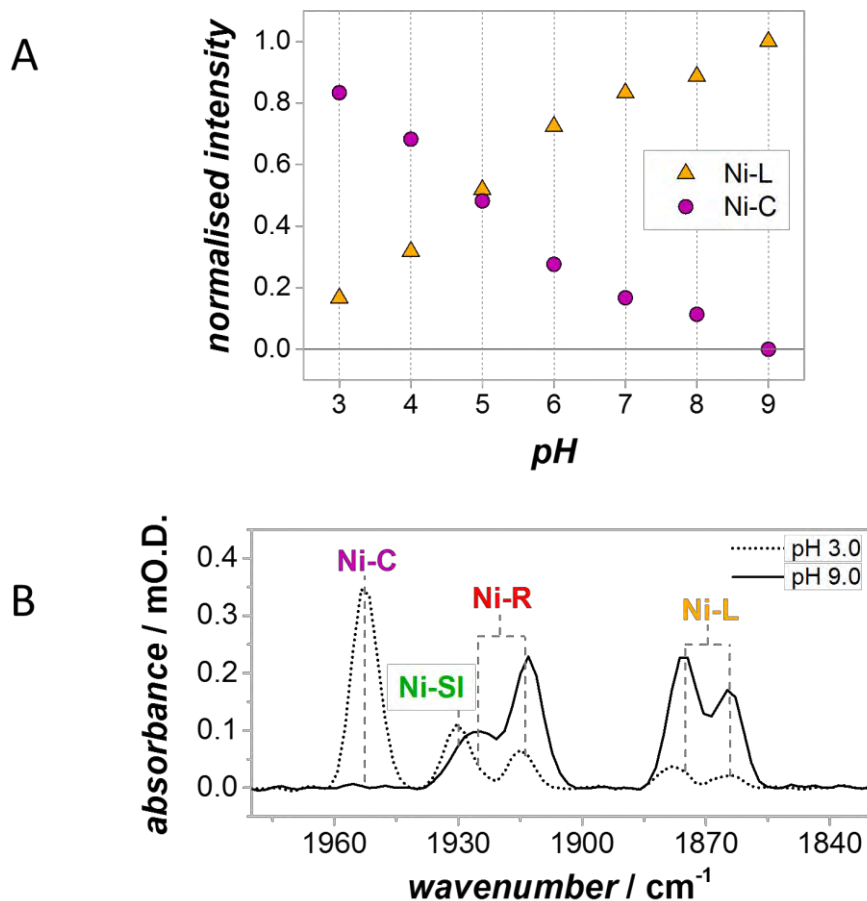


Figure 4.23 A) The relative intensities of Ni-C and Ni-L as a function of pH. The intensity values have been normalised to the total Ni-C + Ni-L concentration. At each pH the potential was set to the value that gives the maximum of Ni-C + Ni-L intensity: these potentials are (in ascending order of pH): -0.054, -0.104, -0.144, -0.199, -0.254, -0.299, and -0.339 V vs SHE respectively. B) Infrared spectra, showing the vco region only, recorded at pH 9 and pH 3.0 at the potential of maximum Ni-C/Ni-L intensity.

This phenomenon is completely reversible. Changing the pH of the spectroelectrochemical cell to high values and then to low values, and *vice versa*, resulted always in the same relative intensities of Ni-C and Ni-L at any given pH. This is the expected normal behaviour from a classic acid-base equilibrium.

The proton in this pH equilibrium between Ni-C (in which it is bound as a hydride) and Ni-L is only removed from the active site when oxidation to the Ni-SI state occurs. This can be inferred from the

fact that the reduction potential for the couple Ni-C/Ni-L \leftrightarrow Ni-SI is that of a proton coupled electron transfer, as discussed in the previous section. Figure 4.21 also demonstrates this.

The proton acceptor in the Ni-L state has been suggested to be one of the terminal thiolate ligands to the Ni,^{37,55,56} which is still within the active site. The fact that two Ni-L signals are observed in this experiments (which is consistent with multiple Ni-L bands observed for other hydrogenases),^{21,34} might be an indication of there being multiple proton acceptors in close proximity to the active site. The affinity for the proton of these acceptors, increases relative to that of the metal centre as the pH is raised.

The Henderson-Hasselbalch equation (equation 4.2) predicts that the logarithm of the ratio of the acid and the conjugate base as a function of pH, should give a slope of -1 for a one proton transfer.

$$\log_{10}\left(\frac{HA}{A^-}\right) = -pH + pK_a \quad [4.2]$$

Figure 4.24 shows this plot for the Ni-C \leftrightarrow Ni-L acid-base equilibrium.

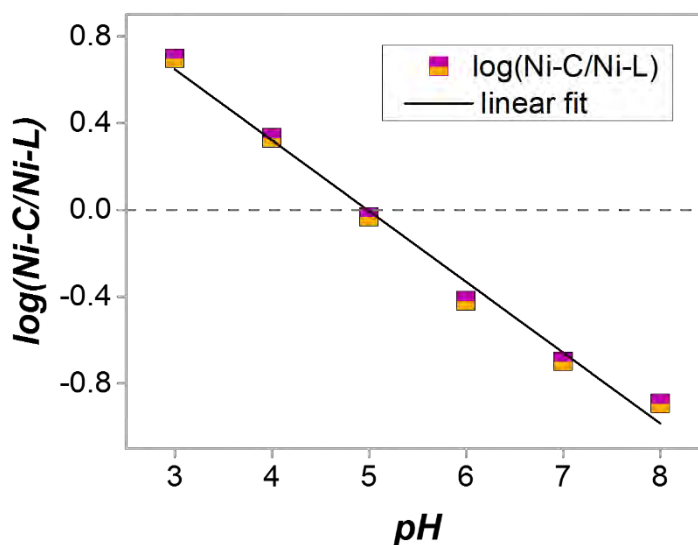


Figure 4.24 Henderson-Hasselbalch plot of the acid-base equilibrium between Ni-C and Ni-L. The slope of the fitted curve is -0.33 and the pK_a , determined from the fit, is 5.0.

The slope of the fitted curve is not -1, but -0.33. This is consistent with there being more than one protonation sites. Figure 4.23A does not fit well a single protonation curve either. It is known from these data that there are at least two detected Ni-L species and that the three states, Ni-C and the two Ni-L states are isopotential. A more complete look at this acid-base equilibrium is described in Figure 4.25.

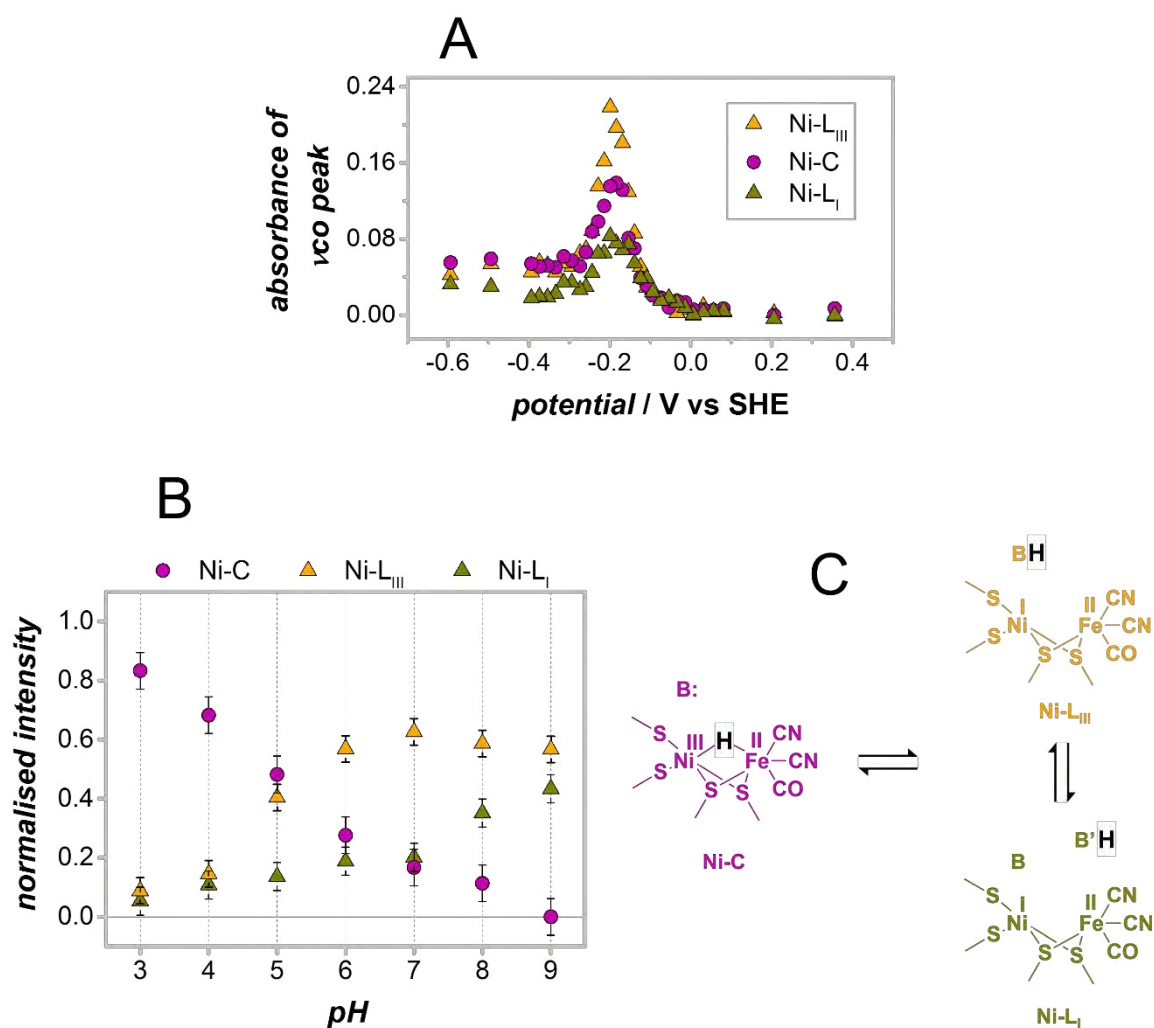


Figure 4.25 A) The dependence of Ni-C, Ni-L_I, and Ni-L_{III} as a function of applied potential at pH 6.0. B) The relative intensities of these three isopotential states as a function of pH shows the behaviour of the Ni-L species. C) The acid-base equilibrium at this redox level consists of the proton dissociating from the bridging position between the metals to a proton acceptor near the active site. There are, it is suggested from the showed data, two protonation states of this un-protonated species. B and B' represent different generic bases in the vicinity of the active site.

Figure 4.25 shows the three observed states of the active site that are present at this redox level. They appear in the same potential window. These states are in chemical equilibrium. The pH dependence between the Ni-L states is not as well defined as that between Ni-C and Ni-L (Figure 4.23A). There is, nonetheless, a pH-dependent behaviour of the ratio of Ni-L_I and Ni-L_{III}. From this it can be suggested that these two Ni-L states are indeed different protonation states of a Ni(I) active site with a vacant bridging position. Figure 4.25B shows that the Ni-L_{III} concentration increases significantly between pH 4 and pH 5. The Ni-L_I species, on the other hand is present in a relatively low concentration below pH 7; and at higher pH values, its concentration starts to increase more significantly.

These observations suggest that Ni-L_I is more favoured at higher pH values than Ni-L_{III}. In addition to that, the wavenumber position of Ni-L_I is lower than that of Ni-L_{III} (1868 vs 1877 cm⁻¹ for the ν_{CO}); this is consistent with Ni-L_{III} being more protonated than Ni-L_I. From these two observations the following model is proposed.

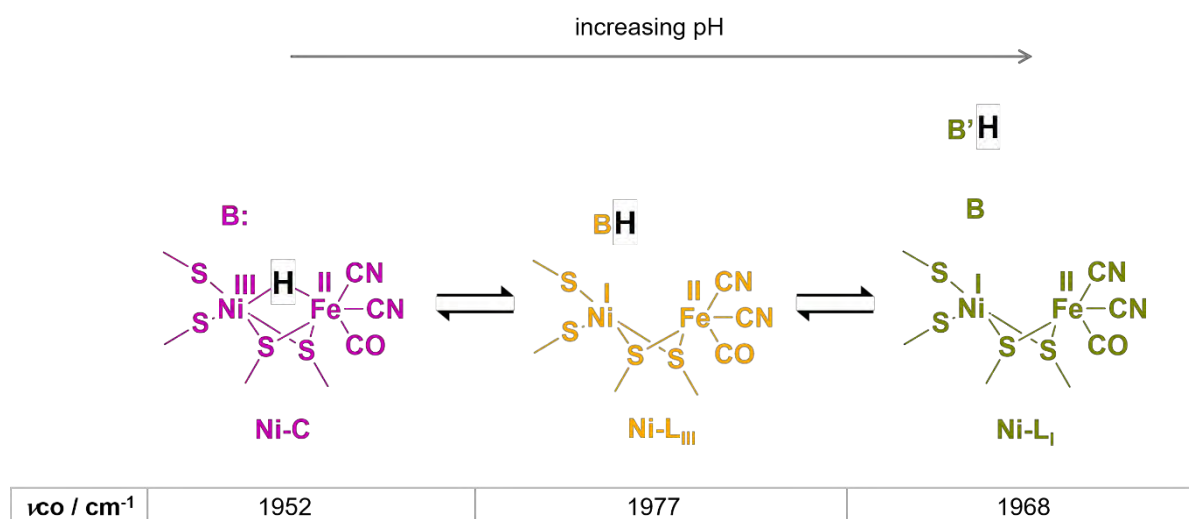


Figure 4.26 The effect of pH on the Ni-C / Ni-Ls equilibrium. The higher the pH, the further the position of the proton from the bimetallic active site. B and B' represent generic bases; where B' is further from the active site than B.

Figure 4.26 shows a model where the pH of the solution determines how far from the active site is the proton located. B and B' represent generic bases with B' being further from the active site than

B (since Ni-L_I shows a lower ν_{CO} wavenumber position than Ni-L_{III}). Low pH values favour the proton to be nearer the active site, even as a bound hydride in the bridging position between the metals, in the case of Ni-C. As the pH is raised, the proton is “withdrawn” from the bimetallic active site to form Ni-L_{III} and it is accepted by B. At even higher pH values the concentration of Ni-L_I increases; that is, the proton is transferred from B to B’ which is further from the active.

Significance of the Ni-C \leftrightarrow Ni-L acid base equilibrium

The data analysed in this section gives a fresh view on the Ni-L state; in which it is no longer perceived as an artefact, attainable only at very low temperatures as a consequence of photodissociation, but as an accessible state which differs from Ni-C only on the protonation of the metal centre. Tai et al. proposed that the transition from Ni-C to Ni-SI is “gated” by the redox state of the proximal Fe-S cluster.⁵⁷ They argue that when the proximal Fe-S cluster is oxidised, the transition from Ni-C to Ni-SI, through Ni-L intermediates, is favourable (Figure 4.27A). In contrast, when the proximal Fe-S cluster is reduced, then the formation of Ni-SI is not favoured as the reduced proximal cluster cannot accept an electron (Figure 4.27B).

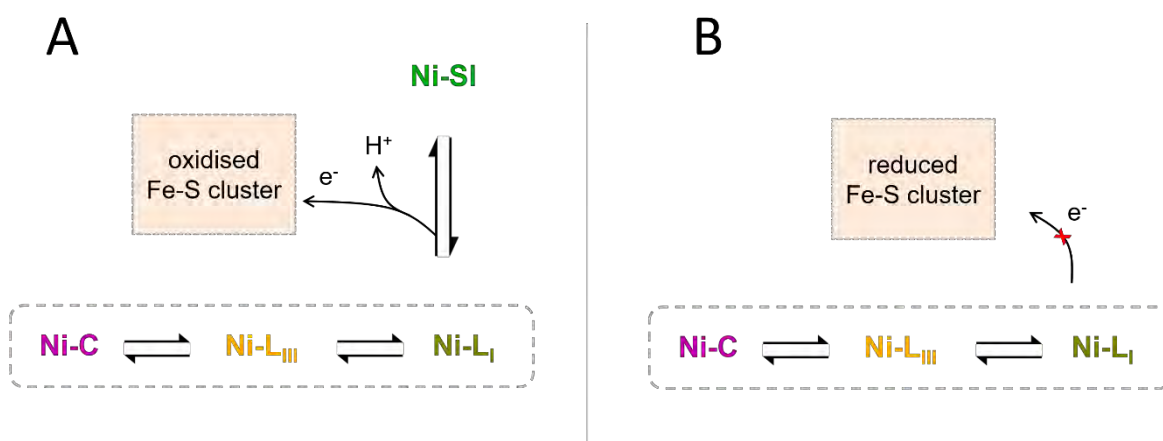


Figure 4.27 Transition from the Ni-C/Ni-L redox level to Ni-SI is gated by the proximal cluster. A) An oxidised proximal cluster allows for the removal of an electron from the active site. A further removal of a proton, through Ni-L intermediate, results in the Ni-SI state. B) A reduced proximal cluster cannot accept electrons; therefore, the active site is “trapped” in the Ni-C / Ni-L level.

Hyd-1 has a special proximal cluster, like several other O₂-tolerant hydrogenases, which is the main responsible for its oxygen tolerance.^{51,58–61} It consists on a 4Fe-3S structure that is able to undertake two redox transitions in a physiologically relevant potential window.²⁰ The reduction potentials of these transitions of the proximal Fe-S cluster are high, which also contributes to its oxygen tolerance; they are more positive than the reduction potential of the Ni-SI ↔ Ni-C at any given pH.^{20,61} This means that for Hyd-1, at the potential window where Ni-C and Ni-L are present, the proximal Fe-S cluster is always in the reduced form. This provides a rationale for the behaviour observed in the data presented in this section; in which the pH is the driving force determining the relative concentration of Ni-C and Ni-L, with the proximal Fe-S cluster being reduced (full) in this potential window. This corresponds to the situation represented by Figure 4.27B.

These results also suggest that Ni-L may be an intermediate, with catalytic significance, between Ni-C and Ni-SI in the cycle. Chapter 5 will investigate the intermediates involved in catalysis, including the role of Ni-L, in more detail.

4.4.2 The equilibrium between the Ni-R species

In many hydrogenases, the Ni-R redox level presents multiple bands. Two, and even three, distinct ν_{CO} bands attributed to Ni-R have been observed for some hydrogenases (see Table 4.1).^{1,2,4,5,9} It has been suggested that this multiplicity of bands is a result of different protonation states of the same redox level.^{2,5,62} However, Fichtner et al. reported that changing the pH did not result in a measurable change in the relative intensities of these bands; they therefore suggest that these bands may correspond to structurally different subforms of the Ni-R state.¹

E. coli Hyd-1 shows two distinct ν_{CO} bands for the Ni-R state at 1922 and 1914 cm⁻¹. According to theoretical studies on models of the active site of NiFe hydrogenases; these wavenumber positions are in agreement with an active site that has a Ni(II) with a bound hydride in the bridging position, and one of the sulfurs of a terminal cysteine protonated.⁶³

Figure 4.28 shows that these two Ni-R species are isopotential.

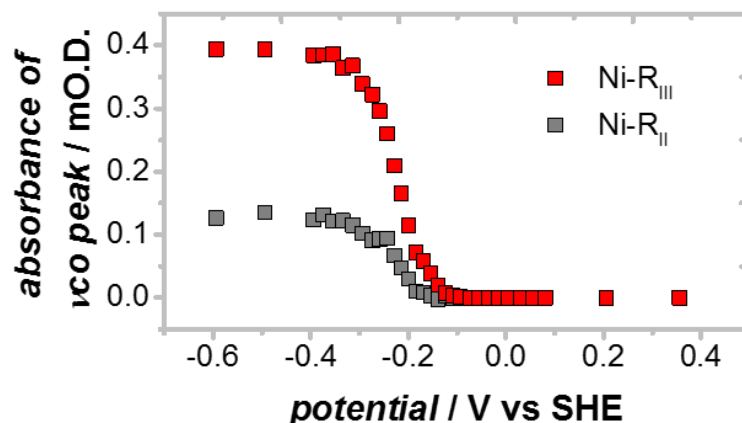


Figure 4.28 The potential distribution of the Ni-R states at pH 6.0. These two states are isopotential, and the ratio of their intensities remains constant, independent of the applied potential.

It can be observed in Figure 4.28, not only that these two species behave the same with potential (appearing in the same potential window), but that the ratio of Ni-R_{III} to Ni-R_{II} remains constant as the potential changes. This confirms that these two bands correspond to the same redox level, Ni-R. There is, nonetheless, a clear dependence on pH of the relative intensities of these two bands as shown by Figure 4.29.

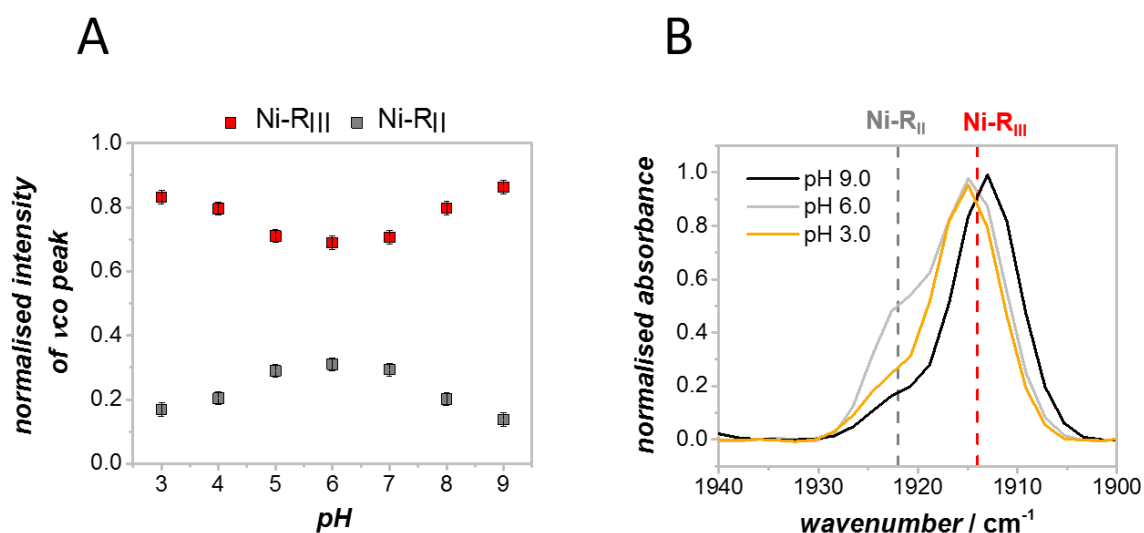


Figure 4.29 A) The relative intensities of Ni-R_{II} and Ni-R_{III} as a function of pH. The intensities have been normalised to the total intensity of the Ni-R species.

Although this behaviour does not seem to be consistent with that expected from a classic Henderson-Hasselbalch acid-base equilibrium, the effect of pH in the ratio of these species is clearly evident, as demonstrated by Figure 4.29. From pH 3.0 to pH 6.0 there is a decrease in Ni-R_{III}, and a corresponding increase in Ni-R_{II}. Such behaviour would suggest that Ni-R_{II} is favoured as the pH increases, but the trend reverses from pH 6.0 to pH 9.0. This kind of behaviour with pH is unusual but not unheard of. Theoretical studies of possible protonation pathways on *D. gigas* NiFe hydrogenase, reported atypically shaped pH titration curves for specific amino acids (proposed to be involve in proton transportation to and from the active site). This unexpected behaviour was attributed to strong electrostatic interactions in this protein, some residues showed strongly correlated protonations, which indicate the sharing of protons between them.⁵⁴ It is possible that the active site itself may participate in such equilibria, and that this might contribute to the explanation for the behaviour observed in Figure 4.29A.

In Figure Figure 4.29B, it can be noted that the wavenumber position of the Ni-R_{III} band at pH 9.0 differs clearly from that of its corresponding lower pH counterparts. This effect of pH on the position of the bands, will be the matter of discussion next.

4.5 The effect of pH. Part 3: the shift in wavenumber positions of the active site bands

Table 4.7 shows how the wavenumber positions of the ν_{CO} bands change with pH. These wavenumber positions were determined from the fitted titrations shown in Section 4.3. This table shows that the pH has, indeed, an effect on the position of the active site bands. All of the redox states exhibit this behaviour, although not to the same extent. The effect is the largest for Ni-C; for which the difference between the wavenumber positions of the two extremes, shown in this table,

is of 6 cm^{-1} . On the other hand, Ni-R_{II} shows only a two wavenumber difference over the same pH range.

Table 4.7. Wavenumber positions of the ν_{CO} bands of the active site of *E. coli* Hyd-1. The values are rounded to the nearest integer, from the fitted parameter.

<i>pH</i>	<i>position of ν_{CO} band centre / cm^{-1}</i>						
	Ni-B	Ni-SI	Ni-C	Ni-L _I	Ni-L _{III}	Ni-R _{II}	Ni-R _{III}
8.0	1941	1928	1947	1865	1875	1921	1913
6.0	1943	1929	1952	1868	1877	1922	1915
4.0	1943	1930	1953	1869	1878	1922	1915

There have been studies like these reported for other hydrogenases,^{1,2} in which potential controlled spectra were recorded at different pH values. However; the only change such as those presented in Table 4.7, this is a change of wavenumber position of bands with pH, was only reported for the Ni-C state, which exhibited a difference of 3 cm^{-1} (of its ν_{CO} band position) between pH 6 and pH 9.²

A high electron density in the metal weakens the bond C—O bond. This results in the appearance of the ν_{CO} bands at lower wavenumber, the more electron-rich the metal centre is (See Section 2.2.3 for a more detailed explanation of the backbonding effect). From such explanation, it can therefore be observed that raising the pH has an effect similar to that of increasing the electron density at the active site; namely, shifting the ν_{CO} bands to lower wavenumber.

The pH has a direct effect on the protonation state of acid-base active groups within the protein structure. The protonation states of acid-base groups in the vicinity of the active site, may have an effect on the wavenumber positions of the ν_{CO} and ν_{CN} bands if these groups are interacting at close distances (hydrogen bonding, Van der Waals) with the active site. Such groups should be close to the active site, so that their protonation state would have an effect on it, but not too close so

that the changes in wavenumber are big (like what it is being suggested as an explanation for the nature of the two Ni-R or the two Ni-L states).

There are amino acids which are at hydrogen-bond, and Van der Waals, distances from the CO and CN⁻ ligands of the active site.^{3,4} De Lacey et al. provide evidence that changing the acid-base properties of these amino acids (by site-directed mutagenesis) results in changes in the wavenumber position of these bands. Moreover, the magnitudes of the changes they observe (up to 4 cm⁻¹) are similar to the ones reported in this work (Table 4.7), and the shifts occurred in both directions (to higher and to lower wavenumber relative to the position of the bands for the wild-type enzyme) depending on the mutations.⁶⁴ The work by De Lacey et al shows that it is plausible, for these shifts in wavenumber positions of the IR bands, to occur as a result of a change in the acid-base properties of amino acids in the vicinity of the active site. In addition to that, Greene et al. reported a 5 cm⁻¹ shift in Ni_a-I ν_{CO} band with pH. They suggest that an isomerisation of a protonated terminal cysteine could account for such a shift.^{65,66} For cases where the shifts are smaller (<2 cm⁻¹), like the one they report for Ni-C, the change in protonation state may be rather from a residue interacting more weakly with the active site.⁶⁵

The testing of the aforementioned hypothesis, or suggestion of alternative explanations for this phenomenon, is beyond the scope of this thesis. The objective of this section is to report the observed trend, as it hasn't been reported as extensively for similar experiments on other hydrogenases (until very recently by Greene et al.)⁶⁵, and provide a plausible explanation for such observation.

4.6 Summary

The results in this chapter provide an overview of the redox states that are detected by means of infrared spectroelectrochemistry for *E. coli* Hyd-1. This represents the first full redox

characterisation of a hydrogenase immobilised in direct electronic contact on a carbon electrode.

Figure 4.30 summarises these redox processes, and Table 4.8 reports the wavenumber positions of the assigned bands.

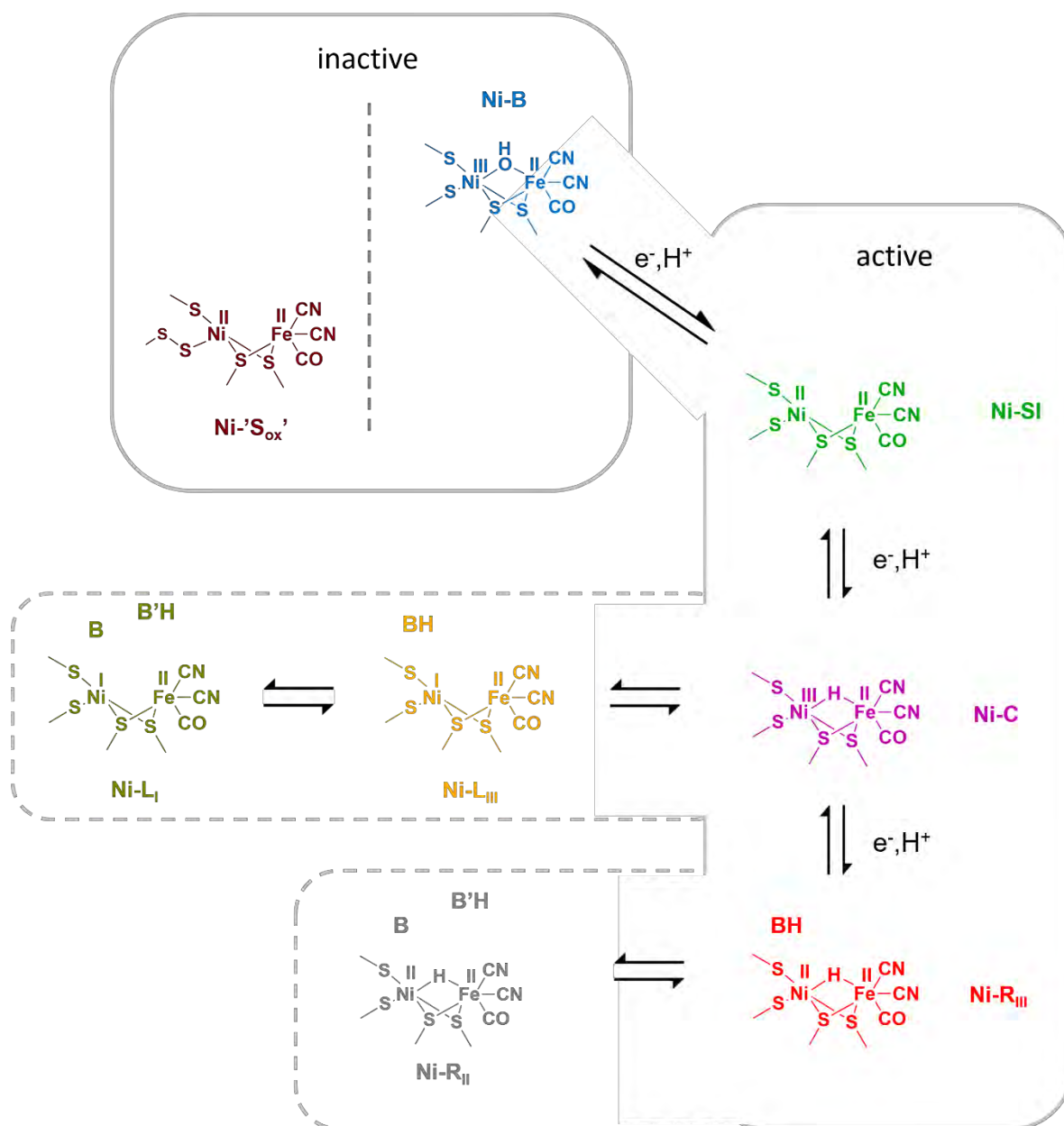


Figure 4.30 The redox states of Hyd-1 immobilised at a carbon electrode. Only one oxidised inactive state is detected and it is proposed to be Ni-B. Ni-S'ox' is another inactive state that appears in some aerobic as-isolated preparations. The three active states Ni-SI, Ni-C and Ni-R have also been identified and it is also suggested that Ni-L may be an active intermediate. B and B' represent generic proton acceptors, with B' being further from the active site than B.

All the states described in Figure 4.30 and Table 4.8 can be electrochemically interconverted reversibly. The only exception to this was Ni-'S_{ox}' which only appears in some as-isolated samples and can be reduced with the application of low potential or exposure to H₂; and once the enzyme has been reduced, this state does not come back again. The Ni-L state was observed, for the first time, at room temperature and in the dark. Its formation and disappearance were also fully reversible and appeared in the same potential window as Ni-C.

Table 4.8. Wavenumber positions of the ν_{CO} and ν_{CN} bands for all the states identified of the active site of *E. coli* Hyd-1.

Unless specified, the values are given for pH 6.0.

<i>redox state</i>	<i>wavenumber / cm⁻¹</i>	
	ν_{CO}	ν_{CN}
Ni-B	1943	2100, 2093, 2081
Ni-'S_{ox}'	1910	2069, 2060
Ni-SI	1929	2085, 2077
Ni-C	1952	2089, 2079 *
Ni-L_I	1868	2028
Ni-L_{III}	1877	2051, 2034
Ni-R_{II}	1922	n.d.
Ni-R_{III}	1915	2066, 2049

*measured at pH 4.0

As seen in many of the spectra in this chapter, the intensity of the ν_{CN} bands is much less than that of the ν_{CO} band. In addition to this, there are two ν_{CN} bands for each state. These shift less than the ν_{CO} band, and the direction and magnitude of these shifts (upon changes in the active site) are not as clear nor as straightforward as the shifts for ν_{CO} band (see Table 4.8), as explained in Section 2.2.3. It is for this reason that the majority of the discussion in this thesis, regarding the IR spectra,

will be based on the ν_{CO} band. The ν_{CN} bands will be used to check the assignments, as established by Table 4.8, for the redox states of the active site of *E. coli* Hyd-1.

The reduction potentials for all the redox reactions were determined, and from their pH dependence, it was confirmed that all these redox processes are indeed proton-coupled electron transfers. Also, based on the changes of these reduction potentials with pH, a range of “apparent” pK_a values for the proton acceptor(s) was suggested. The redox reaction $\text{Ni-B} \leftrightarrow \text{Ni-SI}$ was also demonstrated to be slower than the other redox processes, which is in accordance with electrochemical experiments.⁶⁷ Moreover, a pH dependence on this behaviour was shown; it was demonstrated that the higher the pH, the slower this specific redox step becomes. This is also in agreement with electrochemical literature.^{47,68}

A full redox characterisation as a function of pH was also presented. From these results the relation between Ni-C and Ni-L was investigated further. It was shown that Ni-C and Ni-L are at the same redox level and that they differ in their protonation, and are in an acid-base equilibrium. The ratio of these two states was demonstrated to be pH dependent; and within the pH window investigated (pH 3.0 – 9.0), almost full conversion from one state to another was achieved. This process was also fully reversible.

Evidence of similar pH dependent equilibria was also provided for the multiple Ni-L and multiple Ni-R species. Although not as clear as the pH dependence of the $\text{Ni-C} \leftrightarrow \text{Ni-L}$ couple, these states showed clear changes in their ratio as a function of pH. Finally, the dependence of the wavenumber positions of the bands as a function of pH was presented and a rationale for this behaviour was suggested, based on similar observations and previous studies for other NiFe hydrogenases.

Overall, a broad and extensive picture of the redox chemistry of the active site of Hyd-1 adsorbed on a carbon electrode has been presented in this chapter. This picture shall function as a foundation for deeper mechanistic investigations that shall be carried in subsequent chapters. It

was suggested already in this chapter, the role that Ni-L may have in the catalytic mechanism of the enzyme, as well as the interesting changes observed when the pH is varied.

Chapter 5 will study the redox states of Hyd-1 under turn over conditions, for both H₂ oxidation and H⁺ reduction. This shall provide new insights into the chemistry of the active site, and the relevance of these proton-coupled electron transfer processes and acid-base equilibria herein described, for the catalytic reactions of this enzyme.

References

- 1 C. Fichtner, C. Laurich, E. Bothe and W. Lubitz, *Biochemistry*, 2006, **45**, 9706–9716.
- 2 B. Bleijlevens, F. A. van Broekhuizen, A. L. De Lacey, W. Roseboom, V. M. Fernandez and S. P. J. Albracht, *J. Biol. Inorg. Chem.*, 2004, **9**, 743–752.
- 3 A. L. de Lacey, E. C. Hatchikian, A. Volbeda, M. Frey, J. C. Fontecilla-Camps and V. M. Fernandez, *J. Am. Chem. Soc.*, 1997, **119**, 7181–7189.
- 4 A. Volbeda, E. Garcin, C. Piras, A. L. De Lacey, V. M. Fernandez, E. C. Hatchikian, M. Frey and J. C. Fontecilla-Camps, *J. Am. Chem. Soc.*, 1996, **118**, 12989–12996.
- 5 A. L. DeLacey, C. Stadler, V. M. Fernandez, E. C. Hatchikian, H. J. Fan, S. Li and M. B. Hall, *J. Biol. Inorg. Chem.*, 2002, **7**, 318–326.
- 6 M.-E. Pandelia, V. Fourmond, P. Tron-Infossi, E. Lojou, P. Bertrand, C. Léger, M.-T. Giudici-Orticoni and W. Lubitz, *J. Am. Chem. Soc.*, 2010, **132**, 6991–7004.
- 7 M.-E. Pandelia, P. Infossi, M. Stein, M.-T. Giudici-Orticoni and W. Lubitz, *Chem. Commun.*, 2012, **48**, 823–825.
- 8 M.-E. Pandelia, P. Infossi, M. T. Giudici-Orticoni and W. Lubitz, *Biochemistry*, 2010, **49**, 8873–81.
- 9 M. Saggiu, I. Zebger, M. Ludwig, O. Lenz, B. Friedrich, P. Hildebrandt and F. Lenzian, *J. Biol. Chem.*, 2009, **284**, 16264–16276.

- 10 F. Germer, I. Zebger, M. Saggi, F. Lenzian, R. Schulz and J. Appel, *J. Biol. Chem.*, 2009, **284**, 36462–36472.
- 11 A. J. Pierik, W. Roseboom, R. P. Happe, K. A. Bagley and S. P. J. Albracht, *J. Biol. Chem.*, 1999, **274**, 3331–3337.
- 12 A. J. Pierik, M. Schmelz, O. Lenz, B. Friedrich and S. P. Albracht, *FEBS Lett.*, 1998, **438**, 231–235.
- 13 M. Horch, L. Lauterbach, M. Saggi, P. Hildebrandt, F. Lenzian, R. Bittl, O. Lenz and I. Zebger, *Angew. Chem. Int. Ed.*, 2010, **49**, 8026–8029.
- 14 L. Lauterbach, J. Liu, M. Horch, P. Hummel, A. Schwarze, M. Haumann, K. A. Vincent, O. Lenz and I. Zebger, *Eur. J. Inorg. Chem.*, 2011, **2011**, 1067–1079.
- 15 W. Lubitz, H. Ogata, O. Ruediger and E. Reijerse, *Chem. Rev.*, 2014, **114**, 4081–4148.
- 16 M.-E. Pandelia, H. Ogata and W. Lubitz, *Chemphyschem*, 2010, **11**, 1127–40.
- 17 S. Foerster, M. Stein, M. Brecht, H. Ogata, Y. Higuchi and W. Lubitz, *J. Am. Chem. Soc.*, 2003, **125**, 83–93.
- 18 M. van Gastel, C. Fichtner, F. Neese and W. Lubitz, *Biochem. Soc. Trans.*, 2005, **33**, 7–11.
- 19 M. Saggi, C. Teutloff, M. Ludwig, M. Brecht, M.-E. Pandelia, O. Lenz, B. Friedrich, W. Lubitz, P. Hildebrandt, F. Lenzian and R. Bittl, *Phys. Chem. Chem. Phys.*, 2010, **12**, 2139–48.
- 20 M. M. Roessler, R. M. Evans, R. A. Davies, J. Harmer and F. A. Armstrong, *J. Am. Chem. Soc.*, 2012, **134**, 15581–94.
- 21 M.-E. Pandelia, P. Infossi, M. Stein, M.-T. Giudici-Ortoni and W. Lubitz, *Chem. Commun.*, 2012, **48**, 823–5.
- 22 S. Kurkin, S. J. George, R. N. F. Thorneley and S. P. J. Albracht, *Biochemistry*, 2004, **43**, 6820–31.
- 23 V. M. Fernandez, E. C. Hatchikian and R. Cammack, *Biochim. Biophys. Acta*, 1985, **832**, 69–79.
- 24 H. Ogata, S. Hirota, A. Nakahara, H. Komori, N. Shibata, T. Kato, K. Kano and Y. Higuchi,

- Structure*, 2005, **13**, 1635–1642.
- 25 A. Volbeda, L. Martin, C. Cavazza, M. Matho, B. W. Faber, W. Roseboom, S. P. J. Albracht, E. Garcin, M. Rousset and J. C. Fontecilla-Camps, *J. Biol. Inorg. Chem.*, 2005, **10**, 239–249.
- 26 M. van Gastel, M. Stein, M. Brecht, O. Schröder, F. Lenzian, R. Bittl, H. Ogata, Y. Higuchi and W. Lubitz, *J. Biol. Inorg. Chem.*, 2006, **11**, 41–51.
- 27 H. Ogata, P. Kellers and W. Lubitz, *J. Mol. Biol.*, 2010, **402**, 428–444.
- 28 A. Volbeda, L. Martin, E. Barbier, O. Gutiérrez-Sanz, A. L. De Lacey, P.-P. Liebgott, S. Dementin, M. Rousset and J. C. Fontecilla-Camps, *J. Biol. Inorg. Chem.*, 2015, **20**, 11–22.
- 29 J. L. Barilone, H. Ogata, W. Lubitz and M. van Gastel, *Phys. Chem. Chem. Phys.*, 2015, **17**, 16204–16212.
- 30 K. G. V Sigfridsson, N. Leidel, O. Sanganas, P. Chernev, O. Lenz, K.-S. Yoon, H. Nishihara, A. Parkin, F. a Armstrong, S. Dementin, M. Rousset, A. L. De Lacey and M. Haumann, *Biochim. Biophys. Acta*, 2015, **1847**, 162–70.
- 31 A. Abou Hamdan, B. Burlat, O. Gutiérrez-Sanz, P.-P. Liebgott, C. Baffert, A. L. De Lacey, M. Rousset, B. Guigliarelli, C. Léger and S. Dementin, *Nat. Chem. Biol.*, 2013, **9**, 15–18.
- 32 M. Brecht, M. van Gastel, T. Buhrke, B. Friedrich and W. Lubitz, *J. Am. Chem. Soc.*, 2003, **125**, 13075–83.
- 33 H. Ogata, K. Nishikawa and W. Lubitz, *Nature*, 2015, **520**, 571–574.
- 34 H. Tai, K. Nishikawa, S. Inoue, Y. Higuchi and S. Hirota, *J. Phys. Chem. B*, 2015, **119**, 13668–13674.
- 35 P. Kellers, M.-E. Pandelia, L. J. Currell, H. Görner and W. Lubitz, *Phys. Chem. Chem. Phys.*, 2009, **11**, 8680–8683.
- 36 J. W. van der Zwaan, S. P. J. Albracht, R. D. Fontijn and E. C. Slater, *FEBS Lett.*, 1985, **179**, 271–277.
- 37 M. Kampa, M.-E. Pandelia, W. Lubitz, M. van Gastel and F. Neese, *J. Am. Chem. Soc.*, 2013, **135**, 3915–25.

- 38 D. Moss, E. Nabedryk, J. Breton and W. Mäntele, *Eur. J. Biochem.*, 1990, **187**, 565–572.
- 39 K. A. Bagley, E. C. Duin, W. Roseboom, S. P. J. Albracht and W. H. Woodruff, *Biochemistry*, 1995, **34**, 5527–5535.
- 40 D. Millo, P. Hildebrandt, M.-E. Pandelia, W. Lubitz and I. Zebger, *Angew. Chem. Int. Ed.*, 2011, **50**, 2632–4.
- 41 D. Millo, M.-E. Pandelia, T. Utesch, N. Wisitruangsakul, M. A. Mroginski, W. Lubitz, P. Hildebrandt and I. Zebger, *J. Phys. Chem. B*, 2009, **113**, 15344–51.
- 42 L. Xu and F. A. Armstrong, *Energy Environ. Sci.*, 2013, **6**, 2166–2171.
- 43 H. A. Reeve, L. Lauterbach, P. A. Ash, O. Lenz and K. A. Vincent, *Chem. Commun.*, 2012, **48**, 1589–1591.
- 44 B. J. Murphy, F. Sargent and F. A. Armstrong, *Energy Environ. Sci.*, 2014, **7**, 1426.
- 45 A. J. Healy, University of Oxford, 2013.
- 46 M. J. Lukey, M. M. Roessler, A. Parkin, R. M. Evans, R. A. Davies, O. Lenz, B. Friedrich, F. Sargent and F. A. Armstrong, *J. Am. Chem. Soc.*, 2011, **133**, 16881–16892.
- 47 A. K. Jones, S. E. Lamle, H. R. Pershad, K. A. Vincent, S. P. J. Albracht and F. A. Armstrong, *J. Am. Chem. Soc.*, 2003, **125**, 8505–14.
- 48 J. C. Fontecilla-Camps, A. Volbeda, C. Cavazza and Y. Nicolet, *Chem. Rev.*, 2007, **107**, 4273–303.
- 49 J. Fritsch, P. Scheerer, S. Frielingsdorf, S. Kroschinsky, B. Friedrich, O. Lenz and C. M. T. Spahn, *Nature*, 2011, **479**, 249–252.
- 50 Y. Shomura, K.-S. Yoon, H. Nishihara and Y. Higuchi, *Nature*, 2011, **479**, 253–6.
- 51 A. Volbeda, P. Amara, C. Darnault, J.-M. Mouesca, A. Parkin, M. M. Roessler, F. A. Armstrong and J. C. Fontecilla-Camps, *Proc. Natl. Acad. Sci.*, 2012, **109**, 5305–10.
- 52 E. Szőri-Dorogházi, G. Maróti, M. Szőri, A. Nyilasi, G. Rákhely and K. L. Kovács, *PLoS One*, 2012, **7**, e34666.
- 53 I. Sumner and G. A. Voth, *J. Phys. Chem. B*, 2012, **116**, 2917–26.

- 54 V. H. Teixeira, C. M. Soares and A. M. Baptista, *Proteins*, 2008, **70**, 1010–1022.
- 55 E. Siebert, M. Horch, Y. Rippers, J. Fritsch, S. Frielingsdorf, O. Lenz, F. Velazquezescobar, F. Siebert, L. Paasche, U. Kuhlmann, F. Lenzian, M. A. Mroginski, I. Zebger and P. Hildebrandt, *Angew. Chem. Int. Ed.*, 2013, **52**, 5162–5165.
- 56 M. Horch, J. Schoknecht, M. A. Mroginski, O. Lenz, P. Hildebrandt and I. Zebger, *J. Am. Chem. Soc.*, 2014, **600**, 1–4.
- 57 H. Tai, K. Nishikawa, M. Suzuki, Y. Higuchi and S. Hirota, *Angew. Chem. Int. Ed.*, 2014, **53**, 13817–13820.
- 58 T. Goris, A. F. Wait, M. Saggi, J. Fritsch, N. Heidary, M. Stein, I. Zebger, F. Lenzian, F. A. Armstrong, B. Friedrich and O. Lenz, *Nat. Chem. Biol.*, 2011, **7**, 310–8.
- 59 S. Frielingsdorf, J. Fritsch, A. Schmidt, M. Hammer, J. Löwenstein, E. Siebert, V. Pelmeshnikov, T. Jaenicke, J. Kalms, Y. Rippers, F. Lenzian, I. Zebger, C. Teutloff, M. Kaupp, R. Bittl, P. Hildebrandt, B. Friedrich, O. Lenz and P. Scheerer, *Nat. Chem. Biol.*, 2014, **10**, 378–85.
- 60 P. Wulff, C. C. Day, F. Sargent and F. A. Armstrong, *Proc. Natl. Acad. Sci. U. S. A.*, 2014, **111**, 6606–11.
- 61 R. M. Evans, A. Parkin, M. M. Roessler, B. J. Murphy, H. Adamson, M. J. Lukey, F. Sargent, A. Volbeda, J. C. Fontecilla-Camps and F. A. Armstrong, *J. Am. Chem. Soc.*, 2013, **135**, 2694–2707.
- 62 A. L. De Lacey, A. Pardo, V. M. Fernández, S. Dementin, G. Adryanczyk-Perrier, E. C. Hatchikian and M. Rousset, *J. Biol. Inorg. Chem.*, 2004, **9**, 636–642.
- 63 T. Krämer, M. Kampa, W. Lubitz, M. van Gastel and F. Neese, *ChemBioChem*, 2013, **14**, 1898–1905.
- 64 A. L. DeLacey, V. M. Fernandez, M. Rousset, C. Cavazza and E. C. Hatchikian, *J. Biol. Inorg. Chem.*, 2003, **8**, 129–134.
- 65 B. L. Greene, C.-H. Wu, G. E. Vansuch, M. W. W. Adams and R. B. Dyer, *Biochemistry*, 2016,

55, 1813–1825.

66 A. Pardo, A. L. De Lacey, V. M. Fernández, H.-J. Fan, Y. Fan and M. B. Hall, *J. Biol. Inorg. Chem.*, 2006, **11**, 286–306.

67 K. A. Vincent, A. Parkin and F. A. Armstrong, *Chem. Rev.*, 2007, **107**, 4366–413.

68 V. Fourmond, P. Infossi, M. T. Giudici-Ortoni, P. Bertrand and C. Léger, *J. Am. Chem. Soc.*, 2010, **132**, 4848–4857.

Chapter 5

Mechanistic investigations of H₂ oxidation and H⁺ reduction by Hyd-1: IR electrochemistry under turnover conditions

5.1 Introduction

5.1.1 Mechanism and the active site of NiFe hydrogenases

It has been widely proposed in the literature that the H_2 oxidation catalytic mechanism, by NiFe hydrogenases, involves the states Ni-SI, Ni-C, and Ni-R, as shown in Figure 5.1.

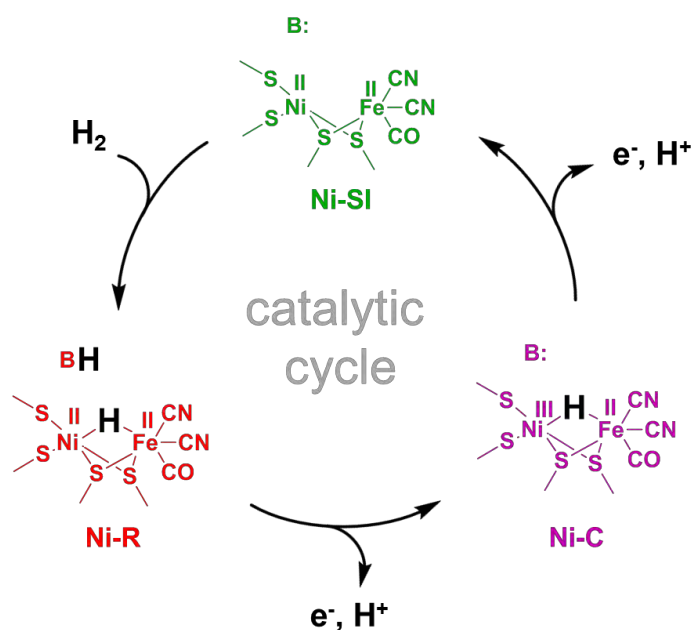


Figure 5.1 The catalytic mechanism of H_2 oxidation by NiFe hydrogenases, as widely proposed. The Ni-SI state is attacked by H_2 , which is heterolytically split at the active site to give the Ni-R state. Two subsequent concerted proton coupled electron transfers give back the Ni-SI state, with Ni-C as an intermediate after the first PCET.

In this catalytic cycle, H_2 attacks the Ni-SI state initially. The H_2 molecule is heterolytically¹ split at the active site to give the Ni-R state. A one-proton one-electron oxidation gives the Ni-C state, and a further one completes the cycle and produces the Ni-SI state which can start another cycle. Such a mechanism has been proposed on the basis of redox states of the active site which have been detected spectroscopically.^{2,3}

However, work from theorists has pointed to a more complex mechanism which involves different protonation and electron transfer steps taking place within the bimetallic active site and surrounding

protein. As early as in 1999, Hall and co-workers proposed a mechanism of H₂ oxidation which included individual proton transfer steps, as well as the presence of a Ni(I) intermediate (Figure 5.2).⁴

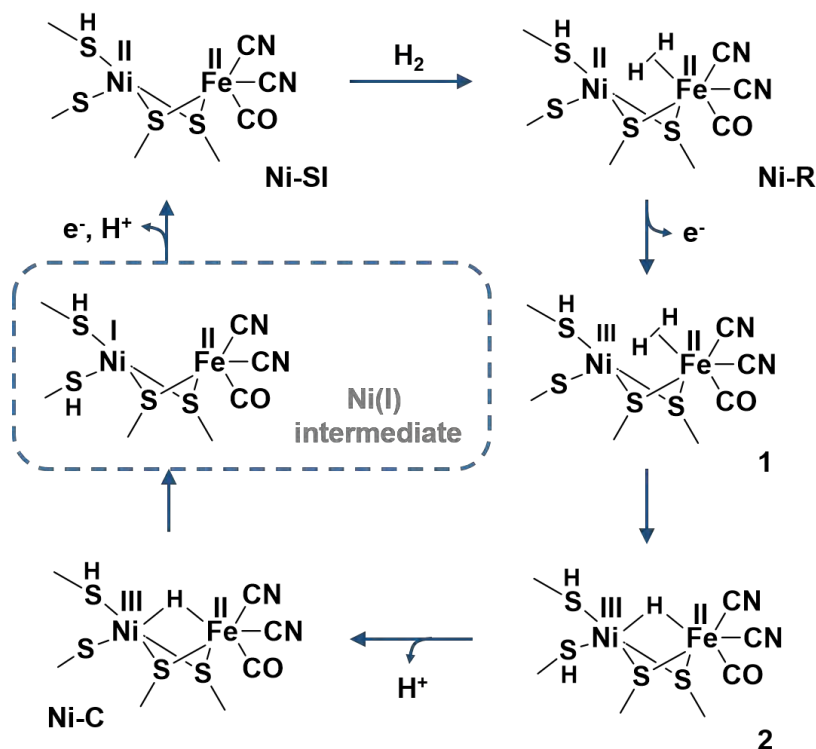


Figure 5.2 Mechanism of H₂ oxidation by a NiFe hydrogenase based on a DFT computational study. It includes multiple species at the redox level of Ni-C; and also a Ni(I) species as an intermediate between Ni-C and Ni-SI. Adapted with permission from Niu, S.; Thomson, L. M.; Hall, M. B. *J. Am. Chem. Soc.* 1999, **121** (4), 4000–4007. Copyright 1999 American Chemical Society.

This mechanism was proposed on the basis of computational DFT calculations on models of the active site of NiFe hydrogenases. It can be seen that there are several species at the Ni-C redox level (structures 1 and 2 in Figure 5.2). In addition to this, the transition from Ni-C to Ni-SI involves a Ni(I) intermediate. Other theoretical studies have suggested mechanisms which also involve Ni(I) intermediates. These mechanisms include either the migration of the proton, within the active site, before the concerted proton-coupled electron transfer takes place; or individual stepwise proton and electron transfer steps.^{5–7} In any case, the proposed mechanisms from theoretical studies suggest a more complex picture of the catalytic cycle than the ubiquitous scheme represented in Figure 5.1.

More recently, along with the development of the work presented in this thesis, experimentalists have begun to contribute directly to the discussion of the mechanism of NiFe hydrogenases by designing experiments that provide information on the intermediates involved in redox transformations of the active site. EPR experiments at cryogenic temperatures on *Desulfovibrio vulgaris* MF NiFe hydrogenase, showed that the transition between the Ni-C and Ni-SI state is controlled by the redox state of the proximal Fe-S cluster. Ni-L was shown to be a viable intermediate between these two states within the catalytic cycle.⁸ In addition to that, time-resolved IR spectroscopy experiments on a NiFe hydrogenase from *Pyrococcus furiosus* have presented intermediates of stepwise proton transfer and electron transfer steps, detected at sub-TOF timescales.^{9,10} Figure 5.3A shows the catalytic cycle of NiFe hydrogenases, as proposed by these authors. It includes alternative routes of stepwise PT and ET steps.

Furthermore, the study of synthetic models of NiFe hydrogenases, has also led to the proposition of a mechanism which includes a Ni(I) as an intermediate in the catalytic mechanism.^{11,12} Chambers et al propose a H⁺ oxidation mechanism by a synthetic complex; which includes this redox state, as well as stepwise proton and electron transfer steps (Figure 5.3B).

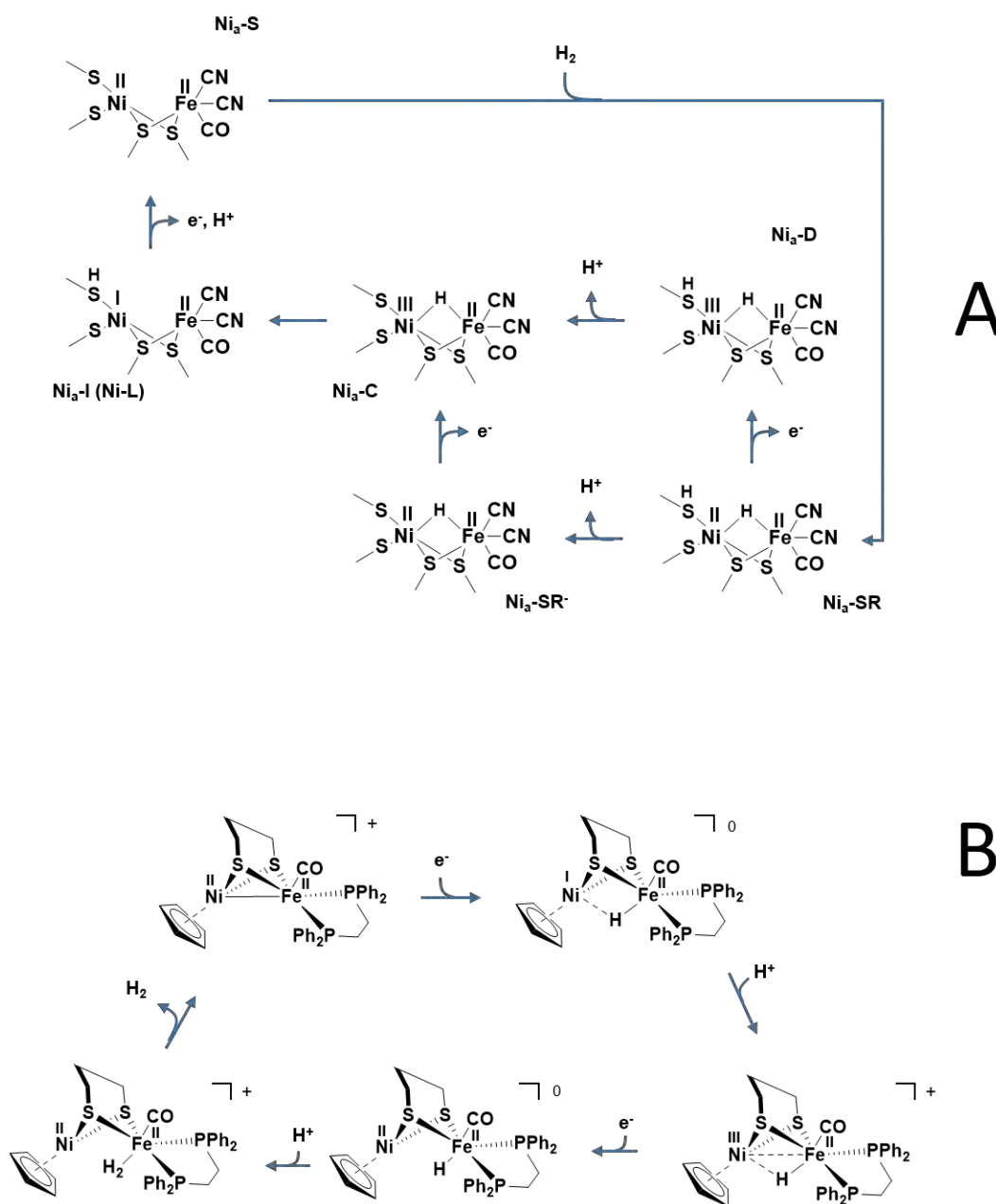


Figure 5.3 Recent experiments on NiFe hydrogenases, and NiFe hydrogenase models, have led to the proposal of more complex mechanisms: A) Time resolved IR spectroscopy by Greene et al. has allowed for the detection of new intermediates (Ni_a-I to be specific). The proposed catalytic cycle involves stepwise PT and ET. Adapted with permission from Greene, B. L.; Wu, C.-H.; Vansuch, G. E.; Adams, M. W. W.; Dyer, R. B. *Biochemistry* 2016, 55, 1813–1825. Copyright 2016 American Chemical Society. B) The H⁺ reduction mechanism for a synthetic model of the active site of NiFe hydrogenases. Adapted with permission from Chambers, G. M.; Huynh, M. T.; Li, Y.; Hammes-Schiffer, S.; Rauchfuss, T. B.; Reijerse, E.; Lubitz, W. *Inorg. Chem.* 2016, 55, 419–431. Copyright 2016 American Chemical Society.

5.1.2 Bringing PFIRE to the discussion of catalytic mechanisms of NiFe hydrogenases

The combination of IR spectroscopy and protein film electrochemistry *in situ* should provide new insights to the understanding of the mechanism of hydrogenase enzymes. This is what this chapter is about. By bringing together information about activity with structural information simultaneously, the technique described in this thesis will be applied to the study of the catalytic mechanism of *E. coli* Hyd-1. This enzyme will be studied under both H₂ oxidation and H⁺ reduction conditions. The detection of different redox states of the active site under steady state conditions will give direct information about the role of these states in the catalytic cycle. The effect of pH, H₂, and potential, on the distribution of the different redox states of the active site under turnover will further provide a better qualitative picture of the kinetics of the mechanism of NiFe hydrogenases. This will be done by analysing the effect of changing these variables (pH, H₂ concentration and potential) on the steady state concentrations of specific redox states. The results presented in this chapter support a complex mechanism that suggests individual proton transfer steps (within the active site) before electron transfer steps take place, as well as the role of Ni-L as an intermediate in the catalytic cycle of NiFe hydrogenases.

5.2 H₂ oxidation: PFIRE

5.2.1 Mechanistic investigations of H₂ oxidation by Hyd-1

The experimental set-up used for the experiments in this chapter is explained in Chapter 3 (Figures 3.9, 3.10, and 3.11). The assignment of the infrared bands to specific active site redox states is extensively discussed in Chapter 4.

Electrochemistry of H₂ oxidation by Hyd-1

Figure 5.4 shows the electrocatalytic H₂ oxidation, at pH 6.0, by Hyd-1 adsorbed on a carbon nanoparticle electrode in the ATR spectroelectrochemical cell. The potential at this electrode was poised at four different values. The current was then measured under a H₂ atmosphere, and under an inert (Ar) atmosphere.

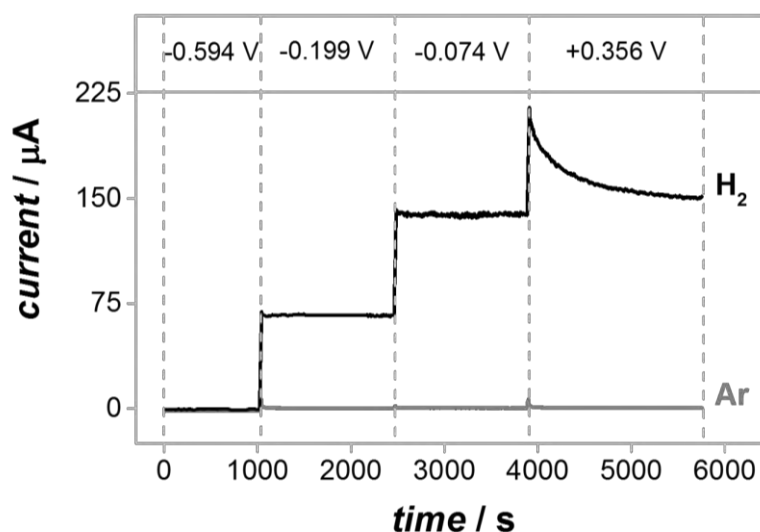


Figure 5.4 Current-time trace of Hyd-1 adsorbed on a carbon nanoparticle electrode inside the ATR spectroelectrochemical cell. The solution was saturated with H₂ (black) or Ar (grey). The buffered solution (pH 6.0) was flowed through the cell at 62 mL min⁻¹.

At -0.594 V, there is no detectable current under either the H₂ or the Ar atmospheres. At this potential, Hyd-1 is not able to oxidise H₂ (see Figure 3.12 A).¹³ There is also no H⁺ reduction detected under Ar, which is consistent with Hyd-1 being a poor H⁺ reduction catalyst at this pH.¹⁴ Moreover, there is no measured electrocatalytic current under Ar at any of the other more positive applied potential steps, as expected.

As the potential is stepped up to -0.199 V, a positive current arises under H₂, due to electrocatalytic H₂ oxidation. The driving force for this process increases with potential, and thus the measured electrocatalytic current increases when the potential is further stepped up to -0.074 V. At these two potential values (-0.199 and -0.074 V), the current is constant. This is indicative of two things

regarding the technique: *i*) that the high flow rate (62 mL min^{-1}) of H_2 -saturated buffer solution through the cell provides efficient mass transport of substrate to the enzyme adsorbed on the surface of the particles; and *ii*), that the enzyme film itself is very stable as it sustains a constant activity over long periods of time.

At the highest potential, $+0.356 \text{ V}$, there is an increase in current followed by an exponential decrease, which stabilises after *ca* 1500 s . This behaviour is consistent with the well-established high potential inactivation at high potentials (Ni-B formation).^{13,15} Inactivation will be a main topic of discussion in Chapter 6.

Infrared spectroscopy under turnover conditions

Infrared spectra were collected at each potential step of the experiment described above, for both under H_2 and Ar atmospheres. The IR spectra under Ar presented in this chapter is equivalent to those presented in Chapter 4. Herein, these spectra are presented slightly differently to show only the ν_{CO} region, and to function as a comparison to the spectra that are recorded under H_2 (where catalysis can take place). Figure 5.5 shows these results for the first potential step, -0.594 V .

In Figure 5.5 A, there is no detectable catalytic current at this potential (-0.594 V) under either H_2 or Ar, as discussed above. The spectra do not show significant differences between them either. Ni-R is the most abundant species for both conditions, and Ni-C and Ni-L are present in smaller quantities at the same ratio. It is interesting to note that, neither under Ar or H_2 , was it possible to completely convert the enzyme sample to the Ni-R state. As was discussed in Section 4.2.2, there is a potential below which the concentration of Ni-R does not increase any further. It can be seen that this is also the case in the presence of H_2 , as can be seen in the corresponding spectrum in Figure 5.5B.

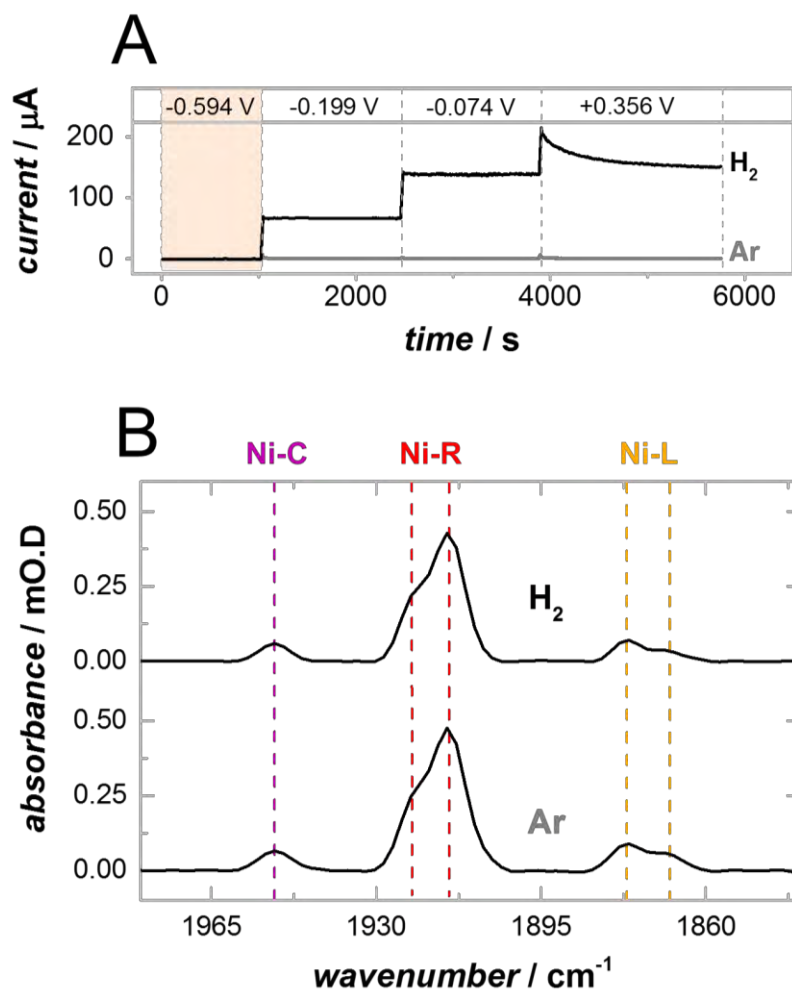


Figure 5.5 IR spectroelectrochemistry of Hyd-1 adsorbed on a carbon electrode. A) Current-time trace. The shaded area shows the region where the IR spectra were collected. B) IR spectra displaying the ν_{CO} region under H_2 and Ar recorded at -0.594 V.

The second potential step, however, does show a difference in the spectral features, as it does in the measured electrochemical current (Figure 5.6). This potential, -0.199 V, corresponds to the potential value at which Ni-C and Ni-L exhibit their highest intensity (under an inert atmosphere), as was determined from the titrations studied in Chapter 4 (See Figure 4.9). The spectrum under H_2 , however, shows a quite different distribution of redox states. Ni-R is still the main feature (as it was in the previous potential step), with a small increase in the concentrations of both Ni-C and Ni-L. However, no Ni-SI is detected.

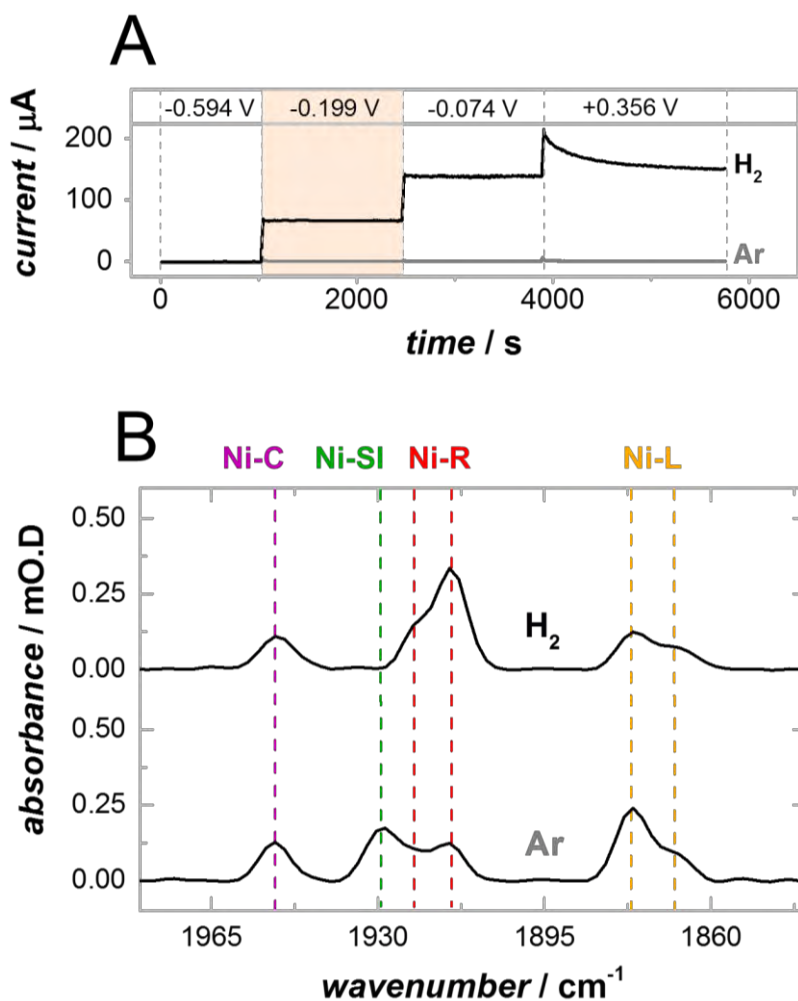


Figure 5.6 IR spectroelectrochemistry of Hyd-1 adsorbed on a carbon electrode. A) Current-time trace. The shaded area shows the region where the IR spectra were collected. B) IR spectra displaying the ν_{CO} region under H_2 and Ar recorded at -0.199 V.

The differences between the spectrum under Ar and the spectrum under H_2 will be explained by reference to a catalytic cycle which involves Ni-SI, Ni-R, Ni-C and Ni-L states (Figure 5.7). The fact that no Ni-SI is detected in the spectrum under H_2 (Figure 5.6B), and that Ni-R is in greater concentration, is consistent with the rapid attack of H_2 to Ni-SI to form Ni-R. The H_2 concentration in this experiment is well above the Michaelis Menten constant for Hyd-1 ($9 \mu\text{M}$),¹³ which means that there is enough substrate at any point in the experiment so that all the enzyme sample is engaging in catalysis. Both Ni-C and Ni-L states are also detected under turnover, which is indicative of both these participating in the catalytic cycle (see dashed-line route in the mechanism depicted in Figure 5.7).

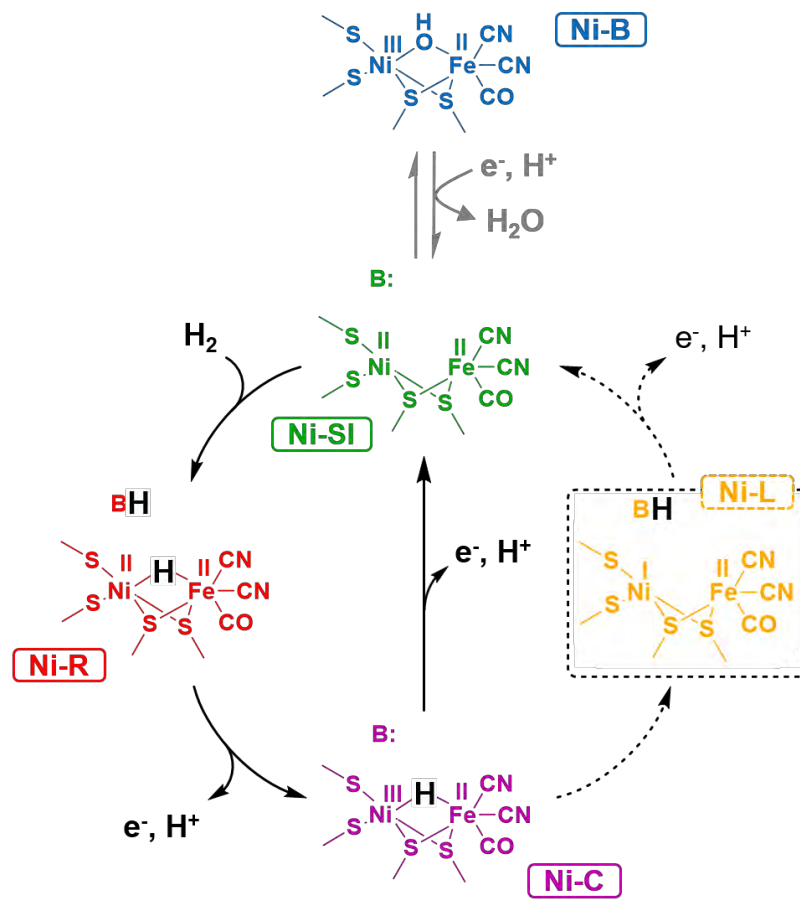


Figure 5.7 H₂ oxidation mechanism of NiFe hydrogenases. The dashed lines represent the proposed route in this work, in which deprotonation of the metal bridging position (to give Ni-L) precedes the second proton-coupled one-electron oxidation. In grey it is shown the anaerobic inactivation at high potential.

The third potential step, at -0.074 V, shows an even larger current from H₂ oxidation (Figure 5.7A). The spectrum under H₂, in Figure 5.8B, continues to show Ni-R as the majority species. Ni-C and Ni-L are still present; and Ni-SI is now detected, although at a significantly lower concentration than under Ar. By referring to the catalytic cycle in Figure 5.7; the appearance of Ni-SI at a higher potential is consistent with the fact that the step which leads to this Ni-SI state in the cycle is precisely an oxidation step. It follows, then, that the higher the applied potential, the faster the formation of Ni-SI becomes (the rate of electron transfer depends on potential, according to Marcus Theory¹⁶).

The consumption of Ni-SI, however, is not directly dependent on potential. It can be observed in the proposed mechanism that the rate of such step is a function of the H₂ concentration only, which is

the same for all the potential steps throughout the experiment. This means that stepping up the potential from -0.199 V to -0.074 V results in an increase in the rate of Ni-SI formation, but not in a decrease of the rate of its consumption. Hence, the steady state concentration of Ni-SI is now larger so that it can be detected spectroscopically.

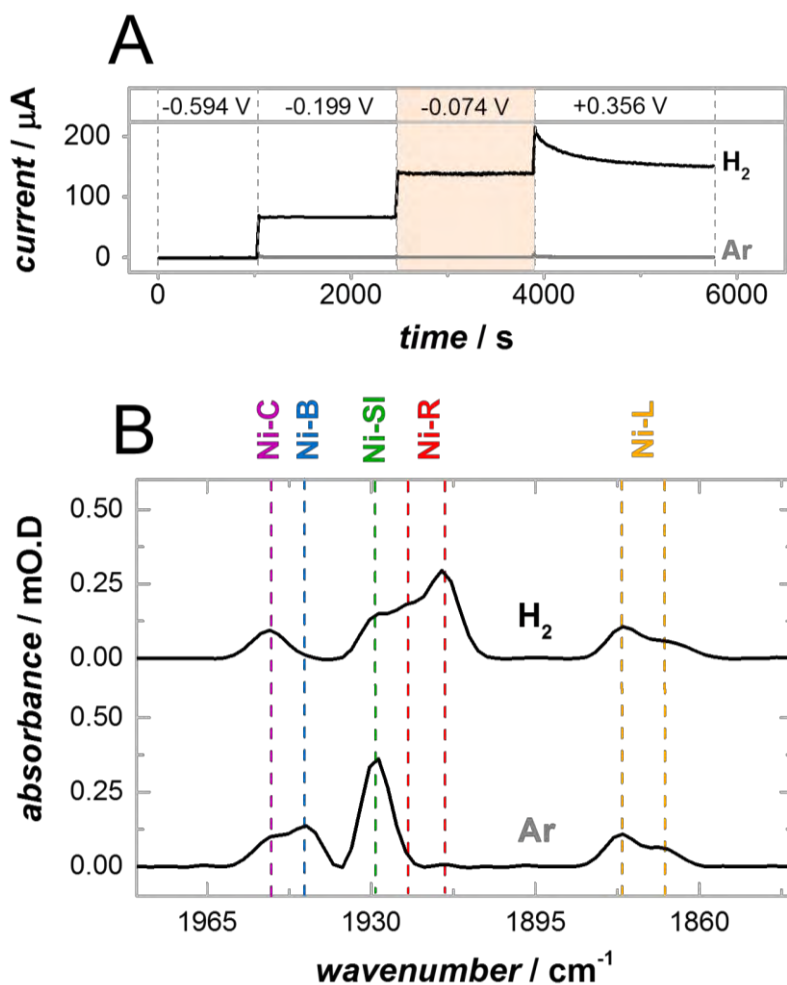


Figure 5.8 Spectroelectrochemistry of Hyd-1 adsorbed on a carbon electrode. A) Current-time trace. The shaded area shows the region where the IR spectra were collected. B) IR spectra displaying the ν_{CO} region under H_2 and Ar recorded at -0.074 V.

The intensities of Ni-R, Ni-C, and Ni-L slightly decrease with this potential step. This can be explained, also, by alluding to the mechanism in Figure 5.7. The two steps that relate to the consumption of Ni-R, and the consumption of Ni-C and Ni-L, correspond to proton-coupled one-electron oxidations. The rates of such reactions increase, therefore, the more oxidising the applied potential is.

On the other hand, the relative intensities of Ni-C and Ni-L under steady state conditions, do not appear to change with potential. It was confirmed in Chapter 4 that these states are in protonation equilibrium but are at the same redox level. In these experiments, under steady state catalytic turnover, changing the potential does not result in a change in the rate of Ni-C to Ni-L conversion (consistent with these two states being at the same redox level). In Section 5.2.3, the effect of pH on the distribution of states under catalytic turnover will be investigated.

Finally, at the most oxidising potential (+0.356 V), the current under H₂ no longer stays constant after the step, but decays over time (Figure 5.9A).

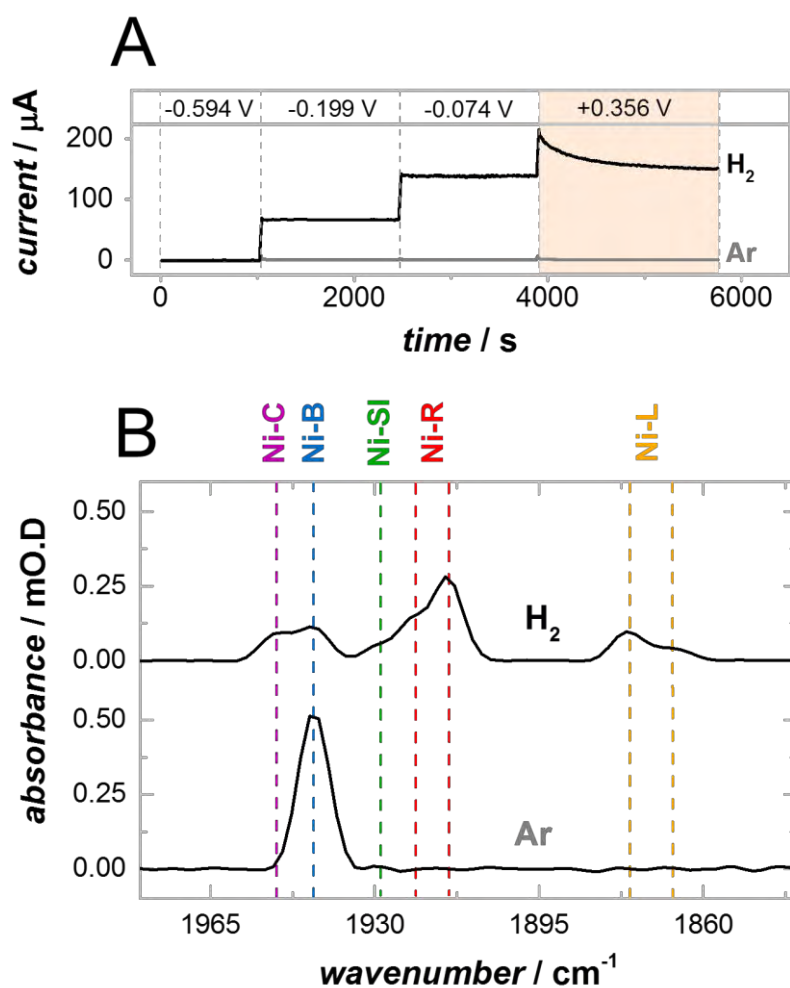


Figure 5.9 Spectroelectrochemistry of Hyd-1 adsorbed on a carbon electrode. A) Current-time trace. The shaded area shows the region where the IR spectra were collected. B) IR spectra displaying the ν_{CO} region under H₂ and Ar recorded at +0.356 V.

The spectrum under Ar exhibits only the most oxidised state, Ni-B. This is, again, in accordance with what is expected at such high potential under non turnover conditions.

In the spectrum under H_2 , on the other hand, Ni-R is the most intense species, as it has been for the previous spectra recorded under H_2 . The ratios of Ni-R, Ni-C and Ni-L remain the same as at the previous potentials. Their intensities, however, decreased by a small amount. More interestingly; the concentration of the Ni-SI state decreased significantly, and Ni-B is now present in important quantities. This last observation becomes relevant in explaining the behaviour of the electrocatalytic current at this potential step; this is, the oxidative inactivation of the enzyme. It can be seen that this inactivation can be in fact related to the formation of Ni-B.

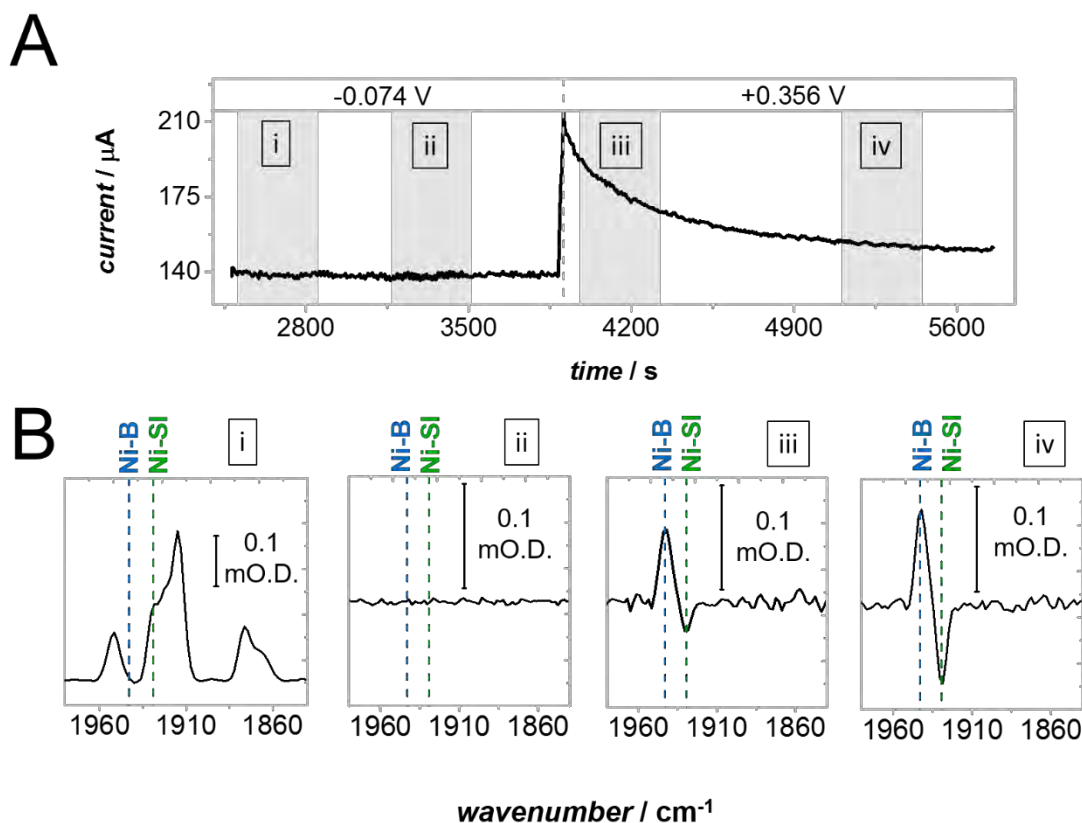


Figure 5.10 High potential formation of Ni-B under H_2 oxidation conditions. **A)** A potential step from -0.074 V to $+0.356$ V. The current at $+0.356$ V is not constant, as it is in the previous step; it decays over time. **B)** Spectra collected at different points during the experiment. (i) shows the absolute ν_{CO} region collected over the time region indicated in panel A. Spectra (ii), (iii), and (iv) show the changes in the intensities of the ν_{CO} peaks, relative to spectrum (i), in their respective time regions as indicated in panel A.

Ni-B is the only new species detected at this potential (that was not present in the spectrum recorded at the previous potential), to which the decay in current can be attributed. It is also important to note that; of the active states Ni-SI, Ni-R, Ni-C and Ni-L, the state that diminished the most upon the formation of Ni-B is the Ni-SI state. Figure 5.10 shows this last potential step in more detail. It shows that the concentration of Ni-B increases and the concentration of Ni-SI decreases with time, at +0.356 V. This is consistent with the well-established formation of Ni-B from Ni-SI.²

The relevance of these initial results for the understanding of the mechanism of H₂ oxidation

The role of Ni-L in the catalytic cycle

First and foremost, the experiments described so far in this chapter, represent the first observation of redox states of the active site under catalytic turnover. This corroborates further the idea that these redox states are indeed involved in the catalytic cycle, as has been previously suggested (in the case of Ni-SI, Ni-C, and Ni-R).^{2,3}

One of the most relevant findings from analysing these experiments is the detection of Ni-L in all the spectra recorded under electrocatalytic H₂-oxidation conditions, even when it is completely absent under Ar. This state is detected alongside Ni-C, and their relative intensities do not change with potential. Such an observation, in addition to the evidence presented in Chapter 4 about the electrochemical reversibility and pH dependence of Ni-L, represents a strong case for this state being a true catalytic intermediate. These results, therefore, unify the spectroscopic and computational discussions.

What might the presence of multiple protonation states of a given redox state mean?

It can be seen in all the spectra under H₂, that the two Ni-R species and the two Ni-L species are consistently present throughout the experiment. In Chapter 4, evidence was presented to support the view that the multiplicity of these states can be attributed to there being more than one protonation state for each of these redox states (Section 4.4). As it was mentioned previously, the conditions of the experiments in this current chapter experiments are such that the H₂ concentration is, at any point, well above the Michaelis Menten constant. In addition to this, mass flow control of

the experiment is efficient, as was explained in more detail in Chapter 3. These two conditions (H_2 concentration above Michaelis-Menten constant and efficient mass transport) imply that the entire enzyme sample is engaged in the electrocatalytic oxidation of H_2 throughout the experiment. An explanation for the presence of multiple bands for Ni-R and Ni-L can be proposed alluding to the fact that it is at these redox states, Ni-R and Ni-L, that the removal of the protons from the active site takes place (see proposed mechanism Figure 5.7). Therefore, this additional protonation states observed for Ni-R and Ni-L may represent different positions of the protons in their way out of active site.

The Ni-R state contains the products of the heterolytic splitting of H_2 , namely the proton and the hydride.^{2,17,18} The step from Ni-R to Ni-C (see Figure 5.7) is a proton-coupled electron transfer.^{19,20} It is possible that the two Ni-R species detected correspond to two different protonation states in the direction of the proton being removed from the active site. Figure 5.11 illustrates this suggested explanation.

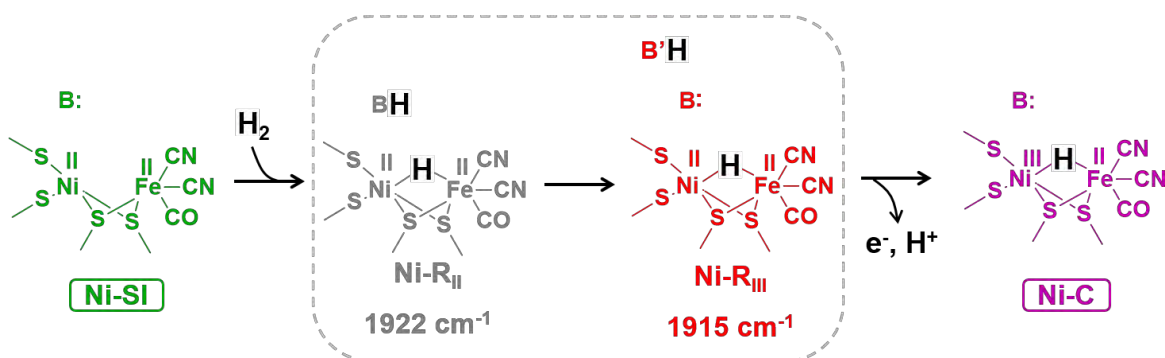


Figure 5.11 Formation of the Ni-R states by the attack of H_2 to Ni-SI, and the PCET oxidation of Ni-R to give Ni-C, in the catalytic cycle of H_2 oxidation. The proton in Ni-R_{II} starts to migrate (hence, forming Ni-R_{III}) before leaving the active site. Then, a proton-coupled electron-transfer gives the Ni-C state. B and B' represent generic bases; the latter being further away from the active site.

In the mechanism proposed by Figure 5.11, and overall for the discussion about this work, the identity of the bases is not relevant, the only difference that B and B' have is that B is closest to the bimetallic active site. The important fact is that two different protonation states of Ni-R were detected under

turnover. It is therefore proposed, as shown by Figure 5.11, that these two protonation states relate to the proton having started to migrate out of the active site. The Ni-R_{II} is assigned to be the one in which the proton is closest to the bimetallic site, and therefore the first one formed in the catalytic cycle. The Ni-R_{III} represents the proton having moved to a based B', which is further away from the active site. This assignment is made on the basis of the wavenumber positions of their ν_{CO} and ν_{CN} . Figure 5.11 shows the wavenumber positions for the ν_{CO} of these states ($\nu_{\text{CO}_{\text{Ni-R}_{\text{II}}}} < \nu_{\text{CO}_{\text{Ni-R}_{\text{III}}}}$). As was demonstrated in Chapter 4 (Figure 4.28), the proton does not actually leave the active site until the oxidation takes place, to form Ni-C state as depicted in Figure 5.11.

A similar phenomenon occurs with Ni-L; that is, that multiple bands are observed for this state. It is from this point where the second proton, along with one electron, leaves the active site to give Ni-SI, so the cycle can restart back again (see Figure 5.7). A model is here proposed, similar to that for the multiple Ni-R species, in which the two Ni-L bands arise as a result of the proton having started to migrate away from the active site. In this step, there are actually three different protonation states involved. As it was explained in detail in Chapter 4, Ni-C and Ni-L are different protonation states of the same redox level. The beginning of the migration of the proton out of the active site, would be therefore described, by three different protonation states of the same redox level: Ni-C and the two Ni-L states. This process is described in Figure 5.12.

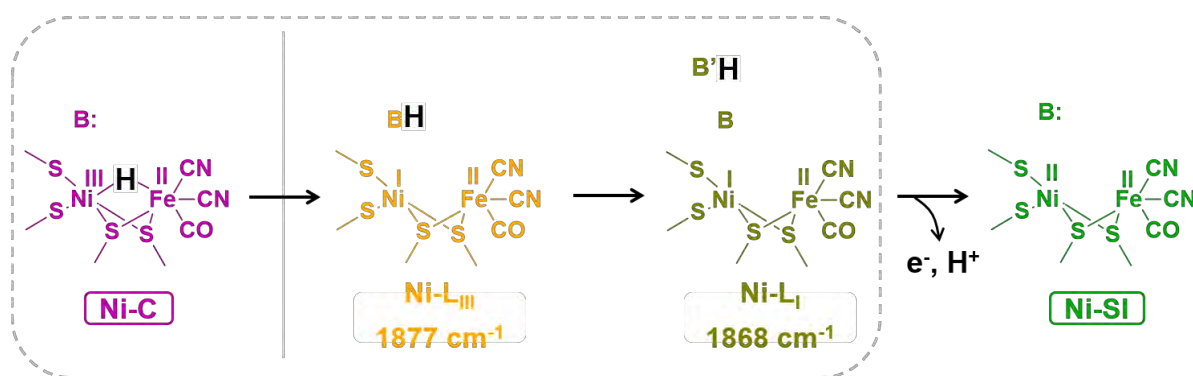


Figure 5.12 The proton coupled electron transfer process from Ni-C to give back the Ni-SI state, and complete one cycle of H₂ oxidation. The metal-bound hydride in Ni-C leaves as a proton to form the Ni-L_{III} state, the proton then moves further away to B' as Ni-L_I is formed. Finally, the proton-coupled electron transfer takes place to form Ni-SI.

The proton, which is in the form of a metal-bound hydride in Ni-C, starts to migrate by leaving the bridging position between the metals to a nearby base B, hence forming Ni-L_{III}. The proton is then transferred to another base B' (located further from the active site) to form Ni-L. At this point, a proton coupled electron transfer gives the Ni-SI state.

B and B', in Figures 5.11 and 5.12, need not be the same for these two different cases. The only criterion they must meet in the proposed model, is that B' is further away from the active site than B. The proton channels whereby these two distinct protons leave the active site need not be the same either. Different proton and water channels have been identified structurally for NiFe hydrogenases.²¹⁻²⁶

A way to further investigate the proposed models (Figures 5.11 and 5.12) would be to change the identity of specific amino acids within the active site cavity (those that are the most likely to be functioning as proton acceptors) by site-directed mutagenesis. These variants can then be studied in experiments under non-turnover conditions, like those described in Chapter 4, to investigate the equilibrium between different protonation species. Changes in wavenumber positions of the bands of Ni-L and Ni-R, or changes in relative intensities between the different Ni-L or Ni-R species, would provide information on the amino acids acting as bases. Moreover, experiments under turnover, like the ones presented in this chapter, would further assess the role of these different protonation states in the catalytic cycle. However, such investigation is beyond the scope of this thesis.

Recently, site-directed mutagenesis has been applied to address a similar question like the investigation just proposed. A conserved arginine that sits above the Ni and Fe atoms was shown to play a major role in catalysis. The replacement of a conserved arginine for a lysine resulted in an enzyme variant that was stable, and with their protein and active site structure virtually unchanged. However, the activity of the variant was 100 times lower than that of the native enzyme. This provided strong evidence for the role of this arginine in catalysis.^{27,28}

In the next section, the effect of varying the H₂ concentration on the distribution of states detected under turnover will be investigated.

5.2.2 The effect of H₂ concentration on the distribution of states under catalytic turnover

Figure 5.13 shows a similar experiment to the one described in Section 5.2.1 but under a 50 : 50 H₂ : Ar atmosphere (at 1 bar). The current-time trace (Figure 5.13A) shows the same behaviour as the one performed under a 100% H₂ atmosphere. This is to say that: at the most negative potential no electrocatalytic current is detected, at the two middle potentials there is a constant and potential-dependent positive electrocatalytic current resulting from H₂ oxidation, and at the highest potential there occurs high-potential inactivation. The difference in the magnitude of the current, between this experiment and the experiment under 100% H₂, is not comparable as these are two different sample preparations (it was determined from separate experiments in the ATR spectroelectrochemical cell, that the concentration of H₂ does correlate with the magnitude of the current for a given sample, consistent with PFE studies²⁹). On the other hand, the IR spectra in Figure 5.13B do show clear differences from those analysed previously under 100% H₂, especially at the higher potentials.

At the most negative potential, -0.594 V where no catalysis is taking place, the spectrum does indeed resemble that under 100% N₂ and 100% H₂ described in Figure 5.5B. Ni-R is the most abundant state with a small amount of Ni-C and Ni-L. When the potential is stepped up to -0.199 V, there is a small increase in Ni-C and Ni-L, and a corresponding decrease in Ni-R. At this potential the sample is engaging in catalytic H₂ oxidation. This spectrum does not show significant differences from that shown in Figure 5.6B, recorded at the same potential but under 100 % H₂.

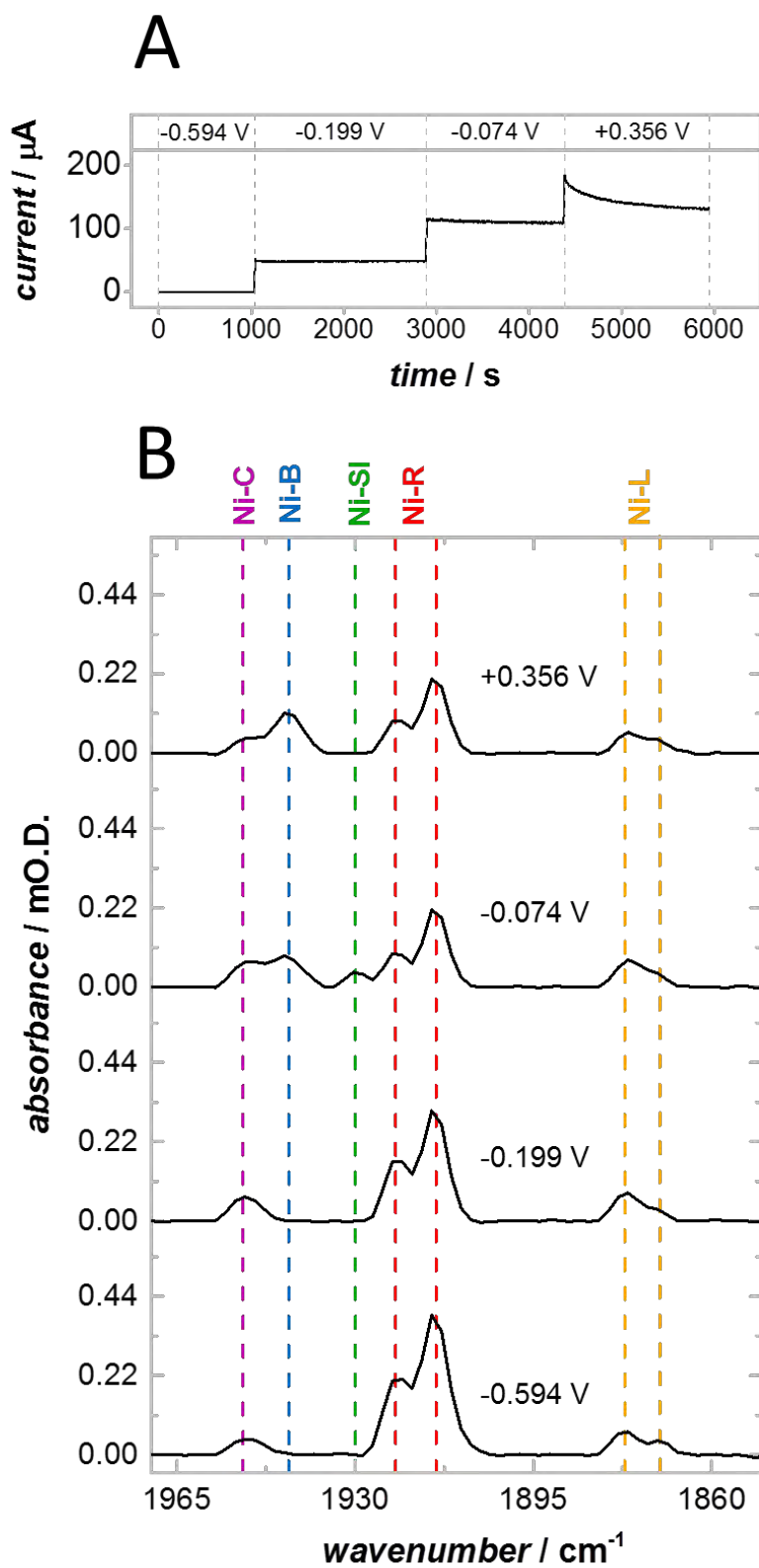


Figure 5.13 Investigation of the steady state distribution of redox states at 50% H_2 . A) Current-time trace at different potential steps shows H_2 oxidation. B) IR spectra showing the ν_{CO} region recorded at each potential. The flow rate of the buffer solution was of 62 mL min^{-1} .

More interestingly, at -0.074 V the spectrum differs significantly to that recorded under 100% H_2 (Figure 5.8B). The main difference is that Ni-B is present in the 50% H_2 experiment. This difference can be explained again by the proposed mechanism in Figure 5.7. Overall, a decrease in H_2 concentration results in an increase in the steady state concentration of Ni-SI. This is because the concentration of H_2 is inversely proportional to the inactivation rate constant, as has been determined in protein film electrochemistry studies.^{30,31} Therefore the steady state concentration of Ni-B can build up at this lower H_2 concentration. When the experiment was done under 100% H_2 (Figure 5.8B), the slower inactivation rate (which results from a high H_2 concentration) explains why no Ni-B was detected in that spectrum.

Finally, when the potential was taken to the most oxidising value ($+0.356$ V) under 50% H_2 (Figure 5.13), the current did show a decreasing behaviour over time. At this stage, the concentration of Ni-B increased, which is consistent with the inactivation shown in the current. In addition to that, Ni-SI is no longer detected. This could result as a consequence of Ni-SI being both attacked by H_2 to form Ni-R and restart a catalytic cycle; and, anaerobically oxidised to form the inactive Ni-B species. The rate of reactivation of Ni-B has been shown to decrease as the potential is raised.³¹ This is in accordance with the increase in Ni-B from Ni-SI in the two higher potential steps in Figure 5.13B.

The spectrum at $+0.356$ V under 100% H_2 discussed in last section (Figure 5.9B), shows Ni-SI, whereas the spectrum under 50% H_2 (Figure 5.13B) does not. The explanation for this observation is not immediately obvious (more about this will be discussed after analysing the experiment under 10% H_2 below). Lowering the concentration of H_2 affects the steady state concentration of Ni-SI in at least two ways (maybe three): *i*) the rate of Ni-SI consumption to form Ni-R decreases (this favours the increase of Ni-SI under turnover), and *ii*) the rate of inactivation to form Ni-B increases (this favours the decrease of Ni-SI under turnover) at high potentials, where the formation of Ni-B is possible. The third way whereby H_2 can affect the steady state concentration has to do with the role of H_2 in the

chemical activation of Ni-B. The extent to which this is possible, or even if it is possible at all, has been a subject of debate.^{31,32} This chemical activation shall be further investigated in Chapter 6.

The H₂ oxidation experiment was performed as well under an even lower concentration of H₂ (10%). The results for both the current time trace and the spectra are shown in Figure 5.14. This experiment was performed on the same enzyme film as the one under 50% H₂. Because of this, the current magnitudes are indeed comparable for these two experiments. The current in Figure 5.14A is significantly lower, relative to that on Figure 5.13A for the 50% H₂ experiment, this is consistent with the lower concentration of H₂. In terms of the IR spectra, there are some differences, mainly at the two higher potentials. The changes concern particularly Ni-SI and Ni-B.

Before proceeding with the discussion of these results, a few things must be noted. First, as it has been mentioned above, Fourmond et al. measured the variation in the rate of inactivation and activation of the O₂-tolerant hydrogenase from *A. aeolicus* with pH, H₂ concentration, and applied potential³¹ (in agreement with earlier results by Jones et al³⁰). The relevant results from such work are summarised by Table 5.1.

Table 5.1 The effect of pH, potential, and H₂ concentration on the inactivation and activation rate constants, as determined by Fourmond et al for *A. aeolicus* O₂-tolerant hydrogenase.³¹

	<i>Effect on increasing</i>		
	<i>potential</i>	<i>[H₂]</i>	<i>pH</i>
<i>inactivation rate constant k_i</i>	independent	decreases	increases
<i>activation rate constant k_A</i>	decreases	independent*	decreases

* Others have suggested that H₂ does play a role on this process, as it is known to activate oxidised samples of hydrogenases, but this may be due to an effect of H₂ on activation of other inactive states.

The results shown in Table 5.1 are of great relevance to the experiments presented in this chapter. The data presented herein (Figures 5.13 and 5.14) will be discussed in light of the findings of protein film electrochemistry in the literature summarised in Table 5.1.

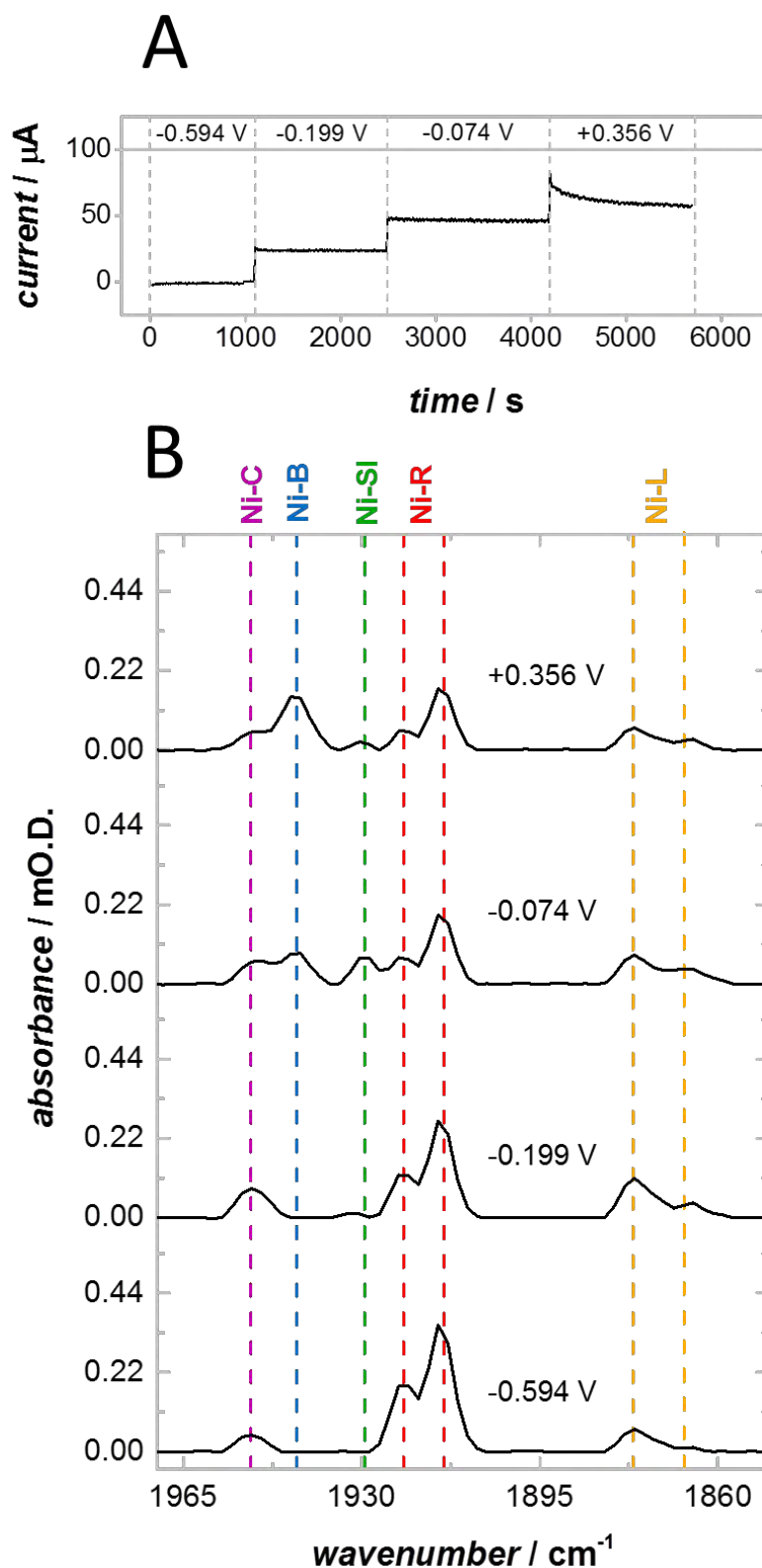


Figure 5.14 Investigation of the steady state distribution of redox states at 10% H_2 . A) Current-time trace at different potential steps shows H_2 oxidation. B) IR spectra showing the ν_{CO} region recorded at each potential. The flow rate of the buffer solution was of 62 mL min^{-1} .

The other point that should be borne in mind is that Ni-SI is involved in four different chemical reactions during turnover (according to the catalytic mechanism proposed in Figure 5.7), and that all of these contribute to the detected steady-state concentration of this state at any point in the experiment. These reactions are: *i)* the formation of Ni-SI by the oxidation of Ni-L, *ii)* the consumption of Ni-SI by its reaction with H₂ to form Ni-R, *iii)* the consumption of Ni-SI, via an oxidation, to form the inactive Ni-B state, and *iv)* the formation of Ni-SI by the reductive reactivation of Ni-B. This is in contrast to the rest of the states involved in the cycle; these are involved in two chemical reactions each, that of its formation and that of its consumption (see proposed catalytic mechanism in Figure 5.7).

The more complex role that the Ni-SI state plays in the cycle, makes it less straight-forward to determine the effect that the variation of conditions (such as potential, pH or H₂ concentration) has on each specific rate of any of the four reactions in which Ni-SI is involved. As was mentioned before, in the discussion on the data under 50% H₂, the concentration of H₂ affects the steady state concentration of Ni-SI in at least two ways. Since H₂ is involved in the attack of Ni-SI to form Ni-R, increasing the H₂ concentration has the effect of increasing this rate of Ni-SI consumption. On the other hand, as has been established in the literature (see Table 5.1),^{30,31} the concentration of H₂ correlates inversely to the rate of inactivation (consumption of Ni-SI to form Ni-B).³¹ In terms of the applied potential, high potential values favour the formation of Ni-SI (from the oxidation of Ni-L) on the one hand. But on the other, they also slow down the rate of reactivation from Ni-B, to form Ni-SI.

The effects of varying the H₂ concentration on the distribution of states detected at various potential values, will be analysed on the basis of what has just been discussed above. In the data in Figure 5.14; at -0.074 V there is a significant amount of Ni-SI present, larger than there was under higher concentrations of H₂. This is again, in accordance with the proposed mechanism (Figure 5.7), in which the steady state concentration of Ni-Si depends inversely on the concentration of H₂. The concentration of Ni-B is significantly higher than it was in the 50% H₂ experiment. This again, can be

explained by the fact that a lower concentration of H_2 increases the rate of Ni-B formation. However; the increase in the steady state concentration of Ni-SI, upon decreasing the H_2 concentration from 50% to 10% at -0.074 V, is larger than the increase in Ni-B (see spectra at this potential in Figures 5.13 and 5.14). This suggests that the extent to which lowering the H_2 concentration decreases the rate of consumption of Ni-SI (to form Ni-R), is higher than the extent to which it increases the rate of Ni-B formation (oxidative inactivation of Ni-SI).

Upon increasing the potential, to +0.356 V, the spectrum shows an even greater concentration of Ni-B. Ni-SI decreased, relative to the previous potential step, but it is still clearly present. An increase in potential favours the formation of Ni-B (because the rate of activation decreases with potential), hence the increase in Ni-B and the decrease in Ni-SI (from which it is formed). This is evidence that an increasing potential decreases the rate of activation (from Ni-B to Ni-SI) to a greater extent than it increases the rate of Ni-SI formation from Ni-L.

On the other hand; Ni-SI is still present in the spectrum at +0.356 V, in contrast to the spectrum recorded at the same potential under 50% H_2 . This is again in accordance with the conclusion made from comparing the spectra at -0.074 V, from the 50% and 10% H_2 experiments, namely that lowering the H_2 concentration decreases the rate of Ni-SI consumption (to form Ni-R and engage in catalytic oxidation) more than it increases the rate of Ni-B formation.

Main points about the effects of H_2 concentration on the steady state distribution of redox species

Overall, H_2 concentration affects mainly the steady state concentrations of Ni-R, Ni-SI, and Ni-B under catalytic turnover. Ni-R is less abundant the lower the concentration of H_2 , this can be noticed more sharply at the higher potentials. Directly related to the decrease in the concentration of Ni-R, is the increase in concentration of Ni-SI, from which Ni-R is formed as a result of the attack by H_2 . On the other hand, the steady state concentration of Ni-B also increases as the concentration of H_2 is lowered. This is because Ni-B formation is favoured by lower concentrations of H_2 .^{30,31} Finally, the

concentrations of Ni-C and Ni-L do not seem to be significantly affected by changing the H₂ concentration. These results are in accordance with the proposed catalytic cycle (Figure 5.7).

In regards to Ni-C and Ni-L, it might be expected that their relative intensities under turnover may be dependent on pH. Proton transfer rates in biological systems have been shown to be pH dependent.³³⁻³⁵ If these two isopotential states (Ni-C and Ni-L) correspond to initial stages of a proton migration process, their relative steady state concentration might be influenced by pH. In the next section, this hypothesis will be investigated.

5.2.3 The effect of pH on the distribution of states under catalytic turnover

Cyclic voltammograms under 100% H₂ were recorded at three different pH values: 4.0, 6.0 and 8.0. Figure 5.15 shows these along with IR spectra recorded in the region of maximum catalytic activity.

The voltammograms show behaviour dependent on pH, in two main ways. First, the onset potential for H₂ oxidation becomes more negative as the pH increases, consistent with the variation of the thermodynamic potential of the H₂/H⁺ couple with pH, which is of -59 mV pH⁻¹ at 298 K and 1 bar H₂. Second, the perceived inactivation at high potential is greater at higher pH values, which can be explained by an increase in the rate of Ni-B formation, as well as from a decrease in the rate of Ni-B reactivation, with pH.

In the IR spectra, it can be seen that the steady state concentration of Ni-L increases with pH, and that of Ni-C decreases. It could be the case that, under turnover conditions, the rate of formation of Ni-L from Ni-C is in fact pH dependent. This step consists only on the transfer of a proton, from the bridging position between the metals (in which it is bound as a hydride) to a nearby base, as was demonstrated in Chapter 4. However, a thermodynamic explanation for this observation cannot be discarded. The pH equilibration between these two states (described in Chapter 4) may be fast, and that could account for the observed behaviour.

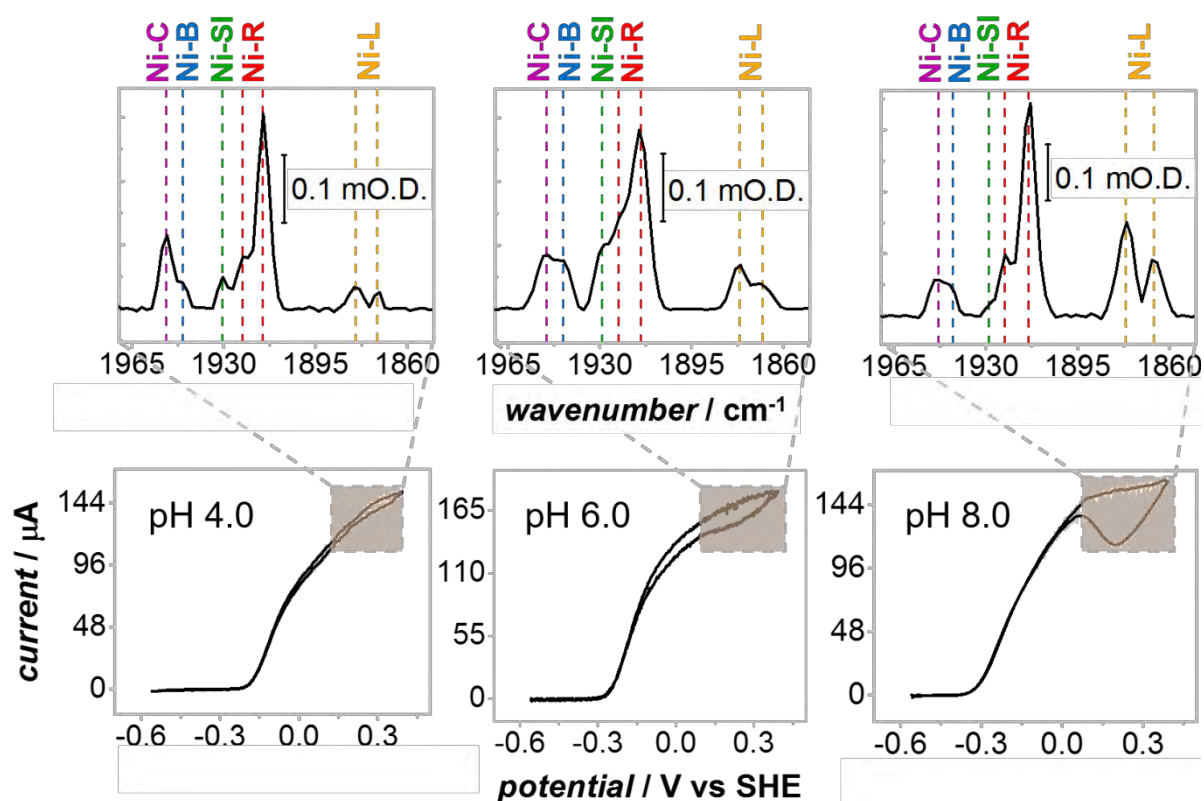


Figure 5.15 Cyclic voltammograms showing H_2 oxidation by Hyd-1 at different pH values, scan rate: 0.5 mV s^{-1} . The flow of buffer (H_2 -saturated, 1 bar) through the spectroelectrochemical cell was of 58 mL min^{-1} . The shaded boxes in the voltammograms represent the potential region over which the spectra (shown above) were recorded. The spectra show the ν_{CO} region under turnover. Each spectrum represents an average of 1200 co-added scans.

The inactivation of O_2 -tolerant hydrogenases, as observed from PFE experiments, has been attributed to the formation of the Ni-B state.^{15,31} In Figure 5.15, it can be seen that it was at pH 8.0 where more inactivation took place. However, the spectrum at pH 8.0 is not the one that shows the largest concentration of Ni-B. It is, nonetheless, the one that shows the least amount of Ni-SI (barely detected), and the highest Ni-B to Ni-SI ratio. The perceived electrochemical inactivation seems to be then better correlated to the availability of Ni-SI (which is the state that initially reacts with H_2), and to the Ni-B to Ni-SI ratio, than to the absolute amount of Ni-B. This is in line with the data shown in Table 5.1; that is, the higher the pH the larger the inactivation rate (Ni-B formation from Ni-SI) and the lower the activation rate (Ni-B consumption to form Ni-SI).^{30,31}

5.3 PFIRE of proton reduction by Hyd-1

O_2 -tolerant membrane-bound hydrogenases are known display low, to non-existent, H^+ reduction.^{13,19,36,37} However, it was recently discovered that Hyd-1 becomes a reversible electrocatalyst and efficient H^+ reducer at low pH values.¹⁴ Protein film infrared electrochemistry investigations of Hyd-1 under H^+ reduction conditions are discussed here.

Figure 5.16 shows electrocatalytic H^+ reduction by Hyd-1 at pH 4.0. The current-time trace (Figure 5.16A) shows how the driving force increases the overall rate of the catalytic process. The infrared spectrum recorded under turnover conditions is shown in panel B.

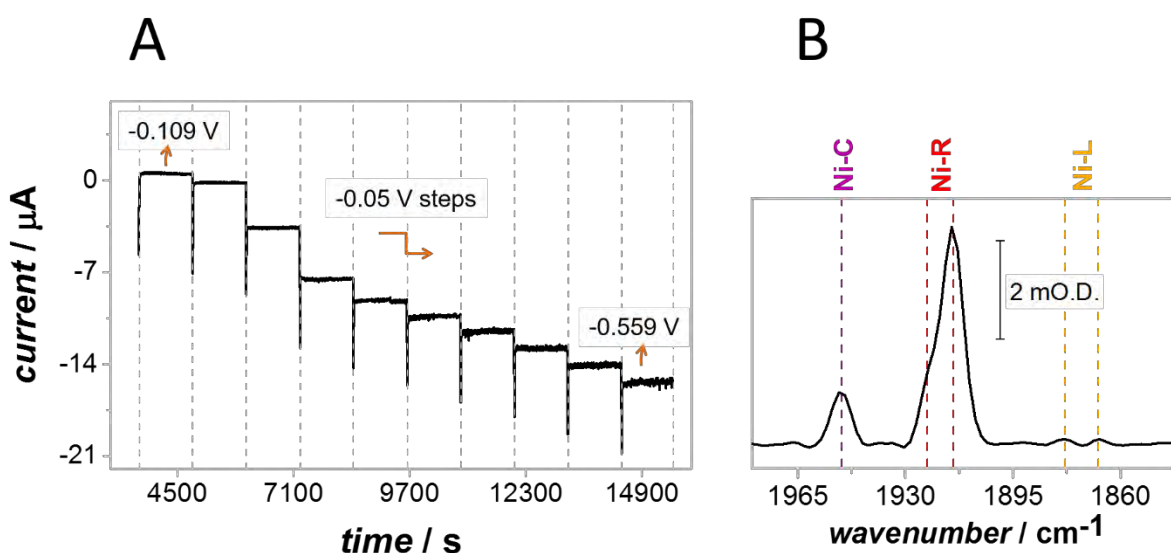


Figure 5.16 A) Current time trace showing proton reduction by Hyd-1 at pH 4.0 under a N_2 atmosphere. The buffer solution is flowed at 60 mL min^{-1} . B) IR spectrum of the ν_{CO} region recorded under catalytic proton reduction conditions: -0.559 V and pH 4.0.

The spectra recorded at any of the potentials under catalytic turnover showed the same features with no significant differences between one another. One such spectrum is displayed in Figure 5.16B. Ni-R is the predominant state, as it is for all the spectra recorded under H_2 conditions in the previous section. Ni-C is clearly present and a fairly small amount of Ni-L can be detected. However, no Ni-SI

is detected in this spectrum. Again, by resorting to a proposed catalytic cycle for H^+ reduction (Figure 5.17), the distribution of the species observed shall be explained. Ni-B is not present in the proposed catalytic cycle because at the potentials at which H^+ reduction occurs, the formation of Ni-B is not thermodynamically favourable, this state is formed by oxidation of Ni-SI at much higher potentials.

First and foremost, the fact that Ni-SI is not present, seem to contrast with the proposed mechanism. However; in the previous section where the enzyme was studied under H_2 oxidation conditions, Ni-SI was not detected either until a high enough potential was applied to the electrode. This was explained by alluding to the fact that at low potentials the rate of its formation is slow, relative to the fast attack by H_2 . Not only is the potential quite low at every point in this experiment, since it is in the H^+ reduction range, but the pH is also low. This further increases the rate of Ni-SI consumption, according to the proposed mechanism in Figure 5.17, which depends on both potential and pH. In Chapter 7, the role of the Ni-SI state under H^+ reduction conditions will be investigated further. For now, it is sensible to propose that Ni-SI is indeed an intermediate in the cycle (Hyd-1 behaves as a reversible catalyst under these conditions¹⁴); and that, given these conditions of low potential and low pH, there are good reasons to support the idea that it is a relatively short-lived intermediate.

The fact that the steady state concentration of Ni-C is greater than that of Ni-L is consistent with the observations in Section 5.2.3. The pH has an effect on the relative concentrations of these isopotential species under turnover conditions. The two bands associated with each of the Ni-R and Ni-L species are also present and can be related to different protonation states, as was mentioned above. However, for H^+ reduction, the direction of the models proposed in Figures 5.11 and 5.12 is the opposite: the species that has the proton further away from the active site (either at the Ni-L or Ni-R redox level) is formed first, protons are being transported from the outside of the protein into the bimetallic active site to be reduced to H_2 .

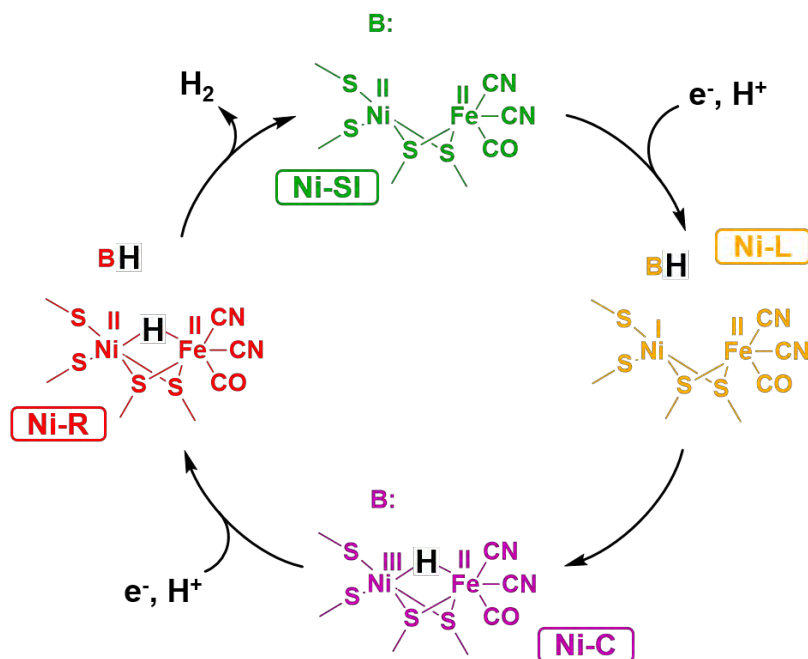


Figure 5.17 The proposed mechanism for H⁺ reduction by Hyd-1. The Ni-SI state is not detected in the experiments mentioned here. It is likely that Ni-SI is particularly short lived under these conditions: low pH and reducing potential.

Finally, Ni-R is the most intense species in the spectrum recorded under catalytic H⁺ reduction. As was mentioned above; the spectra under these conditions do not change noticeably as the potential is taken to lower values, despite the fact that there is indeed an increase in the magnitude of the reductive current. Nonetheless, the magnitude of the maximum current obtained for H⁺ reduction is at least 10 times lower than that obtained for H₂ oxidation (Figure 5.4). It may be the case that, since the changes in activity are small (compared to the changes in activity when stepping up the potential in the H₂ oxidation experiments), significant changes in the distribution of states under turnover are unexpected.

Ni-R is the most long-lived species in both the H⁺ reduction as well as in the H₂ oxidation experiment. This suggests that the fastest step in the oxidation mechanism (Figure 5.6), is the attack of Ni-SI by H₂. This results in the build-up of Ni-R under steady state conditions. In addition to that, the data suggests that slowest step in the reduction mechanism (Figure 5.16), corresponds to the formation of the H—H bond to produce the H₂ molecule and the Ni-SI state, from Ni-R. This justifies the overall

observation that Ni-R is the predominant state, under every set of conditions, when Hyd-1 is engaging in electrocatalysis.

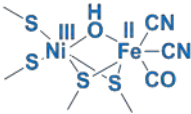
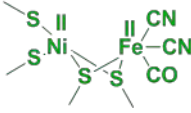
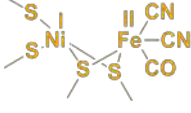
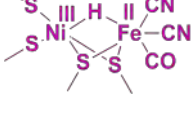
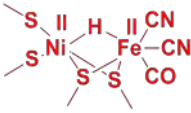
5.4 Summary

This chapter presented a thorough analysis of the intermediates in the catalytic cycle of Hyd-1, under turnover. This was achieved by coupling PFE, an extensively used technique for investigating the dynamics of hydrogenase enzymes, with IR spectroscopy. The detection of specific states, during electrocatalytic turnover, was related to the role of these states as intermediates in a proposed catalytic mechanism. Ni-SI, Ni-C, and Ni-R (the states that have consistently been considered active in the mechanism)², were detected for the first time under catalytic conditions; and thus, confirming their role as intermediates of the catalytic cycle.

An important observation was the detection of Ni-L under catalytic conditions for the first time. This state was detected at all points under turnover conditions; even at potentials at which it would not be present had it been under an inert atmosphere. These observations build upon the results discussed in Chapter 4, in which the discovery of the acid-base equilibrium between Ni-C and Ni-L gave grounds for suggesting its role as an intermediate during catalysis. The evidence presented in this chapter for the presence of Ni-L under turnover conditions, provides even more solid grounds for proposing this state as a true intermediate in the catalytic cycle of Hyd-1.

The variation of different experimental conditions (applied potential, H₂ concentration, and pH), provided a qualitative picture of the changes in the steady state concentration of the intermediates. This gives information about the rates of formation and consumption of the states involved in the catalytic cycle. Table 5.2 summarises the overall effects of pH, potential, and H₂ concentration on the steady state concentration of the intermediates under turnover.

Table 5.2 The effect of pH, potential, and H₂ concentration on the intensity of the intermediates under turnover conditions. "n.e." stands for no clear effect observed upon the variation of the specific variable.

redox state	Effect on steady state concentration by increasing		
	<i>E</i>	[H ₂]	pH
 Ni-B*	increase	decrease	increase
 Ni-SI	increase	decrease	n.e.
 Ni-L	slight decrease	n.e.	increase
 Ni-C	slight decrease	n.e.	decrease
 Ni-R	decrease	increase	n.e.

*Ni-B is not in itself part of the catalytic cycle, it is inactive, and formed upon the oxidation of Ni-SI at high potentials

As to the observation of multiple bands (likely different protonation states) for specific redox levels; an explanation was proposed in which these multiple states correspond to different protonation states as the proton migrates away from the active site and into the proton channels. Similar explanations have been proposed by others very recently.^{9,38} In Chapter 4, the pH dependence of these multiple states was established; and in this current chapter, these multiple states were

detected under turnover conditions. The latter observation is unprecedented and provides a strong support for the aforementioned hypothesis.

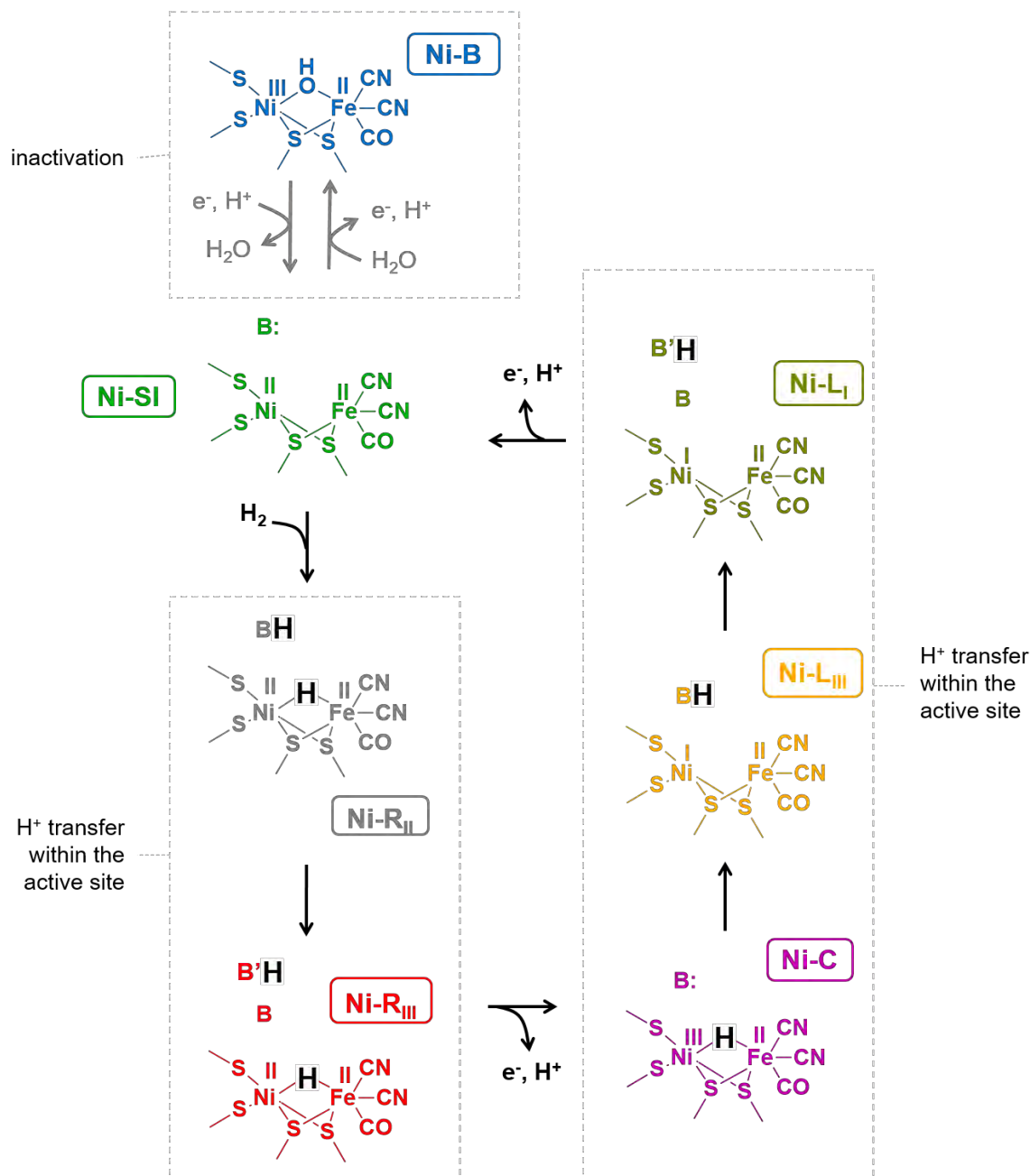


Figure 5.18 Mechanism for H₂ oxidation by Hyd-1. This new scheme is proposed in light of the findings of this chapter, and the most recent discussions in the literature about the role of new intermediates.

A more extensive picture of the catalytic mechanism of Hyd-1 emerges from the evidence presented in this work. It integrates all the concepts that have been discussed in this chapter (and the previous

Chapter 4), and relates strongly to work that has pointed out to a more complex view of the mechanism of hydrogenases. Figure 5.18 shows this new proposed scheme.

All the experimental variables involved in each step are detailed in the scheme, and the summary given by Table 5.2 can be better understood by referring to this new mechanism. It is important to note that this mechanism resembles more the complex mechanism that is shown in Figure 5.2, than the simpler (yet ubiquitous) scheme from Figure 5.1. This mechanism is in agreement with the computational investigations that have proposed the role of a Ni(I) intermediate in the catalytic cycle. Nevertheless, the possibility of Ni-L being a side pH-equilibrium, without being an actual intermediate in the cycle, cannot be ruled out.

Finally, investigations under H^+ reduction conditions were carried out. In these, a similar picture of the intermediates emerged. This is consistent with the fact that Hyd-1 becomes a reversible catalyst at low pH values,¹⁴ and a corresponding catalytic cycle was proposed to explain the observations (Figure 5.15). The role of Ni-SI in H^+ reduction will be further investigated in Chapter 7, when the role of inhibitors studied.

The anaerobic inactivation of Hyd-1 has been discussed in this chapter. However, the formation of Ni-B, and in general the behaviour of hydrogenases towards anaerobic and aerobic inactivation, is a topic of great interest to the scientific community. In the next chapter, the techniques that have been applied so far in this work, will be applied to the investigation of the inactivation and activation properties of this O_2 -tolerant hydrogenase, *E. coli* Hyd-1. A more detailed analysis of the formation of Ni-B, both aerobically and anaerobically, will be a main focus of investigation in the following chapter.

References

- 1 A. I. Krasna, *Enzyme Microb. Technol.*, 1979, **1**, 165–172.
- 2 W. Lubitz, H. Ogata, O. Ruediger and E. Reijerse, *Chem. Rev.*, 2014, **114**, 4081–4148.

- 3 M.-E. Pandelia, H. Ogata and W. Lubitz, *Chemphyschem*, 2010, **11**, 1127–40.
- 4 S. Niu, L. M. Thomson and M. B. Hall, *J. Am. Chem. Soc.*, 1999, **121**, 4000–4007.
- 5 P. E. M. Siegbahn, J. W. Tye and M. B. Hall, *Chem. Rev.*, 2007, **107**, 4414–35.
- 6 A. Pardo, A. L. De Lacey, V. M. Fernández, H.-J. Fan, Y. Fan and M. B. Hall, *J. Biol. Inorg. Chem.*, 2006, **11**, 286–306.
- 7 S. O. N. Lill and P. E. M. Siegbahn, *Biochemistry*, 2009, **48**, 1056–66.
- 8 H. Tai, K. Nishikawa, M. Suzuki, Y. Higuchi and S. Hirota, *Angew. Chem. Int. Ed.*, 2014, **53**, 13817–13820.
- 9 B. L. Greene, C.-H. Wu, G. E. Vansuch, M. W. W. Adams and R. B. Dyer, *Biochemistry*, 2016, **55**, 1813–1825.
- 10 B. L. Greene, C.-H. Wu, P. M. McTernan, M. W. W. Adams and R. B. Dyer, *J. Am. Chem. Soc.*, 2015, **137**, 4558–4566.
- 11 G. M. Chambers, J. Mitra, T. B. Rauchfuss and M. Stein, *Inorg. Chem.*, 2014, **53**, 4243–9.
- 12 G. M. Chambers, M. T. Huynh, Y. Li, S. Hammes-Schiffer, T. B. Rauchfuss, E. Reijerse and W. Lubitz, *Inorg. Chem.*, 2016, **55**, 419–431.
- 13 M. J. Lukey, A. Parkin, M. M. Roessler, B. J. Murphy, J. Harmer, T. Palmer, F. Sargent and F. A. Armstrong, *J. Biol. Chem.*, 2010, **285**, 3928–38.
- 14 B. J. Murphy, F. Sargent and F. A. Armstrong, *Energy Environ. Sci.*, 2014, **7**, 1426.
- 15 K. A. Vincent, A. Parkin and F. A. Armstrong, *Chem. Rev.*, 2007, **107**, 4366–413.
- 16 O. Snir and I. A. Weinstock, in *Physical Inorganic Chemistry: Reactions, processes and applications*, ed. A. Bakac, John Wiley & Sons, New Jersey, 2010, pp. 1–37.
- 17 H. Ogata, K. Nishikawa and W. Lubitz, *Nature*, 2015, **520**, 571–574.
- 18 H. Ogata, T. Krämer, H. Wang, D. Schilter, V. Pelmeshnikov, M. van Gestel, F. Neese, T. B. Rauchfuss, L. B. Gee, A. D. Scott, Y. Yoda, Y. Tanaka, W. Lubitz and S. P. Cramer,

- Nat. Commun.*, 2015, **6**, 7890.
- 19 M.-E. Pandelia, V. Fourmond, P. Tron-Infossi, E. Lojou, P. Bertrand, C. Léger, M.-T. Giudici-Orticoni and W. Lubitz, *J. Am. Chem. Soc.*, 2010, **132**, 6991–7004.
- 20 C. Fichtner, C. Laurich, E. Bothe and W. Lubitz, *Biochemistry*, 2006, **45**, 9706–9716.
- 21 J. Fritsch, P. Scheerer, S. Frielingsdorf, S. Kroschinsky, B. Friedrich, O. Lenz and C. M. T. Spahn, *Nature*, 2011, **479**, 249–252.
- 22 Y. Shomura, K.-S. Yoon, H. Nishihara and Y. Higuchi, *Nature*, 2011, **479**, 253–6.
- 23 A. Volbeda, P. Amara, C. Darnault, J.-M. Mouesca, A. Parkin, M. M. Roessler, F. A. Armstrong and J. C. Fontecilla-Camps, *Proc. Natl. Acad. Sci.*, 2012, **109**, 5305–10.
- 24 E. Szóri-Dorogházi, G. Maróti, M. Szóri, A. Nyilasi, G. Rákhely and K. L. Kovács, *PLoS One*, 2012, **7**, e34666.
- 25 V. H. Teixeira, C. M. Soares and A. M. Baptista, *Proteins*, 2008, **70**, 1010–1022.
- 26 I. Sumner and G. A. Voth, *J. Phys. Chem. B*, 2012, **116**, 2917–26.
- 27 R. M. Evans, E. J. Brooke, S. A. M. Wehlin, E. Nomerotskaia, F. Sargent, S. B. Carr, S. E. V Phillips and F. A. Armstrong, *Nat. Chem. Biol.*, 2015, **12**, 46–50.
- 28 S. B. Carr, R. M. Evans, E. J. Brooke, S. A. M. Wehlin, E. Nomerotskaia, F. Sargent, F. A. Armstrong, S. E. V Phillips, H. Oxford and D. Ox, *Biochem. Soc. Trans.*, 2016, **44**, 863–868.
- 29 R. M. Evans, A. Parkin, M. M. Roessler, B. J. Murphy, H. Adamson, M. J. Lukey, F. Sargent, A. Volbeda, J. C. Fontecilla-Camps and F. A. Armstrong, *J. Am. Chem. Soc.*, 2013, **135**, 2694–2707.
- 30 A. K. Jones, S. E. Lamle, H. R. Pershad, K. A. Vincent, S. P. J. Albracht and F. A. Armstrong, *J. Am. Chem. Soc.*, 2003, **125**, 8505–14.
- 31 V. Fourmond, P. Infossi, M. T. Giudici-Orticoni, P. Bertrand and C. Léger, *J. Am. Chem.*

- Soc.*, 2010, **132**, 4848–4857.
- 32 V. M. Fernandez, R. Aguirre and E. C. Hatchikian, *Biochim. Biophys. Acta*, 1984, **790**, 1–7.
- 33 A. Namslauer, A. Aagaard, A. Katsonouri and P. Brzezinski, *Biochemistry*, 2003, **42**, 1488–1498.
- 34 K. Chen, J. Hirst, R. Camba, C. A. Bonagura, C. D. Stout, B. K. Burgess and F. A. Armstrong, *Nature*, 2000, **405**, 814–817.
- 35 K. Faxén and P. Brzezinski, *Biochim. Biophys. Acta*, 2007, **1767**, 381–386.
- 36 J. A. Cracknell, K. A. Vincent, M. Ludwig, O. Lenz, B. Friedrich and F. A. Armstrong, *J. Am. Chem. Soc.*, 2008, **130**, 424–425.
- 37 G. Goldet, A. F. Wait, J. A. Cracknell, K. A. Vincent, M. Ludwig, O. Lenz, B. Friedrich and F. A. Armstrong, *J. Am. Chem. Soc.*, 2008, **130**, 11106–11113.
- 38 H. Tai, K. Nishikawa, S. Inoue, Y. Higuchi and S. Hirota, *J. Phys. Chem. B*, 2015, **119**, 13668–13674.

Chapter 6

*Inactivation and O₂ inhibition of
Hyd-1*

6.1 Introduction

6.1.1 The inactivation of NiFe hydrogenases

NiFe hydrogenases present catalytically-inactive forms. The aerobically prepared enzyme, is usually present in these states. Once the enzyme has been activated, these inactive forms can be produced again by electrochemical oxidation, or by exposure to O_2 . Mainly two inactive forms have been detected in NiFe hydrogenases, and they differ in the time it takes to activate them. Ni-B (ready) is the inactive state which takes minutes to activate, whereas Ni-A (unready) takes hours.^{1,2} Activation can be attained either by applying a reducing potential, or by the addition of H_2 . It has been proposed, however, that the activation from the unready Ni-A state requires both electrons and H_2 to fully activate.^{1,3}

The difference between O_2 -tolerant hydrogenases and standard hydrogenases is that the former can maintain their activity in the presence of O_2 , whereas the latter are inactivated by trace amounts of it.⁴ This difference is thought to arise as the result of O_2 -tolerant hydrogenases forming only the Ni-B state when inactivated, which can be quickly reactivated. Such property has been attributed to the special proximal Fe-S cluster identified in crystallographic structures of membrane-bound O_2 -tolerant hydrogenases.⁵⁻⁸ This cluster exhibits the ability to undergo two redox transitions at physiologically relevant potentials. In addition to that, the reduction potential of these two transitions are high.⁹ This favours “backward electron transfer” to the active site when O_2 attacks which results in the complete reduction of O_2 to water and the formation of solely Ni-B.⁹⁻

12

The formation of inactive states in NiFe hydrogenases (by both the interaction with O_2 , and the electrochemical inactivation) has been studied extensively by means of PFE. In these experiments, the analysis of the changes in current that arises from H_2 oxidation, upon the addition of O_2 or application of a high potential, is related to the formation of such species.¹³⁻¹⁶ Figure 6.1 shows the

inactivation of the O₂-tolerant hydrogenase 1 from *A. aeolicus*, as determined electrochemically by Pandelia et al.¹⁷

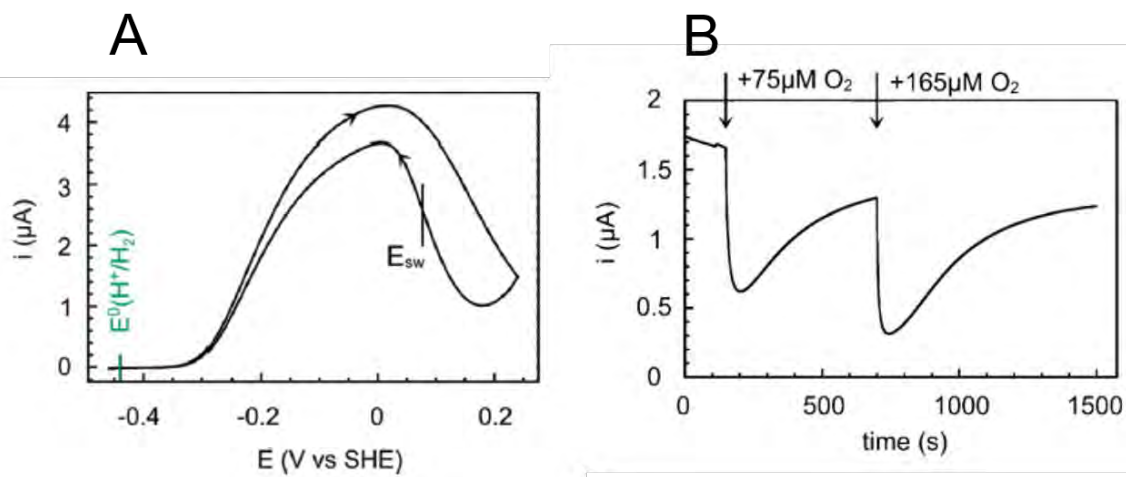


Figure 6.1 A) Cyclic voltammogram showing the anaerobic inactivation of *A. aeolicus* Hase I, adsorbed on a carbon electrode. Scan rate = 0.3 mV s⁻¹. B) O₂ inhibition of H₂ oxidation of Hase I, measured at +0.210 V. Experimental conditions: pH 7, 40 °C, 1 bar H₂, rotation rate = 4000 rpm. Adapted with permission from Pandelia, M.-E.; Fourmond, V.; Tron-Infossi, P.; Lojou, E.; Bertrand, P.; Léger, C.; Giudici-Orticoni, M.-T.; Lubitz, W. *J. Am. Chem. Soc.* 2010, **132** (20), 6991–7004. Copyright 2010 American Chemical Society.

In Figure 6.1A, it can be seen that the electrocatalytic current starts to decrease after +0.020 V in the forward scan. This is the inactivation of the enzyme due to oxidation at high potential. Recovery from the inactive state is attained when the potential is taken down again in the backward scan. Figure 6.1B shows how Hase I from *A. aeolicus* is able to sustain H₂ oxidation activity even in the presence of O₂. Furthermore, it quickly regains its activity afterwards as O₂ is flushed out. This is in contrast to standard NiFe hydrogenases, which are fully inactivated even by trace amounts of O₂.⁴

Additionally to PFE, EPR and IR experiments have investigated the formation of the inactive forms for several O₂-tolerant NiFe hydrogenases under equilibrium conditions.^{6,14,18} These type of hydrogenases have been shown to form only the Ni-B state upon oxidation, provided they have been fully activated beforehand.

6.1.2 IR spectroscopy as a structural insight to the mechanism of inactivation of Hyd-1 on an electrode

The most oxidised states (Ni-B and Ni-A) of several NiFe hydrogenases have been detected by IR spectroscopy in solution, and distinguished by their activation kinetics.^{1,19} However; activation in most IR spectroscopy experiments in solution has been described as the removal of the assigned Ni-B and Ni-A species, along with their one electron reduced counterparts (Ni-SI_r and Ni-SI_o respectively). The aim of this chapter is to describe the formation of the inactive species of Hyd-1 from *E. coli* adsorbed on a carbon electrode by means of IR spectroscopy, for both its anaerobic and aerobic formation. Then, to investigate the relations between the formation of these oxidised species to the inactivation of the enzyme (measured *in situ* using protein film electrochemistry) from O₂. This study will relate the structural information obtained from IR spectroscopy to the activity information gained from electrochemistry, and provide information on the mechanism of inactivation and O₂-tolerance of the membrane bound Hyd-1 from *E. coli*.

6.2 Inactivation of Hyd-1

In this section, the formation of Ni-B in Hyd-1 will be investigated in the absence of H₂. The change in the concentration of the redox states of the active site will be monitored over time to obtain mechanistic information about the mechanism of Ni-B formation.

6.2.1 Anaerobic oxidation of Hyd-1

Figure 6.2 shows the distribution of states of activated Hyd-1 held at -0.594 V. This sample was first reduced for 2 hours under H₂ and at -0.594 V. The H₂ was then flushed out by bubbling 100 % N₂ to the buffer, and the following spectrum was then recorded.

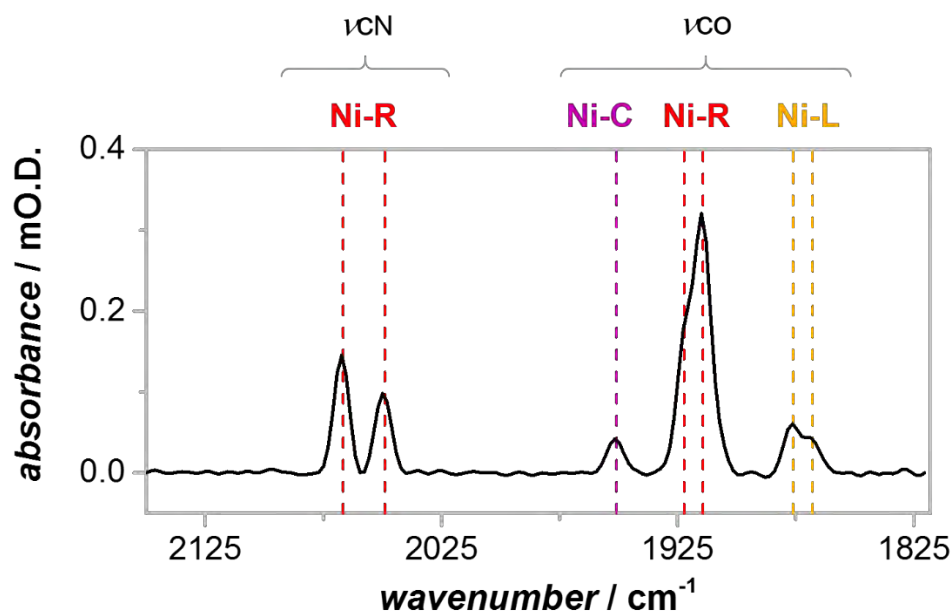


Figure 6.2 IR spectrum of Hyd-1 adsorbed on carbon nanoparticles. Potential applied: -0.594 V. Mixed buffer pH 6.0, 20 °C.

An oxidative potential step to +0.356 V was applied to the above described sample, and the changes in the IR spectrum were measured over time. Figure 6.3 shows these changes produced by the application of this highly oxidising potential. Upon the application of +0.356 V (which is well above the reduction potential of the Ni-SI \leftrightarrow Ni-B couple, -0.004 V) the following changes take place:

- i)* Ni-R decreases steeply until it is completely depleted. It remains like that throughout the rest of the measurement.
- ii)* Ni-C and Ni-L increase slightly in a rapid manner. They decrease back again after a couple of minutes. Their concentration remains quite low for the rest of the measurement.
- iii)* Ni-SI increases rapidly at the beginning. Afterwards, a slow decrease follows.
- iv)* Ni-B slowly but steadily increases over time throughout the whole measurement.

The above observations are consistent with an oxidation in which electrons are removed from the active site one at a time. It is for this reason that all the redox species are observed in this inactivation process.

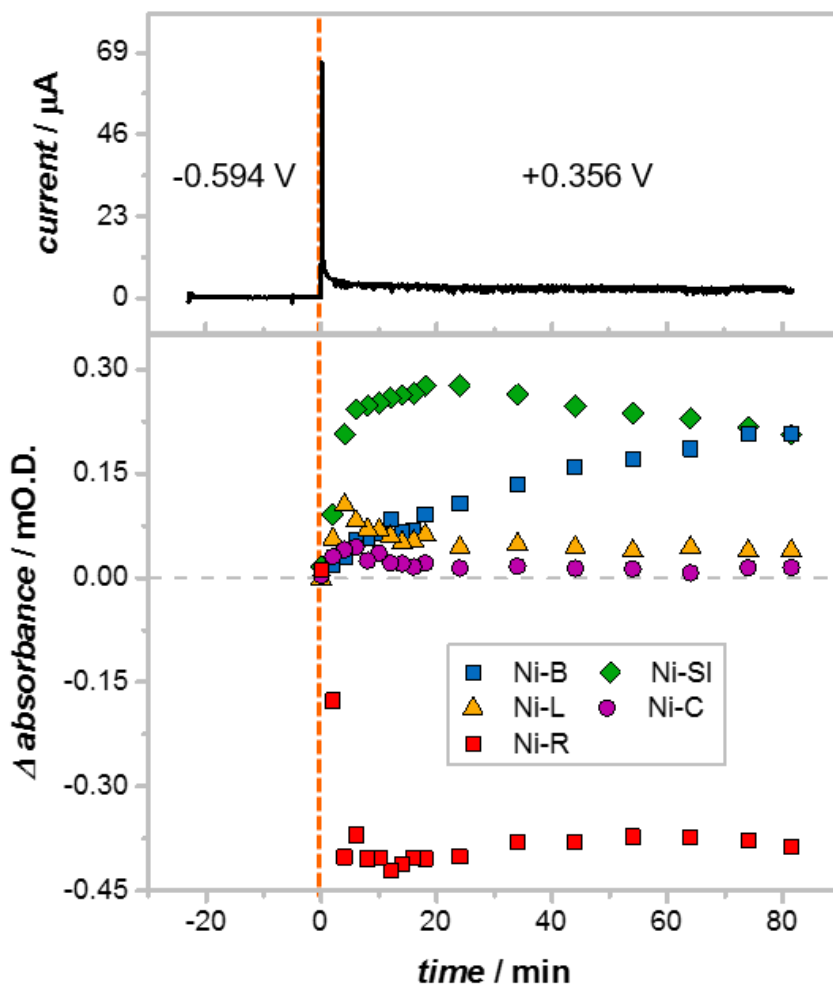


Figure 6.3 The anaerobic inactivation of Hyd-1 to form Ni-B. A potential step, from -0.594 to +0.356 V, was applied. The change in current (upper panel), as well as the changes in the spectrum (lower panel), were recorded over time. The orange dashed line indicates the point in time at which the potential step took place. The spectral changes are relative to the spectrum recorded at -0.594 V. Other experimental conditions: pH 6.0, 100% N₂.

Figure 6.4 shows the proposed mechanism of the anaerobic formation of the inactive Ni-B species, according to the observed data.

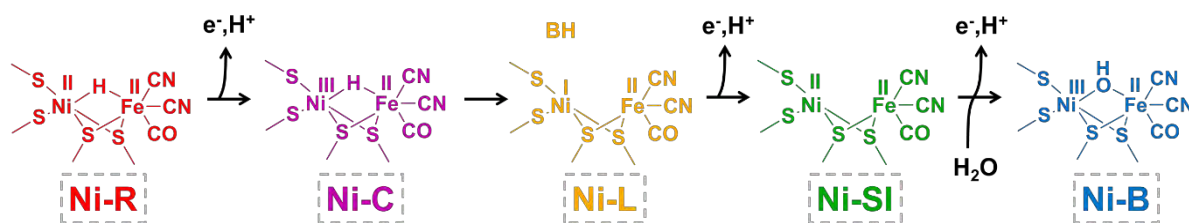


Figure 6.4 Mechanism of anaerobic formation of Ni-B. The electrons are withdrawn from the active (in a PCET) via the Fe-S cluster relay to the electrode, which reports an oxidation current.

The initial decay in Ni-R is accompanied by a fast increase in Ni-C, Ni-L, and Ni-SI (Figure 6.3). Such observation is consistent with the mechanism proposed in Figure 6.4, in which the transition from Ni-R to Ni-SI happens via Ni-C and Ni-L. Nonetheless, it is important to clarify that the initial distribution of states of the sample, contained not only Ni-R but a small amount of Ni-C and Ni-L (Figure 6.2). The fact that Ni-SI is immediately observed upon the application of high potential is not unexpected, since there was Ni-C and Ni-L in the sample to begin with. Had not there been any of these species (Ni-C and Ni-L) from the start, that is, had the initial spectrum contained exclusively the Ni-R state; then there would not have been an initial sudden increase in Ni-SI.

In terms of the actual formation of the inactive Ni-B state, its rate of formation is clearly much slower than that of the other species. This is again consistent with the observations discussed in Chapter 4, in which the rates of Ni-B formation were significantly slower than those of any of the other redox transformations of the active site. Moreover, the fact that the rate of Ni-B formation does not depend on potential, as determined by PFE experiments,^{15,16} is also consistent with it involving a chemical event which renders this reaction slower than the others (which are PCET).

The data in Figure 6.3 also supports the consensus view that, when the enzyme is inactivated anaerobically, Ni-B formation proceeds through Ni-SI. After 20 min, it can be seen that the continuing increase in Ni-B correlates to a corresponding decrease in Ni-SI. Furthermore, at this point these are the only species present detectable in important amounts.

The monitoring of the changes was stopped after 85 min. The applied potential was maintained at +0.356 V for about 8 hours. When the spectrum was measured after this time, the only species present was Ni-B. Subsequent reactivation, by applying a low potential, resulted in a rapid formation of the reduced spectrum (analogous to that shown in Figure 6.2). This is consistent with the reported observation that once Hyd-1 has been activated from its as-isolated form, a re-oxidation forms the Ni-B state (readily activating) exclusively.^{6,14,20}

6.2.2 Aerobic oxidation of Hyd-1

The formation of the inactive Ni-B state by reaction with O₂ is shown in Figure 6.5. The sample to which O₂ was added exhibited the distribution of states of a fully reduced Hyd-1 (Figure 6.5A). It was activated under H₂ and at -0.594 V for 2.3 hours. The H₂ was then flushed out and no potential was applied to this sample. The open circuit potential (OCP) of the activated Hyd-1 equilibrated at -0.303 V. A spectrum recorded under these conditions is shown in Figure 6.5A. Figure 6.5B shows the changes in the distribution of redox states of the active site that result from exposing the fully reduced sample of Hyd-1 (Figure 6.5A), to 1 % O₂ for 5 min. The experimental set-up used for this experiment is that described by Figures 2.9-11. Initially the sample was under a 100 % N₂ atmosphere, after having been fully activated. Then the gas mixture was changed to 1 % O₂ / 99 % N₂ (shaded region in Figure 6.5B) for 5 min, before it went back again to 100 % N₂. After the addition of O₂, the OCP equilibrated at -0.258 V.

During the exposure to O₂, there is an immediate formation of Ni-B and Ni-SI, and a corresponding decrease in Ni-R. No significant changes were observed for Ni-C and Ni-L throughout this experiment. A first important observation is that the formation of Ni-B is faster than that of Ni-SI; unlike for the anaerobic activation, in which Ni-B formation was notably slower than the rest of the transitions.

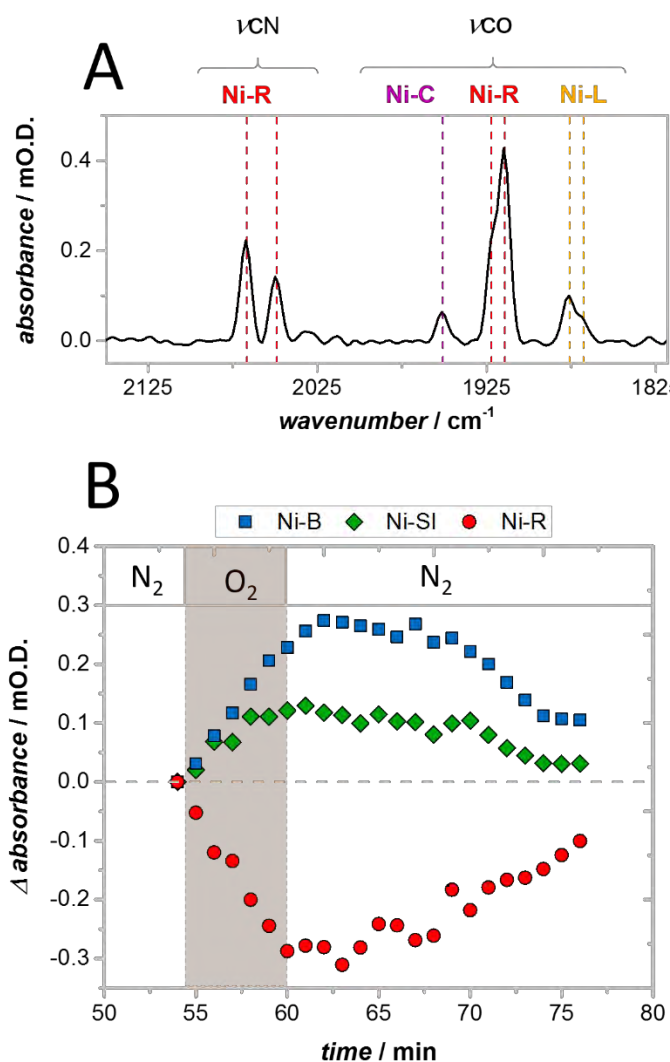


Figure 6.5 Reaction of O₂ with reduced Hyd-1. A) IR spectrum of activated Hyd-1 adsorbed on a carbon nanoparticle electrode. The sample was under a N₂ atmosphere and no potential was applied (OCP: -0.303 V). B) Changes in the intensities over time of the νCO peaks as 1% O₂ was flowed through the spectroelectrochemical cell. After the addition of O₂ was concluded, the OCP equilibrated at -0.258 V. Other conditions: mixed buffer pH 6.0, T= 20 °C.

After the gas mixture was changed back to 100% N₂, the initial changes slowly started to reverse. This behaviour became more noticeable after about 68 minutes, when the decrease in Ni-B and Ni-SI (along with the increase in Ni-R) occurred more rapidly. It is likely that the initial slow change, which occurred immediately after changing the gas composition, is due to the time it takes to remove O₂ from the buffer solution.

This recovery suggests that there is a mechanism whereby an auto-activation process can take place. The OCP at the working electrode equilibrated at -0.258 V after the addition of O₂. This potential is still well below $E^{0'}_{(\text{Ni-Si} \rightarrow \text{Ni-B})}$ and $E^{0'}_{(\text{Ni-C} \rightarrow \text{Ni-Si})}$ at this pH (See Table 4.2). The decrease in concentration of Ni-Si and Ni-B in favour of the increase in Ni-R is therefore expected. Furthermore, the fact that the enzyme molecules in this experiment are “electronically connected” between them through the carbon nanoparticle network, may facilitate the transport of electrons between hydrogenase molecules. It can be seen in Figure 5, that nearly half of the enzyme remained fully reduced, in the Ni-R state, upon the addition of O₂. Transport of electrons from reduced enzymes to inactive ones is not unexpected.²¹

Aerobic vs anaerobic formation of Ni-B

The electron acceptor for the oxidation processes just described are different for each case: it is the electrode in the case of the electrochemical activation shown in Figure 6.3; and O₂ in the example shown by Figure 6.5B. The electron transfer in the former would correspond to the outer-sphere mechanism (electrons being transported from the active site, through the Fe-S clusters, and to the electrode). In the latter case, inner-sphere electron transfer would be the mechanism of the oxidation if O₂ binds the active site.¹¹ Figure 6.6 illustrates these different mechanisms for electron removal from the active site. The reaction with O₂ is shown to be in the active site, and to produce H₂O as a result of the reduction. However, it has been shown that H₂O is not the only product and that the active site may not be the only site where the O₂ molecule can be reduced.^{11,22} It must be borne in mind, however, that O₂ can be reduced at the electrode. This would have an effect on the potential of the electrode and therefore on the distribution of redox states of the active site.

Overall, the experiments shown in Figures 6.3 and 6.5 show a difference in the kinetics of Ni-B formation between the reaction with O₂, and the anaerobic electrochemical oxidation. The aerobic formation of Ni-B is faster than the anaerobic one.

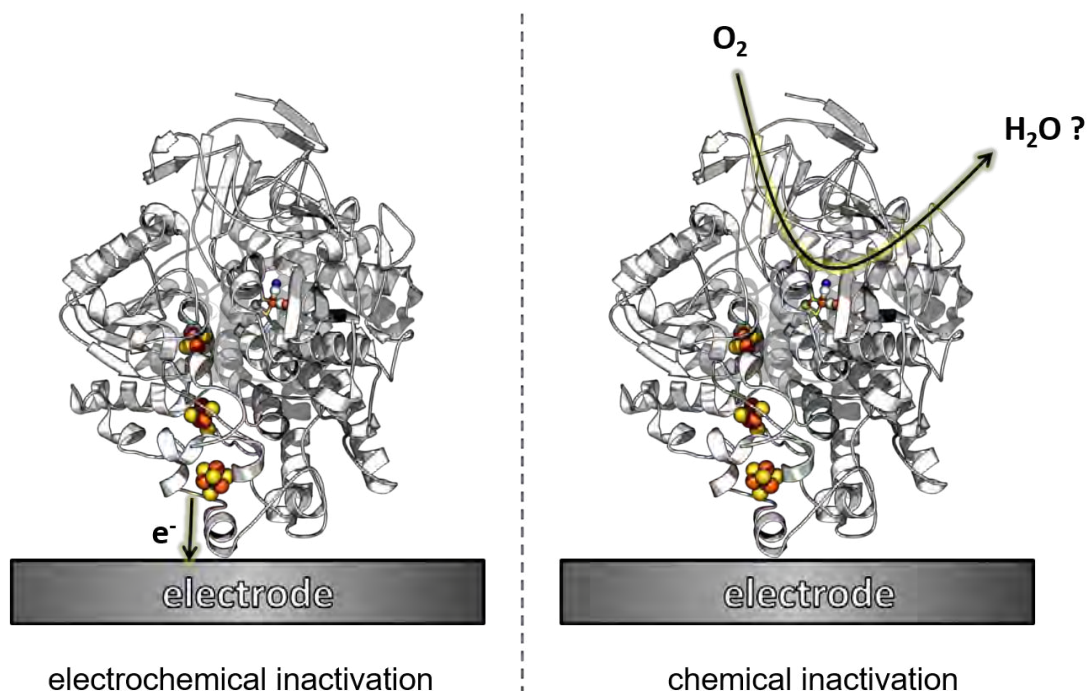


Figure 6.6 Inactivation, by potential and by reaction with O₂, of Hyd-1 adsorbed at an electrode surface. In the inactivation by application of an oxidative potential, the electrons are removed from the enzyme through the Fe-S clusters and into the electrode. In the case of chemical inactivation, the electrons are removed from the enzyme through the active site, by the reduction of O₂.

6.3 O₂ inhibition of catalytic H₂ oxidation

Most of the work on O₂-tolerant hydrogenases, regarding the inactivation and reactivation dynamics, has been done by means of PFV. Changes in the catalytic current of H₂ oxidation upon the addition of O₂, and variations in applied potential, are related to the formation and removal of inactive species of the enzyme. In Chapter 5, the anaerobic inactivation of Hyd-1 under H₂-oxidation conditions was directly linked to the formation of the spectroscopically detected Ni-B state.

In this section, similar investigations will be carried out on the inhibition of O₂ to the catalytic activity of this O₂-tolerant hydrogenase. These enzymes are characterised by their ability to maintain substantial catalytic activity in the presence of O₂. Hyd-1 has been shown to be one of

these enzymes, and it has been shown to be able to fully reduce O_2 to H_2O under turnover conditions.¹¹ Like other membrane-bound O_2 hydrogenases, from group 1, it possess a 4Fe-3S proximal cluster which can undergo two redox transitions in a physiologically relevant potential window; such a cluster has been identified in x-ray structures of other membrane-bound O_2 tolerant hydrogenases.^{5,7,10,23,24}

Figure 6.7 shows the mild inhibition of H_2 oxidation by O_2 . The electrochemistry, shown in panel A, consists of six regions; each with specific conditions of the applied potential and the gas composition being blown through the buffer solution. The grey bar indicates the potential applied at the working electrode. The gas composition, in terms of percentage of O_2 , is specified by the orange bar. There is a constant 99 % H_2 being flowed through the buffer throughout the experiment. Only the other 1 % is changed between N_2 and O_2 . Figure 6.7B shows the changes in the spectrum that result from the addition and the removal of O_2 , under turnover conditions

Step (i) in the electrochemical experiment shows no electrocatalytic current as the enzyme shows no H_2 oxidation activity at such low potential value, -0.594 V. Stepping up the potential to +0.241 V in results in a positive current due to H_2 oxidation, in step (ii). The gas composition was changed from 99:1 $H_2:N_2$ to 99:1 $H_2:O_2$ in step (iii), whilst maintaining the potential at +0.241 V. The current decreased but quickly reached a constant value. This behaviour is consistent with the well-established formation of Ni-B as the only inactive state upon O_2 inhibition of *E. coli* Hyd-1.^{4,11,13} Were there formation of Ni-A, as well as of Ni-B, the addition of O_2 would have resulted in the complete inactivation of the activity since Ni-A takes hours to activate.

Removal of O_2 from the system in step (iv) shows the quick reactivation of the enzyme. In order to ensure that the activation was complete (this is that there was not any Ni-A present); the electrode potential was poised at -0.594 V, in step (v) for quick reduction of inactive states. When the applied potential was raised back to +0.241 V, in step (vi), the electrocatalytic current was no different from that in step (iv). This is in accordance with all the inactive species having been quickly reactivated in

step (iv), upon the removal of O₂. Quick reactivation suggests the exclusive formation of Ni-B, again consistent for the behaviour reported for this enzyme.^{4,13}

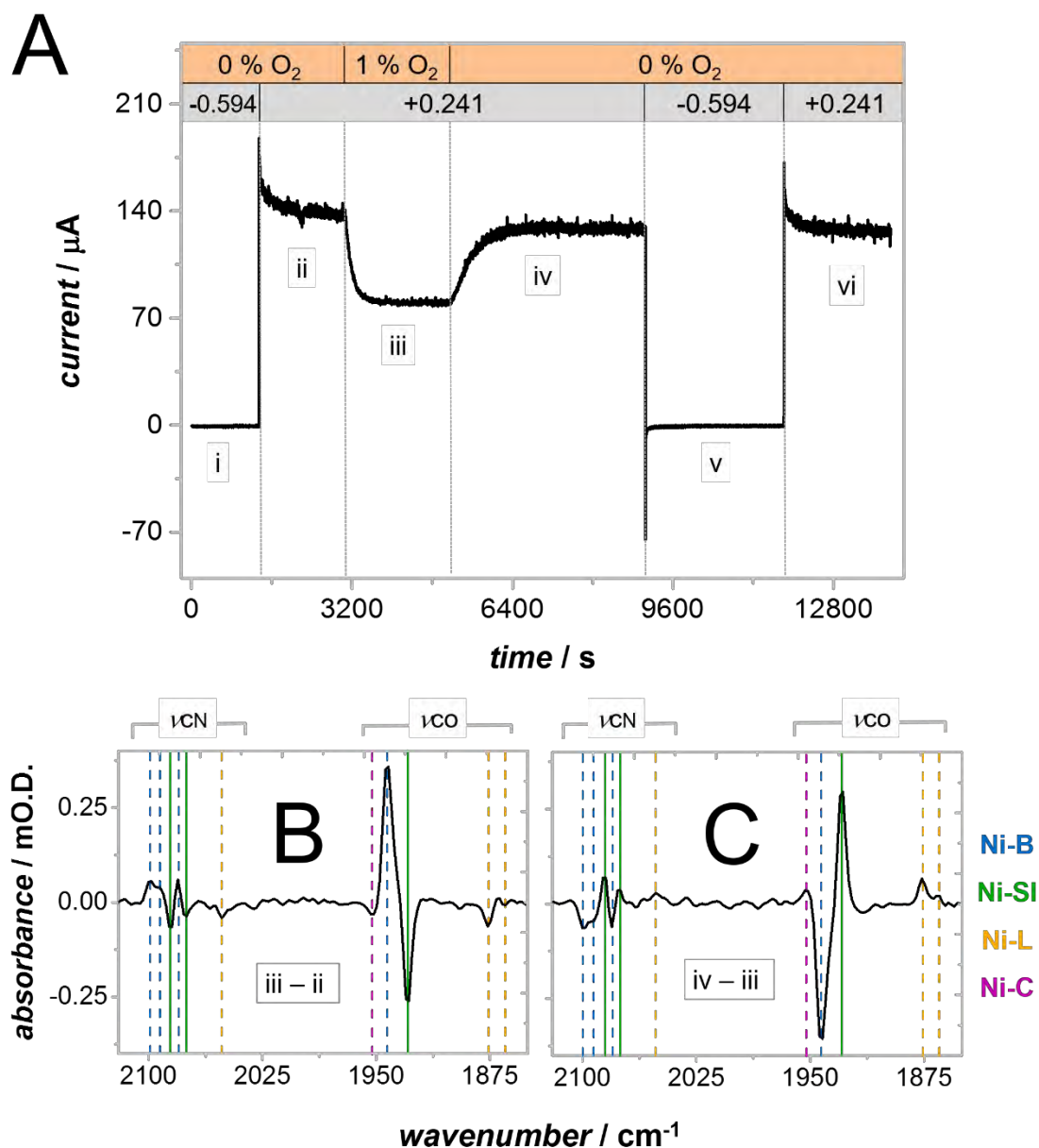


Figure 6.7 The inhibition of H₂ oxidation by O₂. A) Current-time trace of the experiment. The orange bar indicates how the concentration of O₂ was varied over time. The concentration of H₂ was maintained constant at 99 % throughout the entire experiment. The grey bar indicates the applied potential, in V vs SHE, at the working electrode. B) Difference spectrum showing the changes upon the addition O₂ into the system. C) Difference spectrum showing the changes upon the removal of O₂. The changes are fully reversible.

Panels B and C of Figure 6.7 show the changes in the spectral features that result from the addition of O_2 , and its subsequent removal, respectively. Spectrum B shows that the changes in the concentration of active site species under steady state conditions, when the enzyme is maintaining H_2 oxidation whilst being inhibited by O_2 . These changes are: a significant decrease in Ni-SI, a small decrease in Ni-C and Ni-L, and a significant increase in Ni-B. The Ni-B bands that appear are the ν_{CO} at 1943 cm^{-1} , and three ν_{CN} bands at 2081 , 2093 and 2100 cm^{-1} . These are the bands that have been attributed to Ni-B in Chapters 4 and 5. In spectrum C, this is after O_2 has been removed, the changes just described were reversed. This is, Ni-SI increased (along with small amounts of Ni-C and Ni-L); and Ni-B decreased.

These results represent the first direct observation of the spectroscopically-characterised Ni-B (as has been described by IR experiments in solution) being formed as a result of O_2 inhibition, while the loss of activity is being measured simultaneously. This confirms that the “ready” inactive species detected electrochemically from PFE, is in fact the same state that is formed under anaerobic oxidative conditions.

Additionally, these spectra show that the reaction of this hydrogenase with O_2 , under catalytic H_2 -oxidation conditions, is a ‘clean’ reaction. This is in the sense that the aerobic inactivation produces one single product, Ni-B (Figure 6.8); as opposed to forming other several O_2 -damaged species of the active site. This observation provides further evidence that O_2 -tolerant hydrogenases avoid forming damaged oxidised states upon the attack of O_2 . The Ni-B state, that is formed from the aerobic inactivation, is completely and quickly reactivated back to Ni-SI once the O_2 is removed (Figure 6.7C).

The fact that the Ni-B state formed in these experiments also presents three cyanide bands (2100 , 2093 , and 2081 cm^{-1}), indicating the presence of two forms; further confirms that these two species can be attributed to the ready Ni-B state. This on the basis that all the bands appear together as a result of the reaction of the enzyme with O_2 ; and that they are quickly removed as O_2 is taken out

of the system and the activity recovers fully; that is, they show the same kinetic behaviour. Moreover, only one extra ν_{CN} band can be distinguished. This suggests that the ν_{CO} band of the second form must overlap with the main ν_{CO} band of Ni-B at 1943 cm^{-1} . This would indicate that these two species are rather similar structurally, perhaps different protonation species of the Ni-B state.

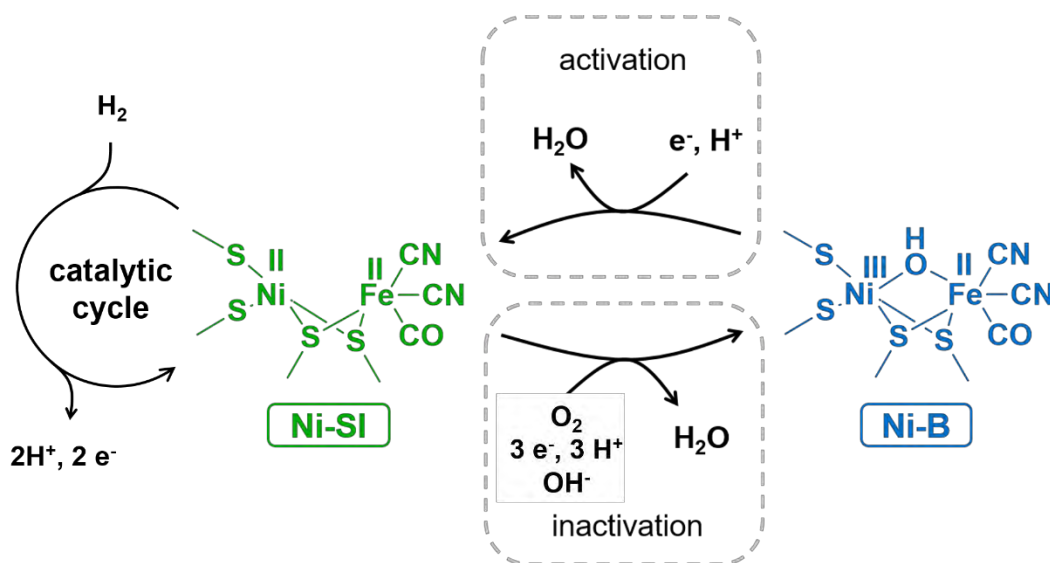


Figure 6.8 O₂ inhibition of H₂ oxidation in an O₂-tolerant hydrogenase. The attack of oxygen in the 'inactivation' step produces only the Ni-B state. This ready species can be quickly reactivated to the Ni-SI state. The H₂ oxidation catalytic cycle is simplified to place an emphasis on the inactivation mechanism.

6.4 Summary

This chapter presented a more careful investigation on the chemistry of the formation and of the inactive species of Hyd-1. This was done by means of the technique presented in this thesis; in which the enzyme, adsorbed on a carbon electrode, is investigated by using electrochemistry and IR spectroscopy simultaneously.

The formation of the inactive Ni-B species was investigated, both aerobically and anaerobically. The same species (same spectral features) was formed under all these conditions. This is in line with

previous observations, from EPR and PFE experiments, which suggest Ni-B is the only inactive species formed in *E. coli* Hyd-1 upon inactivation (anaerobically and aerobically).^{11,14} However, the evidence presented in this chapter suggests that the mechanism whereby Ni-B is formed anaerobically differs from that of its aerobic formation.

It was shown that the reaction of O₂ with Hyd-1, under catalytic turnover, is a 'clean' reaction in the sense that only Ni-B is formed, and it is formed quickly. There is no evidence of other O₂-damaged forms of the enzyme being produced. This provides further evidence on the ability of O₂-tolerant hydrogenases to effectively maintain catalytic activity in the presence of O₂; which is accomplished by a neat formation of a single inactive state from which the enzyme can quickly reactivate.

References

- 1 S. Kurkin, S. J. George, R. N. F. Thorneley and S. P. J. Albracht, *Biochemistry*, 2004, **43**, 6820–31.
- 2 V. M. Fernandez, E. C. Hatchikian and R. Cammack, *Biochim. Biophys. Acta*, 1985, **832**, 69–79.
- 3 S. E. Lamle, S. P. J. Albracht and F. A. Armstrong, *J. Am. Chem. Soc.*, 2005, **127**, 6595–604.
- 4 M. J. Lukey, A. Parkin, M. M. Roessler, B. J. Murphy, J. Harmer, T. Palmer, F. Sargent and F. A. Armstrong, *J. Biol. Chem.*, 2010, **285**, 3928–38.
- 5 J. Fritsch, P. Scheerer, S. Frielingsdorf, S. Kroschinsky, B. Friedrich, O. Lenz and C. M. T. Spahn, *Nature*, 2011, **479**, 249–252.
- 6 M.-E. Pandelia, W. Nitschke, P. Infossi, M.-T. Giudici-Ortoni, E. Bill and W. Lubitz, *Proc. Natl. Acad. Sci. U. S. A.*, 2011, **108**, 6097–102.
- 7 A. Volbeda, P. Amara, C. Darnault, J.-M. Mouesca, A. Parkin, M. M. Roessler, F. A. Armstrong and J. C. Fontecilla-Camps, *Proc. Natl. Acad. Sci.*, 2012, **109**, 5305–10.
- 8 Y. Shomura, K.-S. Yoon, H. Nishihara and Y. Higuchi, *Nature*, 2011, **479**, 253–6.
- 9 M. M. Roessler, R. M. Evans, R. A. Davies, J. Harmer and F. A. Armstrong, *J. Am. Chem. Soc.*,

- 2012, **134**, 15581–94.
- 10 T. Goris, A. F. Wait, M. Saggu, J. Fritsch, N. Heidary, M. Stein, I. Zebger, F. Lenzian, F. A. Armstrong, B. Friedrich and O. Lenz, *Nat. Chem. Biol.*, 2011, **7**, 310–8.
- 11 P. Wulff, C. C. Day, F. Sargent and F. A. Armstrong, *Proc. Natl. Acad. Sci. U. S. A.*, 2014, **111**, 6606–11.
- 12 I. Dance, *Chem. Sci.*, 2015, **6**, 1433–1443.
- 13 R. M. Evans, A. Parkin, M. M. Roessler, B. J. Murphy, H. Adamson, M. J. Lukey, F. Sargent, A. Volbeda, J. C. Fontecilla-Camps and F. A. Armstrong, *J. Am. Chem. Soc.*, 2013, **135**, 2694–2707.
- 14 M. J. Lukey, M. M. Roessler, A. Parkin, R. M. Evans, R. A. Davies, O. Lenz, B. Friedrich, F. Sargent and F. A. Armstrong, *J. Am. Chem. Soc.*, 2011, **133**, 16881–16892.
- 15 A. K. Jones, S. E. Lamle, H. R. Pershad, K. A. Vincent, S. P. J. Albracht and F. A. Armstrong, *J. Am. Chem. Soc.*, 2003, **125**, 8505–14.
- 16 V. Fourmond, P. Infossi, M. T. Giudici-Ortoni, P. Bertrand and C. Léger, *J. Am. Chem. Soc.*, 2010, **132**, 4848–4857.
- 17 M.-E. Pandelia, V. Fourmond, P. Tron-Infossi, E. Lojou, P. Bertrand, C. Léger, M.-T. Giudici-Ortoni and W. Lubitz, *J. Am. Chem. Soc.*, 2010, **132**, 6991–7004.
- 18 M. Saggu, C. Teutloff, M. Ludwig, M. Brecht, M.-E. Pandelia, O. Lenz, B. Friedrich, W. Lubitz, P. Hildebrandt, F. Lenzian and R. Bittl, *Phys. Chem. Chem. Phys.*, 2010, **12**, 2139–48.
- 19 W. Lubitz, H. Ogata, O. Ruediger and E. Reijerse, *Chem. Rev.*, 2014, **114**, 4081–4148.
- 20 M. Saggu, I. Zebger, M. Ludwig, O. Lenz, B. Friedrich, P. Hildebrandt and F. Lenzian, *J. Biol. Chem.*, 2009, **284**, 16264–16276.
- 21 C. Bagyinka, *Int. J. Hydrogen Energy*, 2013, **39**, 18521–18532.
- 22 L. Lauterbach and O. Lenz, *J. Am. Chem. Soc.*, 2013, **135**, 17897–905.
- 23 O. Schröder, B. Bleijlevens, T. E. de Jongh, Z. Chen, T. Li, J. Fischer, J. Förster, C. G. Friedrich, K. a Bagley, S. P. J. Albracht and W. Lubitz, *J. Biol. Inorg. Chem.*, 2007, **12**, 212–33.

- 24 S. Frielingsdorf, J. Fritsch, A. Schmidt, M. Hammer, J. Löwenstein, E. Siebert, V. Pelmeshikov, T. Jaenicke, J. Kalms, Y. Rippers, F. Lenzian, I. Zebger, C. Teutloff, M. Kaupp, R. Bittl, P. Hildebrandt, B. Friedrich, O. Lenz and P. Scheerer, *Nat. Chem. Biol.*, 2014, **10**, 378–85.

Chapter 7

CO binding and inhibition of Hyd-1

7.1 Introduction

7.1.1 CO interaction with NiFe hydrogenases

The binding and inhibition of CO in standard NiFe hydrogenases is well established. Protein film electrochemistry has been used extensively to investigate the inhibition of both H₂ oxidation-, and H⁺ reduction activity in these enzymes; ¹⁻⁴ and CO has been shown to be a strong and reversible inhibitor. Furthermore, the binding of CO to the active site of standard NiFe hydrogenases has been studied by IR and EPR spectroscopy for several standard NiFe hydrogenases of different organisms.⁵⁻⁷

On the contrary, the interaction of CO with O₂-tolerant NiFe hydrogenases is far from clear. For the membrane-bound hydrogenase of *R. eutropha*, H₂ oxidation activity is reported to not be inhibited by CO, even at large excess (13 % H₂, 87 % CO).² The NiFe hydrogenase from *A. aeolicus* was also reported to not exhibit inhibition when exposed to CO.⁸ Nonetheless, CO-bound states of the active site have been identified for this enzyme by means of IR spectroscopy.⁹ On the other hand, the H₂ oxidation activity of Hyd-1, from *E. coli*, has been shown to be weakly inhibited by CO.⁴ Recent reviews describe O₂-tolerant NiFe hydrogenases as being CO resistant,¹⁰ and as not-significantly inhibited by CO.¹¹

For the case of regulatory hydrogenases, which were thought to be resistant to CO and O₂, it has been shown recently that CO does bind at the active site and acts as an inhibitor of H₂ oxidation activity.¹²

7.1.2 Structural characterisation of CO-bound states of the active site

X-ray diffraction studies have identified CO bound to the active site, via coordination to the Ni, in the standard NiFe hydrogenase from *D. vulgaris* MF.¹³ This structural study showed that the CO

binds to the Ni atom only (Figure 7.1). This is in contrast to the hydroxyl ligand in the inactive states (Ni-B and Ni-A), or the hydride (in the Ni-R and Ni-C states), which binds in the bridging position between the metal ions.^{14,15}

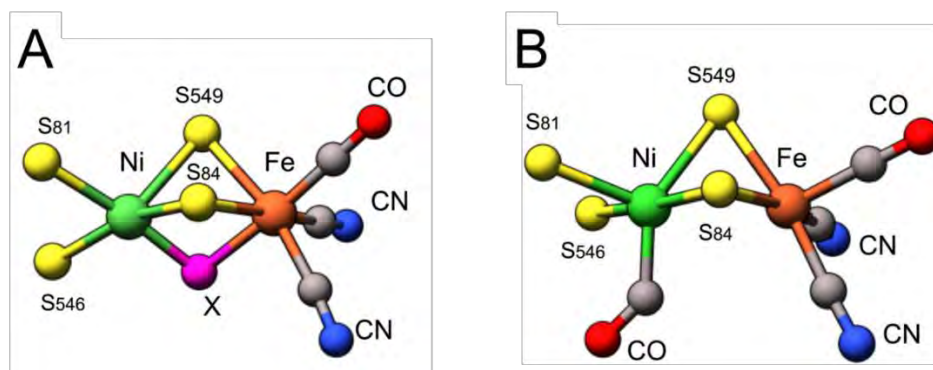


Figure 7.1 X-ray crystal structure of the active site of *D. vulgaris* MF hydrogenase, solved by Ogata et al.¹³ A) The active site in its oxidised or reduced forms carries an oxygenic, or hydrogenic species, (here shown as X) as a bridging ligand. B) CO-bound state (PDB: 1UB), the CO is bound to the Ni atom. Adapted from *Biochim. Biophys. Acta*, 1797, Pandelia, M.-E.; Ogata, H.; Currell, L. J.; Flores, M.; Lubitz, W. Inhibition of the [NiFe] hydrogenase from *Desulfovibrio vulgaris* Miyazaki F by carbon monoxide: An FTIR and EPR spectroscopic study, 304–313, Copyright 2010, with permission from Elsevier.

Three different CO-bound states of the active site have been identified using IR spectroscopy.^{6,7,9} CO can bind the active Ni-SI state to form what is known as Ni-SCO. This species can then be electrochemically reduced to form the Ni-SCO_{red}, which exhibits a shift to lower wavenumber in all the ν_{CN} and ν_{CO} bands (included that of the extrinsic CO). The reduced form has one extra electron in its proximal cluster.^{6,7}

The third CO-bound state that has been identified is a paramagnetic state, known as Ni-CO. This state has been formed by illuminating the Ni-C state in the presence of CO, at cryogenic temperatures. Photoillumination of Ni-C results in the dissociation of the proton (bound as a hydride in the Ni-C state) to give the paramagnetic Ni-L state. Once in the Ni-L state, which has no bridging group bound, CO can bind to the active site so that the monovalent Ni-CO state is formed.^{6,16,17} Figure 7.2 shows the formation of these known CO-bound states.

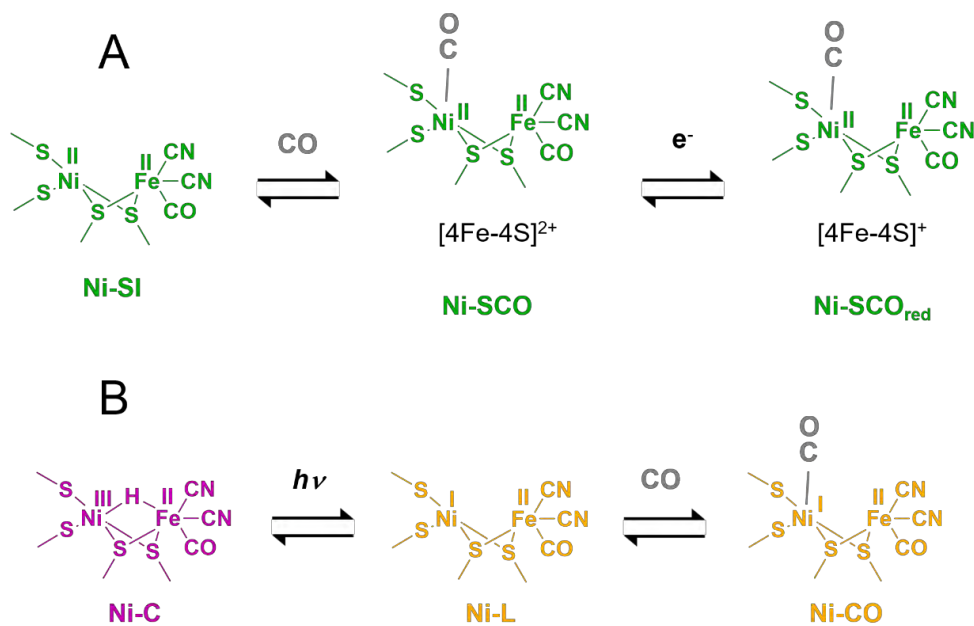


Figure 7.2 The binding of CO to the active site of NiFe hydrogenases. A) CO can bind directly to the Ni-SI state to give the Ni-SCO state. This state can be further reduced (one electron added to the proximal cluster) to give the Ni-SCO_{red} state. B) It has been also shown that, at cryogenic temperatures, the illumination of Ni-C in the presence of CO gives the Ni-CO state.

Of the states shown in Figure 7.2, only the Ni-SCO has been identified in an O₂-tolerant hydrogenase, by IR spectroscopy.⁹ The rest, including the Ni-SCO_{red}, have been detected in standard hydrogenases of several organisms.^{5-7,16,17} All CO-bound states of the active site have been shown to photodissociate at cryogenic temperatures.^{5,6,9,13,16}

In this chapter, the binding of CO to Hyd-1 will be studied under both turnover and non-turnover conditions using the technique developed in this work.

7.2 CO binding to Hyd-1

To initially investigate the binding of CO to *E. coli* Hyd-1; CO was added to the enzyme at different potentials. Figure 7.3 shows the spectra under N₂ and under CO for different potentials, from the most reduced state of the enzyme (at -0.594 V) to the most oxidised state (at +0.356 V). The

experiments on this section were carried out by Eleanor Hall, a part II student, under my supervision. The spectra d and f (in Figure 7.3) are shown as difference spectra. They were obtained by subtracting the spectrum recorded under CO from the that recorded under N₂, at the specified potential.

The enzyme film was held at each potential under N₂ first. Then, the gas bubbled through the buffer was changed from 100 % N₂ to 100 % CO. The sample was allowed to equilibrate to the new gas atmosphere for 25 min, and then a new spectrum was recorded under CO. The addition of CO to the most oxidised sample, at +0.356 V, does not show changes to the ν_{CO} or ν_{CN} bands of the active site. Only Ni-B is present under both N₂ and CO atmospheres. At the most negative potential, -0.594 V, the addition of CO to the system does not produce any changes in the spectrum either.

However, at the two intermediate potentials (-0.074 and -0.199 V) changes in the spectra arise as a result of the addition of CO. In spectrum (d), at -0.074 V, four positive bands appear. There are three new bands in the 2125-2025 cm⁻¹ region (normally the ν_{CN} region) at 2082, 2072 and 2060 cm⁻¹; and one new band at 1929 cm⁻¹ in the ν_{CO} region. Although the 1929 cm⁻¹ band coincides with the ν_{CO} band position of the Ni-SI state, it is unlikely that this band corresponds to such state. The ν_{CN} bands do not correspond to those of the Ni-SI state; and moreover, there is a decrease in intensity for the band at 2086 cm⁻¹, which does correspond to a loss of one of the ν_{CN} bands of the Ni-SI state.

These spectral differential features that arise in spectrum (d) can be attributed to the Ni-SCO state, with the 2060 cm⁻¹ band assigned to the extrinsic CO bound to the Ni. This assignment is made on the basis of observed bands for the Ni-SCO state in other NiFe hydrogenases. Table 7.1 shows a comparison of the wavenumber positions of the Ni-SCO state of other NiFe hydrogenases, and the bands observed in spectrum (d) of Figure 7.3, assigned to this state.

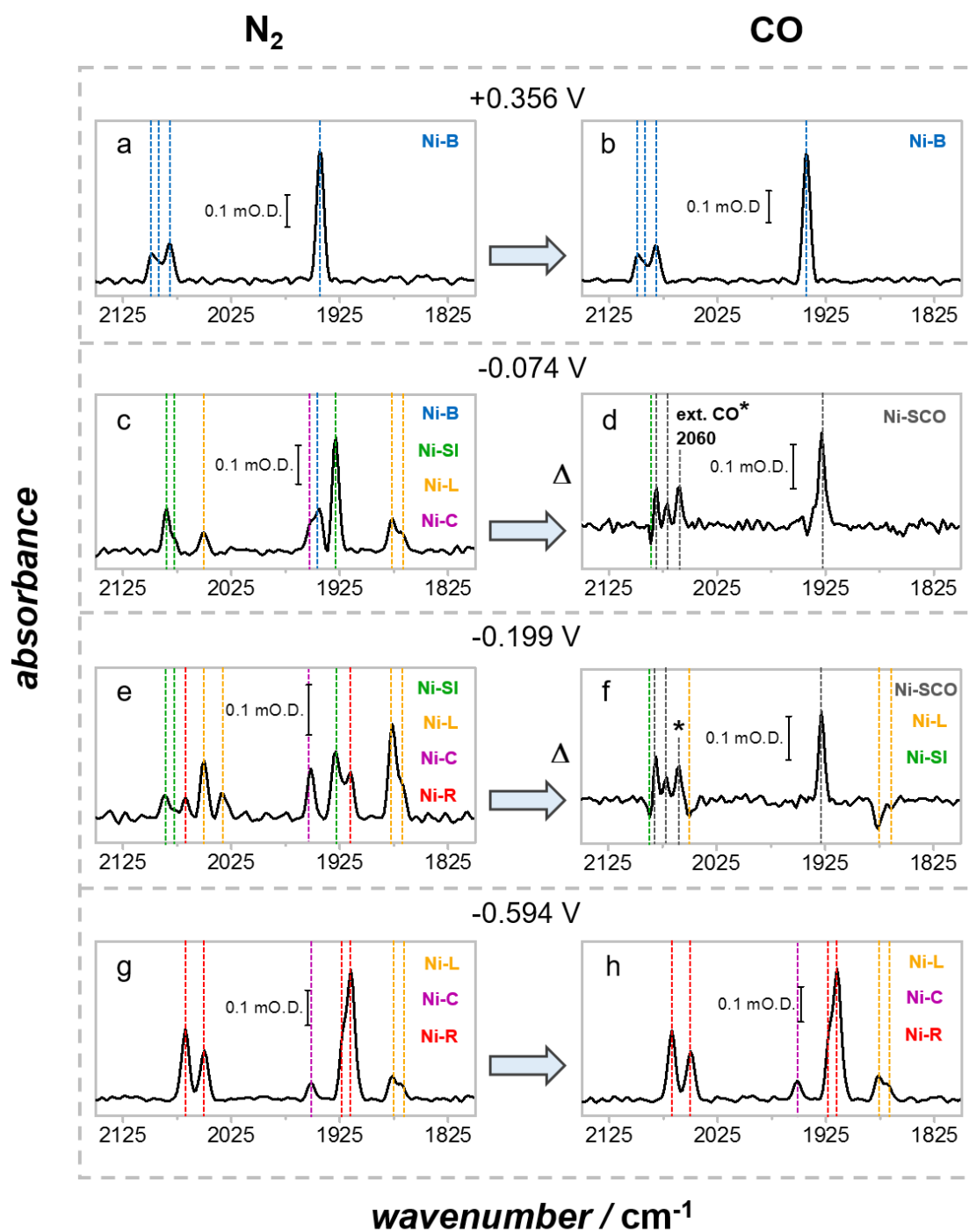


Figure 7.3 The binding of CO to Hyd-1 at different potentials. The column on the left are spectra recorded under a N_2 atmosphere, and the column to the right recorded under a CO atmosphere. At each potential, a spectrum was taken under N_2 and then the gas was exchanged for CO and a second spectrum was recorded after 25 min. Spectra (d) and (f) are shown as difference spectra; the CO saturated sample recorded against the sample under N_2 . Other conditions: mixed buffer pH 6.0, 20 °C.

Table 7.1 Wavenumber position of the ν_{CN} , intrinsic and extrinsic ν_{CO} bands, for the Ni-SCO state in different NiFe hydrogenases.

<i>enzyme</i>	<i>wavenumber / cm⁻¹</i>		
	ν_{CN}	<i>ext. ν_{CO}</i>	<i>int. ν_{CO}</i>
<i>C. (A.) vinosum</i> ⁵	2082, 2069	2060	1929
<i>D. fructosovorans</i> ⁷	2083, 2068	2055	1928
<i>D. vulgaris MF</i> ⁶	2084, 2071	2056	1941
<i>A. aeolicus</i> * ⁹	2082, 2072	2066	1925
<i>E. coli Hyd-1</i> *	2082, 2072	2060	1929

*O₂-tolerant hydrogenases

At -0.199 V, the addition of CO also results in the formation of this Ni-SCO state (spectrum f in Figure 7.3). Additionally, a loss of Ni-L is evident, from both the ν_{CO} and ν_{CN} bands. What is common between the spectra in which the addition of CO results in the formation of Ni-SCO, is that there was Ni-SI present in the spectra recorded under N₂ at those potentials. From this observation it can be inferred that only the Ni-SI state of Hyd-1 can bind CO. The loss of Ni-L in spectrum f results most likely from an equilibration between states after the CO-bound state is formed from Ni-SI.

Similar results to these shown here for Hyd-1, have been reported for the O₂-tolerant hydrogenase 1 from *A. aeolicus*.⁹ This is that only one CO-bound state (Ni-SCO) was formed, and that CO does not bind the most oxidised, nor the most reduced states of the enzyme. Similarly to Hyd-1 in this work, the IR experiments on *A. aeolicus* did not detect a Ni-SCO_{red} upon reduction either. The reason why these O₂-tolerant hydrogenases do not form the reduced Ni-SCO_{red} state is very likely related to the special proximal cluster of these enzymes. The reduction potentials of the 4Fe-3S cluster of Hyd-1 are higher than that of the Ni-B/Ni-SI couple.¹⁸ This means that; unlike the Ni-SCO of standard hydrogenases, which is formed at a potential where the proximal cluster can

accept an electron, the Ni-SCO herein described possess a fully reduced proximal Fe-S cluster already and cannot be further reduced.

The other state that was not detected in these experiments is a Ni-CO; that is, a Ni(I) species with a bound CO (Figure 7.2B). Although this NiFe hydrogenase forms Ni-L under the conditions of the experiment, this state was not detected. This is not completely unexpected since it has been reported that the binding of CO to the Ni(I) species occurs at lower temperatures with respect to the binding of the proton to form Ni-C.^{6,19} All the Ni-CO states detected for standard hydrogenases has been at cryogenic temperatures.^{6,17}

CO has been shown to weakly inhibit the activity of Hyd-1 in protein film electrochemistry experiments.⁴ In the next section the IR, spectroelectrochemical investigations of the inhibition by CO of both H₂ oxidation and H⁺ reduction in Hyd-1 will be discussed.

7.3 PFIRE studies of CO inhibition of Hyd-1 under turnover

7.3.1 Inhibition of H₂ oxidation

Figure 7.4 shows the inhibition by CO of the H₂ oxidation activity of Hyd-1, measured electrochemically. IR spectra were collected with and without CO under turnover conditions simultaneously to investigate the chemistry of the active site under the same conditions.

In Figure 7.4A, it can be seen that the inhibition by CO is fully reversible by removing CO from the system (as has been established previously in the literature⁴). The change in the gas composition from 10 : 90 H₂ : N₂ to 10 : 90 H₂ : CO, results in a loss of activity of approximately 21 %. The activity however, is returned to its original value after 461 s, after flushing out the CO.

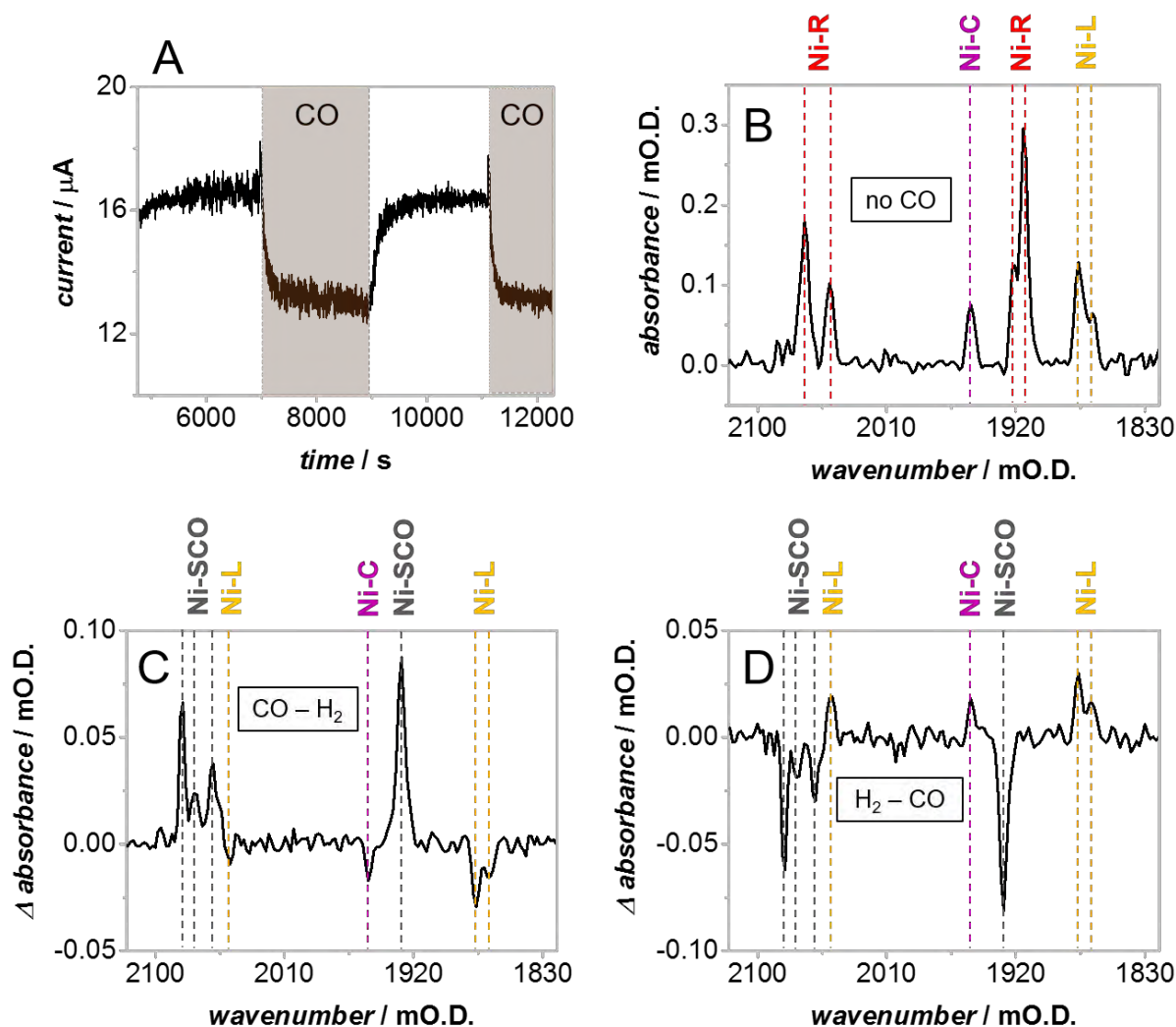


Figure 7.4 CO inhibition of H₂ oxidation in Hyd-1. The potential applied at the working electrode was of -0.199 V. Throughout the experiment the H₂ concentration was kept constant at 10 %, in either N₂ or CO. Panel A shows the electrocatalytic current from H₂ oxidation, the shaded regions represent the time intervals in which the gas composition was changed from 90 % N₂ to 90 % CO. B) A spectrum recorded under turnover conditions before the addition of CO. Spectra (C) and (D) show the changes that result from adding, and removing CO, respectively. Other conditions: mixed buffer pH 6.0, 20 °C. Pump flow rate: 59 mL min⁻¹.

Figure 7.4B shows an IR spectrum (displaying both the ν_{CO} and ν_{CN} regions) recorded under a 10 : 90 H₂ : N₂ atmosphere before any CO was added. It shows mainly Ni-R, with Ni-L and Ni-C also present in significant amounts, under turnover. It does not show, however, Ni-SI. It was explained in Chapter 5 that at this potential (-0.199 V) this state is short lived and hence not detected under turnover, although it is proposed to be an intermediate in the catalytic cycle.

Upon the addition of CO, the spectrum shown in Figure 7.4C was recorded after the current had reached a steady value. This spectrum is shown as a difference spectrum and therefore displays the changes in the bands, relative to the spectrum shown in Figure 7.4B. There is loss in the steady state concentrations of Ni-L and Ni-C; and positive bands for the formation of the Ni-SCO state (described in the last section), including the 2060 cm^{-1} band for the extrinsic CO. Nonetheless, no loss of the Ni-R state is observed, although this is the predominant state under turnover conditions for Hyd-1.

It is important to note that, under turnover, the net formation of new positive bands (as in this case the formation of Ni-SCO) along with the net loss of others (like Ni-C and Ni-L in this experiment) does not necessarily imply that the new species was formed directly from the species that was lost. This is to say that the loss of Ni-C and Ni-L, along with the corresponding formation of Ni-SCO (in Figure 7.4C) does not necessarily mean that Ni-SCO is directly formed from Ni-C and Ni-L. It was shown in the previous section that CO can only bind the Ni-SI state in Hyd-1. The scheme in Figure 7.5 is therefore suggested as the mechanism whereby CO inhibits H_2 oxidation activity in Hyd-1.

The fact that Ni-SCO is formed by the addition of CO under turnover confirms that Ni-SI is present in the system, despite the fact that it is not detected spectroscopically under these experimental conditions (this is, at -0.199 V). CO is then able to “trap” this short-lived intermediate. After the system has equilibrated in the presence of CO, the net steady state concentrations of both Ni-C and Ni-L decrease, but not that of Ni-R. Ni-R continues to be the predominant state under turnover in the presence of CO. An explanation for this can be that the timescale at which the binding of CO happens is faster than the removal of the Ni-R species, which appears to be the slowest step of the cycle (as Ni-R is always the predominant state under turnover, at all conditions studied thus far). Therefore, the steady state concentration of the new Ni-SCO state rises “at the expense” of the steady state concentrations of Ni-L and Ni-C, without there being a significant decrease in the steady state concentration of Ni-R.

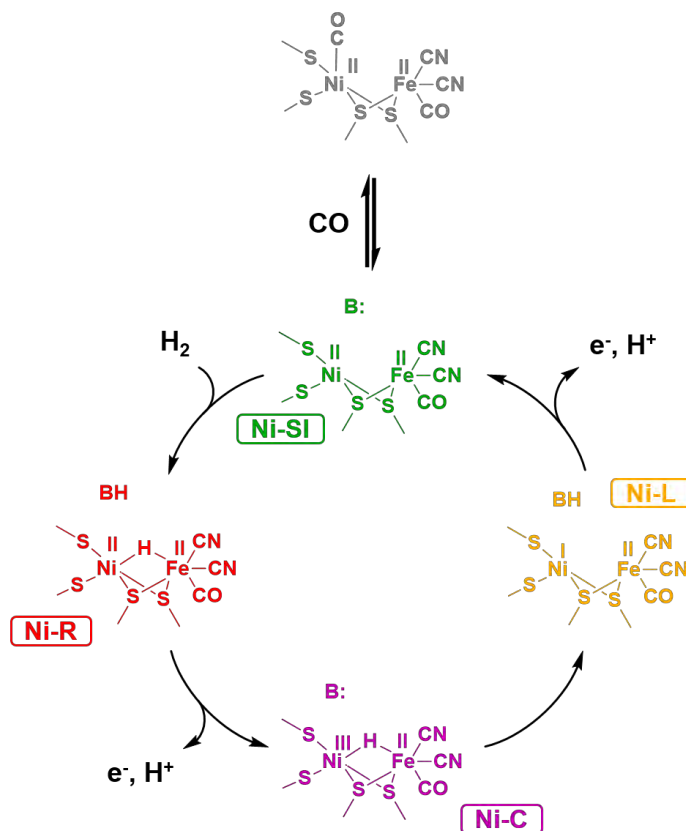


Figure 7.5 The mechanism of CO inhibition of H₂ oxidation in Hyd-1. CO binds the Ni-SI state to give the inactive Ni-SiCO state.

The spectrum shown in Figure 7.4D shows that the changes that resulted from adding CO to the system are fully reversible, this spectrum was recorded after the current had reached a steady value and the enzyme had recovered its initial activity. It is presented as a difference spectrum relative to the spectrum recorded under CO. All the bands of the Ni-SiCO state, including the 2060 cm⁻¹ band corresponding to the extrinsic CO, are lost. In addition to that, the steady state concentration of Ni-L and Ni-C rise again, after CO has been removed from the system.

In the experiments described in Figure 7.4, the formation of the Ni-SiCO state has been directly related to the electrochemical loss of activity for H₂ oxidation by Hyd-1 in the presence of CO. The inhibition of the H⁺ reduction of Hyd-1 at low pH will be investigated next.

7.3.2 Inhibition of H⁺ reduction

It has been reported in the literature that Hyd-1 becomes an efficient H₂ producer below pH 4.²⁰ In Chapter 5, IR spectroelectrochemical investigations of H⁺ reduction showed that under turnover, Ni-R, Ni-C, and Ni-L were the species detected at low potentials (which is where H⁺ reduction can occur). Figure 7.6 shows the CO inhibition of H⁺ activity in Hyd-1, measured electrochemically by PFE, along with IR spectra recorded *in situ*.

Figure 7.6B shows the IR spectrum, both ν_{CN} and ν_{CO} regions, of Hyd-1 under catalytic H⁺ reduction conditions, before the addition of CO (This is under a 100 % N₂ atmosphere). Ni-R is the main species. Ni-C is also present along with just a small quantity of Ni-L, consistent with the pH of the experiment (pH 3.8). The addition of CO results in the formation of the Ni-SCO state. Figure 7.6D shows the increase of this CO-inhibited state along with the loss in the steady state concentration of Ni-R. According to earlier observations in this chapter, in which it was established that Ni-SI is the redox state of the active site that binds CO, it follows that Ni-SI should be formed during H⁺ reduction conditions. It is not detected in the IR spectrum in Figure 7.6B, which is consistent with it being short lived under such experimental conditions (-0.609 V), as was discussed in Chapter 5. However, the fact that Ni-SCO is formed confirms that Ni-SI is indeed present in this catalytic cycle. Figure 7.7 shows the proposed mechanism of CO inhibition of H⁺ reduction in Hyd-1.

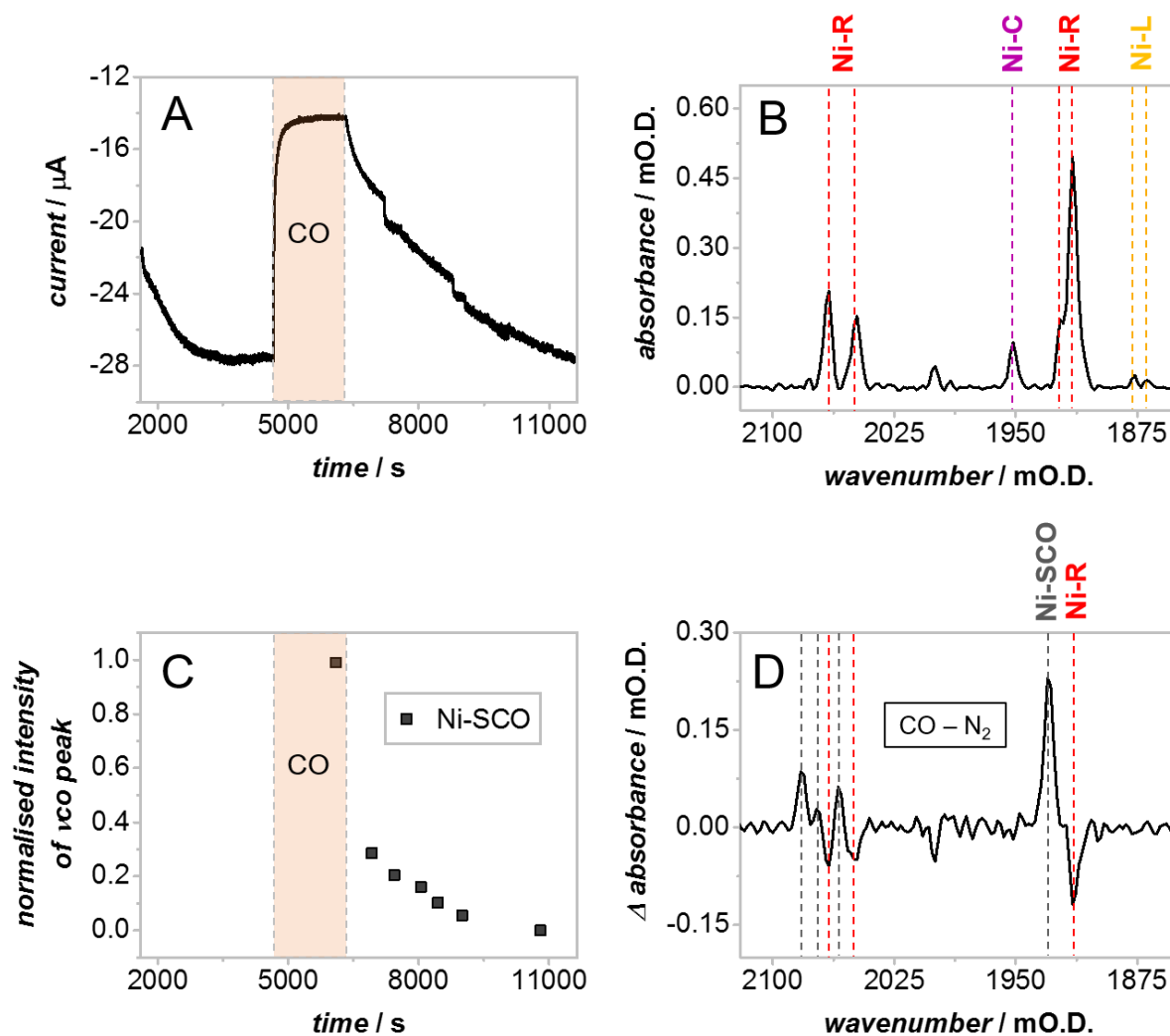


Figure 7.6 CO inhibition of H^+ reduction in Hyd-1. The potential applied at the working electrode was -0.609 V. Panel A shows the electrocatalytic current. The gas atmosphere was 100 % N_2 , except for the shaded area when it was changed to 100 % CO. The change in the initial current is the results of an equilibration from a previous potential step. B) IR spectrum of Hyd-1 under turnover conditions before the addition of CO. C) The normalised intensity of the intrinsic ν_{CO} peak, of the CO-inhibited Ni-SCO state, as a function of time. D) Difference spectrum showing the changes that arise from adding CO to the system, after the current had equilibrated. Other conditions: mixed buffer pH 3.8, $20^\circ C$.

Figure 7.6A shows that the CO inhibition of H^+ reduction activity in Hyd-1 is also fully reversible. However, it is evident that the time it takes to inhibit the enzyme is shorter than the time takes to fully recover the activity after CO is removed from the system. This is in contrast to the recovery from CO inhibition observed for H_2 oxidation, in Figure 7.4A. In the latter, the timescale of the recovery was the same as that of the inhibition.

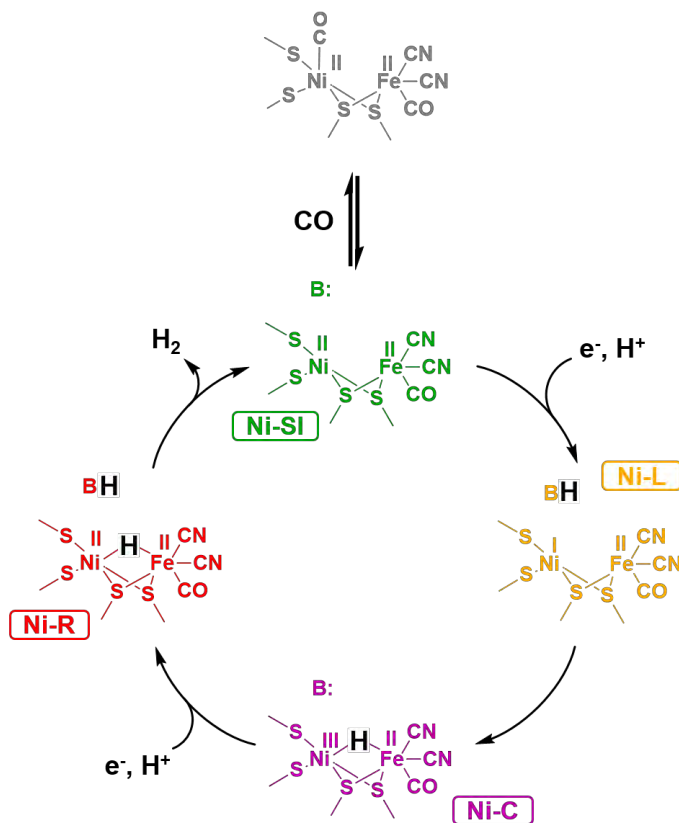


Figure 7.7 The mechanism of H^+ reduction at the active site of Hyd-1. CO binds the Ni-SI state to form the inactive Ni-SCO state.

7.4 Summary

The potential dependence of the binding of CO to the active site of *E. coli* Hyd-1 was characterised by means of IR spectroelectrochemistry. It was found out that only the Ni-SI state can bind the CO. The CO-bound state was assigned to be the Ni-SCO state; such state consists on Ni(II) bound to CO, at the same redox level of Ni-SI. This assignment was done on the basis of Ni-SCO states for other NiFe hydrogenases characterised in the literature, as described on Table 7.1. This Ni-SCO state of Hyd-1 exhibits four IR bands: The bands at 2082, and 2072 cm^{-1} were assigned to the CN^- stretching modes; the band at 1929 cm^{-1} to the intrinsic CO stretch mode, and the 2060 cm^{-1} to the CO stretch

of the extrinsic CO that binds the active site to form the inhibited state. The CO binding behaviour of Hyd-1 is comparable to that reported for another O₂-tolerant hydrogenase from *A. aeolicus*,⁹ for which only the Ni-SCO was detected in an spectroelectrochemical investigation of CO binding.

The CO inhibition of H₂ oxidation and H⁺ reduction activity was investigated by means of protein film IR spectroelectrochemistry. For the case of H₂ oxidation it was shown that the inactivation by CO, as detected electrochemically, coincides with the formation of the just-described Ni-SCO species, as measured spectroscopically. The inhibition was shown to be fully reversible, in the sense that when the current had fully recovered, the Ni-SCO species had been completely removed as well (Figure 7.4).

For the case of H⁺ reduction, the inhibition of this catalytic process by CO was described for the first time in an O₂-tolerant hydrogenase, electrochemically and spectroscopically. It was shown that CO inhibits such process and that it does so in a fully reversible manner. However, unlike in the case of H₂ oxidation, the re-activation from the CO bound state exhibits a slower behaviour than that of the initial inhibition. In terms of IR spectroscopy, it was shown that the Ni-SCO state is formed when the enzyme is inhibited, and that it is removed while the enzyme regains its activity until it does so completely (Figure 7.6). Additionally, this experiment confirmed that Ni-SI is indeed formed under H⁺ reduction conditions, and hence plays a role in the catalytic cycle. Ni-SI was not detected under these conditions in Chapter 5 when such investigation was done. However, the fact that CO can inhibit the enzyme, to form Ni-SCO, provides strong evidence for there being Ni-SI formation under turnover, this because it was established earlier in this chapter that only Ni-SI can bind CO. This provided more solid grounds for the proposed mechanism of H⁺ reduction by Hyd-1, which includes Ni-SI as true intermediate (Figure 7.7).

Overall, the work in this chapter represents the first thorough investigation on the interaction of CO with an O₂-tolerant NiFe hydrogenase. It was shown that CO does bind this enzyme, to form only one state, Ni-SCO. Furthermore, it was also shown that CO does inhibit both H₂ oxidation and H⁺

reduction activity in this O₂-tolerant hydrogenase. This study helps clarify the confusing literature on this topic.

References

- 1 C. Léger, S. Dementin, P. Bertrand, M. Rousset and B. Guigliarelli, *J. Am. Chem. Soc.*, 2004, **126**, 12162–72.
- 2 K. A. Vincent, J. A. Cracknell, O. Lenz, I. Zebger, B. Friedrich and F. A. Armstrong, *Proc. Natl. Acad. Sci. U. S. A.*, 2005, **102**, 16951–4.
- 3 K. A. Vincent, A. Parkin and F. A. Armstrong, *Chem. Rev.*, 2007, **107**, 4366–413.
- 4 M. J. Lukey, A. Parkin, M. M. Roessler, B. J. Murphy, J. Harmer, T. Palmer, F. Sargent and F. A. Armstrong, *J. Biol. Chem.*, 2010, **285**, 3928–38.
- 5 K. A. Bagley, J. C. J. Van Garderen, S. M. Chen, S. J. E. C. Duin, S. P. J. Albracht and W. H. Woodruff, *Biochemistry*, 1994, **33**, 9229–9236.
- 6 M.-E. Pandelia, H. Ogata, L. J. Currell, M. Flores and W. Lubitz, *Biochim. Biophys. Acta*, 2010, **1797**, 304–13.
- 7 A. L. DeLacey, C. Stadler, V. M. Fernandez, E. C. Hatchikian, H. J. Fan, S. Li and M. B. Hall, *J. Biol. Inorg. Chem.*, 2002, **7**, 318–326.
- 8 X. Luo, M. Brugna, P. Tron-Infossi, M. T. Giudici-Ortoni and É. Lojou, *J. Biol. Inorg. Chem.*, 2009, **14**, 1275–1288.
- 9 M.-E. Pandelia, P. Infossi, M. T. Giudici-Ortoni and W. Lubitz, *Biochemistry*, 2010, **49**, 8873–81.
- 10 J. Fritsch, O. Lenz and B. Friedrich, *Nat. Rev. Microbiol.*, 2013, **11**, 106–14.
- 11 W. Lubitz, H. Ogata, O. Ruediger and E. Reijerse, *Chem. Rev.*, 2014, **114**, 4081–4148.
- 12 P. A. Ash, J. Liu, N. Coutard, N. Heidary, M. Horch, I. Gudim, T. Simler, I. Zebger, O. Lenz and K. A. Vincent, *J. Phys. Chem. B*, 2015, **119**, 13807–13815.
- 13 H. Ogata, Y. Mizoguchi, N. Mizuno, K. Miki, S. Adachi, N. Yasuoka, T. Yagi, O. Yamauchi, S.

- Hirota and Y. Higuchi, *J. Am. Chem. Soc.*, 2002, **124**, 11628–11635.
- 14 H. Ogata, K. Nishikawa and W. Lubitz, *Nature*, 2015, **520**, 571–574.
- 15 A. Volbeda, L. Martin, E. Barbier, O. Gutiérrez-Sanz, A. L. De Lacey, P.-P. Liebgott, S. Dementin, M. Rousset and J. C. Fontecilla-Camps, *J. Biol. Inorg. Chem.*, 2015, **20**, 11–22.
- 16 J. W. van der Zwaan, S. P. J. Albracht, R. D. Fontijn and Y. B. M. Roelofs, *Biochim. Biophys. Acta*, 1986, **872**, 208–215.
- 17 R. P. Happe, W. Roseboom and S. P. J. Albracht, *FEBS J.*, 1999, **259**, 602 – 608.
- 18 M. M. Roessler, R. M. Evans, R. A. Davies, J. Harmer and F. A. Armstrong, *J. Am. Chem. Soc.*, 2012, **134**, 15581–94.
- 19 P. Kellers, M.-E. Pandelia, L. J. Currell, H. Görner and W. Lubitz, *Phys. Chem. Chem. Phys.*, 2009, **11**, 8680–8683.
- 20 B. J. Murphy, F. Sargent and F. A. Armstrong, *Energy Environ. Sci.*, 2014, **7**, 1426.

Chapter 8

Conclusions

The work presented in this thesis has demonstrated a novel IR spectroelectrochemical approach for the study of redox enzymes adsorbed on a carbon electrode and in direct electron transfer contact. A spectroelectrochemical flow cell system was designed, and it was shown to provide the good mass transport conditions and electrochemical control of protein film electrochemistry. Additionally, a method for adsorbing the hydrogenase enzyme on a high surface area carbon nanoparticle film was developed. This new combined-approach allows for the structural characterisation of electrocatalytic processes, by means of IR spectroscopy, to be undertaken whilst obtaining information on the activity of the enzyme as it is engaged in turnover, by means of electrochemistry.

In Chapter 4, a complete IR spectroelectrochemical redox characterisation of a hydrogenase adsorbed on a carbon electrode was shown for the first time. The redox states of the active site of hydrogenase 1 from *E. coli* were investigated under different pH conditions over a wide potential window. The following picture of the redox chemistry of the active site emerged.

One of the main important findings from this characterisation was the pH equilibrium that exists at the Ni-C level; which involve three isoelectronic states: Ni-C, Ni-L_{III} and Ni-L_{III}. It was shown that the active site responds to the external pH of the solution, and that this pH acts as a driving force that withdraws the proton away from the active site as the pH is increased. B and B' in the Figure are generic bases; however, B' is further from the bimetallic active site than B. A similar pH equilibrium is proposed for the two states detected at the Ni-R level; for which the dependence on pH on their relative intensities was described.

Another interesting effect that was presented in Chapter 4, was the change in the wavenumber position of the peaks as a function of pH. These changes were small, 1-5 cm⁻¹, and are likely to arise as changes in the protonation in the vicinity of the active site (not in the first coordination sphere), or H-bonding isomerisation of one of the cysteines of the active site. This phenomenon was observed for all the redox states over a wide pH range, for the first time. Previously it had only

been reported for Ni-C. Overall, rich pH dependent chemistry was characterised for Hyd-1, which can be relevant to mechanistic pathways involving the transport of protons from the active site.

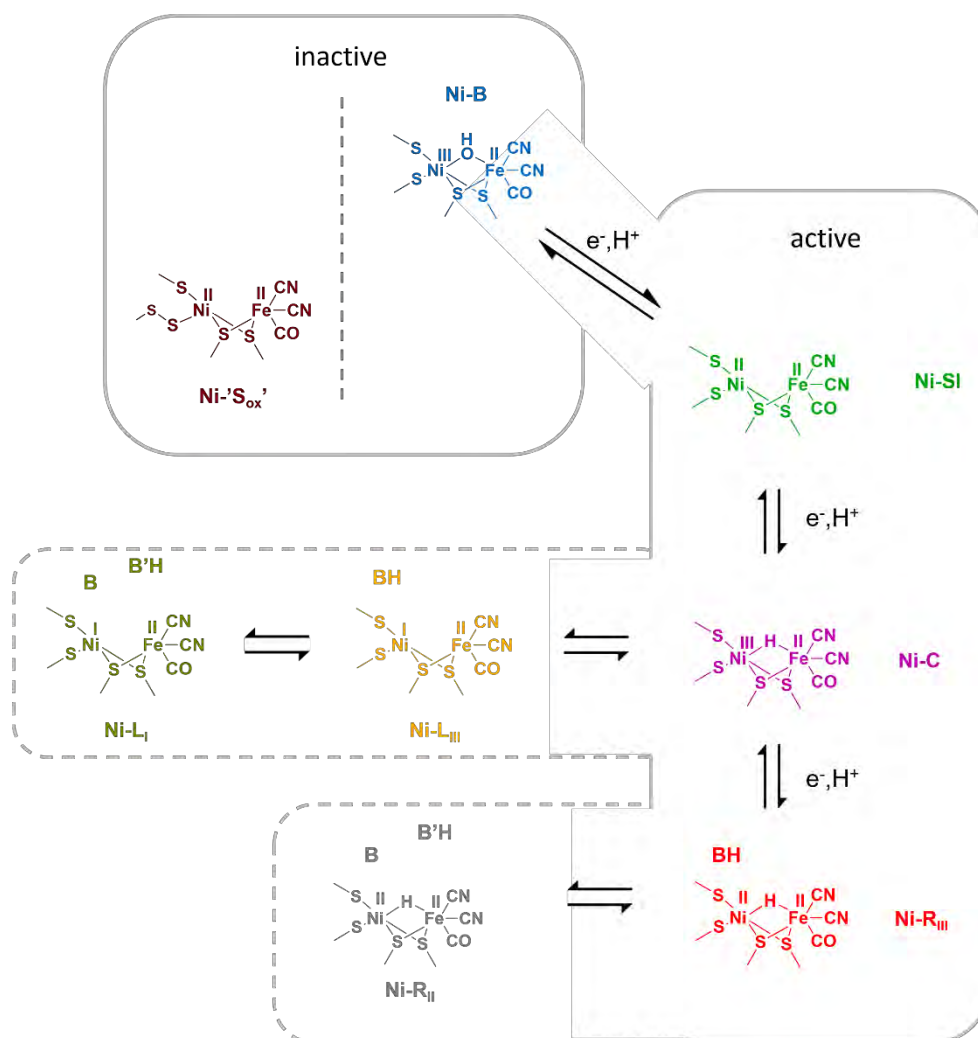


Figure 8.1 Scheme of the the redox states of Hyd-1 immobilised at a carbon electrode. Only one oxidised inactive state is detected, Ni-B. The Ni-'S_{ox}' is another inactive state that appears in some aerobic as-isolated preparations. The three active states Ni-SI, Ni-C and Ni-R have also been identified along with the description of different protonation species of the Ni-R state and of the Ni-L state.

In Chapter 5, Hyd-1 was studied by IR spectroelectrochemistry under turnover conditions. This represents the first study of this kind, of a hydrogenase adsorbed on a carbon electrode. The distribution of the redox states with potential was investigated and it was found that Ni-L is present at all times under catalytic turnover. This provides further, strong evidence for it being an intermediate in the catalytic cycle of this NiFe hydrogenases.

The following catalytic cycle is proposed, which also takes into account the proton as it moves away from the active site within the cycle. All the intermediates in this scheme were detected under turnover conditions. The effect of H_2 was also investigated and it was found that at lower H_2 concentrations the steady state concentrations of Ni-SI, and of Ni-B (when the potential is high enough) increase, consistent with the proposed mechanism. The effect of pH was also investigated, and the changes in the relative intensities of the pH dependent equilibria were also observed under turnover.

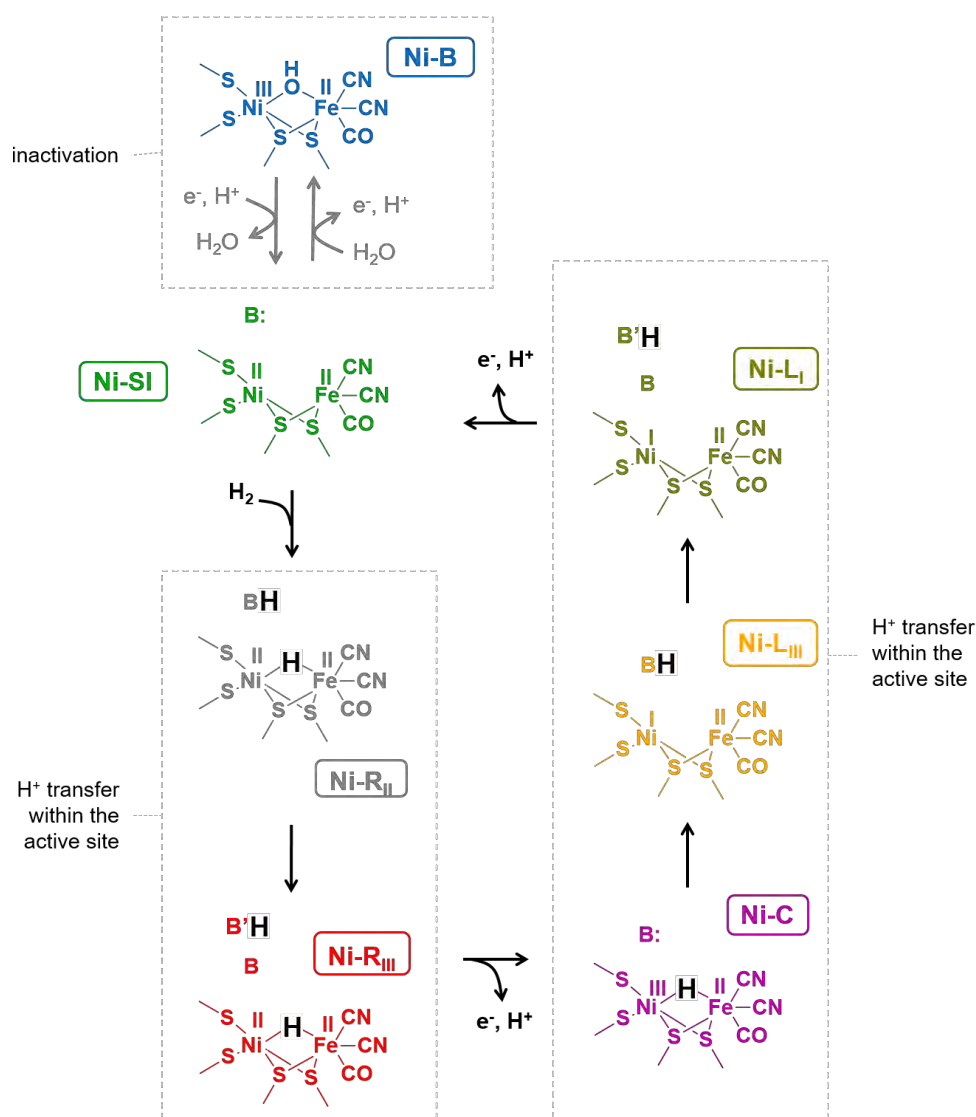


Figure 8.2 Mechanism for H_2 oxidation by Hyd-1. This new scheme is proposed in light of the findings of this thesis, and the most recent discussions in the literature about the role of new intermediates. All these states were detected spectroscopically under turnover. B and B' are not necessarily the same for Ni-R and Ni-L

The effect of O_2 on the catalytic oxidation of H_2 was investigated in Chapter 6. It was shown that the reaction of O_2 with *E. coli* Hyd-1, which is an O_2 -tolerant hydrogenase, is a 'clean' reaction in the sense that the only product detected from the reaction with O_2 , was the Ni-B state. This provides further evidence that O_2 -tolerant hydrogenases avoid forming damaged oxidised states of the active site upon the attack of O_2 , but a single Ni-B state, from which the enzyme can quickly recover once O_2 is taken out of the system.

The inhibition studies of CO in chapter 7 presented the first thorough investigation of an O_2 -tolerant hydrogenase with CO. It was shown that CO binds the active site of Hyd-1 in the Ni-SI state only, to form the Ni-SCO state (which was the only CO-bound state detected over a wide potential window). The spectroelectrochemical investigations of the CO inhibition of H_2 oxidation and H^+ reduction showed that CO does inhibit both of these processes; and that only one inactive CO-bound species formed as a result of this: Ni-SCO. These findings help to clarify the slightly confusing literature on the interaction of CO with O_2 -tolerant hydrogenases.

Overall, this thesis contributed to the understanding of the redox chemistry of the active site of NiFe hydrogenases by means of an approach that combines PFE with IR. Future work should include the investigation of variants of NiFe hydrogenases that could address the role of proton pathways in the vicinity of the active site. The detection of a H_2 -bound active site should be something important to address as well, as it hasn't been reported for these enzymes.

The comparison (by means of this technique) between this and other hydrogenases, not only NiFe hydrogenases, could also be very valuable in discovering key differences between these systems. The technique could be further extended to other redox metalloenzymes, that can bind IR active substrates, and provide new information on chemistry and structure of enzymatic catalytic processes.